LED AND OLED-BASED OPTIC SENSOR ARRAY FOR COLOURIMETRIC ANALYSIS

by

Caylin Jade Nell

Submitted in partial fulfilment of the requirements for the degree
Master of Engineering (Microelectronic Engineering)

in the

Department of Electrical, Electronic and Computer Engineering
Faculty of Engineering, Built Environment and Information Technology

UNIVERSITY OF PRETORIA

July 2020

SUMMARY

LED AND OLED-BASED OPTIC SENSOR ARRAY FOR COLOURIMETRIC ANALYSIS

by

Caylin Jade Nell

Supervisor:	Dr T-H Joubert
Department:	Electrical, Electronic and Computer Engineering
University:	University of Pretoria
Degree:	Master of Engineering (Microelectronic Engineering)
Keywords:	Angular response, colourimetric analysis, electron-hole regeneration, flexible electronics, inkjet printed electronics, LED-based light sensor, light detector, light emitter, OLED, optic sensor, photocurrent, point-of-need, sensor array, wavelength sensitivity.

In this report, the development of flexible OLED-based (organic light-emitting diodes) light emitter and detector array is discussed for low-cost colourimetric analysis of water samples.

LEDs have been used as optical sensors by measuring their discharge time, when exposed to different light intensities. This report investigates whether an LED emitter and detector array, with different colour LEDs and therefore wavelengths, can be used for colourimetric analysis (specifically a colourimetric pH test).

This report also investigates whether flexible OLEDs can be used to create a similar light emission and detection array as the LED array. The flexibility and inkjet printability of OLEDs make it desirable for lab-on-chip, microfluidic, rapid diagnostic devices, which is a growing field of research. Using OLEDs as light detectors is a novel concept; therefore OLED panels were characterized as light detecting devices in this report in terms of wavelength sensitivities, angular response, emission spectra, discharge time, photocurrent, capacitance, and resistance. These results were compared to the results of an LED, used as a light detector. A discrete model of the OLED was also simulated in SPICE software.

The manufacturing of OLEDs was also investigated. Printed electronics is a growing additive manufacturing technique that is capable of printing small, low-cost, printed electronic devices on flexible substrates. Inkjet printed electronics is of special interest as there is little material wastage and high resolutions are attainable. Flexible OLEDs have been manufactured using a combination of screen printing, inkjet printing, and nano-printing techniques. In this report, an investigation was done on whether a fully inkjet printed OLED can be manufactured. A fully inkjet printable OLED structure was simulated, and the layers of the OLED structure and layer thicknesses were then optimized to maximize the number of photons that exit the device.

LIST OF ABBREVIATIONS

ACPEL	Alternating current powder electroluminescent
ACTFEL	Alternating current thin film electroluminescent
ADC	Analogue to digital converter
AMOLED	Active matrix organic light emitting diode
AMQLED	Active matrix quantum dot light emitting diode
BCG	Bromocresol green
CIE	Commission Internationale de l'Elcairage
CMOS	Complementary Metal Oxide Semiconductor
DCPEL	Direct current powder electroluminescent
DCTFEL	Direct current thin film electroluminescent
EIL	Electron injection layer
ELD	Electroluminescent display
EML	Emissive layer
ETL	Electron transport layer
GPVDM	General-purpose photovoltaic device model
HIL	Hole injection layer
HSEL	Hybrid structure electroluminescent display
HTL	Hole transport layer
ILED	Inorganic light-emitting diode
IR	Infrared

ITO	Indium tin oxide
I-V	Current-voltage
LCR	Inductance, capacitance, resistance
LEC	Light-emitting electrochemical cells
LED	Light-emitting diode
LEP	Light-emitting polymer
MEH-PPV	Poly[2-methoxy-5-(2-ethylhexyloxy)-1,4-phenylenevinylene]
MOSFET	Metal-oxide semiconductor field-effect transistor
OLED	Organic light-emitting diode
PC	Polycarbonate
PEDD	Paired emitter detector-diode
PEDOT	PEDOT – poly(3,4-ethylenedioxythiophene)
PEDOT:PPS	PEDOT:PPS - poly(3,4-ethylenedioxythiophene) polystyrene sulfonate
PEI	Polyetherimide
PEL	Powder electroluminescent
pH	Potential of hydrogen
PLED	Polymer light-emitting diode
QLED/QDLED	Quantum dot light-emitting diode
RGB	Red, green, blue
smOLED	Small molecule organic light-emitting diode
SPICE	Simulation Program with Integrated Circuit Emphasis
SPR	Surface plasmon resonance
TFEL	Thin-film electroluminescent

THF	Tetrahydrofuran
TIR	Total internal reflection
UV	Ultraviolet

TABLE OF CONTENTS

CHAPTER 1 INTRODUCTION

1.1 PROBLEM STATEMENT

A flexible OLED-based light emitter and detector array need to be developed for low-cost colourimetric analysis of water for point-of-care and point-of-need applications.

1.1.1 Context of the problem

There is an increasing demand to develop low cost, biodegradable and flexible rapid diagnostic sensors for water quality monitoring and medical diagnosis [1] - [2]. Lab-on-chip technology is a fast-growing field of research. Lab-on-chip technologies can provide low cost, portable and disposable devices that can generate rapid test results for point-of-care and point-of-need applications [1]. Printed electronics is a growing additive manufacturing technique that can be used to manufacture devices such as biosensors [2] and light-emitting structures [3]. Small, low-cost, printed electronic devices can be printed on flexible substrates such as fabric, polymer films, and paper, which can be integrated with microfluidic lab-on-chip devices [3]. Inkjet printed electronics can be used to manufacture small high-resolution OLED structures, with minimal ink wastage. By using a printed OLED structure instead of a discrete LED, smaller dimensions can be attained. Primary detection methods in microfluidic channels include mechanical, electrochemical, and optical detection. The advantage of optical sensing of water is that real-time detection is possible, as opposed to mechanical detection, which often requires up to 30 minutes for detection. Optical detection modes include fluorescence, absorbance, SPR (surface plasmon resonance) and chemiluminescent detection. Optical devices such as photodiodes, LEDs, and waveguides can be developed small enough to be integrated into microfluidic devices, while also being cost-effective [4].

1.1.2 Research gap

LEDs have been used for both light-emitting and light detecting devices [5]. Conventionally phototransistors, photodiodes, and photoresistors are used as light detectors. LEDs have a similar p-n junction to photodiodes, which produces photons and thus emits light when a current passes through the junction and electron-hole regeneration occurs. Because LEDs have a similar p-n junction to photodiodes, LEDs will also generate a current when light is absorbed by the LED and can, therefore, be used as a light detector [6]. The amount of light absorbed by a conventional discrete LED can be determined by measuring the photocurrent that the LED generates when light is absorbed by it [7].

The photocurrent of a reverse biased LED has been used as a light detector for pH sensor applications [8]. The sensitivity of a reversed biased LED detector can be improved by measuring the LED discharge time, as opposed to the LED photocurrent [9]. This is done by using fast switching comparators that compare the capacitive voltage with a threshold value. The capacitive voltages, that are larger than the threshold voltage, are integrated over a specified time interval. The integrated value will decrease if the light intensity is increased because the discharge time of the LED will be faster [8].

The advantage of using an LED as a light detector is that LEDs only detect light over a limited range of wavelength and do not require additional optical filters to detect light in a specific wavelength band as in the case of photodiodes. LEDs, used as light detectors, can detect light that have wavelengths that are the same or shorter than the wavelength it is designed to produce [7]. Typical properties evaluated when analyzing light detectors are the generated photocurrent, angular response, efficiency, resolution, luminance sensitivity and linearity in comparison to absorbed light [7].

There is a growing interest in the development of inkjet printed OLEDs. The typical structure of an OLED consists of a transparent, conductive anode, hole injection layer (HIL), hole transport layer (HTL), emissive layer (EML), electron injection layer (EIL) or hole blocking layer, and an electron transport layer (ETL). When the electrons and holes undergo electron-hole recombination in the EML, photons are emitted, and the OLED emits light [3]. OLED structures can be modeled mathematically, in SPICE software (using relevant SPICE models) or simulated using physical simulation tools.

This research focuses on whether these printed OLEDs can be used as a light detecting sensor for microfluidic, lab-on-chip, rapid diagnosis devices.

1.2 RESEARCH OBJECTIVE AND QUESTIONS

1.2.1 Research objectives

Discrete reverse biased LEDs have been used as light-detecting sensors [5], [10]. This research will investigate whether flexible, printed OLEDs can be used in a similar fashion. It will include the characterization of OLEDs as light detectors in terms of linearity, spectral response, wavelength sensitivity, angular response, light absorbance, capacitive discharge time, and photocurrent. The research will also investigate whether an array of LEDs and an array of flexible OLED light emitters and detectors can be used for low-cost colourimetric analysis of liquid samples for point-of-care or point-of-need applications. The low-cost inkjet printed manufacturing techniques will also be explored and a simulation of a fully inkjet printed OLED will be optimized.

1.2.2 Research questions

- Can an array of LEDs, used as both light emitters and light detectors, be used for colourimetric analysis of liquid samples for point-of-care or point-of-need applications?
- Can an array of flexible OLEDs, used as both light emitters and light detectors, be used for colourimetric analysis of liquid samples for point-of-care or point-of-need applications?
- What is the relationship and characteristics of the generated photocurrent and discharge time in relation to the received illumination of the OLED light detector?
- Specifically:
  - What is the wavelength sensitivity of an OLED, used as a light detector?
  - What is the angular response to light of an OLED, used as a light detector?
- Can a reverse biased OLED be used as a light detecting sensor?

1.3 APPROACH

A discrete, off-of-the-shelf LED array used as both light emitters and detectors will be designed to determine whether they can be used for optical colourimetric analysis of various water samples for point-of-care and point-of-need applications.

Test setups will then be designed to fully characterize a reverse biased OLED when it is used as a light detector. An array of OLED emitters and detectors, with relevant control circuitry, will be designed to determine whether they can be used for optical colourimetric analysis of various water samples for point-of-care and point-of-need applications. The OLED array will be analysed in comparison to the LED array.

Manufacturing techniques of flexible OLEDs will be investigated, and a fully inkjet printable OLED structure will be proposed. The OLED light-emitting structure will be simulated and optimized in software, such as General-purpose photovoltaic device model (GPVDM) [11] or Fluxim, [12] to determine its characteristics and performance.

The OLED array will be compared with the LED array. The following design steps will be followed:

- Design an LED emitter and detector array that can be used for colourimetric analysis of water.
- Analyze the performance of an OLED structure as both a light emitter and a detector using simulation models and theoretical calculations.
- Design a test setup to characterize an OLED as a light detector in terms of linearity, spectral response, wavelength sensitivity, angular response, light absorbance, capacitive discharge time, dominant wavelength, and photocurrent.
- Design an OLED emitter and detector array that can be used for colourimetric analysis of water.
- Investigated manufacturing techniques to manufacturing low-cost, flexible OLEDs.
- Design a fully inkjet printable OLED structure.
- Simulate and optimize the OLED light-emitting structure in simulation software, such as GPVDM or Fluxim.

1.4 RESEARCH GOALS

- To determine the efficiency and accuracy of an array of flexible, printed light-emitting and light detecting OLEDs, used for colourimetric analysis for point-of-care and point-of-need applications.
- To characterize, model and optimize a reverse biased, flexible, OLED, used as a light detector.
- To design, simulate and optimize a fully inkjet printable OLED structure in simulation software.

1.5 RESEARCH CONTRIBUTION

Discrete reverse biased LEDs have been used as light-detecting sensors [5], [10]. This research will investigate whether flexible, printed OLEDs can be used in a similar fashion. It will include the characterization of OLEDs as light detectors in terms of linearity, spectral response, wavelength sensitivity, angular response, light absorbance, capacitive discharge time, dominant wavelength and photocurrent.

The research will also investigate whether an array of LED and an array of flexible OLED light emitters and detectors can be used for low-cost colourimetric analysis of liquid samples for point-of-care or point-of-need applications. Different low-cost manufacturing techniques can be used to manufacture OLEDs [3]. In this research, a fully inkjet printable OLED structure will be proposed, simulated and optimized in simulation software.

1.6 RESEARCH OUTPUTS

[1] C.J. Nell, T-H Joubert, “Reverse-biased OLED as a light detecting sensor.” *MDPI Sensors*, 2020. (Submitted for peer review)

1.7 DISSERTATION/THESIS OVERVIEW

In Chapter 2 a literature study is performed. It was found that colourimetric analysis tests can be used for water quality testing and analysis. It was also seen that LEDs have been used as light-detecting sensors for colourimetric analysis. LED structures consist of different layers in which electron-hole regeneration occurs, there are however many different types of light-emitting structures and the differences between them are discussed, with a specific focus on OLEDs. The manufacturing of light-emitting structures was also discussed, with an emphasis on inkjet printing due to its low cost, high resolutions, and minimal material wastage [13], [14]. Different photometric units used to characterize light sources are also discussed in detail.

In Chapter 3 the test setups and results of characterizing an LED as a light detector were discussed as well as the test setup and results of an LED emitter and detector array, used for colourimetric analysis of pH samples.

In Chapter 4 the test setups and results of characterizing an OLED panel used as a light detector were discussed as well as the test setup and results of an LED emitter and detector array, used for colourimetric analysis of water samples, coloured with food colouring.

In Chapter 5 the results of the simulated and optimized inkjet printable flexible OLED display are given.

In Chapter 6 the manufacturing procedure for inkjet printing the cathode of an OLED structure is given.

In Chapter 7 the LEDs and OLEDs, used for the light emitter and light detector sensor arrays for colourimetric analysis, are compared and discussed.

In Chapter 8 a conclusion is drawn about the research and the objectives that were completed and met.

CHAPTER 2 LITERATURE STUDY

2.1 CHAPTER OVERVIEW

The literature study is subdivided into 4 sections: low-cost methods to test water in rapid-diagnostic devices, LEDs used as light sensors for colourimetric-based optical rapid diagnostic devices, different types of light emitting structures and their operating principles, and manufacturing techniques to manufacture OLED-based light emitting structures that can be used in for colourimetric-based optical rapid diagnostic devices.

Section 2.2 discusses the different technologies used in low-cost diagnostic devices. It also provides a comparison between different optical test methods, with an emphasis on colourimetric optical tests, which is a primary focus in this research. The processes, methods, and reagents used for colourimetric analysis tests for water samples are also discussed.

In Section 2.3 LEDs used as light-detecting sensors are discussed. Different optical devices, which make use of LED light detectors, are also discussed in this section.

The structures and composition of different types of light-emitting structures are discussed in Section 2.4. A comparison is also made between electroluminescent-based devices and LED based devices. LED-based structures, with an emphasis on OLED structures, are discussed as well as the operating principles and light generation mechanisms of OLEDs. The transient characteristics of OLEDs are given, which includes the steady-state transient response, the injection-limited I-V response, and the bulk-limited current I-V response. The different photometry measurements and parameters that can be used to measure light sources, specifically the luminous intensity, luminous flux, illuminance, luminous energy, responsivity and radiance parameters are discussed, mathematically expressed, and compared. Lastly, Commission Internationale de l'Elcairage (CIE) diagrams, which are commonly used in the photometric analysis, are explained.

The manufacturing techniques for flexible OLED panels and devices are discussed in Section 2.5. There is a specific focus on inkjet printing manufacturing techniques as there is minimal ink wastage and high attainable resolutions in comparison to other manufacturing methods and inkjet printing techniques can be used on various flexible substrates.

2.2 LAB-ON-CHIP DEVICES FOR POINT-OF-CARE AND POINT-OF-NEED

Lab-on-chip devices are advantageous for point-of-care and point-of-need applications because they are low-cost, portable, can be massed produced using cheap manufacturing tools [15], fast and have a low power and reagent consumptions [7]. Lab-on-paper based analytic devices is a rising field of interest as it provides low-cost and biodegradable testing [1]. Primary detection methods in microfluidic channels on lab-on-chip devices, include mechanical, electrochemical and optical detection (2.1). The advantage of optical sensing of water is that real-time detection is possible in oppose to mechanical detection, which often requires up to 30 minutes for detection. Additionally, optical detection does not require control of the ion concentrations in the sample before detection as in the case of electrochemical detection [16].

Types of optical detection include fluorescence, absorbance, colourimetric, SPR (surface plasmon resonance) and chemiluminescent detection methods (Figure 2.1) [16]. Optical detection methods, especially colourimetric detection, commonly has a colour read out analysis method. The colour of the sample is compared to know reaction colours in order to determine the composition of the sample [5]. Optical devices such as photodiodes, LEDs, and waveguides can be developed small enough to be integrated into microfluidic devices, as well as being cost-effective. However, conventional instruments of optical detection such as spectrometers, lasers, and microscopes are more complex and are therefore more challenging to miniaturize for microfluidic applications [16].

2.3 COLOURIMETRIC ANALYSIS REAGENTS

Colourimetric analysis of liquid samples is done by adding a reagent to the sample. The sample then changes color, depending on the concentration of the substance being detected in the sample. Reagent test kits can be purchased from various manufacturers to test for different substances and impurities in water samples. Table 2.1 gives a summary of chemical test kits that can be used in the colourimetric analysis. Table 2.1 also gives the detection range of each test kit, analysis method, sample size, test method, test duration, expected color change and manufacturer of the test kit.

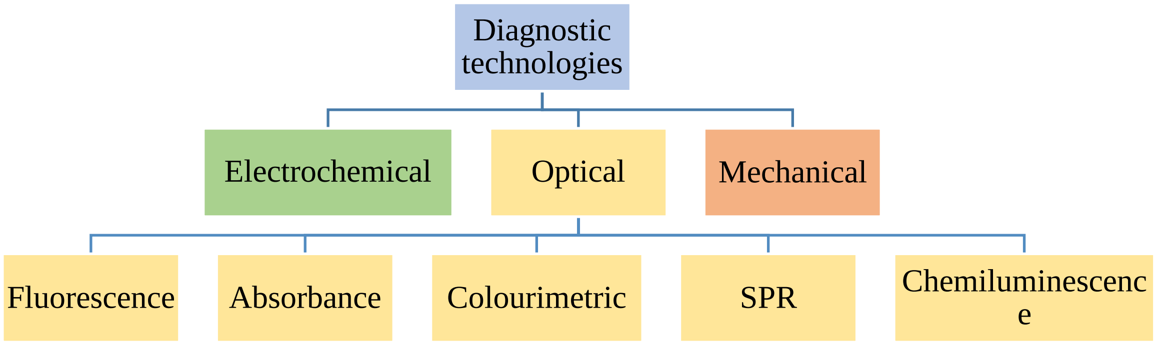

Figure 2.1 Primary detection methods in microfluidic diagnostic technologies.

2.4 USING AN LED AS A LIGHT DETECTOR FOR COLOURIMETRIC ANALYSIS

LEDs have been used as both light-emitting and light detecting devices [6]- [7], [17]- [18]. Conventionally phototransistors, photodiodes, and photoresistors are used as light detectors.

Table 2.1 Chemical test kits.

Sample	**Detection range**	**Sample size**	**Analysis method and test procedure**	**Time**	**Colour/ wavelength**	**Manufacturer**
pH [19], [20].	MQuant pH test	5 mL	Indicator solution: - Add 5 mL sample. - Add 2 drops of pH-1 reagent. - Colourimetrically determine pH [19].	1 min	Various	Merck
Iron (II& III)	0 to 5 mg/ L [21].	10 mL [21].	Conversion of the ferrous (Fe2+) state [21]. Procedure - 10 ml of water - Add HI 3834-0 reagent [21]. - Leave for 4 min Colourimetrically determine concentration [21].	4 min [21].	Orange [21].	HANNA Instruments
Chromium (VI)	0 to 1 mg/L [22].	5 mL [22].	Diphenylcarbohydrazide [22]. - 5 ml of water - Add HI 3846 reagent [22]. - Leave for 6 min Colourimetrically determine concentration [22].	6 min [22].	Purple [22].	HANNA Instruments
Copper	0 to 2.5 mg/L [23].	5 mL [23].	Bicinchoninate [23]. - 5 ml of water - Add HI 3847-0 reagent [23]. - Leave for 6 min Colourimetrically determine [23].	7 min [23].	Red	HANNA Instruments
Nitrate	0 to 50 mg/L [24].	10 mL [24].	Nitrates are reduced to nitrites, using cadmium reduction [24].	4 min [24].	Orange [24].	HANNA Instruments

Sample	Detection range	Sample size	Analysis method and test procedure	Time	Colour/ wavelength	Manufacturer
			• 10 ml of water • Add HI 3874 reagent [24]. • Shake vigorously for 1 min precisely. • Leave for 4 min Colourimetrically determine concentration [24].		Orange = 635–590 nm	
Nitrite	0 to 1 mg/L [25].	10 mL [25].	Chromotropic acid [25] • 10 ml of water • Add HI 3873 reagent [25]. • Shake gently for 15 s. • Leave for 6 min Colourimetrically determine concentration [25].	6.25 min [25].	Tinted pink [25].	HANNA Instruments
Free & total chlorine low range	0 to 0.7 mg/L [26].	10 mL [26].	• 10 ml of water • Fill a demineralized bottle with tap water. • Shake gently for at least 2 min. • Add 10 ml of demineralized water to the sample. • Shake to mix • Add HI 93701 reagent for free chlorine and HI 93711 reagent for total chlorine. • Shake to mix. • For total chlorine: wait 2min. Colourimetrically determine concentration [26].	4 – 5 min [26].	Tinted pink [26].	HANNA Instruments
Free & total chlorine medium range	0 to 3.5 mg/L [26].	5 mL [26].	DPD reagents [26]. • 5 ml of the water sample • Fill a demineralized bottle with tap water. • Shake gently for at least 2 min. • Add 5 ml of demineralized water to the sample. • Shake to mix • Add HI 93701 reagent for free chlorine and HI	4 – 5 min [26].	Tinted pink [26].	HANNA Instruments

Sample	**Detection range**	**Sample size**	**Analysis method and test procedure**	**Time**	**Colour/ wavelength**	**Manufacturer**
			93711 reagent for total chlorine. • Shake to mix. • For total chlorine: wait 2min. Colourimetrically determine concentration [26].			
Chloride	3 – 300 mg/L [27].	6 ml [27].	Mercury (II) thiocyanate followed by iron (III) ion reagents [27]. • Add 6 ml sample. • Add 6 drops of CL-1 reagent. • Add 6 drops of CL-2 reagent. Colourimetrically determine concentration [27].	1 min [27].	Red [27].	Merck
Nickel	0.02 – 0.5 mg/L [28].	20 ml [28].	Oxidation in iodine followed by dimethylglyoxime with an ammonia-based solution. (Merck 1.14420.0007 test) [28]. • Add a 20 ml sample. • Add reagent Ni-1 until a slight yellow colour persists (typically 4 drops). • Leave the solution for 1 min. • Add reagent Ni-2 until the pH of the solution is between 10 and 12 (typically 8 drops). • Add 8 drops of reagent Ni-3. Leave solution for 3 min [28].	4 – 5 min [28].	Red - brown [28].	Merck

Photodiodes consist of a p-n junction, with an intrinsic layer in between the p and n regions. When light is absorbed by the photodiode, electron-hole regeneration occurs in the depletion region which generates a photocurrent. The photocurrent produced is directly proportional to the amount of light that is absorbed by the photodiode [7].

LEDs have a similar p-n junction to photodiodes, which produces photons and thus emits light when a current passes through the junction and electron-hole regeneration occurs. LEDs will also generate a current when light is absorbed by it and can, therefore, be used as a light detector [7].

The advantage of using an LED as a light detector is that LEDs only detect light over a certain wavelength and do not require additional optical filters to detect light in a specific wavelength band as in the case of photodiodes [7]. This makes them a more cost-efficient light detecting device [17]. They are also compact and can be used to detect light over a large spectral range (UV to near-IR) and they filter out different wavelengths without the need for an additional filter, which makes them a cheaper light detection option.

LEDs, used as light detectors, can detect light that have wavelengths that are the same or shorter than the wavelength it is designed to produce [7].

The photocurrent of a reverse biased LED has been used as a light detector in pH sensor applications[8], [29], [30]. The disadvantage of using a reverse biased LED as a light detector is that it has lower sensitivity than other light detectors, such as photodiodes and phototransistors [18].

The light absorbed by an LED can be determined by measuring the photocurrent that the LED generates when light is absorbed by it [7]. The photocurrent is often very small, which makes it difficult to measure accurately and an expensive nano-amperometer is needed to measure such small photocurrents [17]. A reverse biased LED, using as a light sensor can be modeled with a current source and capacitor, as shown in Figure 2.2.

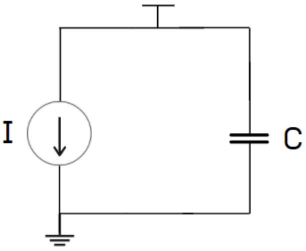

Figure 2.2. Model of an LED used as a light receiver.

Because a reverse biased LED is capacitive in nature (Figure 2.22), the sensitivity of a reversed biased LED detector can be improved by measuring the LED capacitive discharge time instead of the LED photocurrent [17]. This is done by using fast switching comparators that compares the voltage of the reverse bias LED with a threshold value. The voltages that are larger than the threshold voltage is integrated over a specified time interval. The integrated value will decrease if the light intensity is increased because the discharge time of the LED will be faster. A discharge curve of an LED that is discharged under fluorescent light from 5 V to a 1.7 V threshold voltage is shown in Figure 2.33 [8].

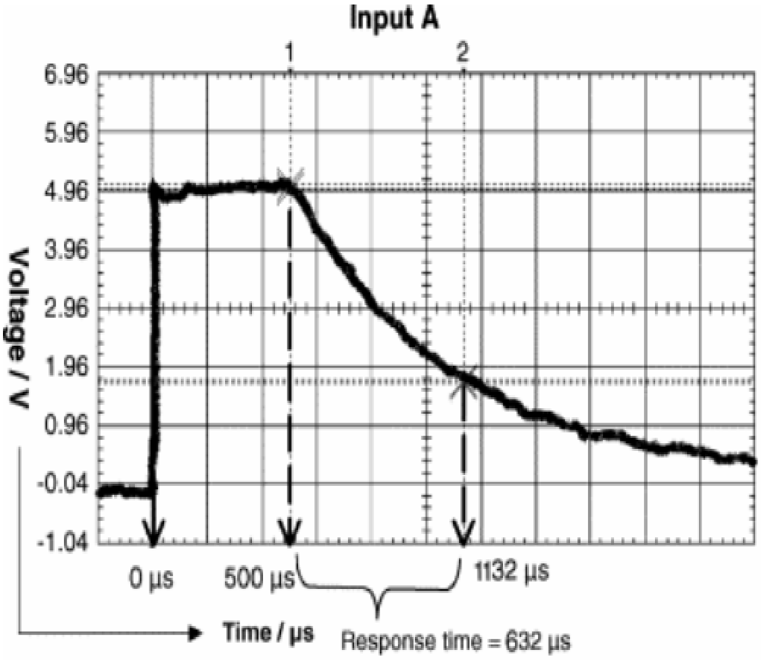

Figure 2.3. A discharge curve of an LED that is discharged under fluorescent light from 5 V to a 1.7 V threshold voltage. Taken from [8], with permission.

The LED can be connected to the analog pin of a microcontroller to measure the discharge time of the reverse bias LED. This is done by applying a reverse bias voltage over the LED to charge the capacitance of the reverse bias LED. The microcontroller port is then switched to input mode, where the discharge of the capacitance can be measured by the microcontroller [7]. This is a much more cost-efficient measurement technique than measuring the photocurrent directly [17].

An emitter LED and detector LED can be optimized for an improved linear detection range by fusing the LEDs together in a paired emitter detector-diode (PEDD) as shown in Figure 2.3 [10].

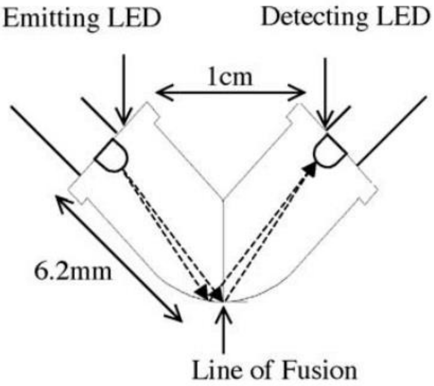

Figure 2.3. Paired emitter detector-diode (PEDD). Taken from [10], with permission.

2.4.1 Colourimetric detection using emitter LED array and detector photodiodes

An LED array can be implemented for colourimetric analysis by implementing an array of LEDs and photodetector [4], [5]. An optical colourimetric sensor has been designed, that makes use of an LED array of multiple wavelengths and two photodiodes, one measuring the light transmitted directly through the water (180 ° detection) and one measuring the light refracted/side-scattered at a 90 ° angle from the LED array emissions [31]. As seen in Figure 2.4, red, green, blue, yellow and IR LEDs were used as the light emitters in the sensor. The sensor was able to detect changes in water opacity and color due to water pollution.

Improvements on the sensor include the ability for it to be quickly and automatically calibrated on-site, improved data analysis techniques [31].

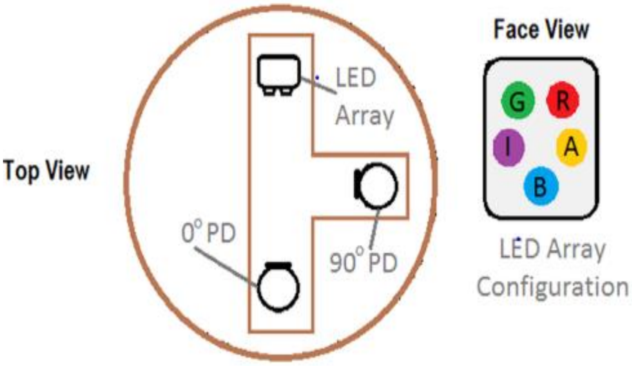

Figure 2.4 Colourimetric sensor, using an LED array and two photodiode detectors. Taken from [31], with permission.

2.4.2 Colourimetric PEDD detection of pH

LEDs have been used as optical sensors, as they have a spectral range from approximately 380-900 nm, are inexpensive, small and are easily available [32]. When an LED is used as both the emitter and the detector it is known as a Paired Emitter Detector Diode (PEDD). A PEDD has been applied for optical sensing in colourimetric flow analysis. The photocurrent generated by the detector LED, when light from the emitter fell on it, caused the capacitance of the reverse bias detector LED to discharge. A timing circuit was used to detect the capacitive discharge time from 5 V to 1.7 V. The system was able to determine the pH of a sample, using bromocresol green (BCG) as an indicator, in a pH range of 2.5 to 6.8. The advantages of the LED emitter and LED detector system was that it is power and cost-efficient and could operate from portably from a 9 V battery [32]. A diagram of the LED as an emitter and detector system, used for the pH determination, is shown in Figure 2.5 [32].

2.4.3 Disco photometer

A disco photometer [33] was made, using an emitter LED array and a single detector LED. An IR LED was used as the receiver LED, because it can be used to detect all wavelengths in the visible spectrum. The LEDs in the emitter LED array ranged from the UV to the IR range. The photometer was used to detect 3 different colour dyes and mixtures that contained all three dyes. Due to the different emission bands of the emitter LEDs, better selectivity can be achieved. It was also found that the LED reduced the complexity of data analysis, when analysing the dye mixtures, and improved the quality and accuracy of the collected data [33].

The samples have a specific absorption band, and the LEDs in the emitter array have distinct emission bands. The correlations between the absorption band of the sample and the emission band of the LED array allows for selectivity between different mixtures of dyes. The disco photometer is illustrated in Figure 2.6 [33]. Because only the reflectance measurements are used in the disco photometer, the photometer can also be used to detect colours of solid surfaces. The disco photometer's sensitivity can be improved by using LEDs with more narrow band gaps and the disco photometer's range can be improved by increasing the number of LEDs in the array [33].

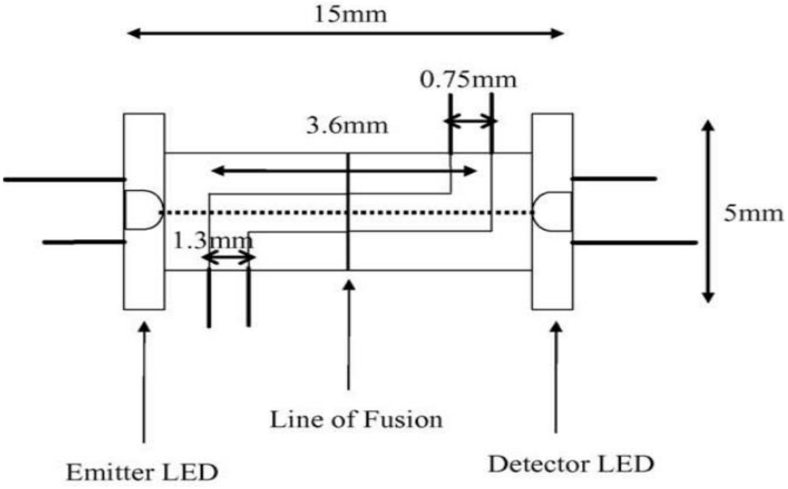

Figure 2.5 A flow analysis PEDD for colourimetric analysis of pH, using BCG. Taken from [32], *w*ith permission.

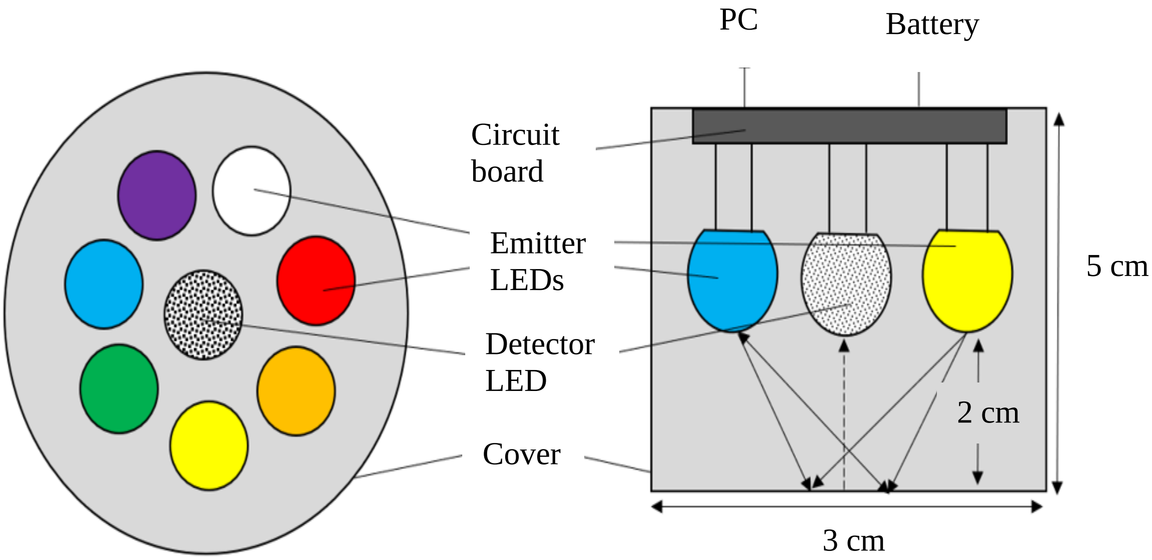

Figure 2.6. Disco photometer for colourimetric analysis. Adapted from [33], with permission.

2.5 LIGHT EMITTING STRUCTURES AND OPERATING PRINCIPLES

Printed light-emitting structures are divided into two types of displays. Namely, light-emitting diode (LED) based displays and electroluminescent displays (ELD). LED-based displays are generally composed of single crystals, while ELD displays are made from multiple inorganic crystals [34]. LED structures can be further categorized into standard LED displays, OLED displays, polymer light-emitting diode (PLED) displays, and quantum dot light-emitting diode (QLED/QDLED) displays. Specialized types of OLED and QLED displays are an active-matrix organic light-emitting diode (AMOLED) and active-matrix quantum dot light-emitting diodes (AMOLED) [3], [35].

Electroluminescent displays are subdivided into two main categories of displays. These are powder electroluminescent (PEL) displays and thin-film electroluminescent (TFEL) displays. Both PEL and TFEL displays can either be supplied with an AC or DC power supply. Therefore, PEL displays can be divided into alternating current PEL (ACPEL) and direct current (DCPEL) displays. Similarly, TFEL displays can be divided into alternating current TFEL (ACTFEL (Alternating current thin film electroluminescent)) and direct current TFEL (DCTFEL) displays [3]. Thick dielectric electroluminescent displays (TDEL) are modified ACTFEL displays, that have a single thick dielectric layer instead of the two dielectric layers [34]. Hybrid structure electroluminescent displays (HSEL) are types of ACPEL, that incorporates a polymer-based binder [36]. Light-emitting electrochemical cells (LEC) are a type of PLED, but with an added solid-state electrolyte [37]. The categorization of printed light-emitting structures is illustrated in Figure 2.7.

2.5.1 Printed Light Emitting diode (LED based displays)

LED-based displays emit light when an electric current goes through the displays. The LEDs generally consist of a single crystal-based material that is placed between two conductive layers. Transport layers and current limiting layers are also added to LED displays to enhance their light-emitting properties [3]. The light emission of LED displays is caused by electron recombination between the conduction and valence band of the light-emitting material. Defects and impurities in the LED can cause electron recombination that does not lead to photon generation. This decreases the luminance of the display [34].

Printed LED's are typically made from an inorganic emitter that is placed between two conductors. They are also known as inorganic light-emitting diodes (ILED). LEDs emit light when a DC voltage is applied across the light-emitting layer. A current limiting layer is often added between the cathode and the light-emitting layer to prevent too much current from passing through the EML and damaging it [3], [37]. Nitride based materials, such as gallium nitride and indium nitride, that are in group III-V, are good light-emitting materials for LED applications and emit green or blue light when a DC voltage is applied [38]. Another good light-light emitting layer for LED applications is nanoparticles that are dispersed in a binding material. The binders enhance current flow and energy transfer to the light-emitting particles so that they illuminate [3].

2.5.2 Quantum dot light emitting diode (QDLED/QLED)

When the light-emitting layer of an LED device is composed of quantum dots it is referred to as a QLED [3]. ETL and HTL are also commonly added between the conductors and quantum dot light-emitting layer. The transport layers in QLED displays are generally organic materials [39].

Quantum dots are nanoclusters that are placed into a solution. The nanoclusters are quasi-zero in dimension and are coated with semiconductors that have large energy bandgaps [40]. The variance of the quantum dot sizes in the ink has a great effect on the quality of the QLED display [39]. Quantum dots that are Cadmium based, such as CdSe (Cadmium Selenide) and CdS (Cadmium Sulfide), have good luminescent characteristics but contain heavy metals that are toxic and therefore have a negative impact on the environment and can be harmful to people. Non-cadmium-based quantum dot materials such as ZnS (Zinc Sulfide) and $CuInS_2$ (Copper Indium Sulfide) have been attempted, but they are not as efficient as cadmium-based quantum dot materials [40].

QLED's can be manufactured using inkjet printed electronic techniques on ITO-based substrates. The luminescent properties of the devices, however, are still not sufficiently optimal for most applications. The performance of the display can be improved by annealing the quantum dot light-emitting layer in a nitrogen chamber after it has been inkjet printed. Additionally, if a layer of poly (9-vinlycarbazole) is spin-coated on top of the quantum dot layer, the turn-on voltage of the display decreases, and display’s efficiency increases [40].

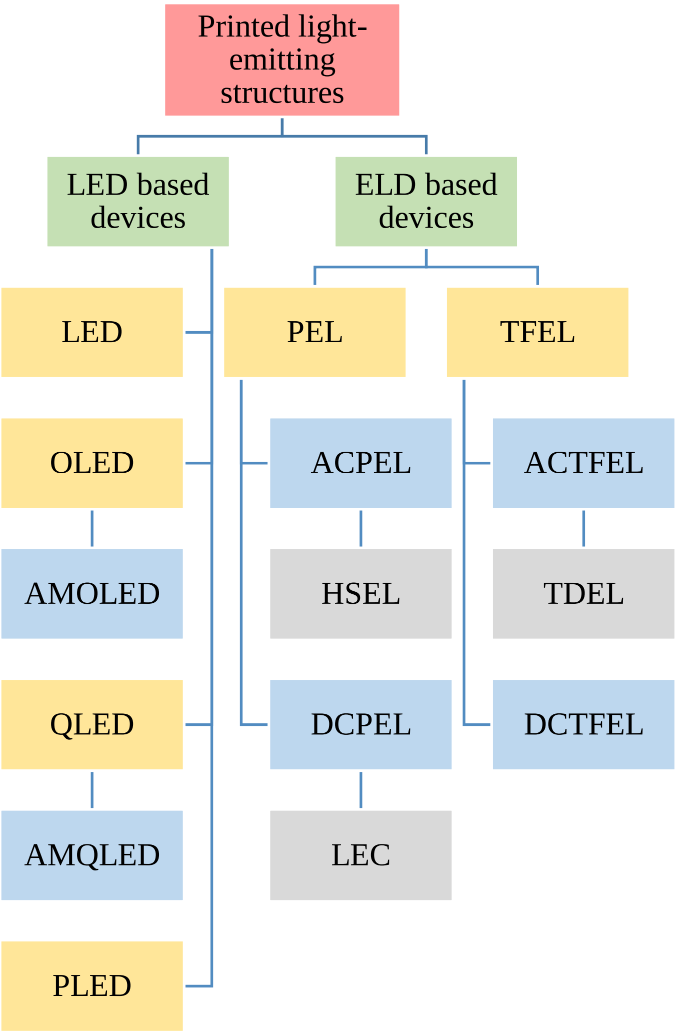

Figure 2.7. Categorization of printed light-emitting structures.

2.5.3 Active matrix organic light-emitting diode (AMOLED) and quantum dot light emitting diode (AMQDLED/AMQLED)

A multi-coloured active-matrix QLED can be achieved if multi-coloured quantum dot-based pixels are printed onto a MOSFET back-panel. AMQLED's displays can be manufactured using inkjet printed electronic techniques and can emit light as bright as 400 cdm^{-2} [35].

As in the case of AMQLED, an active-matrix OLED can be manufactured by printing OLED pixels onto a mosfet back-panel [41].

2.5.4 Polymer organic light-emitting diode (PLED)

PLEDs have a polymer-based light-emitting layer, which is placed between two conductors. The efficiency of the display is reliant on the quantity of holes and electrons that are injected into the light-emitting layer. Therefore, additional ETLs and HTLs are added next to the light-emitting layer to improve functionality [42]. The PLED structure is simpler than OLEDs because electron and hole injection layers are not required next to the transport layers. This makes the manufacturing of PLED's easier than OLEDs [34]. Poly[2-methoxy-5-(2'-ethylhexyloxy)-p-phenylenevinylene (MEH-PPV) is an inkjet printable, polymer-based, light-emitting material that can be used in PLED devices [43].

2.5.5 Organic light-emitting diode (OLED)

A typical OLED structure is illustrated in Figure 2.8**.** The basic structure consists of a bottom conductive anode that is printed onto a substrate, an EML and an upper conductive cathode. An additional HIL, HTL, EIL and ETL are commonly added to the structure to enhance the performance and brightness of the electroluminescent structure [41], [44]. The typical thickness is given in Table 2.2 [3].

Processes, such as the pretreatment of the substrate and printing uniformity of the EML, are critically important in achieving maximal brightness in OLED displays. The advantage of printed OLED displays is that they are typically thinner than other displays. This implies that higher refresh rates and lower power consumption can be achieved in these devices [36].

Table 2.2. Layer thickness in OLED displays **[3]**.

Layer	**Thickness (nm)**
Anode	60
HIL	1
HTL	150
EML	70
ETL	10
EIL	0.5
Cathode	100

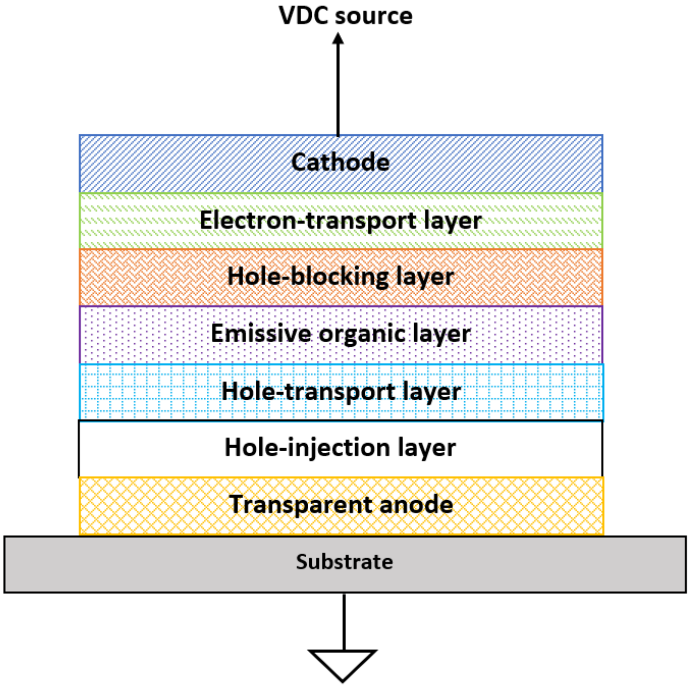

Figure 2.8. OLED light-emitting display structure. Adapted from [45] © 2019 IEEE and [44], with permission.

2.5.6 Comparison of light-emitting structures

The advantages and disadvantages of different light-emitting structures are compared in Table 2.3.

2.6 FLEXIBLE OLED OPERATING PRINCIPLES

Because OLEDs can be used to create thin, low power consumption [46] displays, and the EML layer can be inkjet printed (unlike PLED and electroluminescent based structures) it was selected as the light emitting structure for the PEDD.

OLED displays typically consist of several layers, as shown in Figure 2.8. OLEDs can be optimized, using mathematical and simulation models to optimize light-emission, decrease power consumption and determine the optimal thickness of each layer in an OLED structure. When an electric potential is applied across the anode and cathode of the OLED structure, electrons are injected from the cathode and holes are emitted from the anode.

The electrons and holes are transferred to the EML, through the EIL and ETL and HIL and HTL layers, respectively. When the electrons and holes undergo electron-hole recombination in the EML, photons are emitted and the OLED emits light [49].

When an OLED emits light, thin-film theory can be applied to the OLED structure. The thin-film theory allows the OLED in its emissive state to be modeled as a single cavity with two mirror surfaces on either side of the cavity.

Table 2.3. Comparison of different light displays.

Light display	Advantages	Disadvantages
LED	• Nanoparticle-based EML can be implemented [3]. • Simple structure [3].	• Non-organic [3], [37].
OLED	• Thin displays [46]. • High refresh rates [46]. • Low power consumption [46].	• Complex structure [3].
QLED	• Inkjet printable EML [35]. • Quantum dots are often toxic [40].	• Limited luminescent properties [35].
PLED	• Simpler structure than OLED [34].	• More complex structures than LED and QLED [3].
PEL	• AC or DC application [3]. • Simple structure [3]. • Simple to manufacture [3].	• Nanoparticle-based materials cannot be used as the light-emitting layer in ACPEL (Alternating current powder electroluminescent) [3]. • The EML is typically not inkjet printable. • Limited display brightness [47]. • Short lifespan [34]. • Poor light contrast [34]. • Low pixel resolution [34].
TFEL	• High brightness [48]. • Good display contrast [48]. • Good image clarity [48]. • AC or DC application [3].	• More complex structure than PEL [3].

The single cavity between the two interfaces represents the EML of the OLED. Dipoles in the EML, close to one interface, radiate waves that are scattered in multiple directions and are reflected between the two interfaces. The sum of the waves that propagate through an interface, is the total emitted field of the OLED. To increase the efficiency of the OLED, the waves that exit the device through the interface need to increase, and the reflected waves need to decrease. The thickness of the EML, as well as the boundary of adjacent layers, greatly influences the efficiency of the OLED device [49].

LED-based light-emitting structures emit light due to an electron-hole recombination mechanism. Electrons are excited to higher energy states when a sufficient electric field is applied across a material. These excited electrons in an emissive material fall back to their original energy level and the excess energy is released as photons. The wavelength of the emitted light determines the colour of light emission and the bandgap energy and the wavelength of the emitted light are inversely proportional according to the Planck-Einstein equation [50].

The energy bandgap of the light-emitting materials can be altered by adding donor or acceptor impurities to the material. Therefore, the colour of light emission can be controlled by doping the emissive material [51]. The electron-hole recombination process is illustrated in Figure 2.9 [52]**.** The electron-hole recombination at p-n junctions in devices such as LEDs, can either be radiative or non-radiative. If the recombination process gives rise to a photon being emitted, it is classified as radiative recombination.

While if the recombination process produces heat or occurs in quasi-neutral n-type and p-type regions, no photon is released, and it is classified as non-radiative recombination [53].

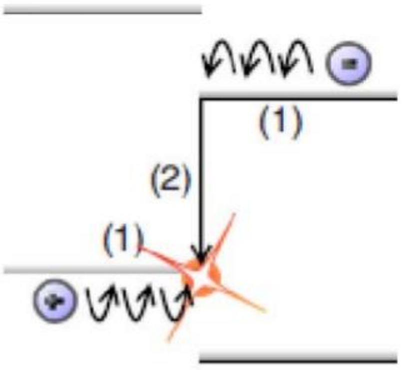

Figure 2.9. Energy states and electron-hole recombination that give rise to light emission. Taken from [52]**,** © 2010 IEEE.

Non-radiative recombination often occurs because of defects or traps in the light-emitting structure. Non-radiative recombination can also occur due to the Auger process, whereby the excited electrons excite other electrons that are already in the conduction band, to a higher energy level within the conduction band, instead of relaxing back to its original energy level and emitting a photon. The excited electrons from the conduction band, release non-radiative phonons when they relax back to their original conduction energy band [53].

The performance of a light-emitting device can be measured by its current density, luminous efficiency or external quantum efficiency (η_{ext}). Equation (2.1) describes external quantum efficiency, whereby η_r is the electron-hole recombination probability, φ_f is the fluorescent quantum efficiency, η_{out} is the radiative decay probability and χ is the fraction of emitted photons that exit the device [54].

$$\boldsymbol{\eta_{ext} = \eta_r \varphi_f \chi \eta_{out}} \tag{2.1}$$

The typical structure of an OLED consists of a transparent anode, HIL, HTL, EML, EIL or hole-blocking layer, ETL and a conductive cathode as can be seen in Figure 2.8 [3]**.** The anode needs to be transparent for the emissive light to be visible. The transparent anode can either be printed as the first layer on transparent substrates, such as glass and certain polymers or it can be printed as the last layer if a non-transparent substrate is used [36], [46], [55], [56]. The function, material, and typical thickness for each layer in an OLED are summarized in Table 2.4.

The cathode of an OLED injects electrons into the OLED. The ETL and EIL layer injects additional electrons and transports the electrons to the EML, which is situated between the ETL and HTL. Similarly, the transparent anode injects holes into the OLED structure. The HTL and HIL inject additional holes and transports the holes to the EML. At the pn-junction, between the HTL and ETL, there is an emissive material. Electron-hole recombination occurs at this pn-junction, causing the EML to release photons, and therefore causes the OLED to emit light which is visible through the transparent anode. Figure 2.10 illustrates the electron and hole movement in an OLED structure for light-emission [57] and Table 2.4 gives a summary of the functionality and typical thickness of each layer.

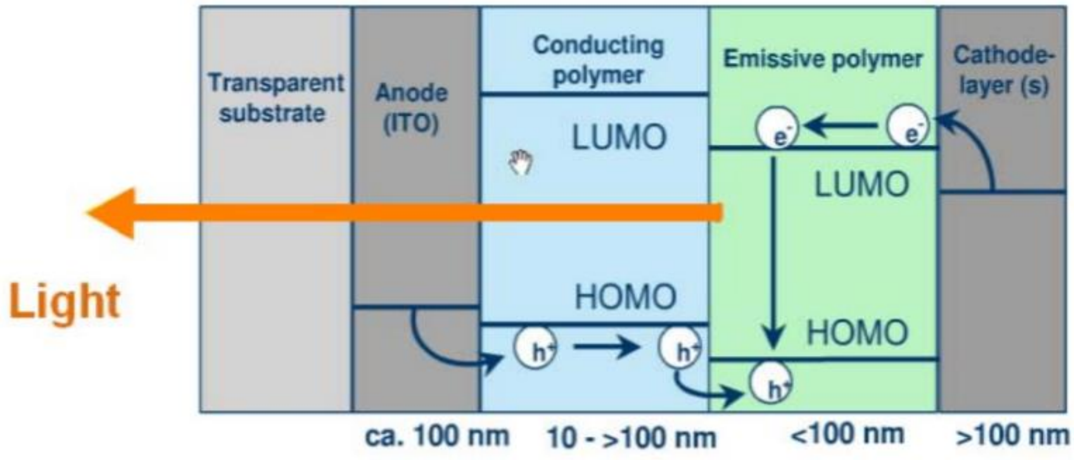

Figure 2.10. Energy diagram and Electron and hole movement in an OLED structure. Taken from [70], © 2012 IEEE.

Table 2.4 OLED layer functionality and materials.

Layer	**Function**	**Typical materials**	**Thickness (nm)** [34]
Cathode	The conductive cathode is used in conjunction with the transparent anode to apply an electric potential across the device so that photons are emitted from the EML [3].	Either silver [58] - [59] or gold [43] can be inkjet printed and used as the cathode. Aluminium can also be used, but it is not inkjet printable [60].	100
ETL	The ETL increases electron transportation in the devices and thus improves the light-emitting properties of the device. The ETLs efficiency can be improved by adding n-type dopants [34].	Manganese doped Cadmium sulfide can be used as an ETL in ZnS based light-emitting devices and Trisphenylbenzimidazolyl benzene (TPBi) [34], [59], [61] or Zinc oxide (ZnO) [62] can be used as the ETL in QLED displays.	10
EIL	The EIL increases the light-emitting properties of the device by decreasing the charge barrier between the ETL and cathode [62], [63].	The EIL is often omitted from the OLED structure but LiF, Na_3PO_4, NaCl. Na_3PO_4 are good EILs in devices that have an Alq3 ETLs [60].	0.5
EML	EML emits photons when an electric potential is applied across the device [64].	Hybrid nanoparticle made from ZnO nanoparticles can be used as the EML in OLED displays [64].	70

Layer	**Function**	**Typical materials**	**Thickness (nm)** [34]
		Fluorescein and Alq (Tris (8-hydroxyquinoline) aluminium) can be used to produce electroluminescent hybrid nanoparticles suitable for OLED applications [64].	
HTL	The HTL is added to decrease the charge barrier that forms between the EML and HIL in OLED displays that have PEDOT: PSS HILs [62]. The efficiency of the HTL can be increased by added p-type dopants [34].	NPB [65], TPD, PC [59] and α-NPD [66] can be used as the HTL in devices that have PEDOT: PPS HIL.	150
HIL	The HIL is added to increase the light-emitting properties of the display [62].	In devices with ITO anodes, PEDOT based materials can be used as the HIL [46], [67]. PEDOT: PSS and ZnO [68] can each be used as a HIL in OLEDS [62]. PEDOT: PSS can also be doped with ZnO and be used as the HIL. ZnOPEDOT: PSS is seen to be a better HIL than PEDOT: PSS and can enhance the luminescence of	1

Layer	**Function**	**Typical materials**	**Thickness (nm)** [34]
		a light-emitting structure by 4.5 times [68].	
Transparent anode	The transparent anode provides a conductive medium that can be used in conjunction with the cathode to apply an electric potential across the device. Its transparency, or semi-transparency, allows the emitted light from the EML layer to be visible through the conductor [3].	ITO [46], PEDOT: PSS or PEDOT: PTS [65] can be used as the transparent anode. Studies have shown that PEDOT: PTS has better performance in the fabrication of OLED displays than ITO [65]. Hydrogen doped ZnO can also be used as a transparent conductive anode and has comparable performance to ITO anodes [69].	60

2.6.1 Steady-state transient characteristics of OLEDs

The *I-V* (steady-state transient) characteristics of an OLED structure is an important characteristic to analyze as the OLED brightness is related to the current density in the OLED structure. The relationship between the current density, operating voltage, and luminescence of an OLED is illustrated in Figure 2.11**.** As the current density in the OLED structure increases, so does the device luminescence [71].

The current in an OLED structure is primarily limited by the injection and bulk limiting currents, which is mathematically modeled in the subsequent subsections.

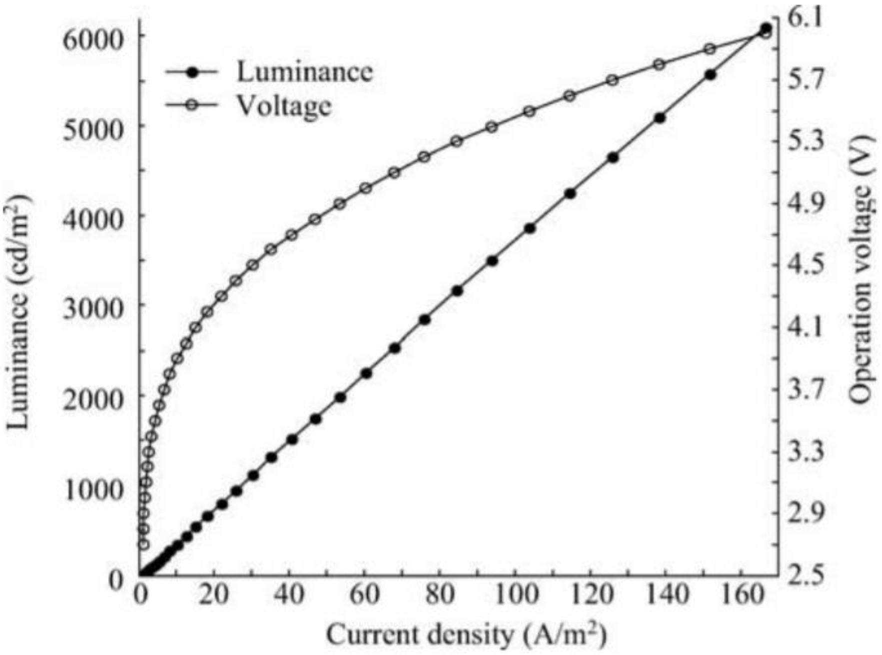

Figure 2.11. A graph illustrating the relationship between the current density, operating voltage, and luminescence in an OLED display. Taken from [71], with permission.

2.6.2 Injection-limited I-V relationship

The current from a metal to an organic material is known as the injection-limited current (I_i). This current occurs between the metal anode and the adjacent organic material in OLED displays. The injection-limited current in OLEDs can be expressed using (2.1) [72].

$$I_i = q\mu EN\exp\left(\frac{-q\emptyset_B}{kT}\right)\exp\left(\frac{q\gamma}{kT}\sqrt{E}\right), \tag{2.1}$$

where E is the electric field, μ is the electron mobility, q is the charge on the conductive metal layer, N is the density of charge, T is the temperature, k is the Boltzmann constant and $\emptyset_B$ is the height of the injection barrier between the metal and the organic material. A Schottky barrier exists between the conductive metal layer and the organic layer. The reduction in this barrier due to image force is expressed by γ [72].

The Poole-Frenkel model can be used to model the charge mobility in OLED displays (μ_{PF}) and is shown in (2.2) [72], where β is the Poole-Frenkel factor, μ_o is the temperature-independent pre-factor mobility and ε_o is the thermal activation energy of the trapped carrier charge.

$$\boldsymbol{\mu_{PF} = \mu_o \exp\left(\frac{-q\varepsilon_o}{kT}\right) \exp\left(\frac{q\beta}{kT}\sqrt{E}\right)} \tag{2.2}$$

The simplified relationship between the electric field (E), applied voltage (V) and layer thickness (L) for a parallel plate capacitor can be expressed as shown in (2.4) [72].

$$\boldsymbol{E = \frac{V}{L}} \tag{2.3}$$

By combining (2.1), (2.2) and (2.4), the *I-V* relationship for electrons and holes can be expressed as (2.4) and (2.5) respectively [72].

$$\boldsymbol{I_{i_e} = q\mu_{oe}N_e\frac{V_e}{L_e}\exp\left(-\frac{q(\varepsilon_{oe}+\emptyset_{Be})}{kT}+\frac{q(\gamma_e+\beta_e)}{kT}\sqrt{\frac{V_e}{L_e}}\right)} \tag{2.4}$$

$$\boldsymbol{I_{i_h} = q\mu_{oh}N_h\frac{V_h}{L_h}\exp\left(-\frac{q(\varepsilon_{oh}+\emptyset_{Bh})}{kT}+\frac{q(\gamma_h+\beta_h)}{kT}\sqrt{\frac{V_h}{L_h}}\right)} \tag{2.5}$$

2.6.3 Bulk-limited current I-V relationship

Poisson’s equation, with the charge mobility’s dependency on the electric field, can be used to express the bulk current as shown in (2.7), whereby , β is the Poole-Frenkel factor, E is the electric field, I_b is the bulk current, μ_o is the free space permeability, ε_r is the relative permittivity and ε_o is the free space permittivity [72]

$$\frac{I_b}{\mu_o\varepsilon_r\varepsilon_o}x = \frac{2}{\beta^4}\exp\left(\beta\sqrt{E}\right)\left(\beta^3E^{\frac{3}{2}} - 3\beta^2E + 6\beta\sqrt{E} - 6\right) \tag{2.7}$$

The *I-V* characteristic for the bulk-limited current (I_{b_h}) can be expressed using (2.8) and (2.9) for the electrons and hole respectively, provided that $\beta\sqrt{E}$ is greater than 1. Whereby, *α,* is the term used to adjust the value of *E* to a real number when (2.7) is integrated and simplified to obtain the *I-V* characteristic that is shown in (2.8) and (2.9) [72].

$$I_{b_e} = \frac{2\mu_{oe}\varepsilon_{re}\varepsilon_{oe}}{\beta_e}\alpha_e^{\frac{3}{2}}\frac{V_e^{\frac{3}{2}}}{L_e^{\frac{5}{2}}}\exp\left(\beta_e\sqrt{\alpha_e\frac{V_e}{L_e}}\right) \tag{2.8}$$

$$I_{b_h} = \frac{2\mu_{oh}\varepsilon_{rh}\varepsilon_{oh}}{\beta_h}\alpha_h^{\frac{3}{2}}\frac{V_h^{\frac{3}{2}}}{L_h^{\frac{5}{2}}}\exp\left(\beta_h\sqrt{\alpha_h\frac{V_h}{L_h}}\right) \tag{2.9}$$

2.6.4 Photometry measurements of LEDs and OLEDs

There is a few parameters that are commonly used for photometric analysis. These include luminous intensity, luminous flux, luminance, illuminance, and luminous energy. Luminous intensity (candela) measures how bright the area is that a light source lights up, while luminous flux is a measure of the total light emitted or radiative energy emitted by the light source. Luminous flux is the most accurate photometric parameter to measure when characterizing a light source, but it also requires the most complex and expensive test setup to measure accurately [73]. Table 2.5 gives a summary of photometric parameters and their SI units [73].

2.6.4.1. Luminance

The luminous intensity (candela) that is emitted perpendicular to a light-emitting device is known as luminance and is given in candela per square meter or foot-Lamberts.

Table 2.5. Photometric SI units [73].

Quantity	Symbol	Unit
Luminous intensity	I_v	Candela (cd or lm/sr)
Luminous flux	Φ_v	Lumen (cd·sr or lm)
Luminance	L_v	Cd/m^2
Illuminance	E_v	Lx (lumens/ m^2)
Luminous energy	Q_v	lm·s

The measurement also typically takes the sensitivity of a human eye to different wavelengths of light into consideration [74].

It can be said to measure the brightness and illustrates how the brightness of the emitted light varies over wavelength [73] and can be mathematically calculated using (2.10), whereby L_v is the luminance of the light source, E_v is the illuminance, R_i is the fraction of incident light, b is the reflectance factor of the light surface, I_v is the intensity of the light beam and θ is the incident angle of the light beam [73].

$$\boldsymbol{L_v = \frac{1}{\pi} \times E_v = \frac{R_i}{\pi} \times E_v = \frac{1}{\pi} \times b \times I_v \times \cos\theta} \qquad (2.10)$$

For visible light, the light intensity of a light source is measured in lumen per unit solid angle (lm/sr) or candela [18]. Contrary to luminous flux, luminous intensity gives the power of light in a specific direction and not in all directions. Luminous intensity is described as shown in (2.11), whereby *lm* is the number of lumens measured and *st* is one steradian solid angle [73].

$$I_v = \frac{lm}{st} \tag{2.11}$$

2.6.4.2. Illuminance

The visible flux density is known as the illuminance of a light source and is measured in lumen per square meter (lux). Illuminance measurements consider the light that a human's eye perceives. Because a human's eye is more sensitive to some wavelengths than others and is weighted by a factor known as the luminosity factor [7].

It can also be said that the amount of light that illuminates a surface at a distance from the light source is known as illuminance. The illuminance is the lumens per unit area squared and is measured in lux [73], [75].

Illuminance in lux is described by (2.12), whereby *Ev* is the surface illuminance (lux), Φ_v is the luminous flux (lumen) and A is the area of the illuminated surface [73].

$$E_v = \frac{\Phi_v}{A} \tag{2.12}$$

Another method of calculating the illuminance is depicted by (2.13), whereby l is the luminous intensity of the light that is directed at the illuminated surface, d is the distance between the light source and the object and θ is the angle between a point on an illuminated surface and the light coming from the light source [7].

$$E_v = \frac{l}{d^2} \times \cos\theta \tag{2.13}$$

2.6.4.3. Luminous flux

The light that is emitted in all directions across the visible spectrum per unit time is known as the luminous flux (Φ_v) of a light source and is measured in lumen [73].

One lumen is emitted from a device when one candela of luminous intensity (l_v) is emitted from a light source towards a one steradian solid angle (ß) (2.14) [73].

$$\boldsymbol{\Phi_v = l_v}\text{ß} \tag{2.14}$$

Luminous flux expresses the relationship between radiometric measurements and the human eye's ability to see the emitted light [75]. Luminous flux can be calculated by multiplying the luminous efficiency of a light source by the radiant flux of the light source. Equation (2.15) can be used to determine the luminous flux of a light source, where K_m is the maximum value of the spectral luminous efficiency, $V(\lambda)$ is the standard luminous efficiency and $\Phi_E(\lambda)$ is the radiant flux [75].

$$\boldsymbol{Luminous\ flux = K_m \times \Phi_E(\lambda) \times V(\lambda)} \tag{2.15}$$

If a light source does not have a single narrow-band spectral component, but rather a distributed light spectrum (Figure 2.12), the luminous flux can be calculated by integrating the radiometric power at each wavelength of the light spectrum from a wavelength of 380 nm to 780 m, and then multiplying it by the maximum spectral luminous efficiency (K_m) (2.16) [75]. Equation (2.16) can also be used to convert the measured results of a spectrometer to luminous flux.

$$\boldsymbol{\Phi_v = Km \int_{380}^{780} \Phi_e(\lambda)\, V(\lambda)\, d\lambda} \tag{2.16}$$

2.6.5 Photometry measurements of photodetectors

There are a few parameters that are commonly used for photodetectors. These include irradiance and responsivity.

2.6.5.1. Irradiance

The irradiance of a light source is the radiometric flux density emitted by the light source and is given in W/cm^2 or W/m^2 [76].

2.6.5.2. Responsivity

The responsivity (R_λ, with a unit A/W) of a light detecting device is the ratio of output photocurrent (I_p/cm^2) and radiant energy, P (Watt/cm^2) and is expressed as shown in (2.17) [77].

$$\boldsymbol{R_\lambda = \frac{I_p}{P}} \tag{2.17}$$

2.6.6 Luminance versus radiance

The amount of heat that is generated from the surface of an OLED structure is known as the OLED radiance. Luminescence, on the other hand, is the product of the constant k_m and the integral of the radiance $L_{e,\lambda}$ multiplied by the spectral luminosity $V(\lambda)$ of the device, as shown in (2.18) [78].

$$\boldsymbol{L_v = K_m \int_{\lambda min}^{\lambda max} L_{e,v} \times V(\lambda)\ d\lambda} \tag{2.18}$$

2.6.7 CIE diagrams

The CIE Chromaticity Diagram (Figure 2.13) visually illustrates the different characteristics of visible colour in a single diagram [79]. The centre of the diagram is located at (0.333, 0.333) and represents white. The RGB components of a light source is mapped onto the CIE diagram axis.

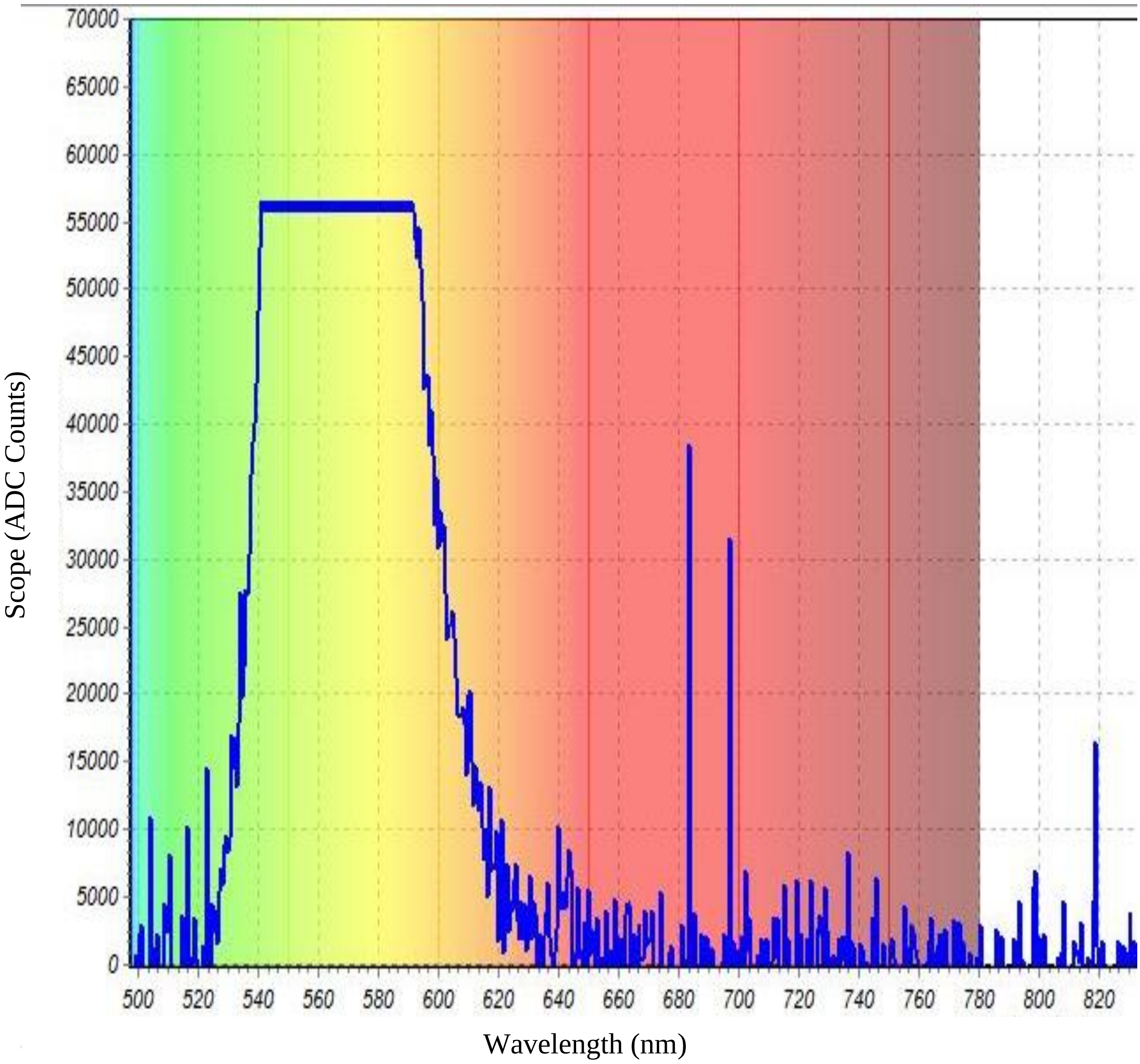

Figure 2.12. The distributed light spectrum of a LED.

The outer edge of the diagram represents the wavelengths of pure colour. To determine the dominant wavelength of a colour, a line should be drawn from the centre of the diagram through the colour point and to the edge of the diagram. Where the line intercepts with the outer perimeter of the diagram, is the dominant wavelength. The purer the colour, the closer to the edge of the diagram the colour's dominant wavelength will fall [79], [80].

2.7 LOW-COST MANUFACTURING PRINTED ELECTRONIC OLED DEVICES

Printed electronics manufacturing techniques make it possible to manufacture duplicable, flexible, lightweight electronic devices on various substrates. Devices that have been printed using printed electronic techniques include, but are not limited to, sensors, antennas, LEDs, and light displays [3]. Additionally, disposable biosensors can be manufactured using printed electronic manufacturing techniques [2], [81]. The ability to print devices onto recyclable substrates, such as paper, provides a means to produce lightweight, low cost, flexible biodegradable sensors. Light-emitting structures are created by placing an electroluminescent material between two conductive layers [82].

In top emissive light display structures, the emitted light is visible through the upper conductive layer of the electroluminescent structure. If the structure is printed on a non-transparent substrate, the upper conductive layer is required to be transparent for the emitted light to be visible [82]. While as for bottom emissive structures, the electroluminescent structure is printed on top of a transparent substrate. The emitted light is visible through the substrate and bottom conductive layer [82].

2.7.1 Printed electronics in microfluidic channels

Inkjet printed electronic techniques will also be developed for printing a fully inkjet printable light-emitting structure that can be used for various applications. Light-emitting structures can be used to create pixels in a light-emitting display that can be used to display results of rapid diagnostic biomedical devices. Printed light-emitting structures can also be used in microfluidic channel photodetectors [59].

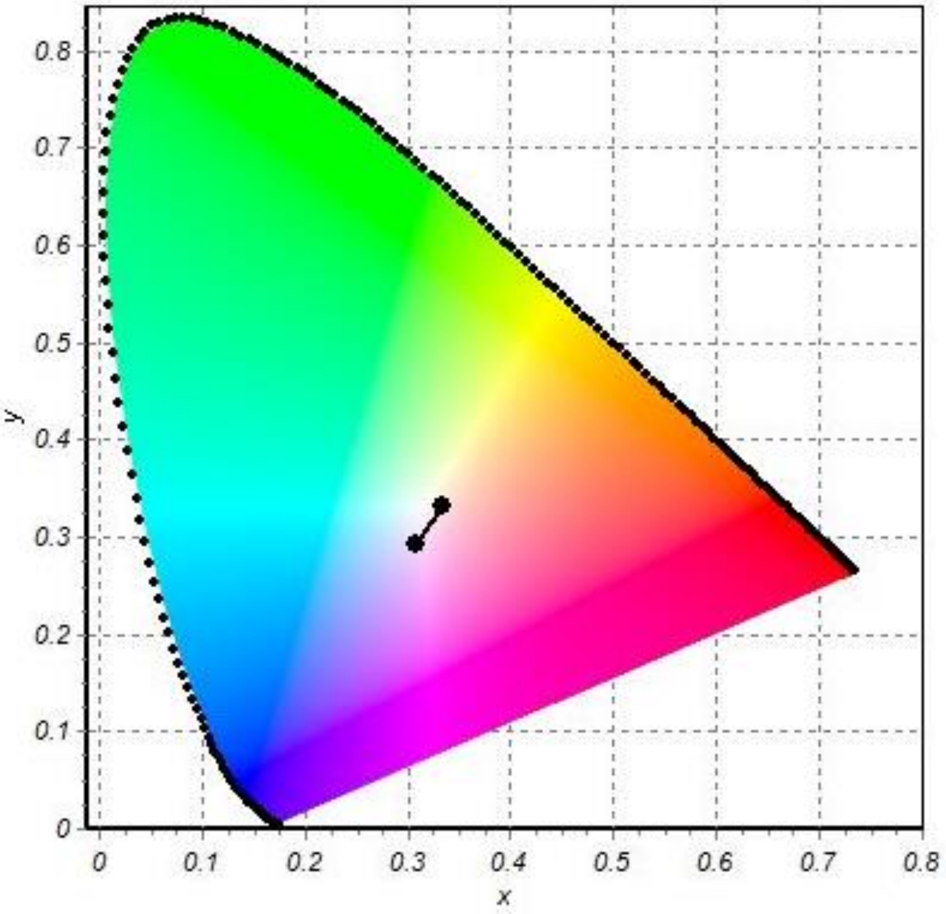

Figure 2.13. Measured CIE Chromaticity Diagram of white LED.

The effects of paper substrates for inkjet printed electronics will also be investigated and inkjet printing techniques will be developed to optimize the manufacturing of devices on photo-paper substrates.

The reflected light, through a solution, can be measured by placing an emitter LED parallel to a detector LED directed at the solution. The emitted light travels through the solution, gets reflected back through the solution by the opposite side, and the discharge time of the detector LED is measured. An ideal reflectance is measured when the solution doesn't have any solvents or additives. The ideal reflectance and the measured reflectance is related by

(2.19), whereby t_0 is the ideal discharge time and t is the measured discharge time of the sample [33].

$$\boldsymbol{R = \frac{t_0}{t}} \tag{2.19}$$

The relative absorbance is the amount of light that gets absorbed by the sample when the light passes through the sample and is described using (2.20) [33].

$$\boldsymbol{Relative\ absorbance}\ (\%) = \frac{\boldsymbol{t - t_0}}{\boldsymbol{t}} \times \boldsymbol{100} \tag{2.20}$$

2.7.2 Inkjet printability of materials

The primary disadvantage of inkjet printed electronic manufacturing is that a limited number of materials can be printed, using an inkjet printer, due to the printer's nozzle and cartridge dimensions. The size, shape, and speed of droplets that exits the inkjet printers nozzle can have a large effect on the performance of the printed material. For example, the shape of the droplet when it dries and is cured on the substrate can influence the conductance of the printed material [83].

The three primary considerations for inkjet materials are the material's printability, rheological properties, and molecular components. The printability of the material includes all printing parameters and printing quality, the rheological properties are the parameters that affect the flow of the material such as surface tension, viscosity, and molecular components which incorporate everything the material consists of, including additives and colorants [84].

The viscosity and surface tension of materials have a large impact on the inkjet printability of materials. If droplets do not form readily enough, the printer’s nozzle clogs, and droplets do not exit the inkjet printer's nozzle. However, if the droplets form too readily, the body of the droplet detaches from the droplets tail. This can cause satellite droplets around the printed tracks, which can cause defects and imperfections in the inkjet printed device [3], [81], [85]-[86]. Many variables can influence droplet formation, which needs to be carefully determined and controlled during inkjet printed electronic manufacturing [3]. A summary of printing aspects that need to be carefully controlled and the reasons and methods of control are summarized in Table 2.7 [87], [3].

Materials with a viscosity above 30 cP are not inkjet printable because their large molecular structures clog the printer's nozzle. The surface tension of the material being printed also needs to be 0.028 and 0.033 N/m for them to be inkjet printable [83].

The inkjet printability of materials is of great importance in the manufacturing of printed OLED displays. The ink viscosity and surface tension determine whether the ink will print without clogging the nozzle or spluttering onto the substrate [88]. The Reynolds (*Re*), Ohnesorge (*Oh*) and Weber (*We*) numbers can be used to determine the inkjet printability of materials as shown in (2.21) - (2.23) [86],

$$\boldsymbol{Re} = \frac{\boldsymbol{vpa}}{\eta_{v}} \tag{2.21}$$

$$\boldsymbol{We} = \frac{\boldsymbol{v^{2}pa}}{\eta_{v}} \tag{2.22}$$

$$\boldsymbol{Oh} = \frac{\sqrt{\boldsymbol{We}}}{\boldsymbol{Re}} = \frac{\eta_{v}}{\sqrt{\boldsymbol{\gamma pa}}} \tag{2.23}$$

whereby v is the droplet velocity exiting the nozzle, γ is the surface tension, a is the droplet diameter (same as the diameter of the inkjet printer's nozzle), ρ is the density of the material and η_{v} is the viscosity. The kinetic energy of the material and the surface energy at the nozzle is represented by the Weber number, the relationship between the ink viscosity and the inertial forces are related using the Reynold number and the Ohnesorge number is used to eliminate the velocity of the drop from the nozzle and compares the dimensions of the nozzle with the physical characteristics of the material [86]. Materials are considered inkjet printable if the relationships in (2.24) and (2.25) are satisfied [86].

$$\mathbf{0.1 < \boldsymbol{Oh} < 1} \tag{2.24}$$

$$(\boldsymbol{We})^{\frac{1}{2}}(\boldsymbol{Re})^{\frac{1}{4}} < \mathbf{50} \tag{2.25}$$

If *Oh* is greater than 1 (2.24), the material is too viscous to be jetted and if *Oh* is less than 0.1 (2.24) the material exits the nozzle too quickly satellite droplets form [86]. If *We* is less than 4 (2.25) there is insufficient energy for droplet formation and droplets do not exit the nozzle, while if $(We)^{1/2}(Re)^{1/4}$ is greater than 50 (2.25) splashing occurs [86].

Measuring the viscosity of the inks is not straight forward because most of the materials used for inkjet printing applications are Non-Newtonian fluids. Newtonian materials can be described by a linear relationship of the shear rate and the shear stress, while a Non-Newtonian material has a nonlinear relationship between the shear rate and the shear stress. Non-Newtonian materials can also be time-dependent, have yield stresses, or have deformities in the material.

Non-Newtonian characteristics that are present in materials, such as inks used for printed electronics, are typically caused by the structural organization of the molecules [88]. The inkjet printing parameters for the Fujifilm Dimatix inkjet printer is shown in Table 2.6 [89].

2.7.3 Substrates

The substrate selected has a large influence on the efficiency of the light display. The advantages and disadvantages of commonly used substrates are summarized in Table 2.8.

Paper substrates are not commonly used for printed light-displays as there are still many challenges that need to be overcome. The low cost, recyclability, and availability of a paper substrate, does, however, make it an attractive choice for future research [3].

2.7.4 Materials for light emitting structure manufacturing

Materials that have been used for the different layers of OLED displays, as well as their manufacturing methods are given in this section.

2.7.4.1 Transparent anode

To obtain sufficient conductivity in the transparent anode, an anode sheet resistance of less than 200 Ω/sq is suggested [90]. Commonly used inks for the transparent anode include hydrogen plasma-treated zinc oxide (ZnO) [2], Indium Tin Oxide (ITO) [36] and PEDOT: PPS [91]. Other inkjet printable transparent anodes include Cd_2SnO_4, TaO_3, $MgIn_2O_4$, and Ga_2O_3 [92].

2.7.4.1.1 Zinc oxide (ZnO)

Zinc oxide has a typical sheet resistance of 10^7 Ω/sq. When ZnO is plasma treated with hydrogen the sheet resistance can be reduced to an optimal sheet resistance of 200 Ω/sq and can, therefore, be used for the transparent anode in light-emitting displays [2], [69]. The cost of a hydrogen treated zinc oxide anode (ZnO: H) is substantially less than an ITO anode, but they have comparable device performance [69].

Other doped ZnO compounds that have been used as a transparent anode include ZnO: Ga, ZnO: Al and ZnO: In. These compounds are typically applied using sputtering or thermal evaporation techniques [38]. There are also ZnO compounds that can be inkjet printed and used as a transparent anode. These compounds include Zn_2SnO_4 and $Zn_2In_2O_5$ [92].

Table 2.6. Fujifilm Dimatix Ink parameters.

Printing parameter	Purpose	Printable values
Viscosity	To allow ink to be jetted.	10-12 cP [89].
Surface tension	Prevent ink from dripping out of or clogging the nozzle.	32-42 dynes/cm [89].
Volatility	Optimal jettability.	Boiling point > 100 °C [89].
Specific gravity	Prevent ink from drying too rapidly and clogging the nozzle.	>1 [89].
Particle size	Prevent clogging.	< 0.2 microns [89].
Filtration	Prevent clogging.	Filtered through a 0.2 μm filter. [89].
pH	Prevent nozzle and cartridge damage.	4 – 9 [89].

2.7.4.1.2 Indium tin oxide (ITO)

ITO is an alloy that is composed of 90% In_2O_3 and 10% SnO_2. Both compounds that ITO is composed of have band gaps of 3.5 eV, making the ITO transparent and suitable to be used as a transparent conductor. The reason for the high conductivity of ITO of the Sn_4 impurities in the alloy [38].

Table 2.7. Printed electronic printing control aspects, purposes, and methods of control [87], [3].

Printing aspect	**Purpose of control**	**Method of control**
Droplet size and shape	The size and shape of a droplet have a direct effect on the resolution of the printed material. Additionally, the shape of the droplet when it dries on the substrate can affect the conductance of conductive inks [87].	The voltage waveform applied to the piezo element causes droplets to exit the printer's nozzle. By adjusting the voltage waveform, the size and shape of the ejected droplets can be controlled [87].
Droplet speed	If droplets are ejected at speeds that are too rapid, the ink can splatter out of the nozzle and land at multiple places on the substrate. Thus, the accuracy and precision of printing are compromised [87].	The speed at which the droplets exit the nozzle is controlled by the amplitude of the voltage waveform applied (200-240VAC [93]) to the ink by the piezo element of the printer [87].
Dripping	Undesired dripping out of the nozzle must be prevented to ensure the accuracy and precision of printing on the substrate [87].	The nozzle tip undergoes high frequency "tickling" [3] which keeps the nozzle tip wet and prevents undesired dripping from the nozzle [87].
Droplet formation	If droplets formation occurs too readily, the droplets will spread across the nozzle and cover the nozzle with a layer of liquid. This prevents	The surface tension of the printing ink or liquid determines how readily it will form a droplet. The lower the surface tension,

Printing aspect	Purpose of control	Method of control
	printing from being precise. On the other hand, if droplet formation does not occur readily, droplets will not exit the printing nozzle [87].	the more readily a droplet will form. Substances that have a large surface tension will not exit the nozzle because the pressure in the nozzle will not be high enough to overcome the large surface tension in the substance [3]. Surface tension can be altered by changing the concentration of the printed substance [87].
Alignment of ink ejection from the nozzle	For accurate and precise printing, the alignment and angle that the substance is printed at must be carefully monitored [87].	The Fujifilm-Dimatix printer has a fiducial camera mounted on it. This camera can be used to monitor and adjust the printing alignment and angle [87].
Droplet tails	If droplets exit the nozzle as long elongated drops (have long tails), they run the risk of splitting into numerous smaller droplets in flight. This will cause smaller droplets to land randomly across the material, which is detrimental to printing accuracy [87].	The viscosity of the substance being printed determines its elongation when it exits the nozzles and falls onto the surface it is being printed onto [87].

Table 2.8 Comparison of different substrate choices.

Substrate	Advantages	Disadvantages
Silicon	• Commonly available for microelectronic application [3].	• Inks readily diffusive into the substrate [3].
Glass	• Non-reactant [3]. • Non-absorptive [3]. • Smooth surface [3]. • Most inks can be printed onto it. • Can withstand high processing temperatures [3]. • Transparent.	• Non-flexible. • Non-biodegradable. • Brittle.
PET	• Smooth surface [81]. • Low cost [81]. • Reactive to certain inks (undesirable reaction with inks) [3].	• Cannot withstand high processing temperatures [3]. • Reactive to certain inks (good for pre-treatment) [3]. • More expensive than paper-based alternatives.
Conductive films	• Fewer layers need to be printed. • Can be further doped [94]. • Heat stabilizing can be added [55].	• Reactive with certain inks [55]. • Higher cost.
Paper	• Low cost [81], [3]. • Recyclable [81], [3]. • Flexible [81], [3]. • Biodegradable [81], [3]. • Disposable [7].	• Cannot withstand high manufacturing temperatures [3]. • Surface irregularities [3]. • Absorptive [3]. • Coated paper reacts with PEDOT: PSS [72]. • Increased sheet resistance for printed conductors [72].

ITO is commonly used as the transparent anode in OLED and other printed light-emitting displays. The ITO layer is generally printed onto a transparent substrate and is used for bottom light-emitting displays [36], [46], [55]- [56]. Spin coating [61] and screen printing [90] are commonly used methods of depositing ITO onto a substrate. ITO can be deposited using a piezoelectric inkjet printed and is often deposited above a PEDOT based hole-injection layer [46], [67].

2.7.4.1.3 PEDOT (poly(3,4-ethylenedioxythiophene) polystyrene sulfonate)

PEDOT: PSS can be used as the transparent anode in a light-emitting display; however, it does have a higher sheet resistance in comparison to an ITO anode [95]. PEDOT: PSS can be spin-coated, or inkjet printed onto a substrate. PEDOT: PSS generally requires a post-printing drying process at approximately 130 ° C, making it unsuitable to be printed on a substrate that cannot withstand high temperatures [91].

When PEDOT: PSS is printed on glossy paper, 7 layers of inkjet printed PEDOT: PSS are required for sufficient conductivity. This is because the glossy paper substrate is absorptive and when the ink is absorbed into the substrate the conductivity drastically diminishes. The glossy coating of the paper substrate also interferes with the printed PEDOT: PSS layer, which causes the ion transportation in the PEDOT: PSS to diminish [94].

PEDOT: PTS can also be used instead of PEDOT: PSS for the transparent anode. PEDOT: PTS has a sheet resistance of 100 Ω/sq, making it a good conductor for the anode. It is also approximately 80% transparent, making it sufficiently transparent for the emitting light from the light display to be visible. The performance of PEDOT: PTS is seen to be better than ITO when used as the transparent anode in OLED displays [65].

2.7.4.2 Conductive cathode

The cathode is not required to be transparent in either top-emissive or bottom-emissive structures. It does, however, need to be a good conductor [43]. In LED devices with transport layers, the cathode must have a low work function. This is because the mobility of holes in the HTL is generally larger than the mobility of electronics in the ETL. By using a cathode with a low work function, the barrier between the ETL and the cathode is minimized, thus improving electron mobility [60].

A commonly used metal, that can be inkjet printed with a piezoelectric printer, is silver [58], [59]. Gold is also inkjet printable, with good conductive properties, and can be used to print the cathode [43]. Another common method of manufacturing a silver cathode is spray coating [96].

Aluminium is a favorable material to use as a cathode material, it is not, however, inkjet printable, but can be applied using other manufacturing techniques. It is also advantageous to implement an aluminium cathode as it does not oxidise as rapidly as other conductive cathode materials [60].

2.7.4.3 Light-emitting layer for led based displays

Zinc sulfide (ZnS) and doped ZnS can be used as the light-emitting layer of light-emitting displays. ZnS can be doped with manganese (ZnS Mn), copper (ZnS:Cu) [97] and silver (ZnS: Ag). ZnS: Ag is specifically used as the quantum dot layer in QLED displays. Mn is a better dopant than Cu and Ag as it has a longer life span and better device efficiency [34].

When zinc oxide (ZnO) is doped with rare-earth ions, such as Tb^{3+}, Sm^{3+}, and Tm^{3+}, it can be used as the light-emitting layer in thin-film electroluminescent displays (TFEL). The ZnO must be doped with approximately 10% of the rare-earth ion for optimal electroluminescent properties [98], [99].

Hybrid nanoparticles made from ZnO and fluorescein can be used as an electroluminescent layer in OLED displays. Tris(8- hydroxyquinoline)aluminium (Alq) can be used instead of fluorescein to produce electroluminescent hybrid nanoparticles suitable for OLED application [64].

2.7.4.4 Carrier injection and transport layers

Polymer-based layers can be used for these electron and hole layers in OLED displays, however, inorganic solution-based metal oxides have higher carrier mobility and chemical stability making then more efficient EIL, ETL, HIL and HTL layers in non-organic light-emitting displays [62].

2.7.4.5 Electron transport layer

The addition of an ETL improves the efficiency of light-emitting displays [42]. By doping the ETL with n-type dopants the efficiency of the ETL can be improved [34]. Cadmium sulphide, doped with manganese is a good ETL in devices with a ZnS based light-emitting layer [34]. Tris-phenylbenzimidazolyl benzene (TPBi) can also been successfully used as an ETL for an inkjet printed QLED. The TPBi is vacuum depositing onto a substrate before the quantum dots are inkjet printed [61]. Tris(8-hydroxyquinolinato)aluminium (Alq) can also be used as an ETL layer and is deposited using a vacuum process [34], [59].

Zinc oxide (ZnO) has been successfully used as an ETL in inkjet printed AM-QLED's on ITO substrates. A disadvantage of using ZnO for the ETL is that a barrier often forms between the ETL and cathode, preventing electrons for being sufficiently injected to the EML [62]. This barrier can, however, be minimized by incorporating an EIL or by doping the ZnO with Cs [100].

2.7.4.6 Electron injection layer

The EIL is often omitted from the OLED structure [82]. It can, however, significantly increase the luminescence of a display. Some materials that can be used as an EIL include

LiF, Na_3PO_4, and NaCl. Na_3PO_4 is seen to be a good EIL, in devices that have an Alq_3 ETL [60]. In displays with a ZnO ETL, polyethyleneimine (PEI) can be used as an effective EIL because the PEI layer decreases the work function of ZnO and prevents an electron injection barrier from forming between the cathode and the ETL [100].

2.7.4.7 Hole injection layer

PEDOT: PSS can be used as a HIL in OLEDs. PEDOT: PSS can be inkjet printed, screen printed or spin-coated on top of an ITO anode for OLED applications [46]. It is an ideal HIL because it is a good conductor and is transparent. The disadvantage of using PEDOT: PSS as a HIL is that it is highly acidic, which can degrade an ITO based anode and shorten the life span of the OLED device. It also is moisture absorbent, which can give rise to a charge barrier between the HIL and other layers in the device. This barrier can lead to a charge accumulation, which can further lead to device degradation [62]. The efficiency of the HIL can further be increased by using a composite of PEDOT: PSS and ZnO as the HIL. Adding ZnO to the composite has been seen to improve the power efficiency of the OLED display [68].

2.7.4.8 Hole transport layer

In OLED displays with PEDOT: PSS as the HIL, a charge barrier forms between the EML and the HIL. This can be prevented by placing a HTL between the EML and HIL [62]. By doping the HTL with p-type dopants the efficiency of the ETL can be improved [34]. In devices that have PEDOT: PPS HIL, specially formulated inks such as: PC [59], NPB [65] or α-NPD [66] can be used as the HTL.

CHAPTER 3 LED ARRAY FOR COLOURIMETRIC ANALYSIS

3.1 CHAPTER OVERVIEW

Colourimetric analysis of the different pH samples, between 4 and 9, was performed using an LED emitter and LED detector array. The emission and detection properties of white, green, blue, yellow, orange and white LEDs were tested and analysed. Section 3.2 and Section 3.3 discusses the spectral analysis and luminous flux analysis of the LED array. Both the photo current (Section 3.4) and the discharge time (Section 3.5) of reverse bias detector LEDs were measured and analysed. The discharge time versus the distance the emitter and detector are away from each other is measured in Section 3.6 and statistical analysis is performed on the data in Section 3.7. The angular spectral response of the LED is evaluated in Section 3.8. Lastly colourimetric analysis, using an LED array is discussed in Section 3.9.

3.2 SPECTRAL ANALYSIS OF THE LED ARRAY

Spectral sensitivity analysis was performed on different colour LEDs of the LED array [7], using an AvaSpec Spectrometer, as shown in Figure 3.1. A series resistor, *Re,* was placed next to the emitter LED. In Figure 3.1 the white LED emission spectrum bandwidth covers the entire visible range. This makes the white LED a good choice for the emitter LED in the array. An enlarged spectral response of a white LED is shown in Figure 3.2 and the CIE colour diagram is shown in Figure 3.3. In Figure 3.3, the black dots are close to the white point in the centre of the CIE diagram. The further away from the edges of the diagram the point falls, the less pure the colour is. If the point falls on the edge of the diagram, the colour is pure e.g., pure red. The points are close to the white point but fall slightly towards the red wavelengths. Therefore, the white LED emits a white light, with a slightly larger red wavelength component. The higher red wavelength component in the CIE diagram can also be due to the spike at 860 nm in the spectral response diagram (Figure 3.2).

The ADC count of the white LED, measured with an Evo Spec spectrometer, is approximately 275000 across the visible spectrum, and there is a peak in the IR range at approximately 859 nm.

A spectrometer measured signal is the product of the integration time (seconds), spectrometer sensitivity (counts·Watt^{-1}seconds^{-1})) and optical power (Watts) and is given as a “count” value as the Watts and second units cancel out. The sensitivity of the spectrometer is dependent on the ADC size of the spectrometer [101].

It can be visually seen that the blue, green, yellow, orange, and red LEDs filter out certain bandwidths of light (Figure 3.1). If different colour LEDs are used as light-detecting LEDs, light detection in specified bandwidths is possible.

A resistor was placed in series with each emitter LED. The resistor values were optimised for the emitter LEDs light emission illumination, linearity properties of the detected light and narrow emission bandwidth and is discussed in subsequent sections.

The blue, green, yellow, orange and red LEDs each have a distinct spectral response, with a bandwidth between 20-40 nm. The green and yellow LEDs, as well as the orange and red LEDs, have an overlap in wavelengths in the emission spectra. The white LEDs emission spectrum covers the entire visible light band. A summary of the LEDs approximate bandwidths, as measured using the AvaSpec Spectrometer, is given in Table 3.1. Each LED was measured individually, with the emitter LED parallel and in the centre of the detector LED.

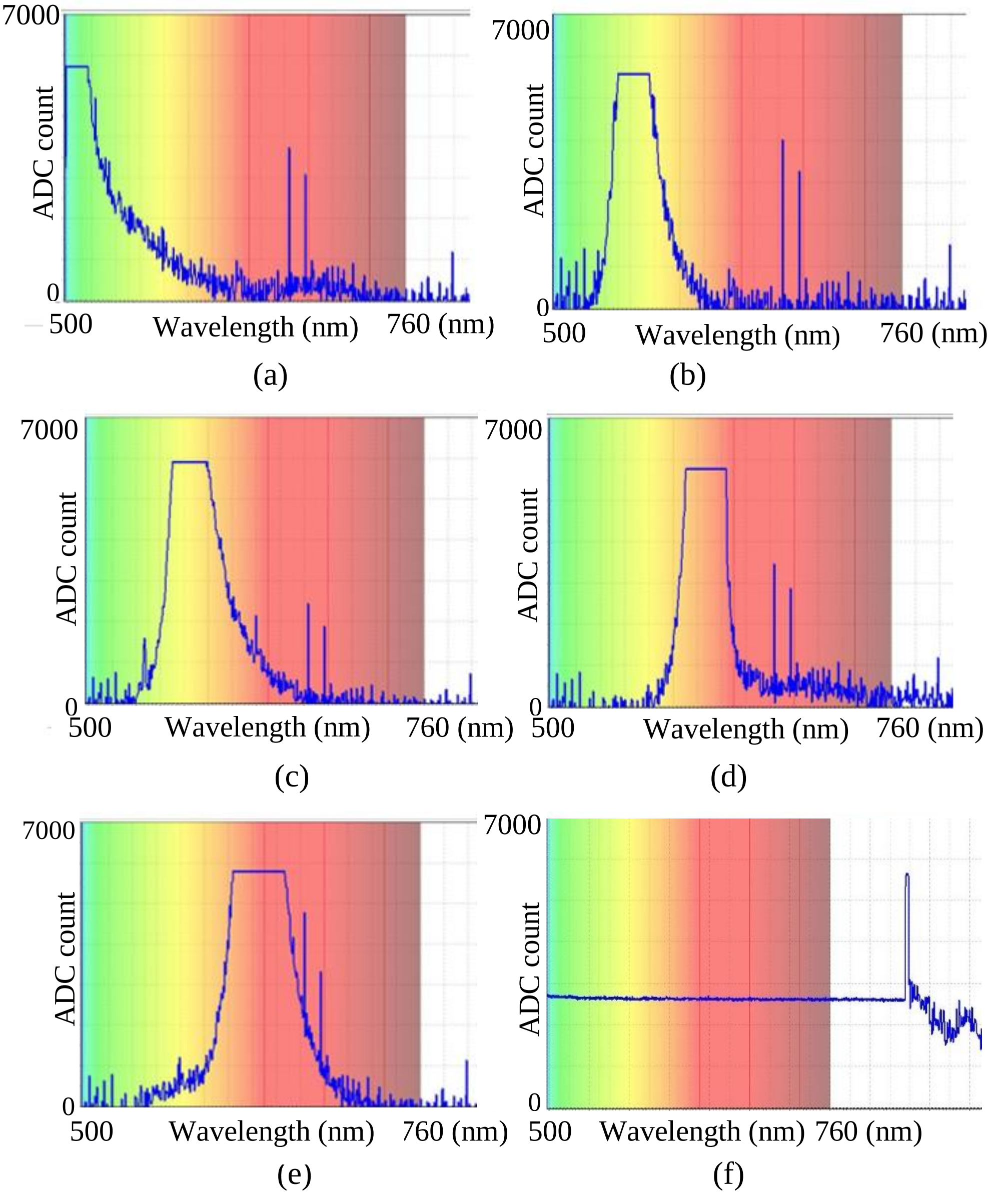

Figure 3.1. Spectral sensitivity analysis of LEDs in the LED array.

(a) Blue LED, Re = 10 kΩ. (b) Green LED, Re = 2.2 kΩ. (c) Yellow LED, Re = 2.2 kΩ. (d) Orange LED, Re = 10 kΩ. (e) Red LED, Re = 39 kΩ. (f) White LED, Re = 27 kΩ.

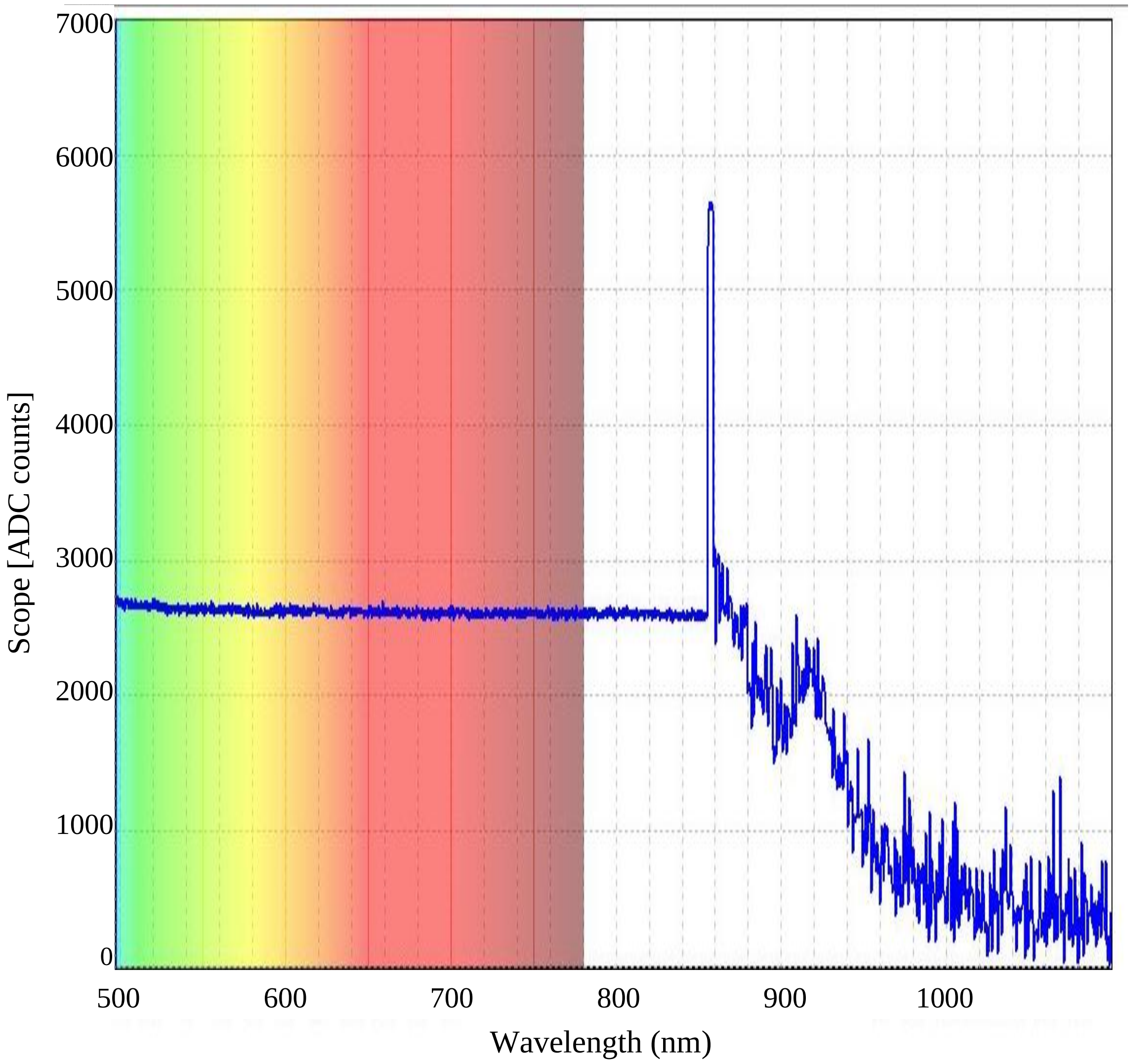

Figure 3.2 Spectral response of a white LED, measured perpendicular to the panel (0 ° viewing angle).

3.3 LUMINOUS FLUX ANALYSIS OF LED ARRAY

The luminous flux (lumens) of a blue, green, yellow, orange, red and white LED was measured using an AvaSpec Spectrometer. The luminous flux was measured at different brightness’s for each of the LEDs. The brightness of each LED was adjusted by placing a resistor in series with the emitter LED as can be seen in Figure 3.4. An optically isolated container, that had a hole the same size as the LED (5 mm), was used to ensure that the measurements were done in an optically isolated environment. The opening was also sealed with optically isolating material, once the LED and probe were securely placed. The container also ensured that the probe remained, exactly parallel to the LED under test. The LED and the probe head touched in the centre of the container. A diagram, illustrating the container, used for the illuminance test is shown in Figure 3.4.

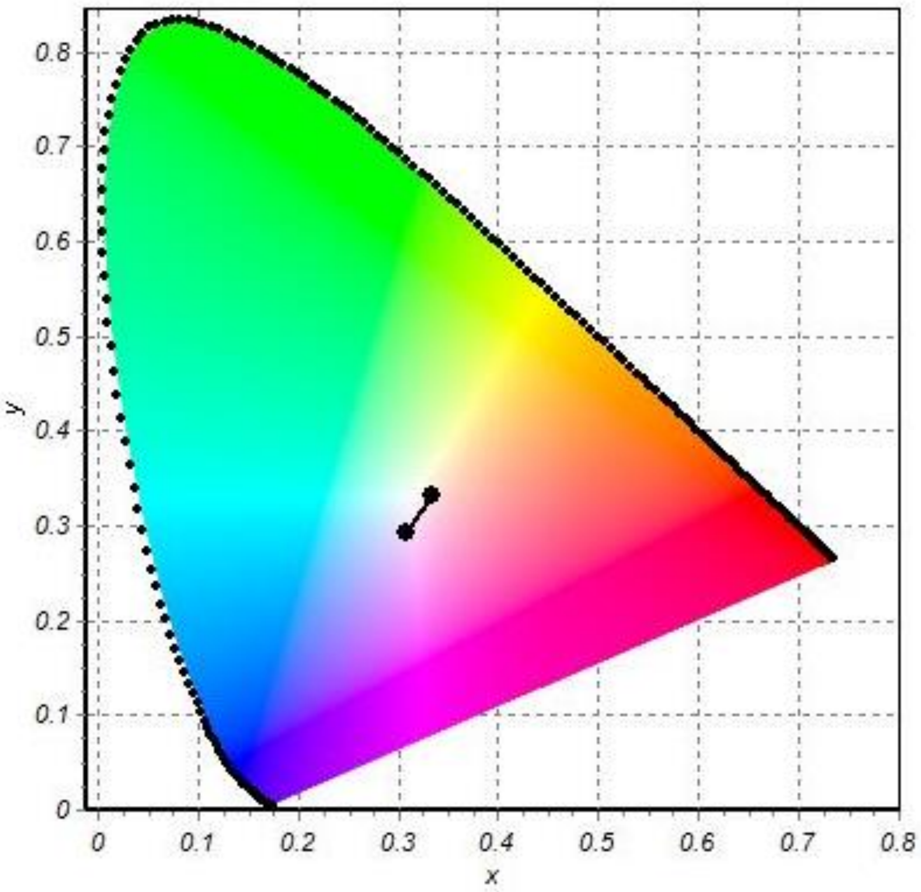

Figure 3.3 CIE colour chart of a white LED, measured perpendicular to the panel (0 ° viewing angle).

Table 3.1. Measured bandwidth of the emitter LEDs in the LED array.

LED colour	Measured bandwidth (nm)
Blue	500-518
Green	550-576
Yellow	568 – 600
Orange	623-667
Red	610-644
White	500-679

The luminous flux of different coloured LEDs at different light intensities were measured, using an AvaSpec spectrometer from Avantes. Different emitter resistances (*Re*) were used to alter the light intensity of the LEDs. The results of white, red, blue, green, orange and yellow LEDs can be seen in

Table **3.2** and Figure 3.5.

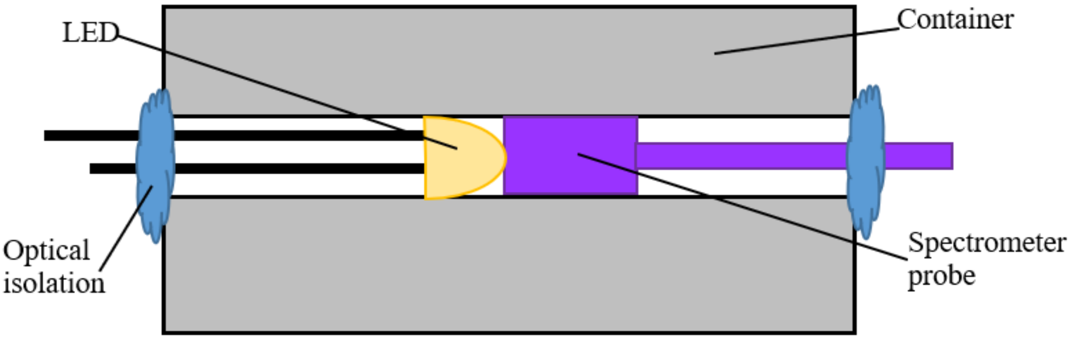

Figure 3.4. Container, LED under test and Spectrometer probe setup for the illuminance analysis.

It can be seen (Figure 3.5) that the luminous flux of a white LED is the largest, and the luminous flux of a blue LED is the smallest. As the series resistance of the light-emitting

LED is increased, the brightness of the LED decreases and thus the luminous flux measurement decreases.

Table 3.2. Luminous flux (Lumens) of LEDs with different emitter resistances.

Re	**Blue**	**Green**	**Yellow**	**Orange**	**Red**	**White**
470	1.18E-06	8.77E-07	7.41E-07	3.07E-07	4.68E-07	5.80E-07
1 k	1.22E-06	7.41E-07	6.31E-07	2.42E-07	4.10E-07	5.96E-07
2.2 k	1.13E-06	5.20E-07	4.59E-07	1.99E-07	3.72E-07	6.05E-07
4.7 k	9.24E-07	1.74E-07	1.89E-07	1.84E-07	3.47E-07	6.23E-07
6.8 k	7.42E-07	1.17E-07	1.26E-07	1.51E-07	3.27E-07	7.10E-07
10 k	5.84E-07	1.01E-07	8.51E-08	1.04E-07	3.03E-07	8.45E-07
27 k	3.50E-07	1.87E-08	6.23E-10	1.51E-08	2.36E-07	1.23E-06
39 k	2.77E-07	1.87E-08	6.23E-10	1.51E-08	2.25E-07	1.23E-06
47 k	2.60E-07	1.87E-08	6.23E-10	1.51E-08	2.07E-07	1.22E-06
68 k	1.77E-07	1.87E-08	6.23E-10	1.51E-08	1.93E-07	1.20E-06
82 k	1.40E-07	1.87E-08	6.23E-10	1.51E-08	1.75E-07	1.17E-06
100 k	1.08E-07	1.87E-08	6.23E-10	1.51E-08	1.34E-07	1.12E-06
470 k	1.53E-08	1.87E-08	6.23E-10	1.51E-08	4.08E-08	1.12E-06
1 M	3.24E-09	1.87E-08	6.23E-10	1.51E-08	7.71E-09	1.12E-06

3.4 PHOTOCURRENT OF REVERSE BIASED LIGHT DETECTING LEDS

The output current of a reverse bias LED, when light falls onto it, can be described as shown in (3.1). The LED has an internal resistance, which is depicted as Z_{input}. The load resistance and the voltage over the load resistance is depicted as R_{load} and V_{load} respectively [7].

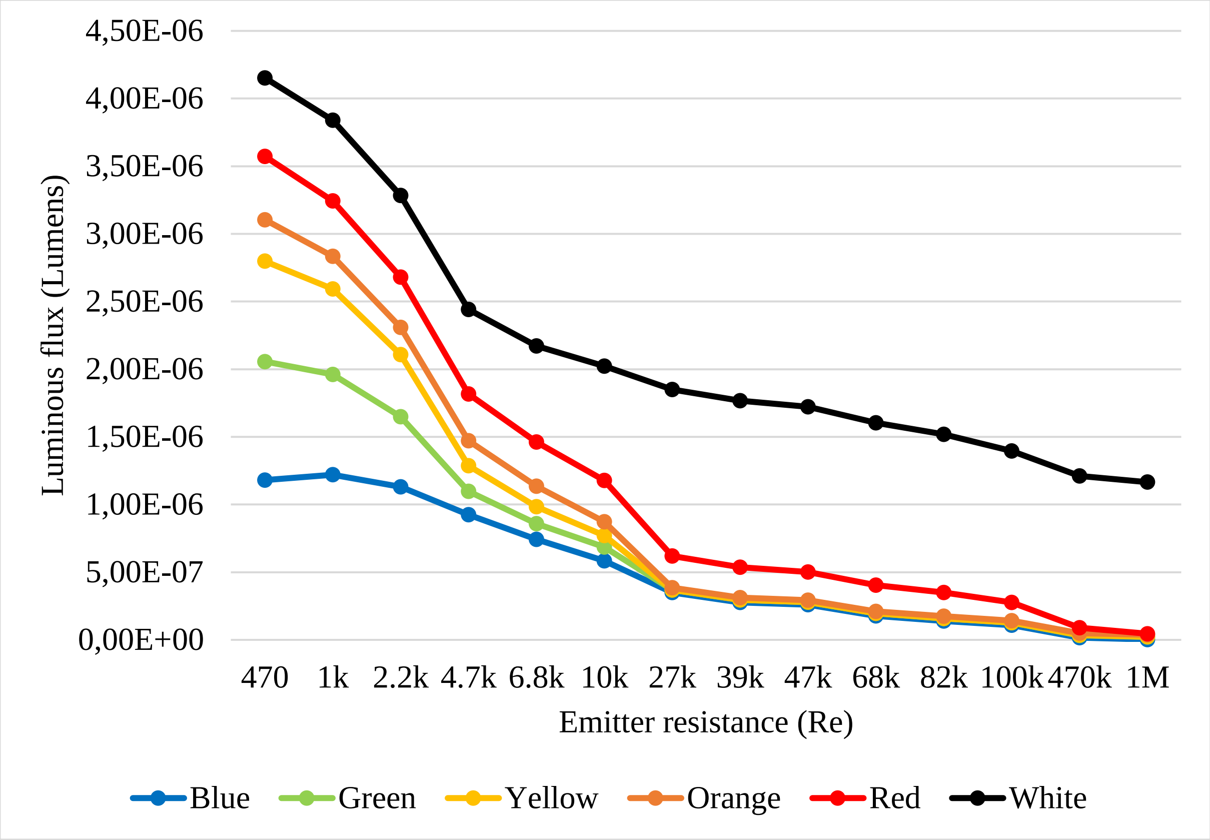

Figure 3.5. Luminous flux of LEDs with different emitter resistances.

$$\boldsymbol{I_{out}} = \frac{\boldsymbol{V_{load}}}{\frac{\boldsymbol{R_{load}} \times \boldsymbol{Z_{input}}}{\boldsymbol{R_{load}} + \boldsymbol{Z_{input}}}} \tag{3.1}$$

The expected photocurrent range of white, reverse bias LED was measured using a Hewlett Packard 4155B semiconductor parameter analyser. The mean photocurrent over a 1 minute was measured in office lighting when the lights were off, but some ambient light was present and when it was completely dark in an optically isolated laboratory. The current was measured when a reverse biased voltage of 5 V was applied across the LED. The results are summarized in Table 3.3. When more light fell onto the reverse bias LED, more photocurrent was generated by the LED.

Table 3.3. Photocurrent of reverse biased LED measured with a semiconductor parameter analyser.

Lighting conditions	Measured current (pA)
Office lighting	74.41
Partially dark	48.96
Completely dark	26.25

The measured current is in the pico-ampere range and the measured current is noisy, as can be seen in Figure 3.6. Using the photocurrent measurements of a reverse bias LED, used as a light sensor, for colourimetric analysis is challenging without expensive equipment.

3.5 DISCHARGE TIME OF REVERSE BIASED LIGHT DETECTING LEDS

A reversed biased LED detector that makes use of the measured discharge time is more sensitive than a reversed biased LED detector that uses the measured photocurrent [17]. A reverse biased LED is capacitive in nature, so the discharge time is the capacitive discharge time. The discharge time is the time taken for the reverse biased LED, which is capacitive in nature, to discharge from being maximally charge to 63 % of the voltage it is being charge to.

Instead of using the photocurrent measurements, the discharge time of the reverse bias light-detecting LEDs are measured, using an Arduino Uno, to improve detection sensitivity.

To approximate the discharge time range, of the LED detectors, the time constant was calculated (3.2). The input impedance (R) of the Arduino Uno is 100 MΩ and capacitance of each colour LED was measured, using a GW Instek Precision LCR meter (LCR-8110G). The measured capacitances and calculated time constants are given in Table 3.4.

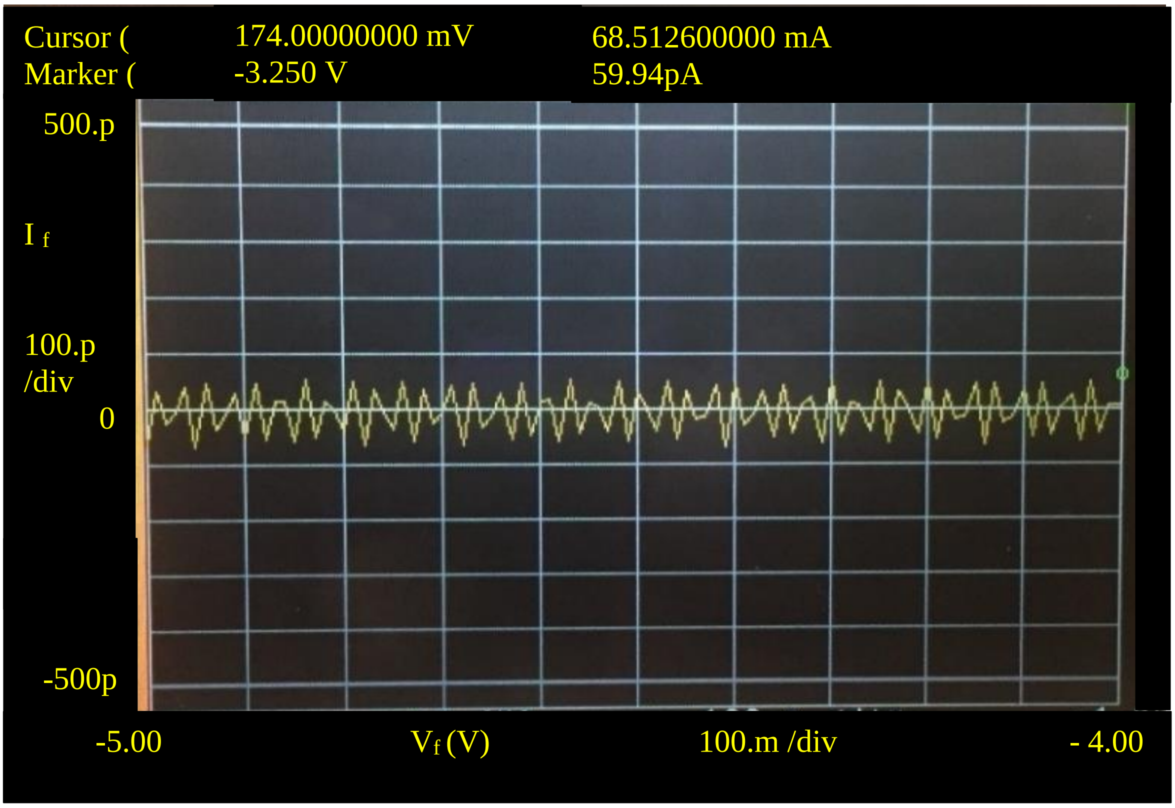

Figure 3.6. Measured photocurrent of a reverse bias LED, using a semiconductor parameter analyser.

$$\tau = RC \tag{3.2}$$

Figure 3.7 illustrates a flow diagram of the Arduino Uno code implementation. The Arduino was first initialized with serial communications, so that the measured results could be seen and transferred, via the serial port. All data, from any previous test, were then cleared to ensure that previous results did not affect current results.

The light detecting LEDs anode and cathode were connected to analog pins of the Arduino Uno and both the analog pins were set to output mode. The LED was then forward bias, by setting the anode pin high and the cathode pin low. This was done so that the LED, which acts as a capacitor, could charge. Enough delay time was given for the LED to fully charge.

Table 3.4. LED capacitances and time constants.

Colour LED	Measured capacitance (pF)	Time constant (ms)
White	19.422	1942
Orange	3.273	327.3
Yellow	5.306	530.6
Green	8.179	817.9
Blue	14.84	1484 s

The LED was then reversed biased, by setting the cathode pin high and the anode pin low. The cathode pin was then put in analog read mode so that the discharge time of the reverse biased LED could be measured on the serial port.

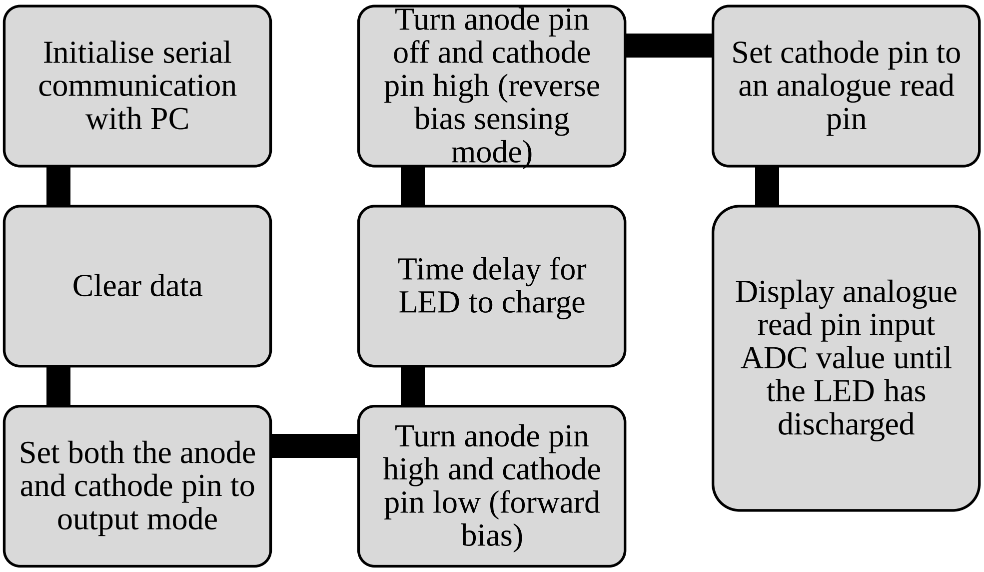

Figure 3.7. Flow diagram of the Arduino Uno code implementation.

The maximum ADC value on the analog pin is 1023. The time when the ADC value was at 63 %, 50 % and 25 % of the maximum ADC value was taken. This was when the ADC value is 644, 512 and 256 respectively. The serial monitor recorded the analog values, with the time stamp it was measured at. The time stamps were used to determine the discharge time of the reverse bias green LED, with the Arduino Uno interface test setup. The recorded results are given in Figure 3.8.

To test the setup, a green LED emitter and green LED detector were placed, facing each other, in the testing container that was used to test the LED emission spectra (Figure 3.4). Different resistances were placed in series with the emitter LED, to adjust the brightness of the light emission, and the discharge plot of the detector LED was monitored in the serial plotter in the Arduino software.

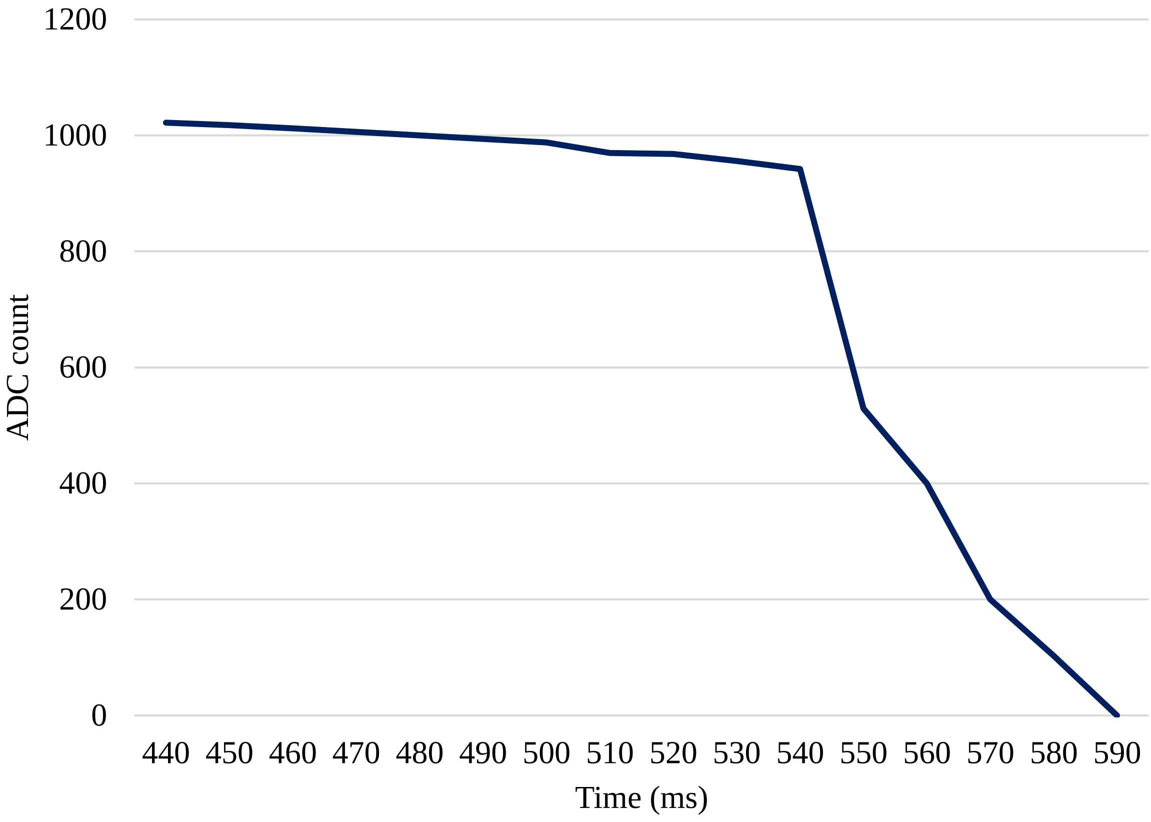

Figure 3.8. Discharge time of a reverse biased green LED, measured with an Arduino Uno serial monitor.

The discharge plots of the detector LED when the resistor in series with the emitter LED was 470 Ω, 1 kΩ and 10 kΩ, are shown in Figure 3.9, Figure 3.10 and Figure 3.11 respectively.

The blue line indicates the maximum ADC value, the red line indicates the discharge time to 63 % of the maximum ADC value, the purple line shows the discharge time to 50 % of the maximum ADC value and the green line show the discharge time to 25 % of the maximum ADC value.

When the series resistance increases, and therefore the emitter LEDs brightness decreases, the discharge time increases. This is because the more light that is shone onto the detector LED, the faster the capacitive discharge will be.

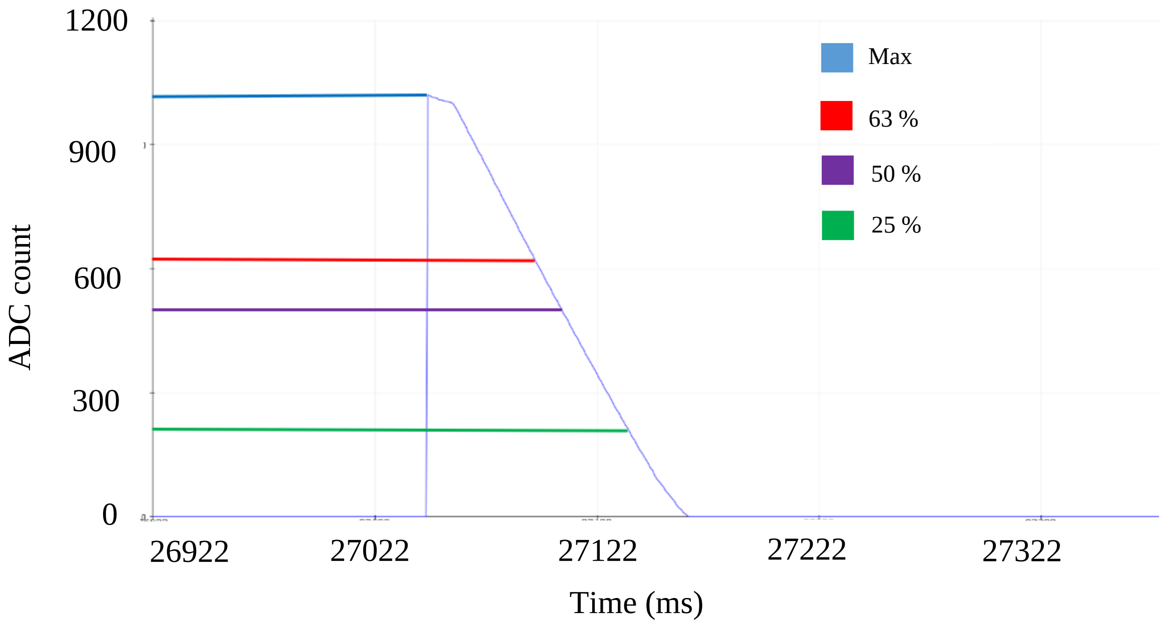

Figure 3.9 Green LED discharge plot with a 470 Ω resistor.

A green LED emitter and detector pair was placed in the test setup in Figure 3.4 (results for a yellow, orange, red, blue and white emitter, and detector pairs are given in Addendum A). Different size resistors were placed in series with the green emitter LED to adjust the brightness of the emitted light. The luminance (lux), luminous flux (lumens) and luminous intensity (candela) of the green emitter LED were measured, using the AvaSpec spectrometer. At each of the resistor values, the discharge time to 63 %, 50 % and 25 % of the maximum ADC value of the green detector LED was recorded. The results are tabulated in Table 3.5.

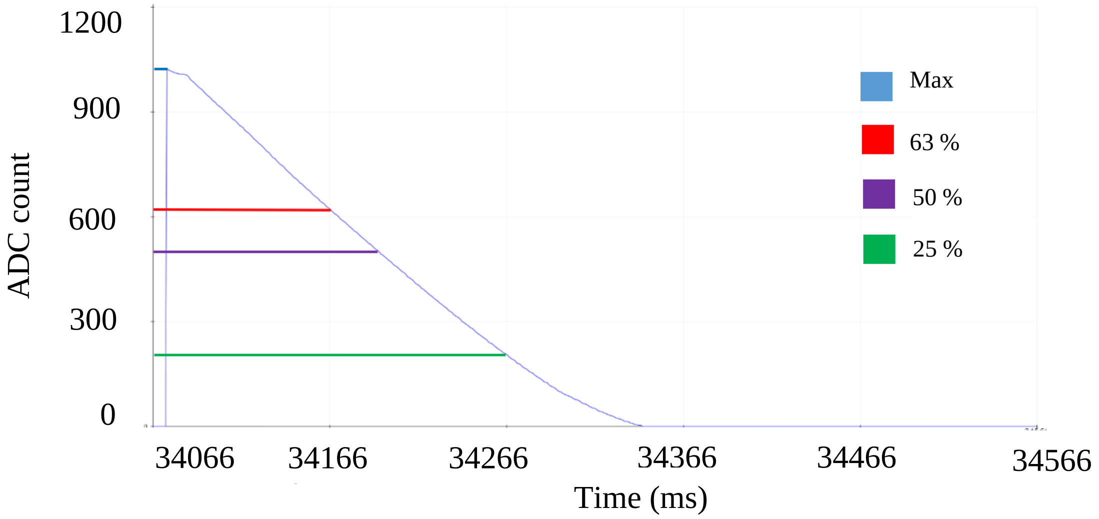

Figure 3.10 Green LED discharge plot with a 1k Ω resistor.

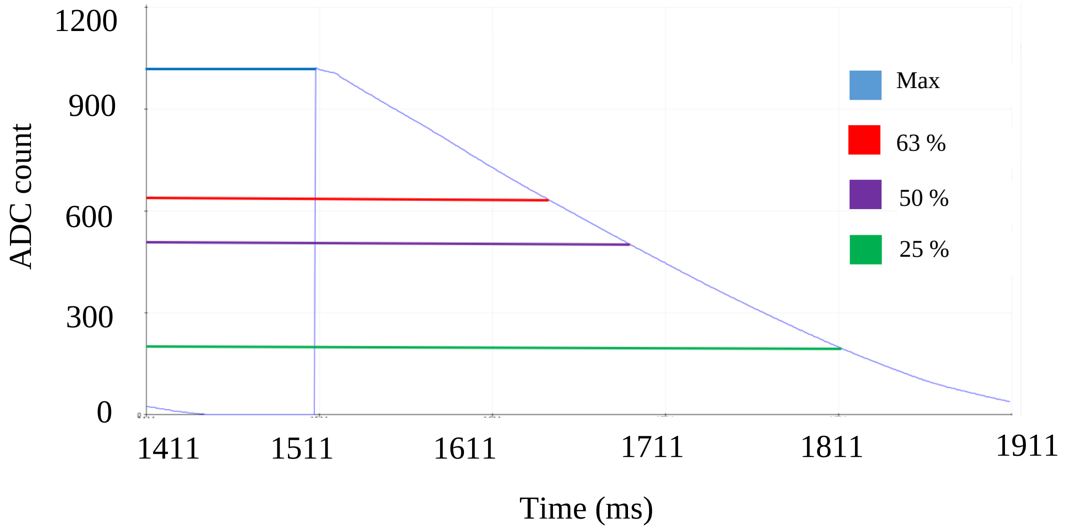

Figure 3.11 Green LED discharge plot with a 10k Ω resistor.

The discharge times versus luminance (lux), luminous flux (lumens) and luminous intensity (candela) are shown in Figure 3.12, Figure 3.13 and Figure 3.14 respectively. Because luminance (lux), luminous flux (lumens) and luminous intensity (candela) linearly correlate with each other, the three plots have the same shape. In all three plots it can be seen that as the luminance value increases, the discharge time decreases.

Table 3.5 Green LED emitter parameters with corresponding light detector discharge time.

Re	**Luminance (lux)**	**Luminous Flux (Lumens)**	**Luminous Intensity (Candela)**	**Time to 63% (ms)**	**Time to 50% (ms)**	**Time to 25% (ms)**
470	27.918	8.77E-07	33.78	218	253	387
1000	23.581	7.41E-07	28.534	373	489	746
2200	16.549	5.20E-07	20.025	644	847	1392
4700	5.5514	1.74E-07	6.7172	1393	1912	3549
6800	3.7082	1.17E-07	4.4869	1624	2269	4239
10000	3.2054	1.01E-07	3.8785	1718	2429	4777
27000	0.595	1.87E-08	0.72	1824	2562	5008

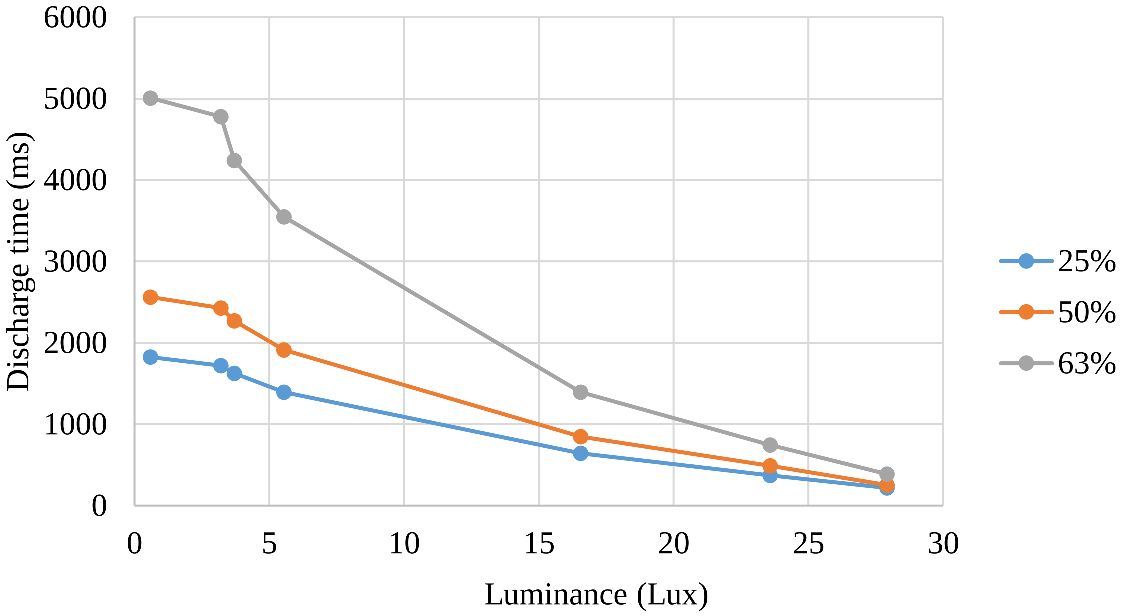

Figure 3.12. Time to 63 %, 50 %, 25 % of maximum discharge voltage, versus luminance (lux) of received light of green LED detector.

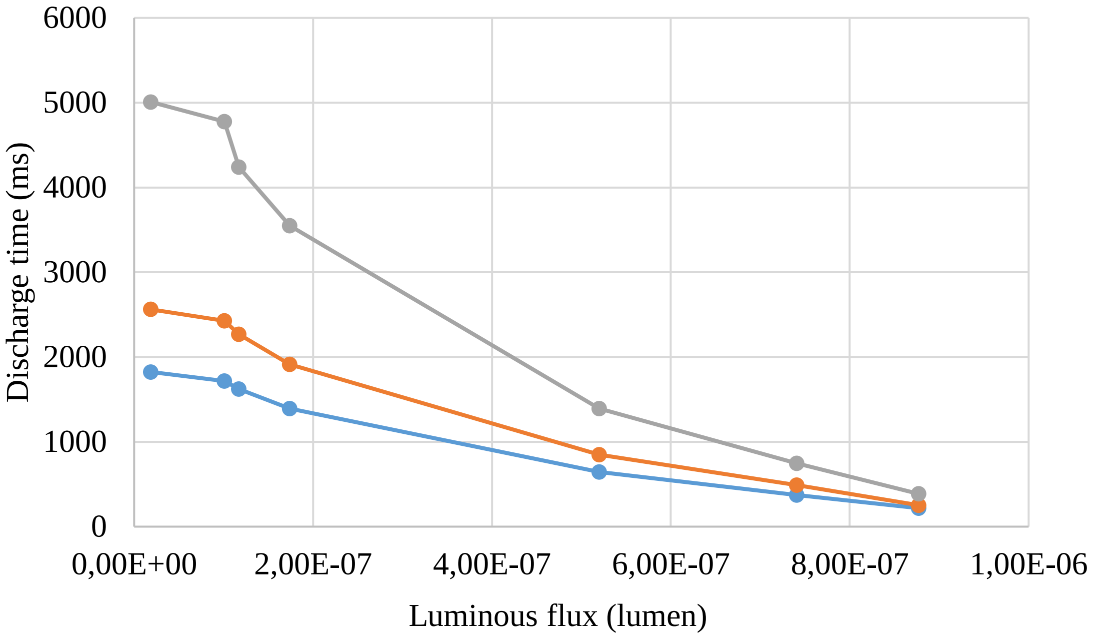

Figure 3.13 Time to 63 %, 50 %, 25 % of maximum discharge voltage, versus flux (lumen) of received light of green LED detector.

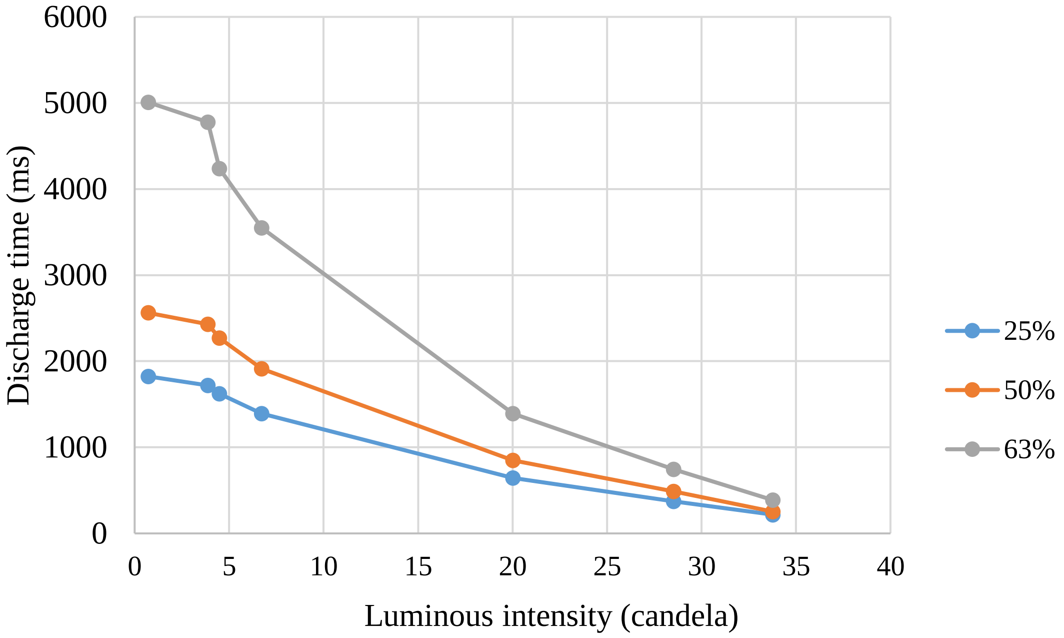

Figure 3.14. Time to 63 %, 50 %, 25 % of maximum discharge voltage, versus luminous intensity (candela) of received light of green LED detector.

3.6 DISCHARGE TIME VERSUS DISTANCE FROM EMITTER

A white emitter LED and a white detector LED were placed at different distances from each other. The discharge time to 63 % of the maximum discharge voltage of the detector LED and the illumination of the emitter LED, measured with the AvaSpec spectrometer at the set distance from the emitter LED, were measured. The discharge time to 63 % of the maximum voltage was selected because in Table 3.5 it can be seen that 63 %, 50 %, and 25 % are all adequate to differentiate between different light intensities. Additionally, the time to 63 % of the maximum voltage is the fastest, therefore reducing the time taken for colourimetric analysis, which is desirable in this research paper. Therefore, the LED was characterized for the discharge time to 63 % of the maximum discharge voltage.

All the measurements were performed in a dark optically isolated laboratory, where the only light present was that of the light-emitting OLED. The discharge time to 63 % of the maximum distance voltage was plotted against distance and illuminance (lux) as can be seen in Figure 3.15 and Figure 3.16 respectively. It can be observed that as the distance increases the discharge time increases. This is because as the LEDs move further away from each other, less light falls on the detector LED, and the detector LED takes longer to discharge (Figure 3.15). Additionally, the discharge time is seen to exponentially decrease, with an increase of illumination (Figure 3.16).

3.7 STATISTICAL ANALYSIS

In the research proposal, an investigation of the linearity of the light detector (reverse biased OLED) is required to be investigated.

Although the data is exponential in nature, statistical analysis was performed on the data in Table 3.6 to determine how linear the discharge time was, in relation to distance to detect light detection linearity. Linear regression analysis [102] was performed on the data from 1-50 cm and then again on the data from 1-11 cm. Linear regression analysis was also performed on discharge time in relationship to illumination (lux) to determine how linear the discharge time was in relationship to the light that is detected by the detector LED.

A white emitter LED and detector LED was used for all the tests in this section.

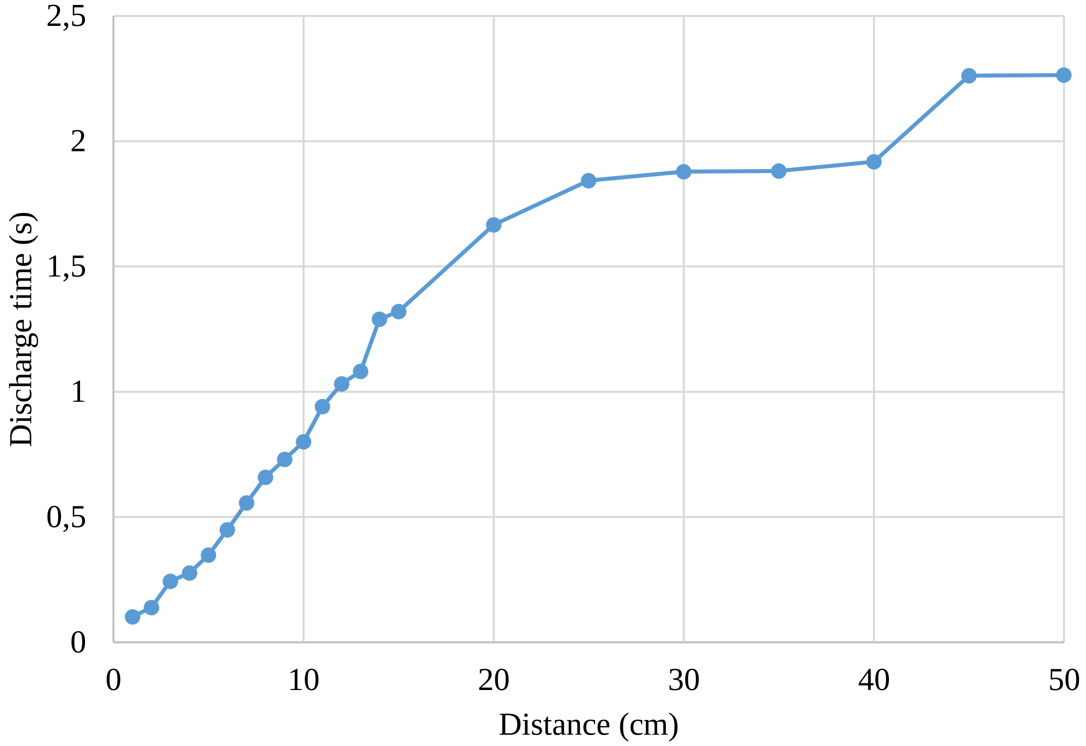

Figure 3.15. Discharge time to 63 % of maximum voltage (s) versus distance (cm).

Linear regression analysis indicates how two variables relate to one another and is based on the sum of squares. The smaller the sum of squares is the better the mathematical model of the data is [102]. The R square value is also known as the coefficient of determination and is used to show how well the data fits the linear regression line. To calculate the R square value, the data deviation of each point from the mean is squared and then summed together.

The multiple R value is also known as the correlation coefficient and is used to indicate how linear the data is. If the multiple R value is 1, there is a strong linear relationship in the positive direction and if the R value is -1, there is a strong linear relationship in the negative direction.

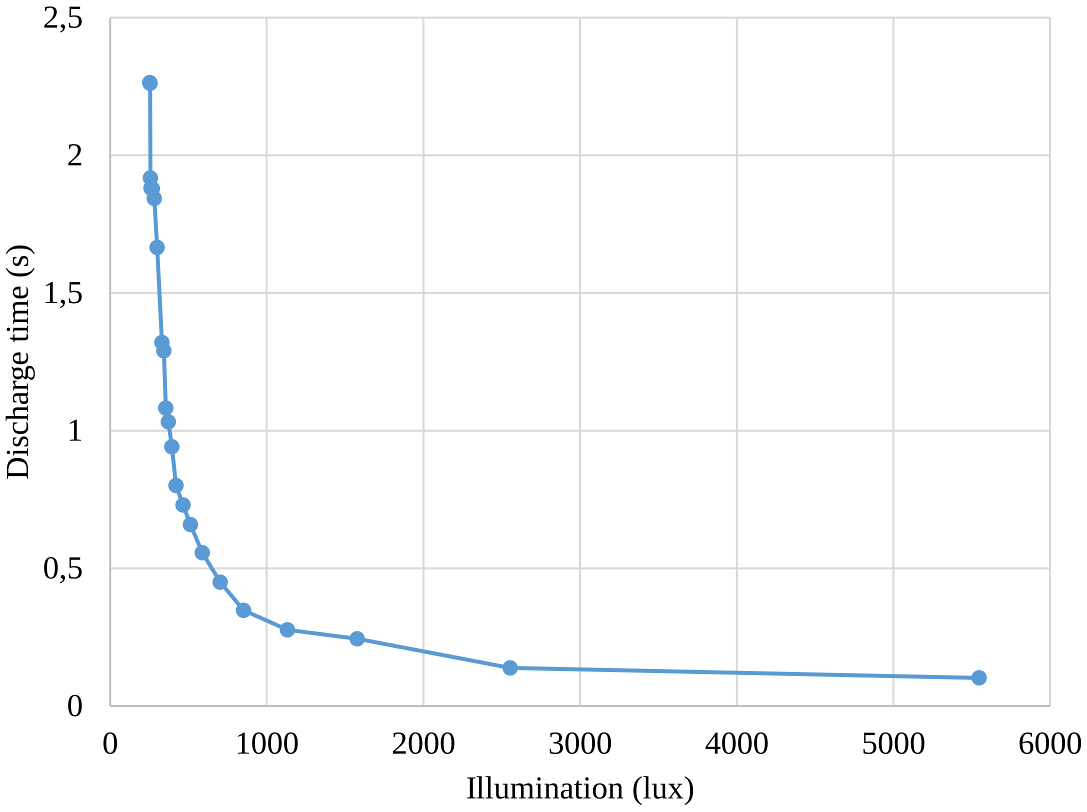

Figure 3.16. Discharge time to 63 % of maximum voltage (s) versus illumination (lux).

The further away from 1 and -1 the multiple R value is, the less linear the data is. A multiple R value of 0 indicates that there is no relationship or linearity between two variables at all [102].

The standard error is the absolute average value that each of the data points deviates from the linear regression line and can also be used as an indicator of the accuracy of the linear regression analysis [102].

Table 3.6. Discharge time to 63 % of maximum voltage and illumination at different distances from the emitter LED.

Distance from emitter LED (cm)	Discharge time to 63 % of maximum voltage (s)	Illumination (lux)
1	0.102	5548.4
2	0.139	2553.7
3	0.244	1578.3
4	0.277	1132.2
5	0.348	851.77
6	0.45	701.79
7	0.557	587.33
8	0.659	513.20
9	0.73	466.54
10	0.801	421.01
11	0.941	394.68
12	1.032	372.52
13	1.082	355.25
14	1.29	342.51
15	1.32	330.80
20	1.666	300.22
25	1.843	281.47
30	1.879	268.82
35	1.881	261.83
40	1.918	257.84
45	2.262	254.98
50	2.264	252.79

3.7.1 Statistical analysis of discharge time and distance 1-50 cm away from the light emitter.

Linear regression analysis was performed on the data in Table 3.6 for the discharge time to 63 % of the maximum discharge voltage versus distances in the range of 1-50 cm. The linear regression plot, equation, and R squared value are shown in Figure 3.17. Other linear regression statistics are given in Table 3.7.

The multiple R value (Table 3.7) is 0.944891, which is close to 1, and a multiple R value of 1 indicates a strong positive linearity. The R squared value indicates how well the linear regression model, given in Figure 3.17 fits the data and is calculated as 0.89282. This means that 89.92% of the data fit the linear regression model. This is not particularly desirable, as R squared values that are above 95 % are considered to be good models. Additionally, the standard error is calculated as 0.238332.

Table 3.7. Linear regression analysis parameters for discharge time to 63% of maximum discharge value, versus distance in the range of 1-50 cm.

Linear regression analysis parameters	
Multiple R	0.944891
R Square	0.89282
Standard Error	0.238332

3.7.2 Statistical analysis of discharge time and distance 1-11 cm away from the light emitter.

The linear analysis was redone on the data in Table 3.6 for the discharge time to 63 % of the maximum discharge voltage versus distance. However, a smaller distance range of 1-11 cm was used. The linear regression plot, equation, and R squared value are shown in Figure 3.18 and other linear regression statistics are given in Table 3.8.

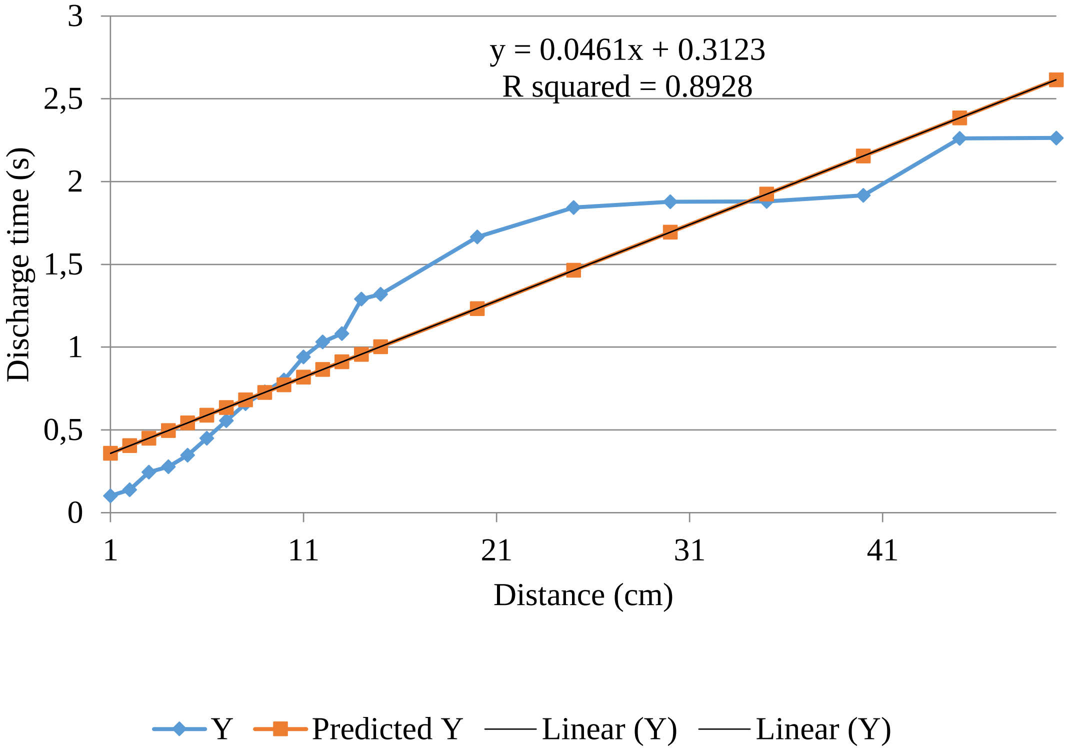

Figure 3.17. Discharge time to 63 % of maximum discharge value, versus distances in the range of 1-50 cm.

The linear regression analysis for distances 1-11 cm away has a much better linear relationship that the linear regression analysis for distance 1-50 cm. For distance 1-11 cm the multiple R value is 0.99464, which is closer to one than the calculated R value of 0.944891 for distances 1-50 cm.

The R squared value is also 0.989308, which means that 98.9308 % of the data fit the linear regression model. This is a good fit, as it is above 95 %, unlike the R squared value for distances between 1 and 50 cm. Lastly, the standard error for distances 1-11 cm is much smaller than the standard error for distances 1-50 cm.

Table 3.8. Linear regression analysis parameters for discharge time to 63 % of maximum discharge value, versus distance in the range of 1-11 cm.

Linear regression analysis parameters	
Multiple R	0.99464
R Square	0.989308
Standard Error	0.030642

3.7.3 Statistical analysis of discharge time at different illuminance values.

Linear regression statistical analysis is performed on the data from Table 3.6 for discharge time to 63 % of maximum discharge value versus illumination (lux). It can be seen from the linear regression plot Figure 3.19 and the linear regression analysis parameters in Table 3.9 that the discharge time versus illumination is not very linear.

It has a multiple R value of 0.572533, which means that there is not a very strong linear relationship and the R square value of 0.327794 indicates that only 32.7794 % of the data fit the linear regression model.

Table 3.9. Linear regression analysis parameters for discharge time to 63 % of maximum discharge value, versus illumination (lux).

Linear regression analysis parameters	
Multiple R	0.572533
R Square	0.327794
Standard Error	0.596865

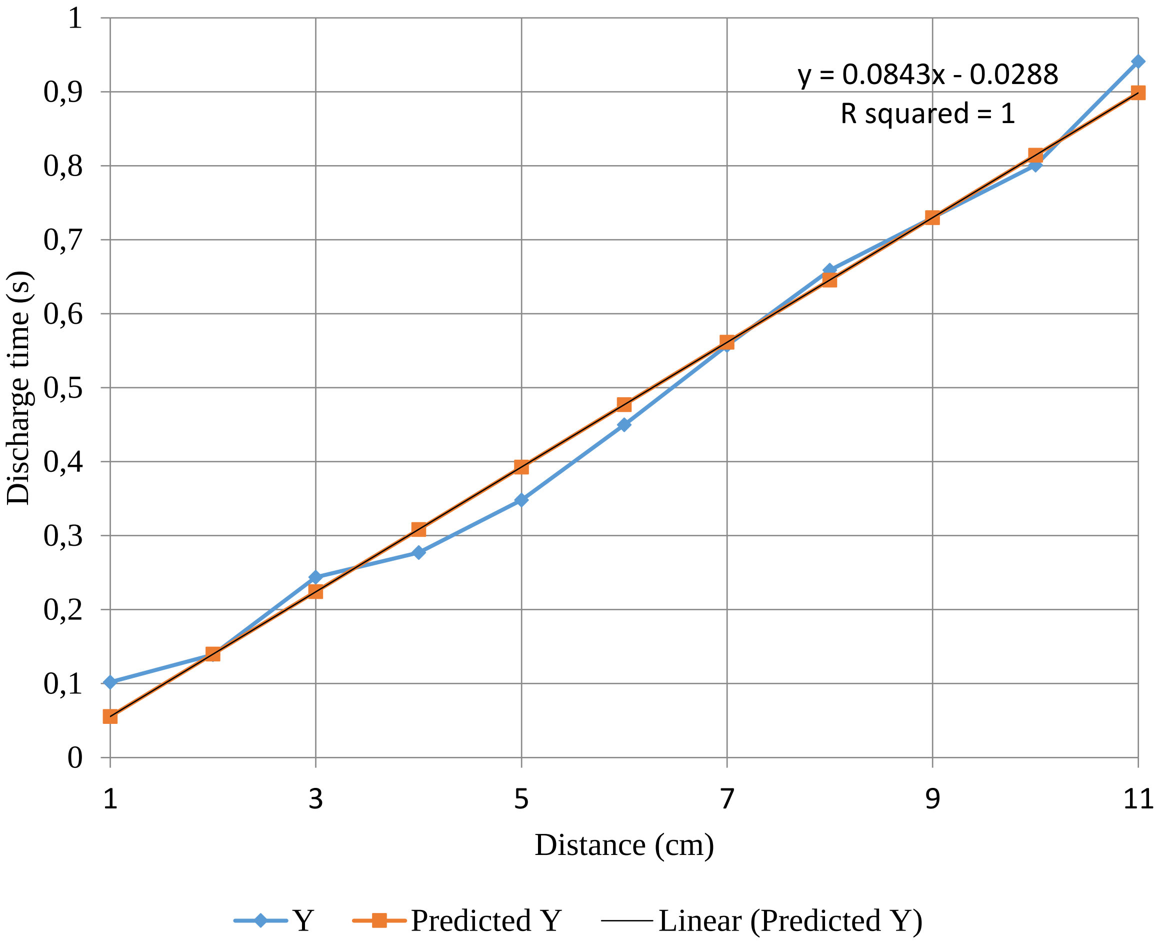

Figure 3.18. Discharge time to 63 % of maximum discharge value, versus distances in the range of 1-11 cm.

3.8 TESTING THE ANGULAR SPECTRAL RESPONSE OF LEDS

The angular spectral response of both emitter and detector LEDs were measured by measuring the emission and detection characteristics of the devices at various viewing angles [7], [103]. A 0 ° viewing angle of a panel is the viewing angle perpendicular to the panel. Viewing angles are then measured from the 0 ° viewing angle as a reference point.

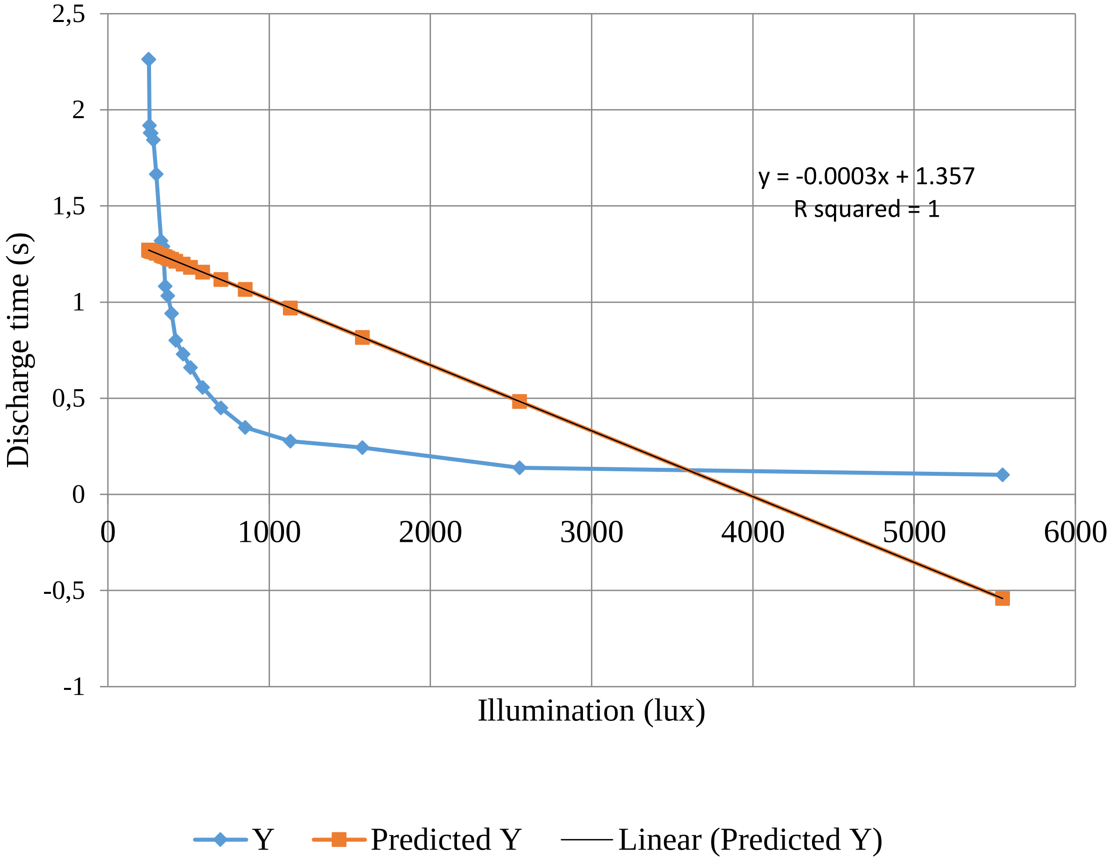

Figure 3.19. Discharge time to 63 % of maximum discharge value, versus illumination (lux).

3.8.1 Emitter LED

The light spectrum of a light source, used as an emitter, is dependent on the angle the emitted light is viewed from [103]. The transmittance measurement can be taken, using a spectrophotometer to determine the intensity of emitted light at different angles (viewing angles) [103]. The test setup to test the angular response of the emitter LED is shown in Figure 3.20. A semicircular block that has a hole every 15 °, which the Evo Spec Spectrometer probe can be inserted into, was used to measure the angular response of the emitter LED at 15 ° increments (Figure 3.20).

A rectangular container, that an LED can be placed into vertically, was placed below the semicircular block. The containers and holes were ensured to be optically isolated so that only the light emitted from the LED was measured.

The spectral parameter of the LED at viewing angles from 0 ° to 75 ° in 15 ° increments was measured. Table 3.10 summarizes the various spectral parameters of the emitter OLED panel, measured with an AvaSpec spectrometer, at different viewing angles. The irradiance and luminous intensities were given in both polar form and rectangular form.

The spectral response of the white LED at a 75 ° viewing angle to the panel is shown in Figure 3.21. The peak of the spectrum was in the red visible range, instead of the IR range as in the case of the white LED measured with a 0 ° viewing angle (Figure 3.2).

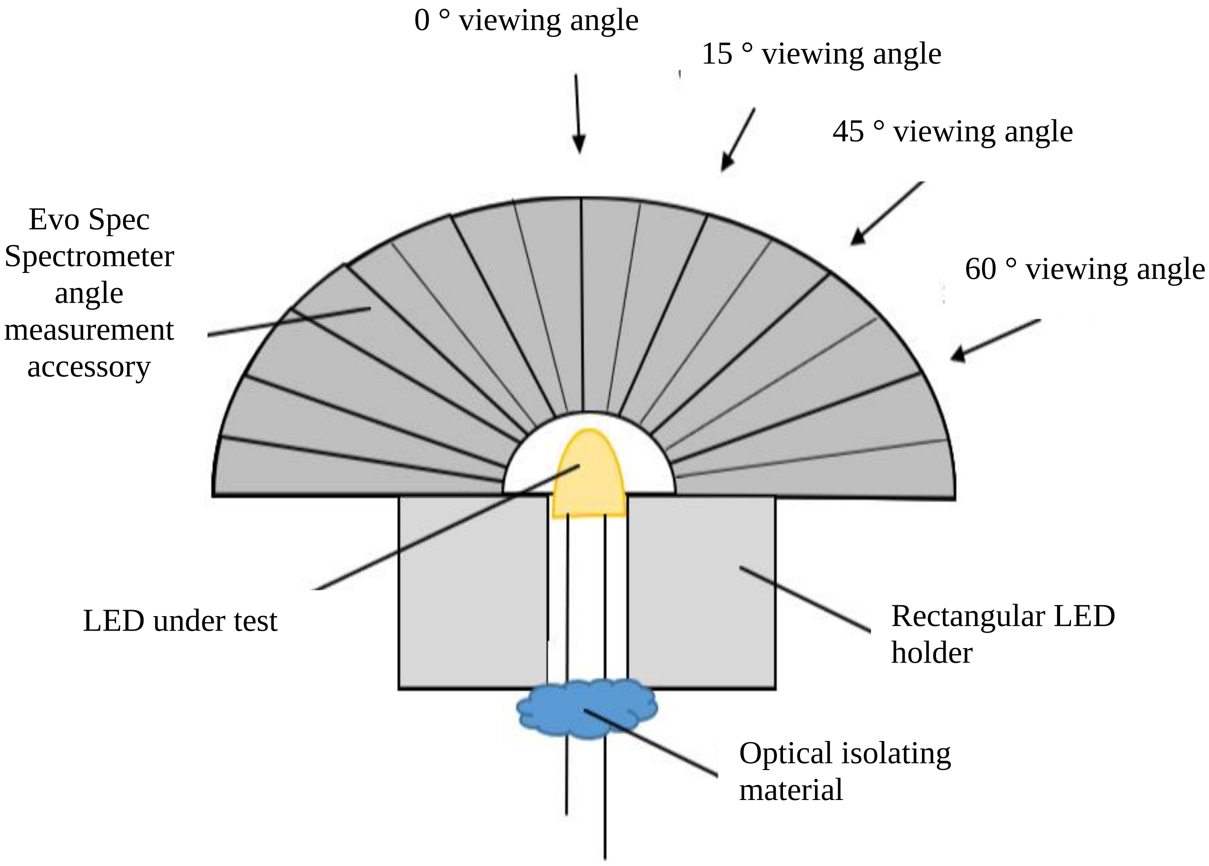

Figure 3.20. Test setup to measure the angular spectral response of LEDs.

The rectangular coordinates of the luminous intensity and luminous flux of the white LED were plotted in Python and are shown in Figure 3.22. Similarly, the angular response of irradiance was plotted in Python and is shown in Figure 3.23.

The angular response for irradiance (Figure 3.23) has a smaller magnitude at a 0 ° viewing angle than at a 15 ° viewing angle. This is because the LED packages typically have 3 distinct radiation patterns, Lambertian, batwing, and side-emitting [104]. The Lambertian packaging causes the intensity at a 15 ° degree viewing angle to be the largest, and the intensity at a 0 ° viewing angle to have a slightly smaller intensity than the maximum intensity. The batwing packaging causes the intensity to be a maximum at a 45 ° viewing angle and for there to be an approximately 25 % dip from the maximum intensity at a 0 ° viewing angle [104]. A simulation of illuminance for a batwing packaged LED is shown in Figure 3.24. Lastly, a side-emitting LED package causes the intensity to be a maximum at an 80 ° viewing angle and for there to be an approximately 60 % decrease from the maximum intensity between the 0 ° and 40 ° viewing angle [104].

The reason that the dip in intensity at 0 ° is not evident in the luminous intensity (Candela) and luminous flux (E-7 lumens) plots (Figure 3.22) is that both luminous intensity and luminous flux are scaled for how the human eye perceives light [74], [75].

3.8.2 Detector LED

To determine the angular response of a LED, used as a light detector, the light detection sensitivity, relative to the maximum light sensitivity, needs to be measured [7]. The light-emitting device needs to be rotated about the detection device from -90 ° degrees to +90 ° on the x-axis and -90 ° to +90 ° on the y-axis. The geometrical shape, as well as the internal composition of an, LED affect the angular response of an LED as a detector [7].

Table 3.10. Angular spectral response of a white LED.

Parameter	**75 °**	**60 °**	**45 °**	**30 °**	**15 °**	**0 °**
Dominant wavelength (nm)	458.91	457.56	456.82	458.15	458.15	458.13
Irradiance (μWatt/cm^2)	29.632	45.344	90.911	144.08	167.12	125.51
Irradiance (μWatt/cm^2) in rectangular form	28.62 + 7.67*j*	39.27 + 22.67*j*	64.28 + 64.28*j*	72.04 + 124.78*j*	43.25 + 161.43*j*	0.00 + 125.51*j*
Luminous Intensity (Candela)	27.957	27.283	26.810	25.632	24.934	25.494
Luminous Intensity (Candela) in rectangular form	27.00 + 7.24*j*	23.63 + 13.64*j*	18.96 + 18.96*j*	12.82 + 22.20*j*	6.45 + 24.08*j*	0.00 + 25.49*j*
Luminous Flux (Lumens)	7.259E-7	7.084E-7	6.961E-7	6.655E-7	6.474E-7	6.619E-7
Centre wavelength (nm)	1096.7	1097.2	1097.2	1097.2	1097.3	1097.3
Amplitude of centre wavelength	0.7094	0.7786	2.5168	4.0125	4.9410	3.4724

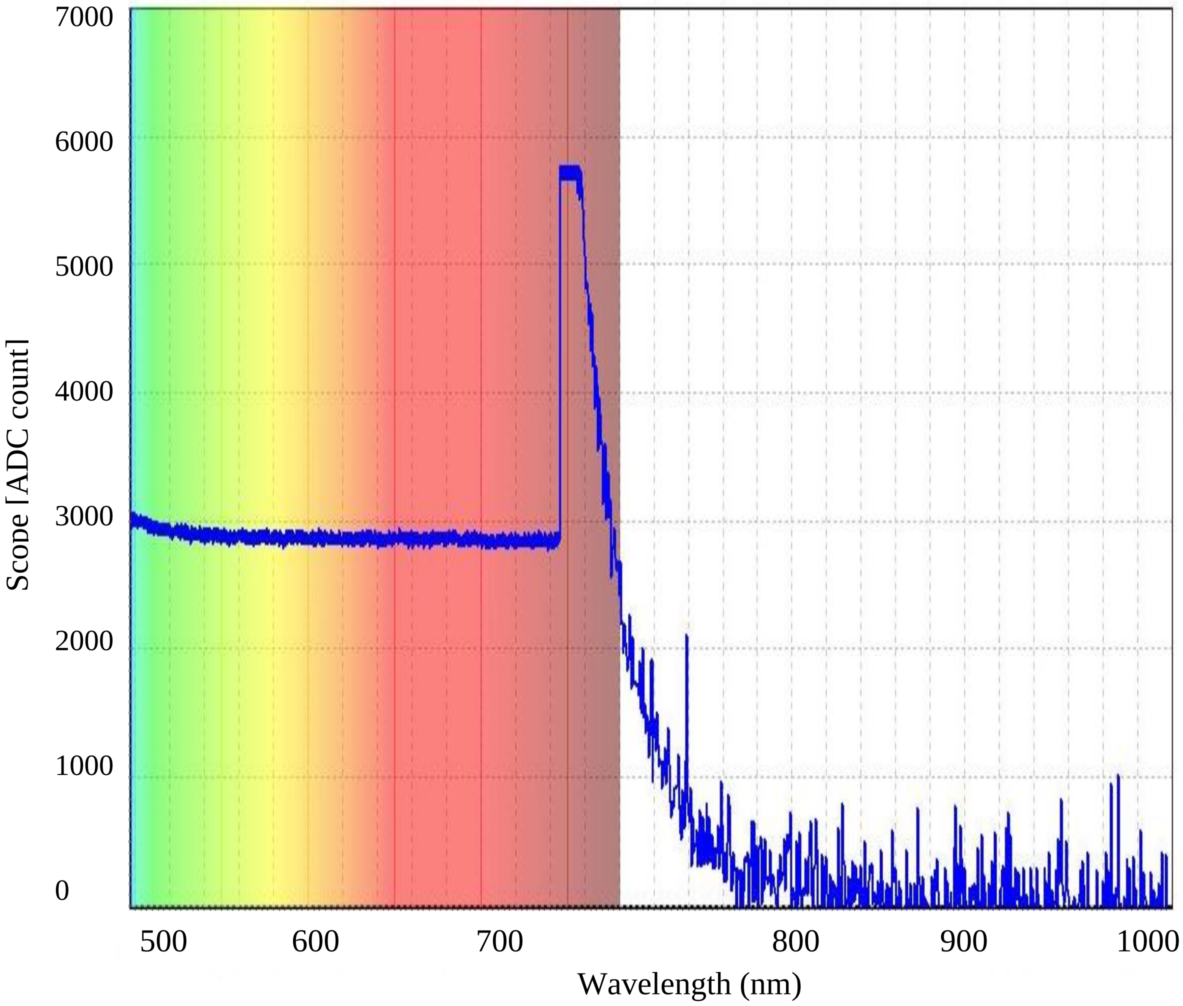

Figure 3.21 Spectral response of a white LED measured at a 75-degree viewing angle.

A white emitting LED was placed 10 cm away from a white detector LED, which were ensured to be parallel, using tape measures. A protractor was then used to measure the viewing angle, as the detector LED was rotated. The front centre point of the LED was always kept in the centre point of the protractor.

The discharge time to 63 % of the maximum discharge voltage, at viewing angles -90 ° to 90 ° were measured in 10 test repetitions. The average of the test results are shown in Table 3.11 and the discharge time versus viewing angle are plotted (Figure 3.25).

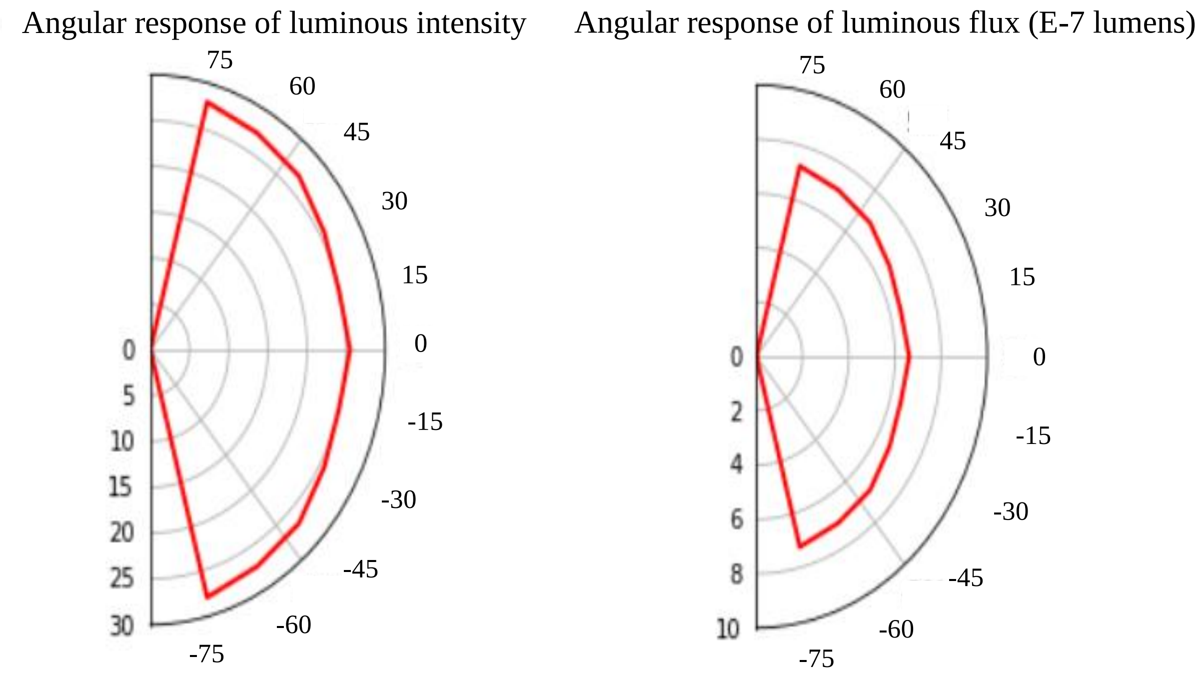

(a) (b)

Figure 3.22 Angular response of a white LED plotted in Python. (a). Luminous intensity (Candela). (b). Luminous flux (E-7 lumens)

As mentioned previously, the discharge time to 63 % of the maximum voltage was selected because in Table 3.5 it can be seen that 63 %, 50 %, and 25 % are all adequate to differentiate between different light intensities. Additionally, the time to 63 % of the maximum voltage was the fastest, therefore reducing the time taken for colourimetric analysis, which is desirable in this research paper.

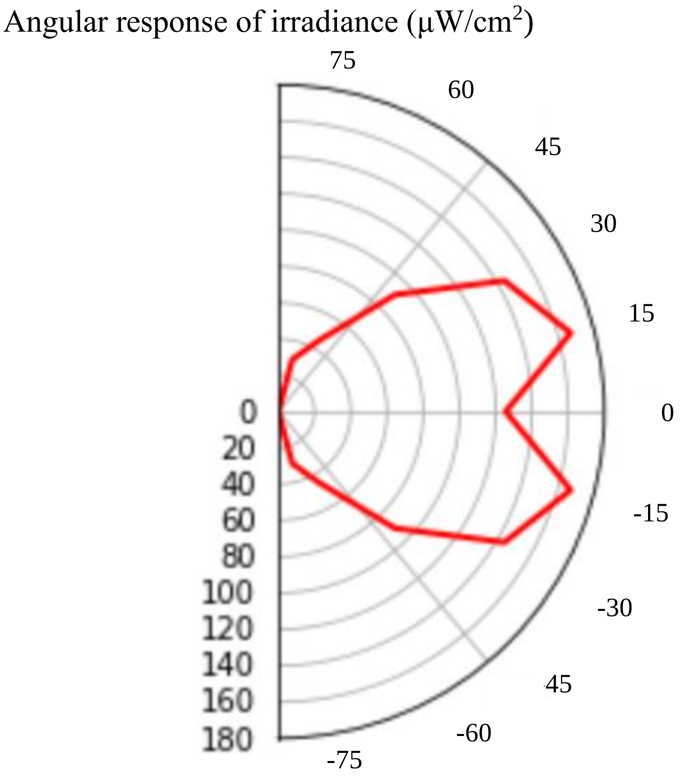

Figure 3.23 Irradiance (μWatt/cm^2) angular response of a white LED plotted in Python.

Table 3.11. Discharge time (s) at different viewing angles (°).

Viewing angle (°)	**Discharge time (s)**
0	0.886
15	0.9
30	0.936
45	1.044
60	1.404
75	1.728
90	1.62

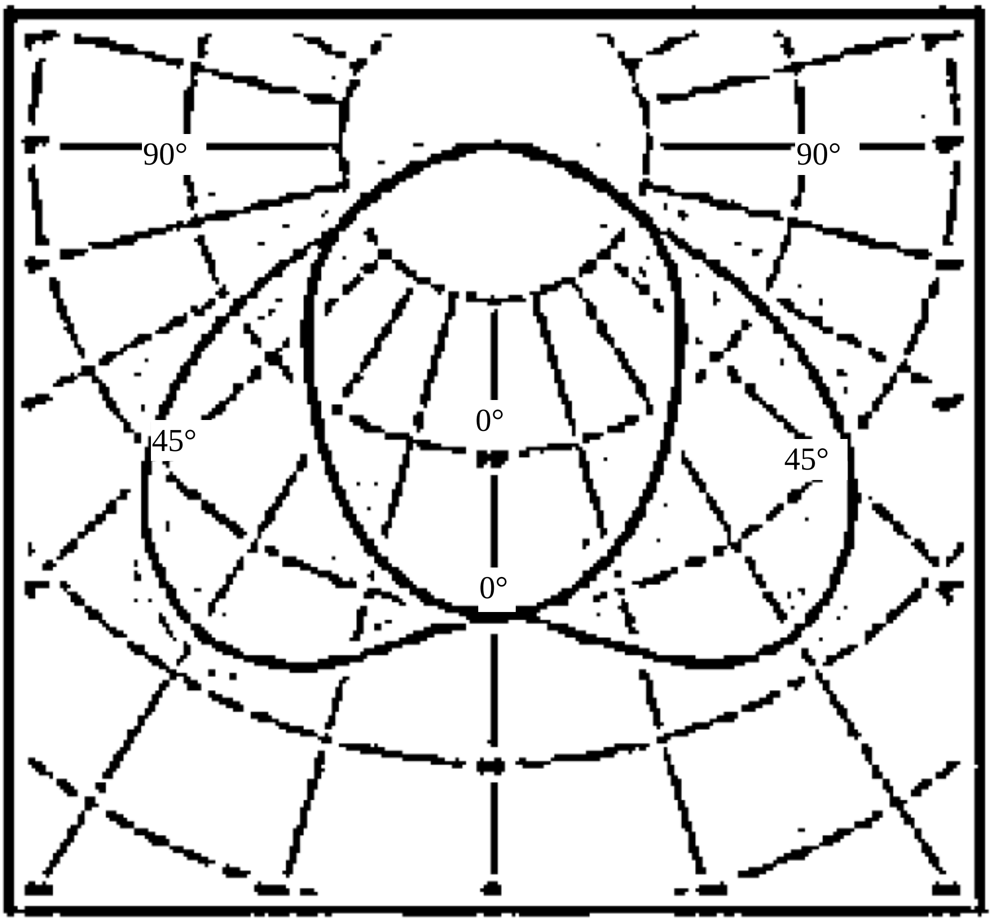

Figure 3.24. Simulation of illuminance for a batwing LED. Taken from **[105]**, © 2014 IEEE.

It can be seen from Figure 3.25 that the discharge time at a 0 ° viewing angle the discharge time is the shortest. This is because the most emitted light gets detected by the light detecting LED at a 0 ° viewing angle and the more light that is detected, the shorter the discharge time will be.

The maximum discharge time is seen to be at a 75 ° angle and not at a 90 ° angle. This can be accounted for the fact that at a 90 ° viewing angle, light is emitting/detected through the LED packaging perpendicular to the packaging. This causes the light detected at a 90 ° angle to be brighter than at 75 °, and therefore the discharge time to be shorter.

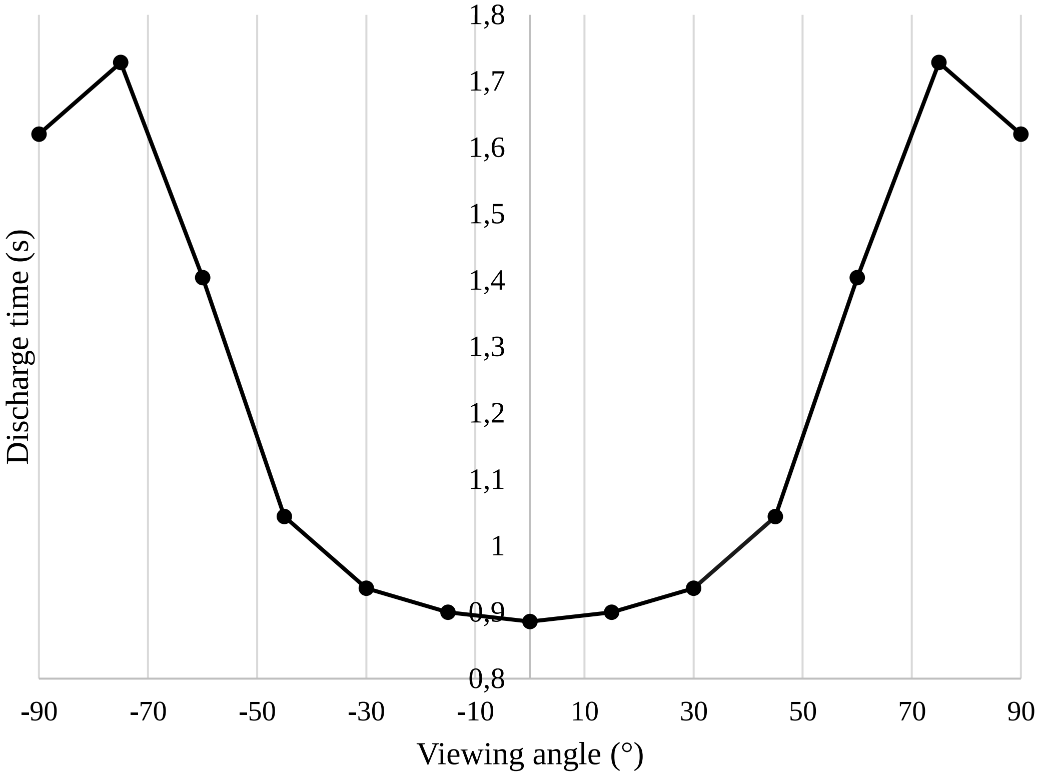

Figure 3.25. The discharge time of the white LED detector versus viewing angle (°).

3.9 COLOURIMETRIC ANALYSIS

A pH colourimetric analysis test was performed, using LEDs as both light emitters and light detectors. A pH test kit (JBL pH Test 3.0-10.0 test kit), with a range of pH 4-10 was used as the reagent indicator that changes the colour of the water sample depending on the pH level. Four drops of the reagent indicator were added per 10 ml liters of liquid of the test sample. Bleach and vinegar were used to change the pH levels of water, and the pH levels were measured with a PH-107 digital pH meter, for calibration purposes. The reagent was then added to the sample, and the sample changed colour according to the pH level. The sample turned red for a pH of 4, orange for a pH of 5, yellow for a pH of 6, light green for a pH of 7, dark green for a pH of 8 and purple for a pH of 9. A picture of liquid samples, at each pH level in glass bottles, is shown in Figure 3.26.

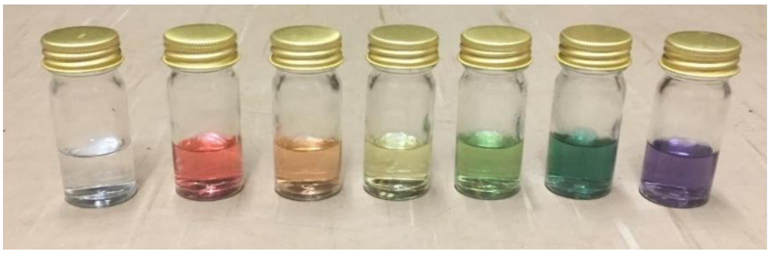

Figure 3.26. Liquid samples at different pH levels: Red (pH 4), Orange (pH 5), Yellow (pH 6), Light green (pH 7), Dark green (pH 8), Purple (pH 9).

An LED array of LEDs with various bandwidths were used to perform colourimetric analysis on liquid samples. A blue, green, orange, and yellow LED were used as light detectors. The blue, green and orange LEDs were selected because their spectral responses cover different regions of the visible light spectrum, with minimal overlapping wavelengths. A yellow LED was later added to the LED detector array to improve the accuracy of the colourimetric analysis.

The emission spectra of the blue, green, orange and yellow LEDs, when a 470 Ω resistor (*Re*) was placed in series with them, is shown in Figure 3.27. White LEDs were used as the light-emitting LEDs because they have a bandwidth that covers the entire bandwidth of all the other coloured LEDs that are used in the array (Figure 3.2). The first detector LED was placed parallel to a white emitter LED to measure the reflected light, the second detector LED was placed at a 90 ° angle to the emitter LED to measure the light that was scattered, and the third LED is placed at a 180 ° angle from the emitter LED in order to measure the light that was transmitted through the liquid. A CAD design of the LED array sensor box can be seen in Figure 3.28.

The plot to 63 % of the total ADC value (Figure 3.12, Figure 3.13 and Figure 3.14) shows the most variation (greatest decrease) over the range. The time taken to 63 % of the total ADC value was taken for each of the detector LEDs, for each of the different solutions. It was also advantageous to use the discharge time to 63 % of the maximum voltage, instead of the 50 % or 25 % discharge time because it was faster and therefore reduced the time of the colourimetric analysis. The results are summarized in Table 3.2.

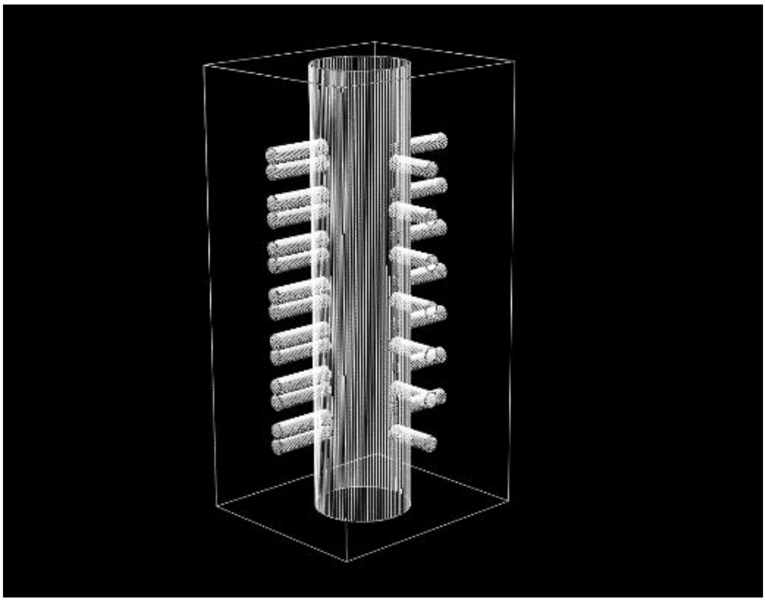

Figure 3.28. CAD design of an LED array sensor box.

The discharge times for the different coloured LED light detectors for light reflection, refraction and transmission through each of the pH samples are shown in Figure 3.27, Figure 3.28 and Figure 3.29, respectively. The discharge times are also measured for an empty glass bottle and a bottle with clear water in it, for calibration purposes.

The more light that is exposed to the detecting LED, the faster the discharge time will be. The largest distinction between the discharge times, for each pH level, is observed when measuring the light transmitted through the samples (Figure 3.26). The yellow detector LED has the fastest discharge time for the majority of the pH samples. This is because the yellow LED has the largest bandwidth (Figure 3.27). For light transmitted through the sample, the blue LED has a fastest discharge time when detecting a pH of 4 (pink) and 9 (purple), this is because the pink and purple pH samples filter out more light in the yellow LEDs bandwidth range than the blue LEDs bandwidth range.

When observing the yellow LED detector for the transmitted light plots, the discharge time is shortest for a pH of 6 (yellow), an empty bottle and a clear water sample.

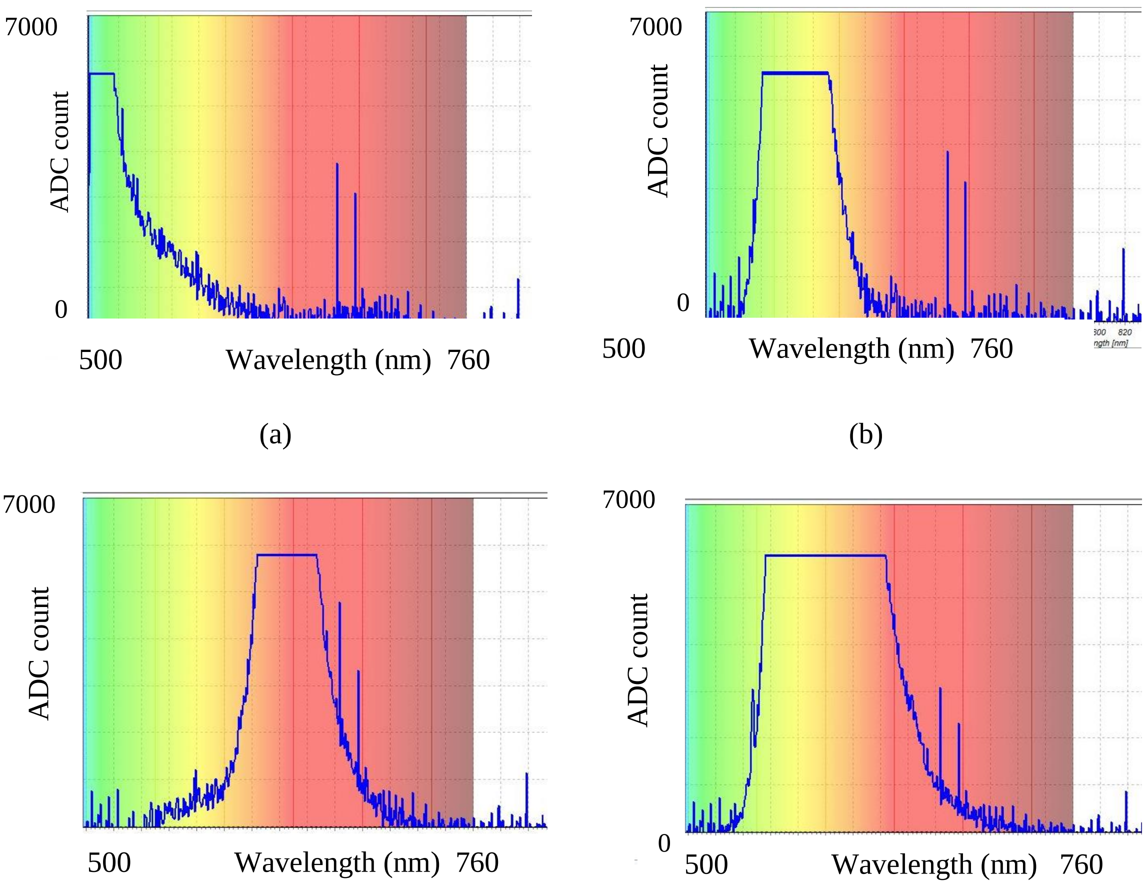

(a) (b)

(c) (d)

Figure 3.27 Different colour LED emission spectra, with Re = 470 Ω.

(a) blue LED (b) green LED (c) orange LED (d) yellow LED

This is because all the light that is present in the yellow LED bandwidth gets transmitted through the sample, without being filtered out by another colour filter. The yellow LEDs discharge time is the longest when detecting a pH of 9 (purple) and 4 (pink) because the most amount of light in the yellow bandwidth range gets filtered out when the light is transmitted through the purple and pink pH samples.

A similar trend can be seen for the green and orange LEDs, that detect light transmitted through pH samples. However, the orange LEDs discharge time, when detecting a pH of 8 (dark green), is much larger than when detecting a pH of 9 (purple); while for a yellow LED detector it is larger when detecting a pH of 9 (purple).

Table 3.12. Time (seconds) to 63 % of the total ADC value for the detector LED, measuring each of the pH solutions.

LED detector colour	**Detector orientation**	**pH**							
		Empty	**Water**	**4**	**5**	**6**	**7**	**8**	**9**
Blue	Reflect	0.712	0.76	0.986	0.982	0.949	0.982	0.984	0.958
	Refract	1.052	0.981	2.745	2.739	2.716	2.79	2.521	2.651
	Transmit	0.704	0.644	0.949	1.017	0.95	0.951	0.951	0.99
Green	Reflect	1.054	1.019	1.861	1.693	1.525	1.602	1.7	2.499
	Refract	1.176	1.224	2.549	2.239	2.01	2.145	2.387	2.284
	Transmit	1.016	0.817	1.742	1.322	1.084	1.156	1.436	1.392
Orange	Reflect	1.072	1.098	0.922	1.568	1.126	0.984	1.903	0.987
	Refract	1.255	1.361	2.027	2.072	1.979	2.081	2.592	2.036
	Transmit	0.883	0.765	1.711	1.192	1.226	1.386	2.213	1.838
Yellow	Reflect	0.78	0.776	0.94	0.858	0.828	0.845	0.88	0.917
	Refract	0.95	1.043	1.33	1.219	1.049	1.149	1.288	1.427
	Transmit	0.54	0.43	0.982	0.611	0.439	0.587	0.745	1.219

This is because the green pH sample filters out more light in the orange LEDs bandwidth than the yellow LEDs bandwidth; while the purple pH sample filters out more light in the yellow LEDs bandwidth than the orange LEDs bandwidth. For the green detector LED, a similar discharge time is observed when detecting a pH of 8 (dark green) and 9 (purple). This is because the dark green and purple pH samples, filter out the same amount of light in the green LEDs bandwidth.

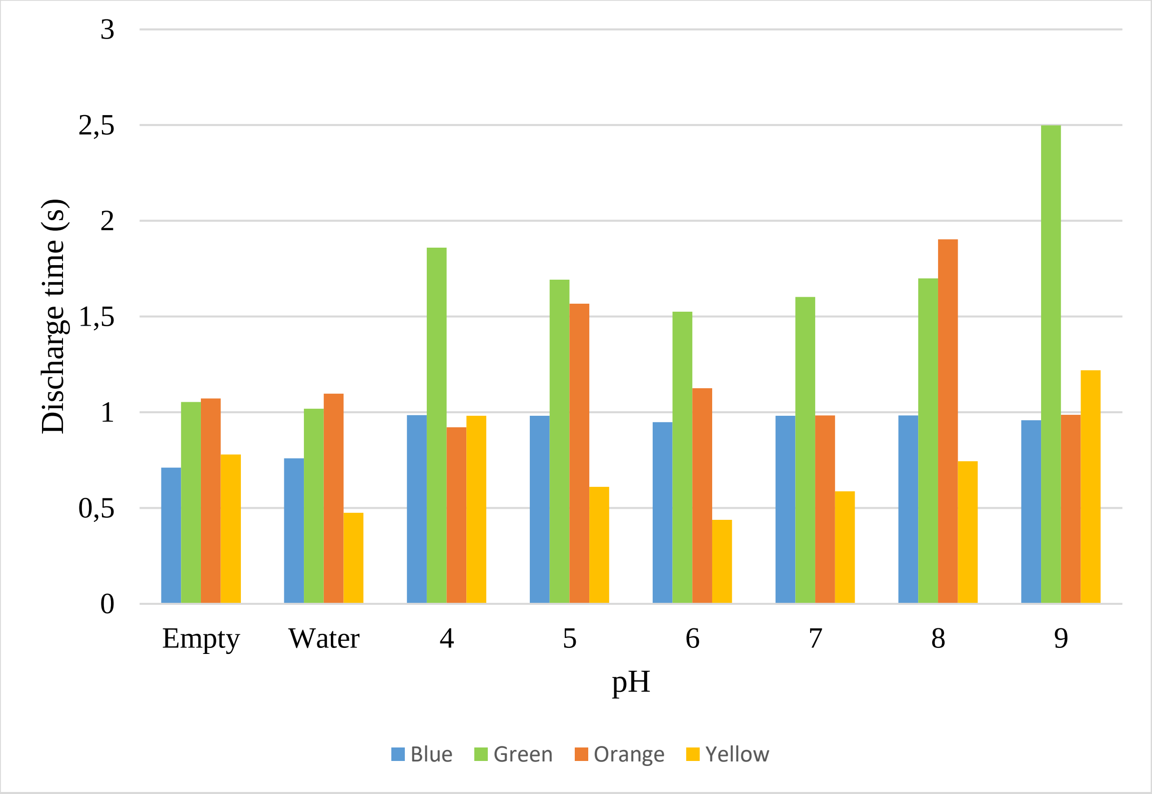

Figure 3.27. Discharge time to 63% of ADC value, measuring light reflected by each pH sample.

The ideal transmission, reflection, and refraction measurements are when the solution does not contain any reagents, additives or other solvents [33]. The sample that contains clear water was used as the ideal measurements. The measured transmission, reflection and refraction discharge time is related to the ideal discharge time using (3.3), whereby t_0 is the ideal discharge time and t is the measured discharge time. The ratio between the ideal and measured transmission, reflection and refraction discharge times were calculated and summarized in Table 3.13.

$$\boldsymbol{R} = \frac{\boldsymbol{t_0}}{\boldsymbol{t}} \tag{3.3}$$

The relative transmission, reflection and refraction values are calculated using (3.4) [33]. The calculated values are given in Table 3.14.

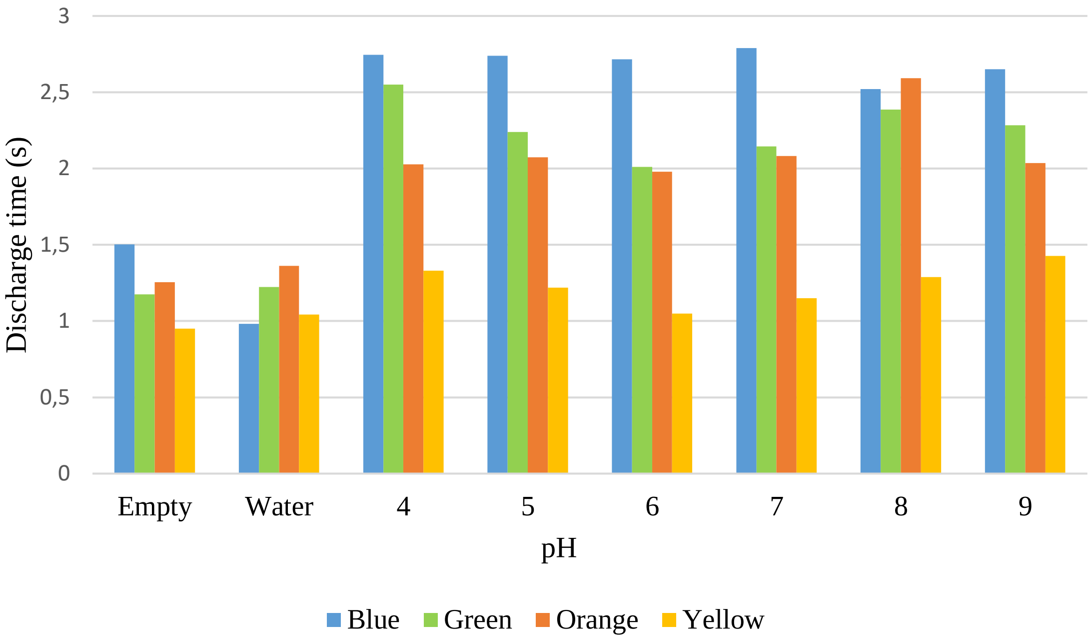

Figure 3.28. Discharge time to 63% of ADC value, measuring light refracted by each pH sample.

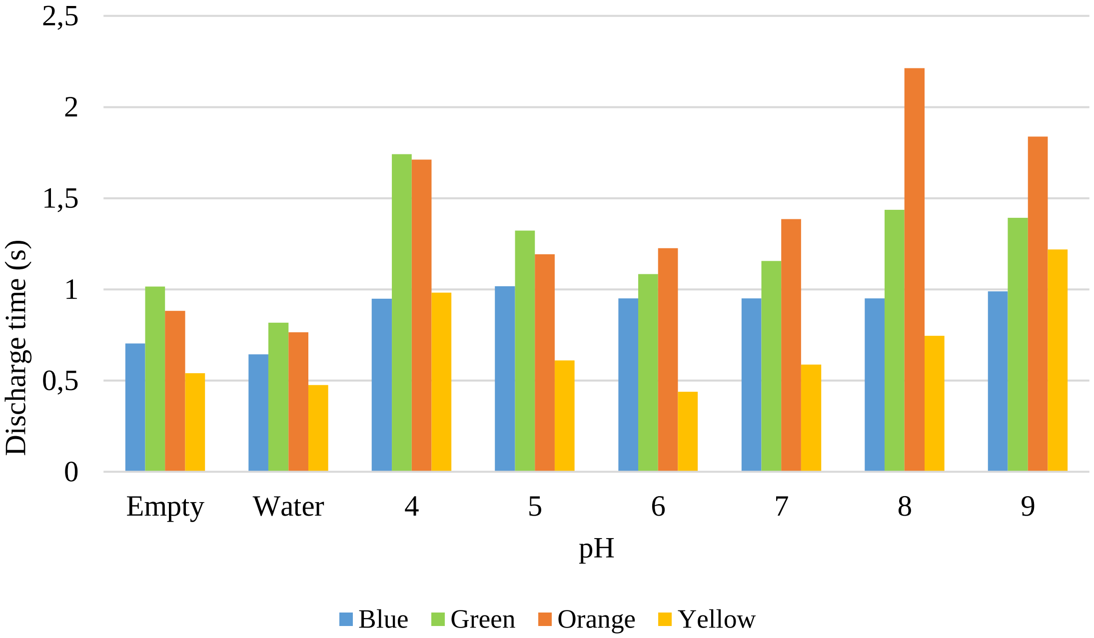

Figure 3.29. Discharge time to 63% of ADC value, measuring light transmitted through each pH sample.

Table 3.13. Ideal reflectance/refraction/transmission of each detector LED, measuring each of the pH solutions.

LED detector colour	**Detector orientation**	**pH**						
		Water	**4**	**5**	**6**	**7**	**8**	**9**
Blue	Reflect	1	1.2974	1.2921	1.2487	1.2921	1.2947	1.2605
	Refract	1	1.33	1.219	1.049	1.149	1.288	1.427
	Transmit	1	1.4736	1.5792	1.4752	1.4767	1.4767	1.5373
Green	Reflect	1	1.8263	1.6614	1.4966	1.5721	1.6683	2.4524
	Refract	1	2.0825	1.8292	1.6422	1.7525	1.9502	1.8660
	Transmit	1	2.1322	1.6181	1.3268	1.4149	1.7577	1.7038
Orange	Reflect	1	0.8397	1.4281	1.0255	0.8962	1.7332	0.8989
	Refract	1	1.4893	1.5224	1.4541	1.5290	1.9045	1.4960
	Transmit	1	2.2366	1.5582	1.6026	1.8118	2.8928	2.4026
Yellow	Reflect	1	1.2113	1.1057	1.0670	1.0889	1.1340	1.1817
	Refract	1	1.2752	1.1687	1.0058	1.1016	1.2349	1.3682
	Transmit	1	2.2837	1.4209	1.0209	1.3651	1.7326	2.8349

$$\boldsymbol{Relative\ absorbance}\ (\%) = \frac{\boldsymbol{t - t_0}}{\boldsymbol{t}} \times \mathbf{100} \tag{3.4}$$

The negative values for the light reflecting, when using an orange LED detector, is due to that fact that more light in the orange LED bandwidth gets reflected for a pH of 4, 7 and 9 than gets reflected when clear water is in the bottle.

Table 3.14. Relative absorbance (%) of each detector LED, measuring each of the pH solutions.

LED detector colour	**Detector orien-tation**	**pH**						
		Water	**4**	**5**	**6**	**7**	**8**	**9**
Blue	Reflect	0.0000	22.9209	22.6069	19.9157	22.6069	22.7642	20.6681
	Refract	0.0000	64.2623	64.1840	63.8807	64.8387	61.0869	62.9951
	Transmit	0.0000	32.1391	36.6765	32.2105	32.2818	32.2818	34.9495
Green	Reflect	0.0000	45.2445	39.8110	33.1803	36.3920	40.0588	59.2237
	Refract	0.0000	51.9812	45.3327	39.1045	42.9371	48.7222	46.4098
	Transmit	0.0000	53.0999	38.1997	24.6310	29.3253	43.1058	41.3075
Orange	Reflect	0.0000	-19.0889	29.9745	2.4867	-11.585	42.3016	-11.246
	Refract	0.0000	32.8564	34.3147	31.2279	34.5988	47.4923	33.1532
	Transmit	0.0000	55.2893	35.8221	37.6020	44.8052	65.4315	58.3787
Yellow	Reflect	0.0000	17.4468	9.5571	6.2802	8.1657	11.8182	15.3762
	Refract	0.0000	21.5789	14.4381	0.5720	9.2254	19.0217	26.9096
	Transmit	0.0000	56.2118	29.6236	2.0501	26.7462	42.2819	64.7252

The relative transmission (%) for each sample, using each colour detector LED is plotted in Figure 3.32. The relative reflection and refraction plots are given in addendum B. Both the discharge time and relative transmission (%) values can be used to differentiate between the different pH samples. The advantage of using the relative values, is that it is relative to the container used and can therefore be recalibrated for any container.

The advantage of using the discharge values is that no additional computation and processing time is required. For the LED colourimetric test, the discharge values are compared to differentiate between the different pH samples.

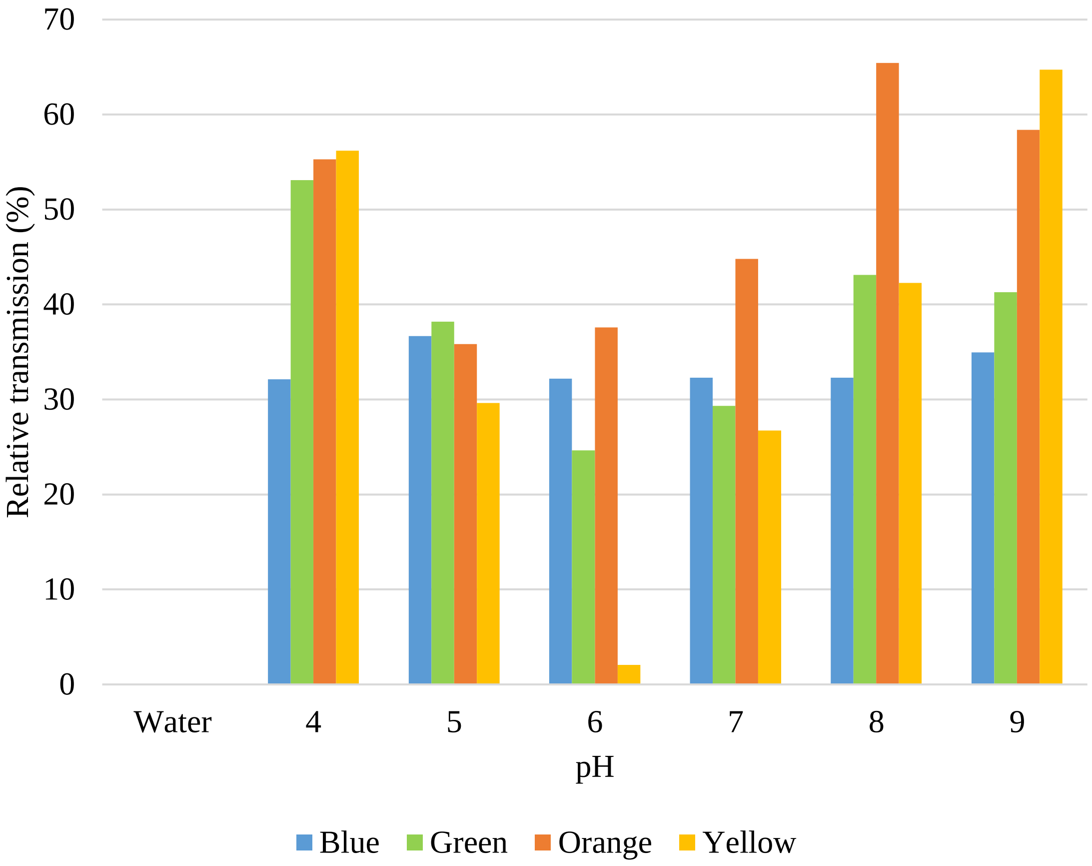

Figure 3.30. Relative transmission (%) for each of the pH samples.

Even a small deviation in light affects the discharge time, therefore, to ensure accuracy, a test was set up to run consecutive tests for 10 minutes and determine the maximum and minimum detected value for each sample, using each colour LED detector.

Instead of using the discharge time, a variable “count” was incremented each time the ADC value was measured and sent the serial port. The maximum and minimum “count” variable values for each pH sample, using each colour LED detect was recorded and is summarized in Table 3.15.

Table 3.15. Maximum and minimum ADC values measured for the detector LEDs, measuring the transmitted light, through each pH solution.

LED	Empty	Clear	4	5	6	7	8	9
Yellow	1775 to 1886	1572 to 1669	1905 to 1975	1723 to 1810	1587 to 1695	1780 to 1859	1906 to 1971	1949 to 2042
Blue	1824 to 1908	1882 to 2001	1841 to 1936	1882 to 1952	1811 to 1914	1860 to 1922	1836 to 1952	1806 to 1890
Orange	1803 to 1899	1709 to 1799	1754 to 1858	1737 to 1832	1719 to 1795	1843 to 1907	1930 to 1985	1932 to 1969
Green	1994 to 2080	1858 to 1918	2112 to 2212	2059 to 2127	1897 to 1954	1983 to 2062	2058 to 2186	2106 to 2202

The maximum and minimum “count” variable values, when measuring transmitted light with a yellow LED detect is plotted in Figure 3.31. The maximum and minimum count ranges fall into 3 distinct regions which is indicated as group 1, group 2 and group 3 in the plot. Because the count range for a pH of 6 is the only count range that falls in group 3, a pH of 6 can be differentiated from other pH values, using the transmission reading of a yellow LED detector.

In order to distinguish between the count ranges in group 1 and group 2, the count ranges for transmission using an orange (Figure 3.32) and green (Figure 3.33) LED detector were used. When an orange LED detector is used to measure transmission, the pH of 4 can be differentiated from pH of 8 and 9, all of which are in group 1 when a yellow LED detector is used. This is because more light in the orange LED bandwidth is transmitted through the pink, pH 4 sample, than in the yellow LEDs bandwidth. Because more light is transmitted in the orange LEDs bandwidth, the discharge time or count value is much smaller for an orange LED detector than a yellow LED detector.

In order to differentiate between a pH of 5 and 7, which both fall in group 2 when a yellow LED detecting transmitted light is used (Figure 3.33), measurements from both the orange (Figure 3.32) and green (Figure 3.33) LEDs detecting transmitted light are used.

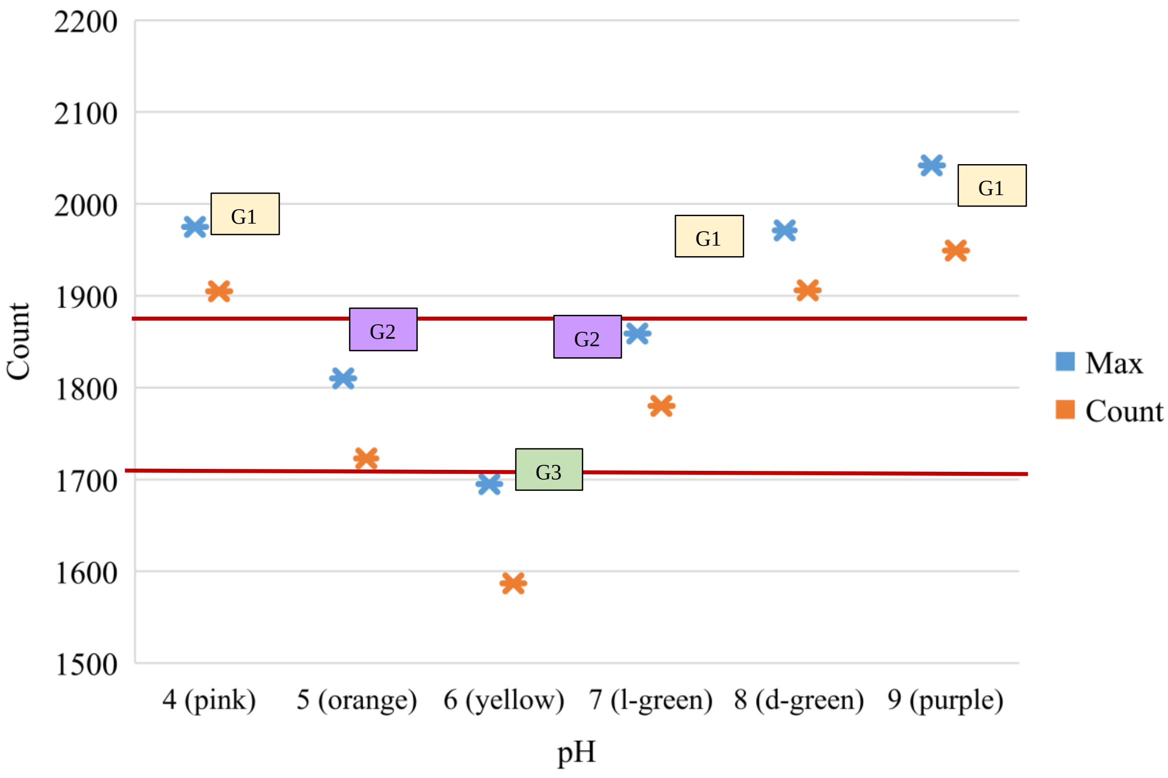

Figure 3.31. Maximum and minimum ADC count readings with the yellow LED detector, detecting transmission measurements.

In both cases a pH of 5 and 7 fall into different count ranges. For an orange LED detector, a pH of 7 has a larger count value than for a pH of 5. The ranges are quite close to each other, therefore, to confirm the result the results of the green LED detector are looked at. For a green LED detect the pH of 5 and 7 also fall in different count range, but the pH 5 count values are larger than the pH 7 count values.

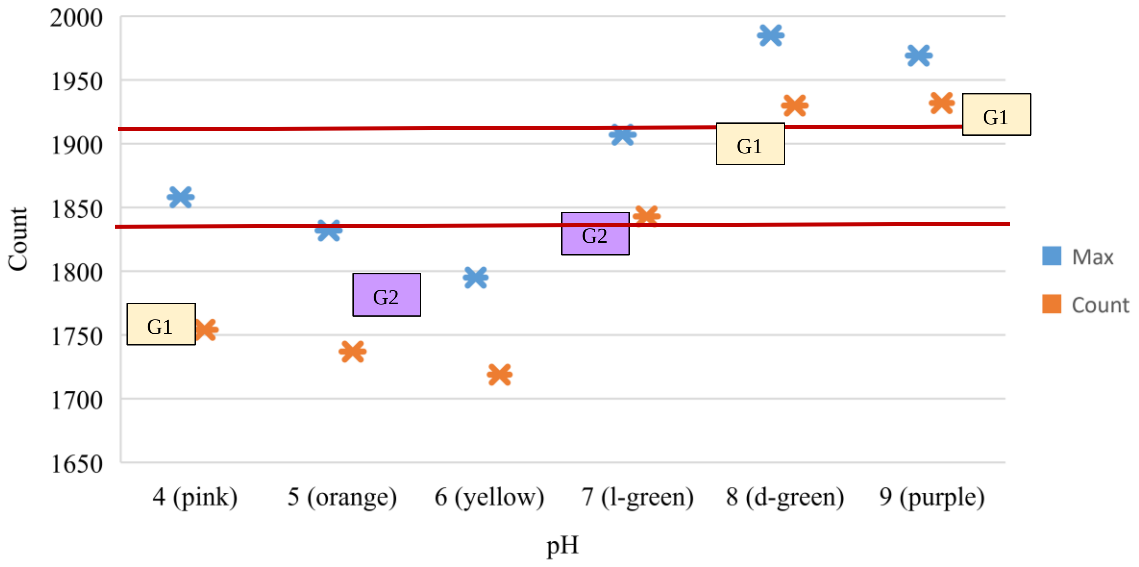

Figure 3.32. Maximum and minimum ADC count readings with the orange LED detector, detecting transmission measurements.

As in the case of the orange LED detector, the green LED detectors range for pH 5 and pH 7 are quite close together. Therefore, if the count value of a sample falls in group 2 for a yellow LED detect, is above 1845 for an orange LED detector and smaller than 2052 to a green LED detector, then it can be confirmed that the sample has the pH of 7. Similarly, if the count value of a sample fall in group 2 for a yellow LED detector, is below 1845 for an orange LED detector and larger than 2052 to a green LED detector, then it can be confirmed that the sample has the pH of 5. If the results do not satisfy all of the conditions, the sample is retested until the count values fall in the specified ranges and the pH value is confirmed.

To differentiate between a pH of 8 and 9, the count values for a green an orange LED detector, measuring reflected light, was used (Table 3.16). There is a slight overlap in count values for the green detector LED, but for the orange LED the count ranges fall in distinct range, as shown in Figure 3.34.

Therefore, if a count values is in group 1 for a yellow LED measuring transmitted light, above 1900 for an orange LED measuring transmitted light and below 2190 for an orange

LED, measuring reflected light then the sample has a pH of 8. Similarly, if a count values is in group 1 for a yellow LED measuring transmitted light, above 1900 for an orange LED measuring transmitted light and above 2190 for an orange LED, measuring reflected light then the sample has a pH of 9.

Therefore, an array of 4 emitter and 4 detector LEDs can be used for colourimetric analysis of pH samples, between 4 and 9. A yellow, orange, and green LED detector needs to be directly opposite a white emitter LED to detect light transmitted through the sample and an orange LED needs to be directly next to a white emitter LED to measure the light reflected off of the sample.

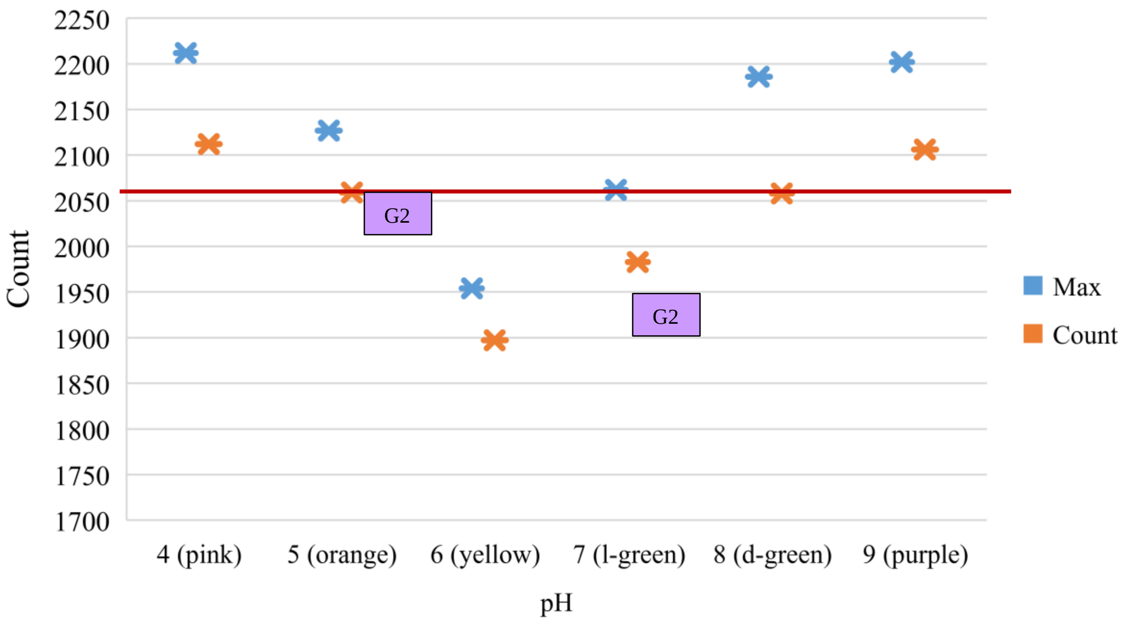

Figure 3.33. Maximum and minimum ADC count readings with the green LED detector, detecting transmission measurements.

Table 3.16. Maximum and minimum ADC count readings for the green and orange LED detector, detecting reflection measurements.

LED	**8**	**9**
Green	2200-2306	2261-2366
Orange	2056-2187	2200-2271

The emitter and detector pair must be activated one pair at a time to ensure that the light for other emitter-detector pairs do not influence the results. The emitter LED should also be switch on about 0.1 s before the detector LED is signal to measure the discharge time so that there is ensured to be maximum brightness from the emitter LED.

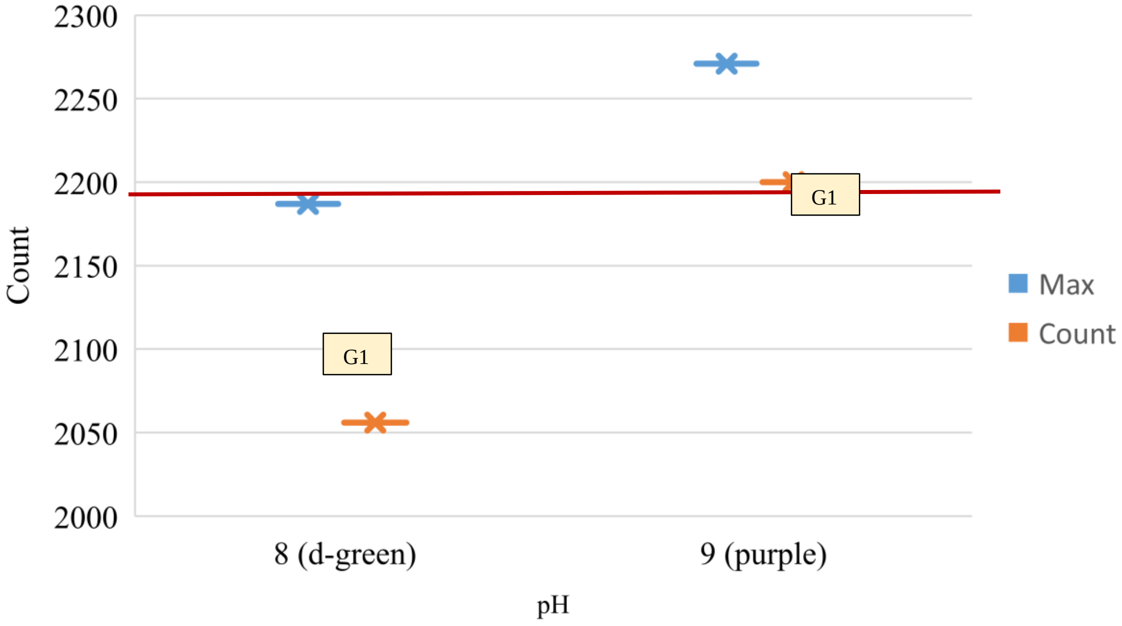

Figure 3.34. Maximum and minimum ADC count readings with the orange LED detector, detecting reflection measurements.

CHAPTER 4 OLED ARRAY FOR COLOURIMETRIC ANALYSIS

4.1 CHAPTER OVERVIEW

In this chapter the use of an OLED array for colourimetric analysis is discussed. An off-the-shelf OLED panel, that is discussed in Section 4.2, was used as both the light emitter and light detector for colourimetric analysis. The OLED is modelled in Section 4.3 and the spectral response, reverse bias photocurrent and reverse bias discharge time is given in Sections 4.4, 4.5 and 4.6 respectively. Statistical analysis of the measured reverse bias discharge time for the OLED detector is analysed in Section 4.7 and the angular spectral response of the OLED panel is analysed in Section 4.8. Lastly, the use of an OLED emitter and OLED detector array to distinguish between different pH samples colourimetrically is discussed in Section 4.9.

4.2 MANUFACTURED OLED PANEL

Due to ink, cost and facility accessibility, the simulated, optimized OLEDs were not inkjet printed for the OLED array. A flexible OLED panel from Applelec was used as the emitter and receiver OLED for the array. The OLEDs dimensions are 190 mm x 40 mm x 0.51 mm. The OLEDs operate between 5 and 8.6 V and 175 mA and consume 1.51 W each. A picture of the Applelec panel is shown in Figure 4.1.

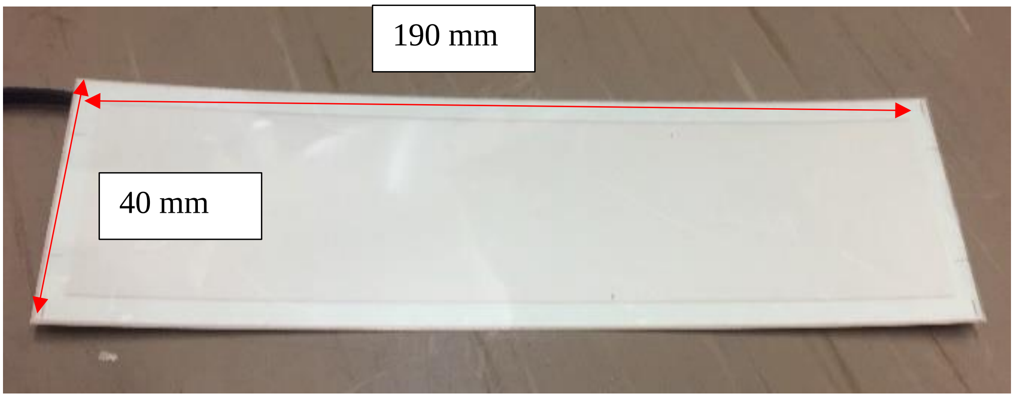

Figure 4.1. Applelec OLED panel.

The electrical and optic properties of the flexible, manufactured OLED panels were unknown and are were tested and characterized as shown in subsequent sections. Additionally, using flexible OLEDs as light detectors is still a novel concept and is explored, analyzed and characterized in subsequent sections.

4.3 MODELING A MANUFACTURED OLED PANEL

Theoretical models of the manufactured OLEDs were theoretically investigated and a GW Instek Precision LCR meter (LCR-8110G) was used to obtain various measurements from the OLED panel in order to design and simulate a theoretical model of the manufactured, flexible OLED panel.

4.3.1 Theoretical models

Different simulation models can be used to determine the voltage and operating current needed to drive an OLED display. SPICE models, used to represent OLEDs include the double diode model (Figure 4.2a), the multiple-diode parallel model (Figure 4.2b), the physical-based model (Figure 4.2c) and the single diode model (Figure 4.2d). The double-diode parallel model (Figure 4.2a), models the *I*-*V* relationship of the OLED with two diodes; one diode models the OLED behavior when a large voltage is applied and the other diode models the OLED behavior when a small voltage is applied across. This model is not very accurate, and errors up until 8 % have been seen [71].

Each layer of the OLED display can be modelled individually with a capacitor, diode and resistors, in the multiple-diode SPICE model (Figure 4.2b). The capacitors, *C*, model the capacitance of each layer and *R1* models the resistance of a layer, specifically in layers that do not have a high charge mobility. The additional resistor, *R*, that is in series with the OLED, represents the sheet resistance of the anode as well as the external contact resistance. The multiple-diode model does, however, does not always converge and yield desired outputs in SPICE transient and DC simulations [71]. There is a built-in voltage that arises between adjacent organic layers in an OLED and there is also ohmic effects that occur at the junction between organic and conductive metals layers. These two characteristics of OLEDs can be models using a physical-based OLED model (Figure 4.2c), but it only models the OLED that it is fully turned on [71].

A single-diode model (Figure 4.2d) is a simplified version of the multiple-diode model (Figure 4.2b) and does not result in conversion errors, when simulated. The diode represents the current flow, and the capacitor represents the capacitance of the entire OLED structure. As in the case of the multiple-diode model, the resistor in series with the OLED represents the sheet resistance of the anode as well as the external contact resistance [71].

4.3.2 Single diode model of the manufactured OLED

A signal diode model was chosen to model the manufactured OLED. It was selected as it has fewer conversion errors when simulated [71] and could be easily modelled using measurements from a precision LCR meter and the *I-V* characteristics of the OLED panel. The OLED LCR parameters were measured at 10 kHz, using an LCR precision meter, as can be seen in Table 4.1. The LCR parameters of a white LED was also measured in order to compare it to the OLED. The parameters that were measured with the LCR meter was the series capacitance (C_s), parallel capacitance (C_p), series inductance (L_s), parallel inductance (L_p), impedance (Z), admittance (Y) and quality factor (Q).

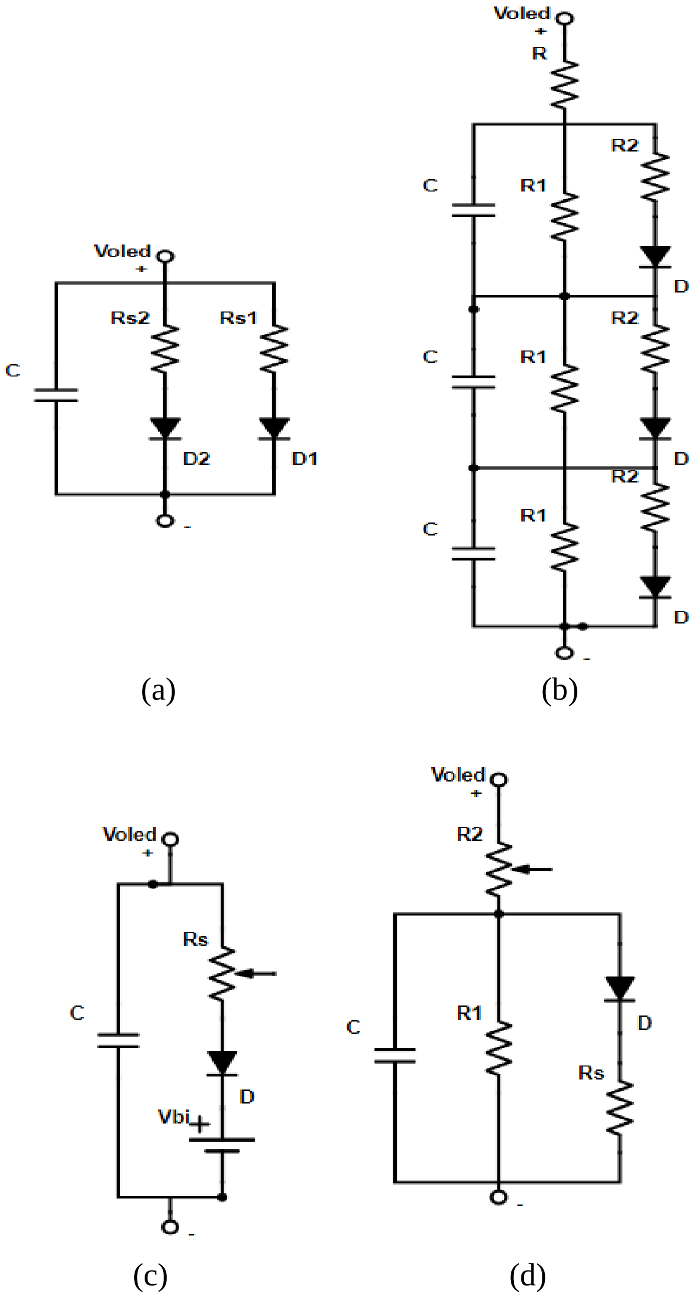

(a) (b)

(c) (d)

Figure 4.2. OLED SPICE models. Adapted from [71], with permission.

(a) Double-diode model. (b) Multiple-diode model. (c) Physical-based model. (d) Single-diode model.

Figure 4.3 illustrate a theoretical multiple-diode model of the OLED display. The parallel capacitance, C_p is chosen as 360 nF, in accordance to the measured results of the LCR meter (Table 4.1). Because the manufactured OLED operates at 8.6 V and 175 mA, the resistor R, is selected as 50 Ω using Ohms Law. The parallel resistance of resistor R and R_p is designed to be equal to the measured parallel resistance, from the LCR meter results (Table 4.1). Therefore, using (4.1), R_p is calculated as 76 Ω.

$$\boldsymbol{R||Rp = \frac{R \times Rp}{R + Rp} = 30}\ \Omega \tag{4.1}$$

The sheet resistance of the anode, of the manufactured OLED, is estimated as 30 Ω/square from literature [103]. The unit Ω/square implies that the sheet has that resistance, regardless of the size of the square.

Table 4.1. OLED parameters measured on an LCR precision meter.

Parameter	**OLED Measurement**
Cs	808.23 nF
Ls	-313.39 µH
$Z_{(polar)}$	29.522 Ω -41.827 degrees
$Z_{(rectangular)}$	22 – 19.69j
Cp	359.45 nF
Lp	-704.68 µH
Y	33.875mS 41.818 degrees
Q	0.89

In order to estimate the sheet resistance of the anode, of the manufactured OLED, the estimated sheet resistance of 30 Ω/square is multiplied by 4, because the physical dimensions of the manufactured OLED panel are 200 mm x 50 mm. Finally, the external contact of the OLED is estimated as 1 Ω. The OLED theoretical model was simulated in OrCAD and the simulated Bode plot is shown in Figure 4.4. It can be seen from the Bode plot that the band width of the OLED theoretical model is 9.5 kHz.

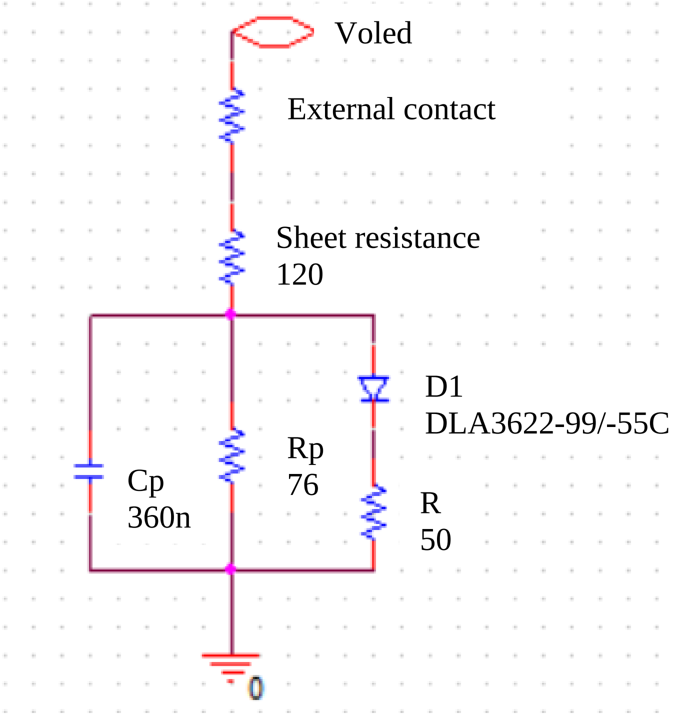

Figure 4.3. OLED theoretical model.

4.3.3 LCR characteristics of the manufactured OLED panel

A frequency sweep of the manufactured, flexible OLED panel’s impedance (Figure 4.5a), phase (Figure 4.5b), series capacitance (Figure 4.5c), parallel capacitance (Figure 4.5d), series resistance (Figure 4.5e) and parallel resistance (Figure 4.5f) were measured and plotted, using a precision LCR meter.

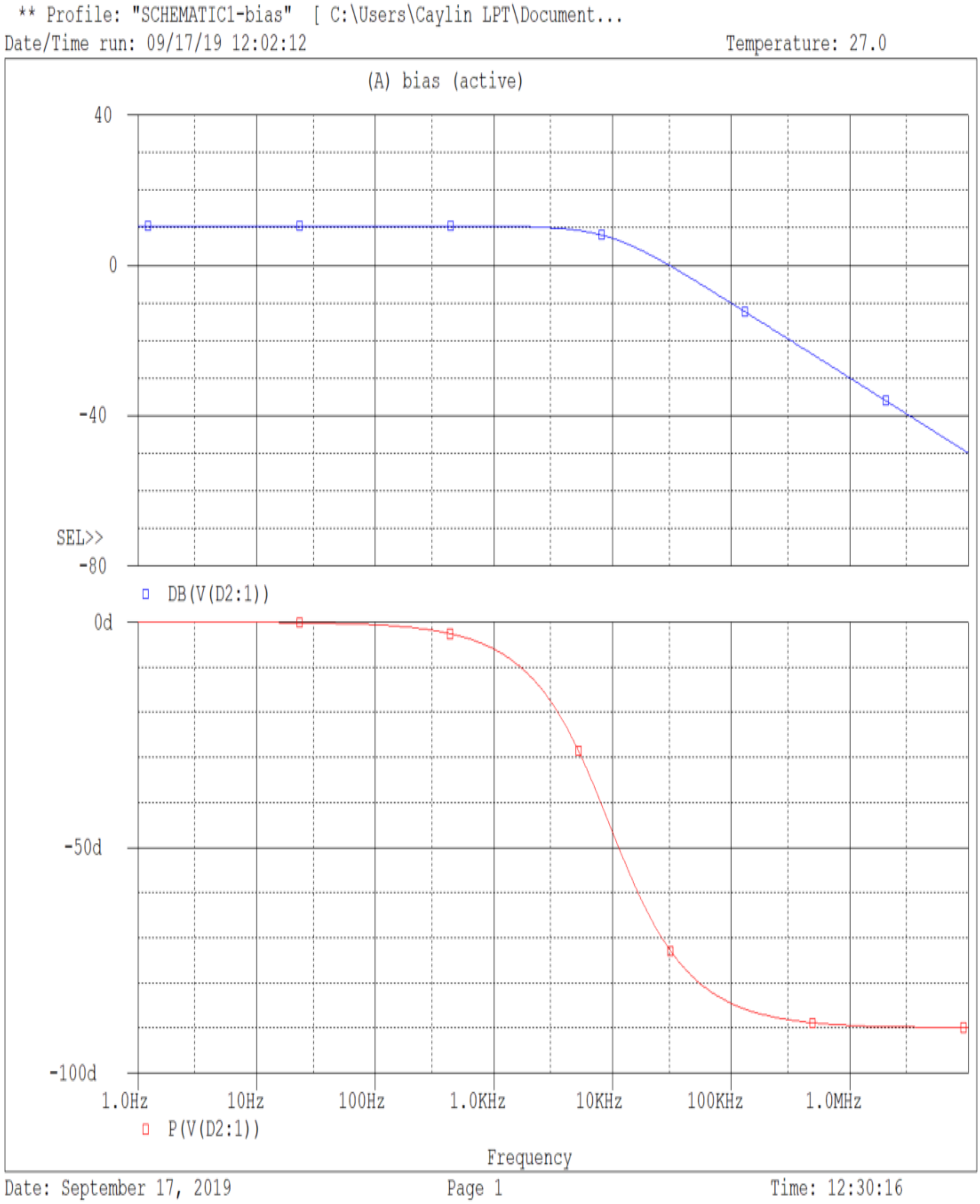

Figure 4.4. Simulated Bode plot of the OLED theoretical model.

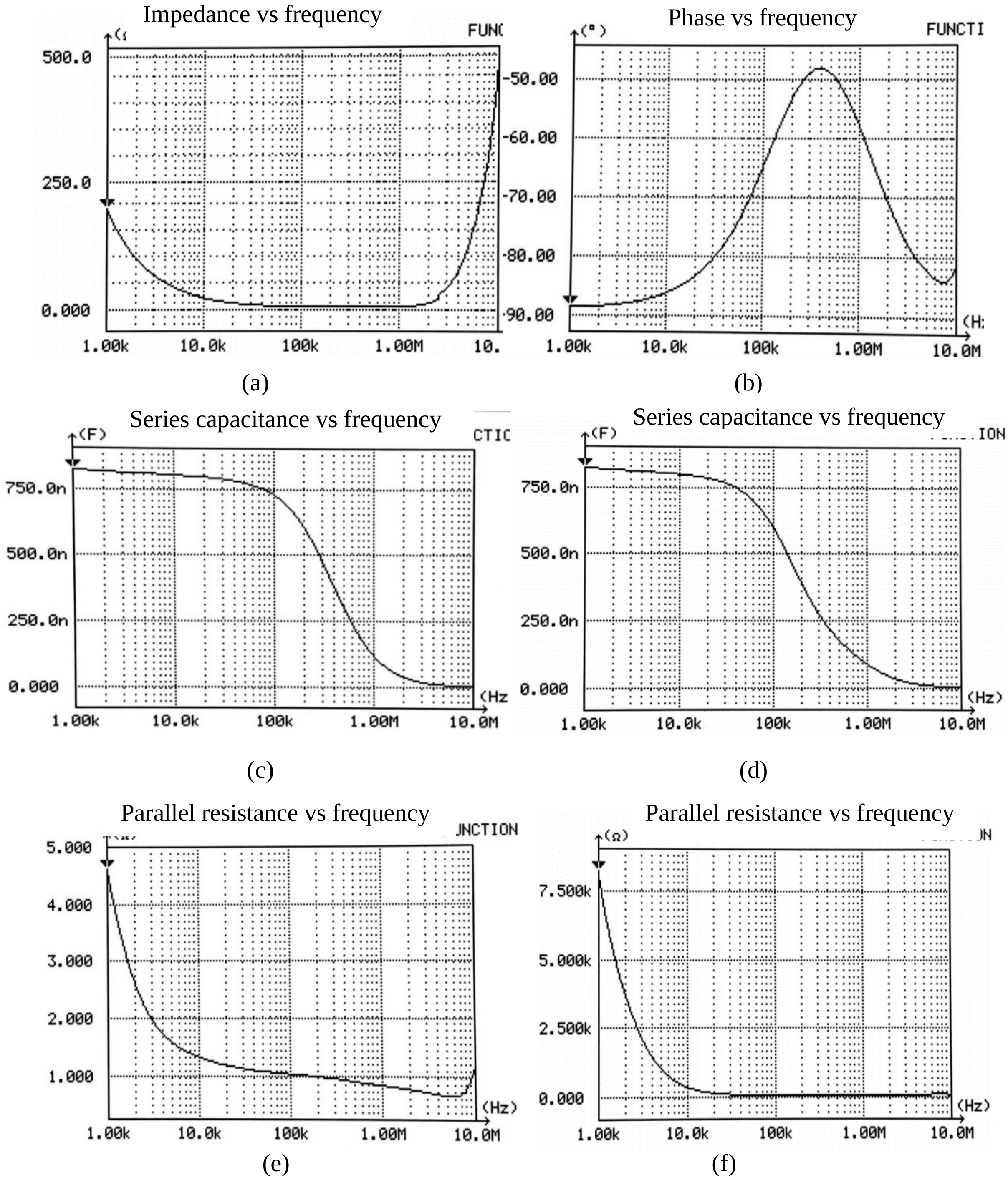

Impedance vs frequency (a)

Phase vs frequency (b)

Series capacitance vs frequency (c)

Series capacitance vs frequency (d)

Parallel resistance vs frequency (e)

Parallel resistance vs frequency (f)

Figure 4.5 Frequency sweep of OLED panel LCR meter parameters.
(a) Impedance versus frequency. (b) Phase versus frequency. (c) Series capacitance versus frequency. (d) Series capacitance versus frequency. (e) Parallel resistance versus frequency. (f) Parallel resistance versus frequency.

4.4 SPECTRAL RESPONSE OF THE MANUFACTURED FLEXIBLE OLED PANEL

The light spectrum of the emitter OLED panel is measured perpendicular to the OLED panel. It was measured using the AvaSpec angular response measurement accessory block and AvaSpec spectrometer (Figure 4.6). The measurement hole that is 90 degrees to the OLED panel was used to measure the light spectrum. The light spectrum is shown in Figure 4.7 and the CIE diagram is shown in Figure 4.8. It can be seen from the CIE diagram that the emitted light is predominantly orange. Using the light spectrum, the bandwidth of the OLED panel is seen to be 528 nm to 672 nm. It can also be seen that there is a small dip in light intensity in the yellow light band, from 568 nm to 600 nm.

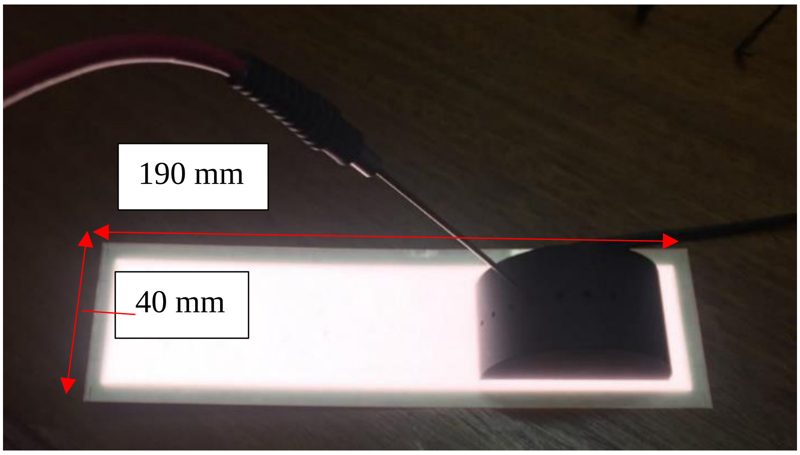

Figure 4.6 Frequency sweep of OLED panel LCR meter parameters.

Comparing the measured optic parameters of the white LED (Table 3.10) and the OLED panel **(**Table 4.2), the irradiance and luminous flux of the OLED panel is larger than that of the white LED by more than a factor of 10. This may be due to the physical dimensions, light emitting properties and intensity of emitted light.

The optic parameters of the OLED panel, that were measured using the AvaSpec Spectrometer is summarized in Table 4.2.

Table 4.2. Measured parameters of the OLED panel, using an AvaSpec Spectrometer.

Parameter	Value
Dominant wavelength	581.96 nm
Irradiance	5788.2 uWatt/cm^2
Luminous Intensity	22865 Candela
Luminous Flux	5.937E^-4 Lumens
Centre wavelength	600.79 nm
Amplitude of centre wavelength	32.740

4.5 OLED PHOTOCURRENT

The expected photocurrent range of a reversed biased OLED was measured, using a Hewlett Packard 4155B semiconductor parameter analyser.

The photocurrent was measured in office lighting, when the lights were off, but some ambient light was present and when it was completely dark in an optically isolated laboratory. The voltage was swept from -15 V to 8 V (Figure 4.9) and again from -5 V to 0 V (Figure 4.10).

The *I-V* plot of the OLED has a similar shape to that of a diode, which is expected for an OLED. The currents, measured when a 5 V reverse bias voltage was applied across the OLED, are summarized in Table 4.3. When more light fell onto the reverse bias LED, more photocurrent was generated by the LED.

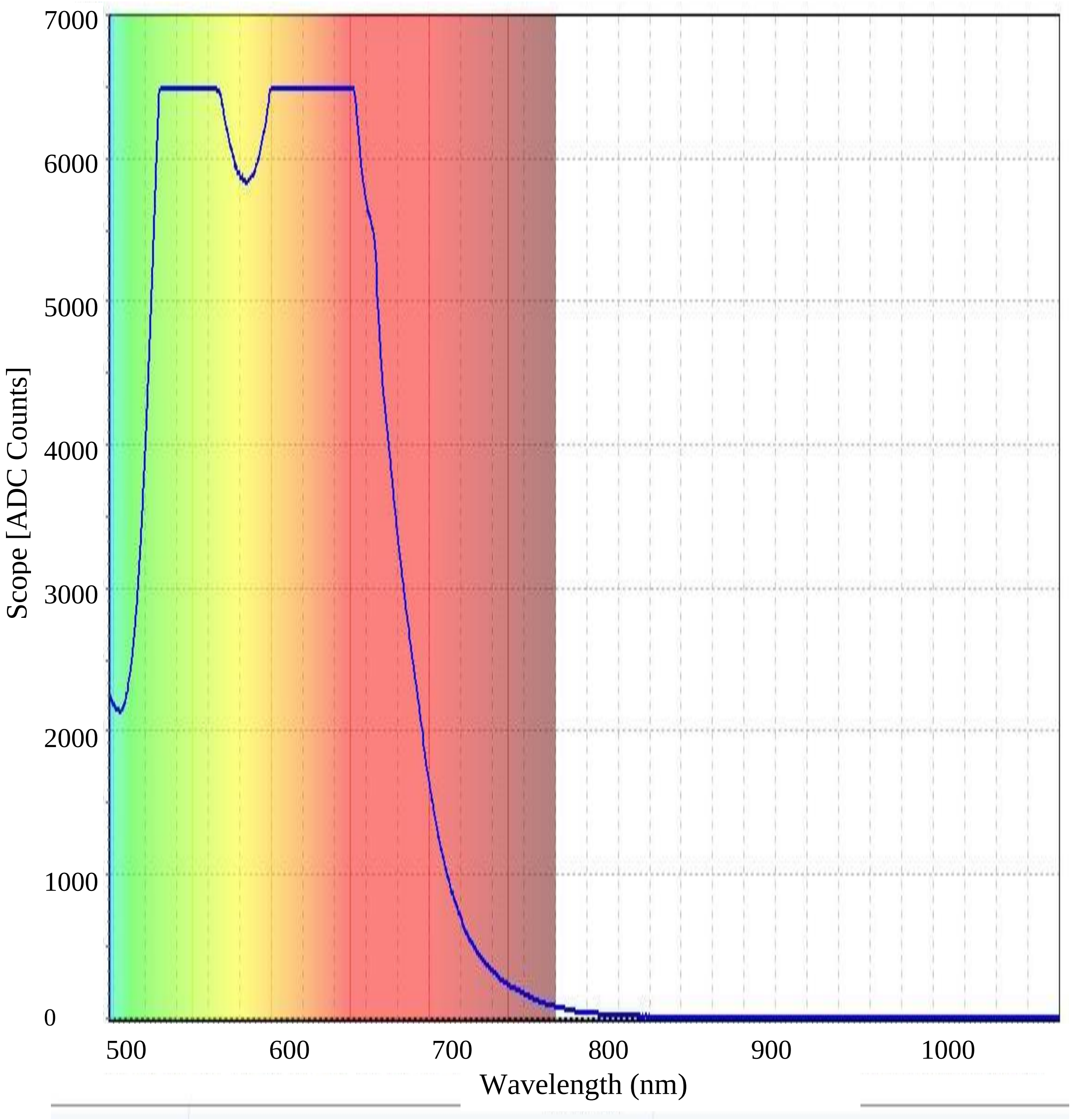

Figure 4.7 Spectral response of a flexible OLED panel, measured perpendicular to the panel (0 ° viewing angle).

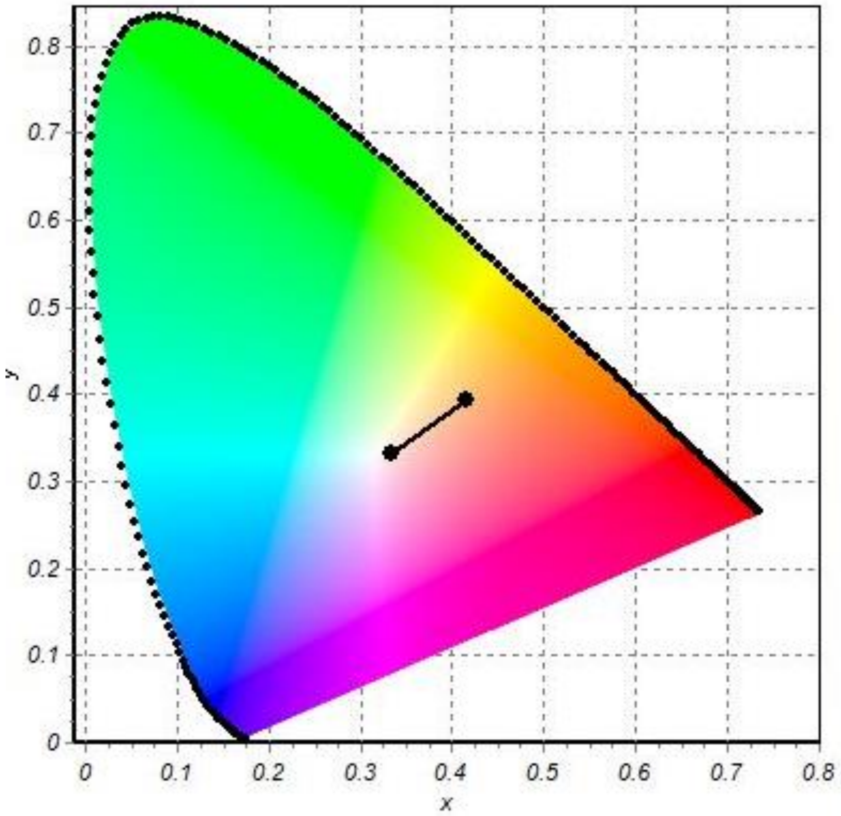

Figure 4.8. CIE Colour chart of a flexible OLED panel, measured perpendicular to the panel (0 ° viewing angle).

Table 4.3. Photocurrent of reverse biased OLED panel in different lighting conditions.

Lighting conditions	**Measured current**
Office lighting	934.13 nA
Partially dark	884.5 nA
Completely dark	788.90 nA

4.6 OLED LIGHT DETECTOR DISCHARGE TIME.

In order to approximate the discharge time range, of the OLED detectors, the time constant was calculated (3.2). The input impedance (*R*) of the Arduino Uno is 100 MΩ and capacitance of each colour OLED was measured as 359.45 nF (Table 4.1), using a GInstek Precision LCR meter (LCR-8110G).

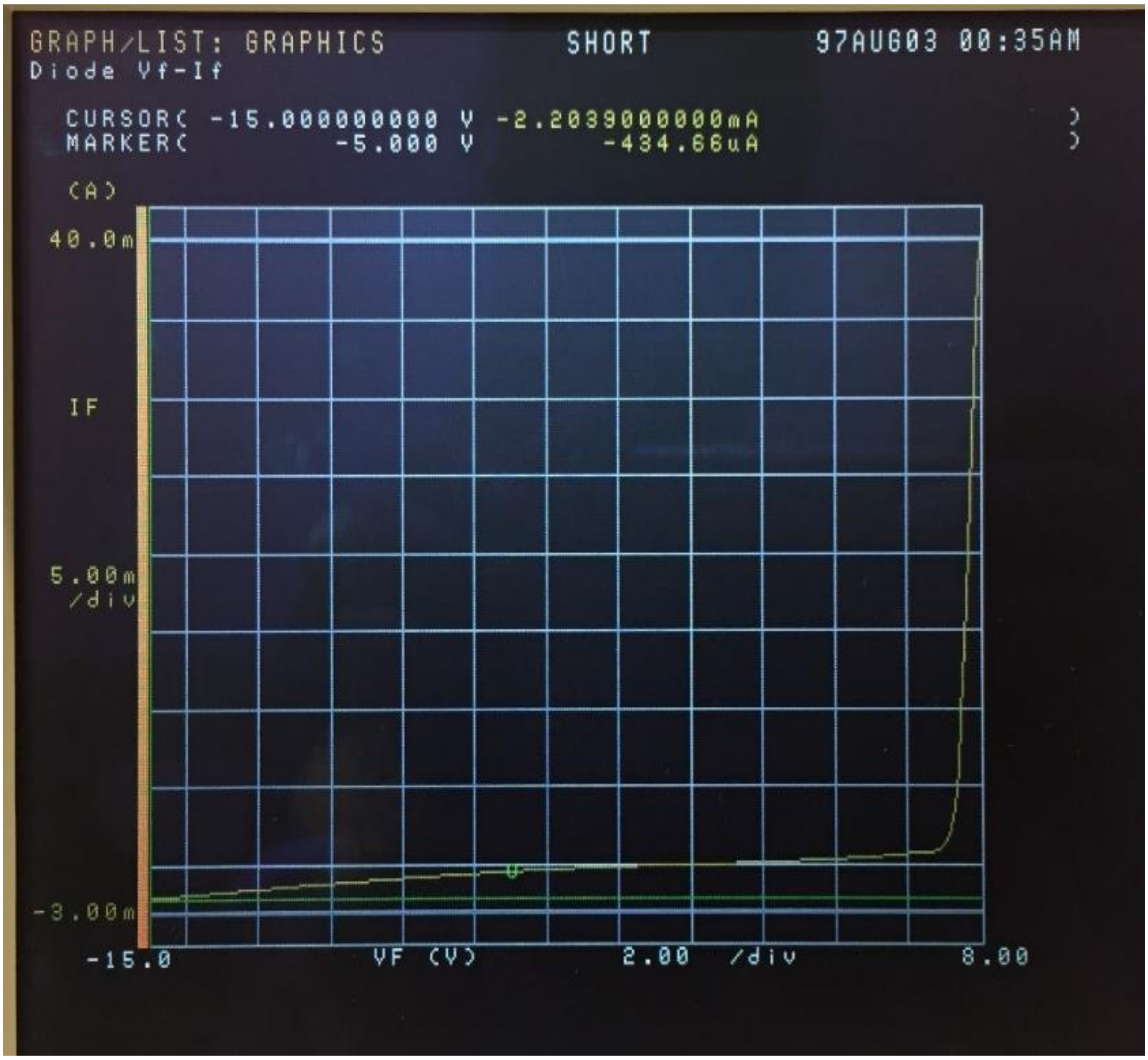

Figure 4.9. *I-V* curve of a reversed biased OLED panel from -15 V to 8 V.

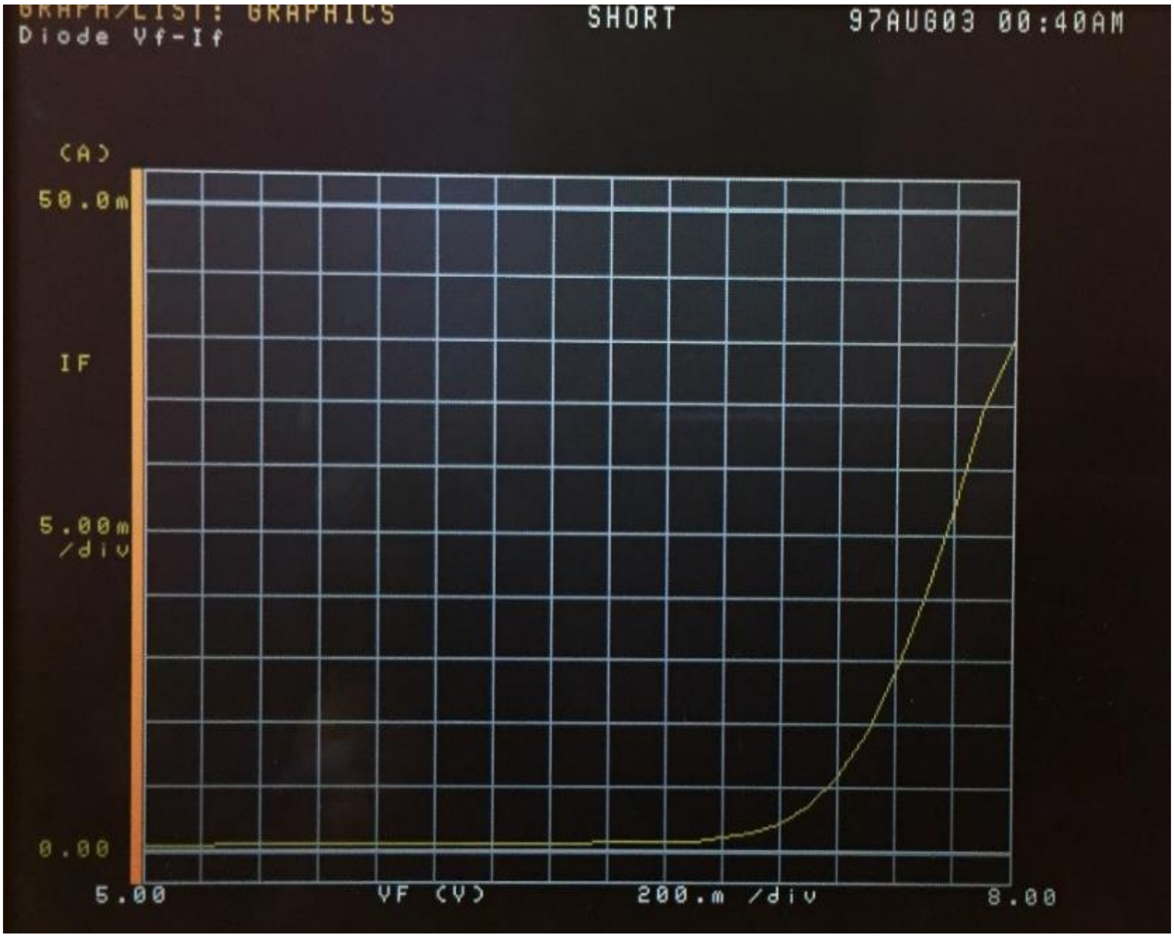

Figure 4.10. *I-V* curve of a reversed biased OLED panel from 5 V to 8 V.

The time constant of the OLED is calculated as 35.945 s. This is a substantially long discharge time, especially if an entire array of light detecting OLEDs is implemented and is measured sequentially. For this reason, the discharge time to 63 % of the maximum voltage is used throughout the report.

The discharge time of the OLED panel is also since the manufactured OLED panel, which has the smallest dimensions commercially available, is still very large. For future microfluidic application, inkjet printed OLED panel, which very small dimensions in the micrometre range is advised.

The discharge time to 63 % and 50 % of the maximum voltage is summarized in Table 4.4. When the detector OLED panel is exposed to less light, the discharge time increases, as in the case of LEDs.

Table 4.4. Discharge time of an OLED detector exposed to ambient light and no light.

	Time to discharge to 63 % of maximum voltage (s)	**Time to discharge to 50 % of maximum voltage (s)**
Ambient light	13.579	20.59
No light exposure	27.922	44.024

As in the case of the LEDs, a light emitter OLED and a reverse biased, light detector OLED was placed at different distances from each other. The discharge time to 63 % of the maximum discharge voltage of the detector OLED and the illumination, measured with the EvoSpec spectrometer at the set distance from the emitter LED, were measured.

All the measurements were performed in an optically isolated laboratory, where the only light present was that of the light emitting OLED. The measured values at distances 1-50 cm away from the light emitting OLED is given in Table 4.5.

The discharge time to 63 % of the maximum distance voltage was plotted against distance and illuminance (lux) as can be seen in Figure 4.11 and Figure 4.12 respectively. It can be observed that as the distance increases the discharge time increases. As in the case of LEDs, this is because as the OLEDs move further away from each other, less light falls on the detector OLED, and the detector LED takes longer to discharge (Figure 4.11). Additionally, the discharge time is seen to exponentially decrease, with an increase of illumination (Figure 4.12).

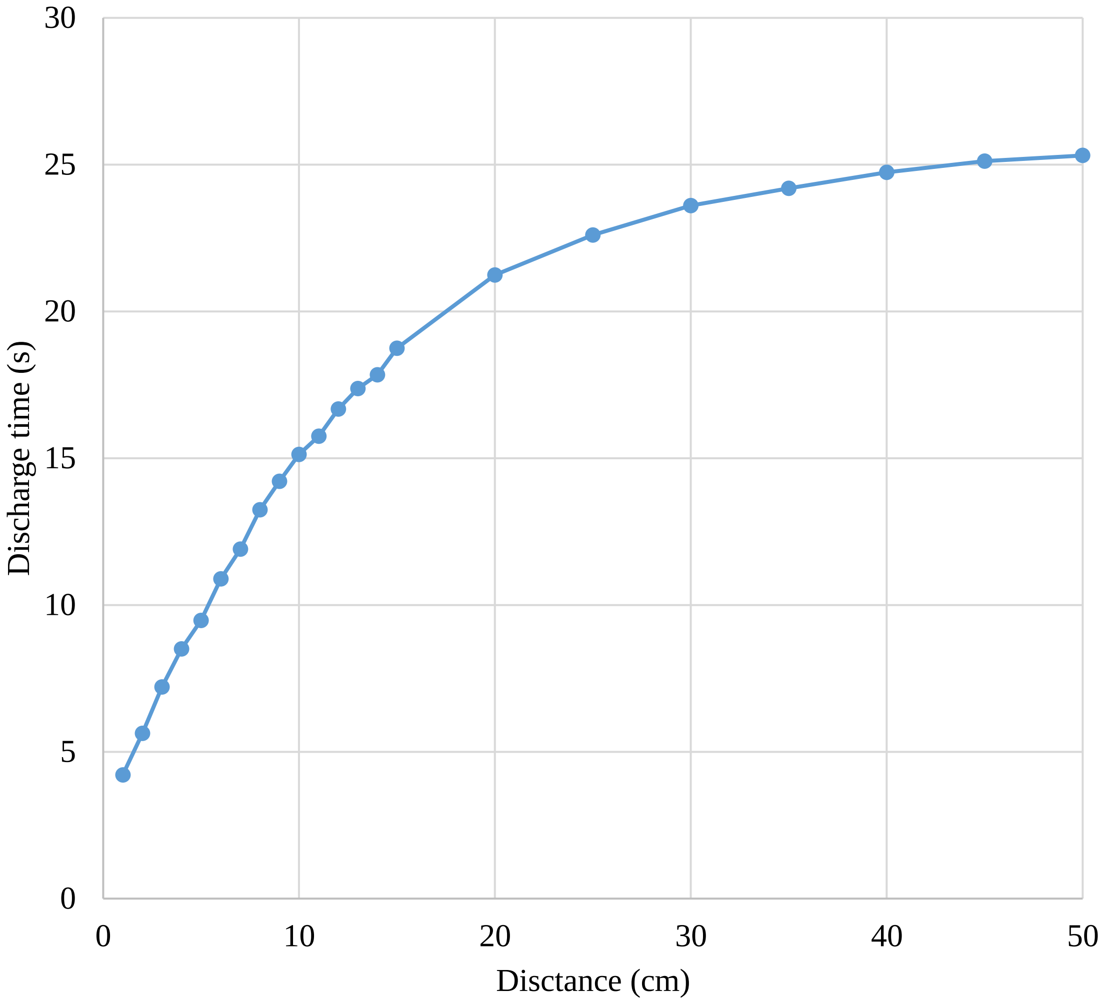

Figure 4.11. Discharge time versus distance (cm).

4.7 STATISITCAL ANALYSIS OF DISCHARGE TIME MEASUREMENTS

Statistical analysis was performed on the data in Table 4.5 to determine how linear the discharge time is, in relation to distance. Linear regression analysis [102] was performed on the data from 1-50 cm and then again on the data from 1-11 cm**.**

Table 4.5. Discharge time of an OLED detector at different distances away from an OLED emitter, without light filters.

Distance from emitter OLED (cm)	**Discharge time to 63 % of maximum voltage (s)**	**Illumination (lux)**
1	4.215	297.27
2	5.63	296.53
3	7.213	292.55
4	8.5	288.15
5	9.48	283.88
6	10.888	280.62
7	11.908	278.79
8	13.245	271.45
9	14.211	269.54
10	15.127	267.78
11	15.745	263.85
12	16.679	262.30
13	17.376	257.48
14	17.843	256.29
15	18.741	252.86
20	21.236	219.01
25	22.598	206.26
30	23.606	158.06
35	24.195	133.25
40	24.734	90.855
45	25.125	83.663
50	25.311	68.543

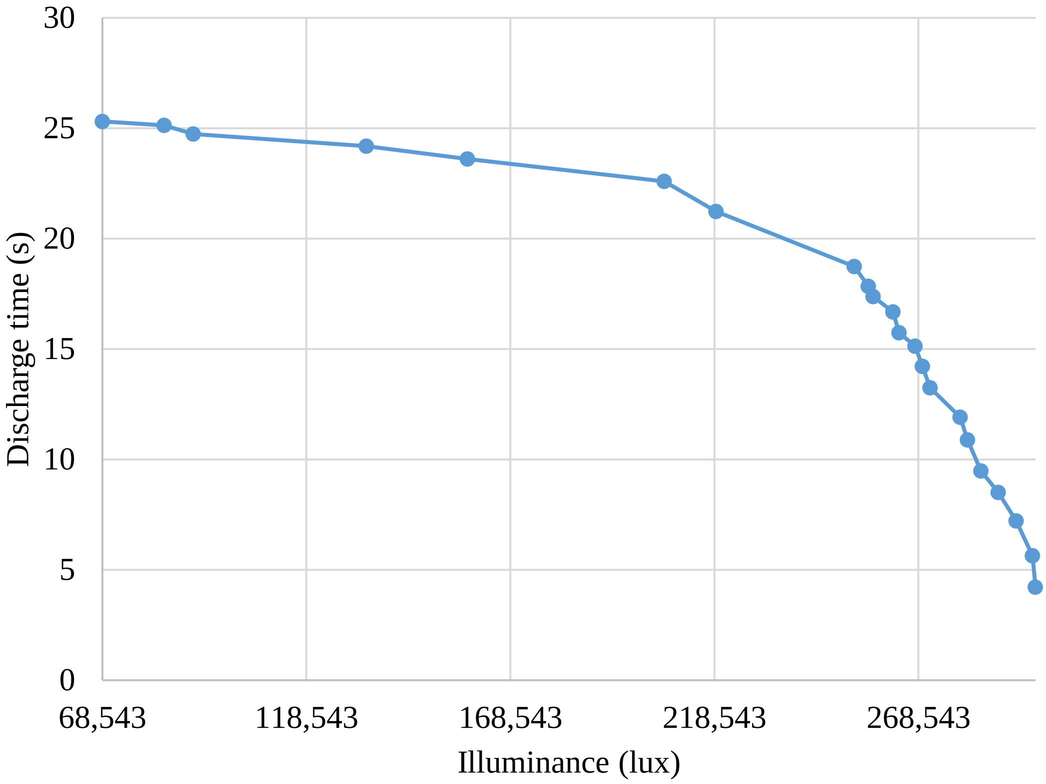

Figure 4.12. Discharge time (s) versus illuminance (lux).

4.7.1 Linear regression analysis for discharge time 1-50 cm.

Linear regression analysis gives an indication on how two variables relate to one another and is based off the sum of squares. The smaller the sum of squares is the better the mathematical model of the data is [102].

Linear regression analysis was performed on the data collected when the OLED detector was between 1 and 50 cm, away from the OLED emitter (Table 4.5).

The scatter plot and linear regression line of the discharge time of an OLED detector at different distances away from an OLED emitter (Table 4.5) is shown in Figure 4.13. The equation of the linear regression line as well as the R squared value is shown on the plot.

The calculated R squared value is 0.8198, which means that 81.98 % of the data fits the regression model. This indicates that the data is not a particularly good fit as R squared values that are above 95 % are typically considered to be good.

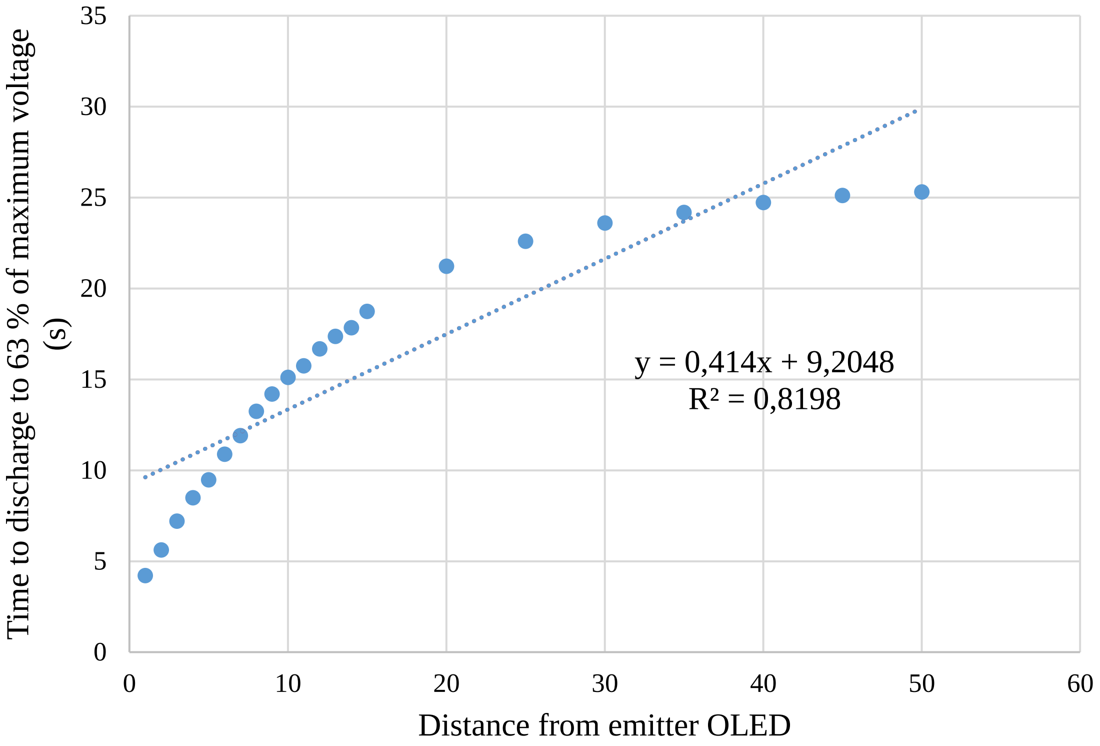

Figure 4.13. Discharge time of an OLED detector at distances 1-50 cm away from an OLED emitter.

Other regression analysis statistics of the discharge time of an OLED detector at 1-50 cm away from an OLED emitter (Table 4.5) is given in Table 4.6.

Table 4.6. Regression analysis statistic of the discharge time of an OLED detector at 1-50 cm away from an OLED emitter.

Regression Analysis Statistics	
Multiple R	0.905406139
R Square	0.819760277
Standard Error	2.898502631

In Table 4.6 the multiple R value is calculated as 0.905406139, which means there is a reasonable positive linear relationship between the distance and discharge time.

The standard error is calculated as 2.898502631 (Table 4.6). This is the absolute average value that each of the data points deviates from the linear regression line and can also be used as an indicator of the accuracy of the linear regression analysis [102].

4.7.2 Linear regression analysis for discharge time over 1-11 cm.

Linear regression analysis was redone on the data when the OLED detector and emitter were 1 and 11 cm apart (Table 4.5), instead of the entire 1-50 cm range. The scatter plot and linear regression line of the discharge time is shown in Figure 4.14. The equation of the linear regression line as well as the R squared value is shown on the plot.

Other regression analysis statistics of the discharge time of an OLED detector at 1-50 cm away from an OLED emitter (Table 4.5) is given in Table 4.7.

Table 4.7. Regression analysis statistics of the discharge time of an OLED detector at 1-11 cm away from an OLED emitter.

Regression Analysis Statistics	
Multiple R	0.996183
R Square	0.99238
Standard Error	0.358013

The multiple R value for the 1 – 11 cm range is 0.996183 (Table 4.7) is closer to 1 than the multiple R value of 0.905406139 for the 1- 50 cm (Table 4.6), which means the data in the 1-11 cm range is more linear than the data in the 1-50 cm range. The standard error for the 1-11 cm is calculated as 0.358013 (Table 4.7), is 87 % smaller than the standard error for the

1-50 cm range which is calculated as 2.898502631 (Table 4.6). Comparing the multiple R value and standard error of the 1-11 cm and the 1-50 cm range, the data in the 1-11 cm range is more linear than over the entire 1-50 cm range.

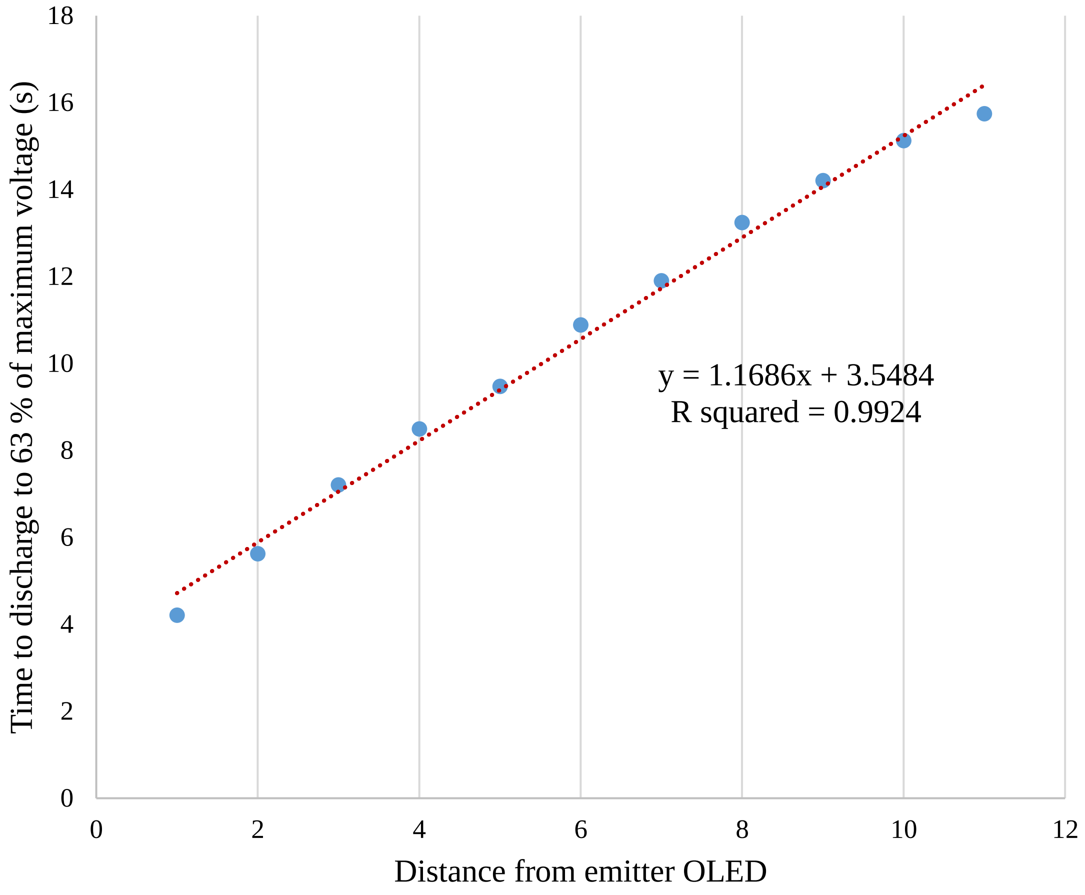

Figure 4.14. Discharge time of an OLED detector at distances 1-50 cm away from an OLED emitter.

4.7.3 Linear regression analysis for discharge time versus illumination (lux) from 0 to 300 lux.

Linear regression analysis was performed on the discharge time to 63 % of the maximum voltage and the illumination (lux) data (Table 4.5). The scatter plot, with the regression line, equation for the linear regression line and R squared value is illustrated in Figure 4.15.

It can be seen from the regression analysis values in Table 4.18 that the multiple R values is 0.863731, which is relatively close to 1, which means that discharge time versus illuminance is relatively linear. It can be seen, from Figure 4.15, that there is an exponential decrease in discharge time from approximately 200 lux and upwards. The R squared value indicates that approximately 74.60 % of the measured data fits the linear regression model in Figure 4.15, which is not ideal as R squared values above 95 % are considered as good fits.

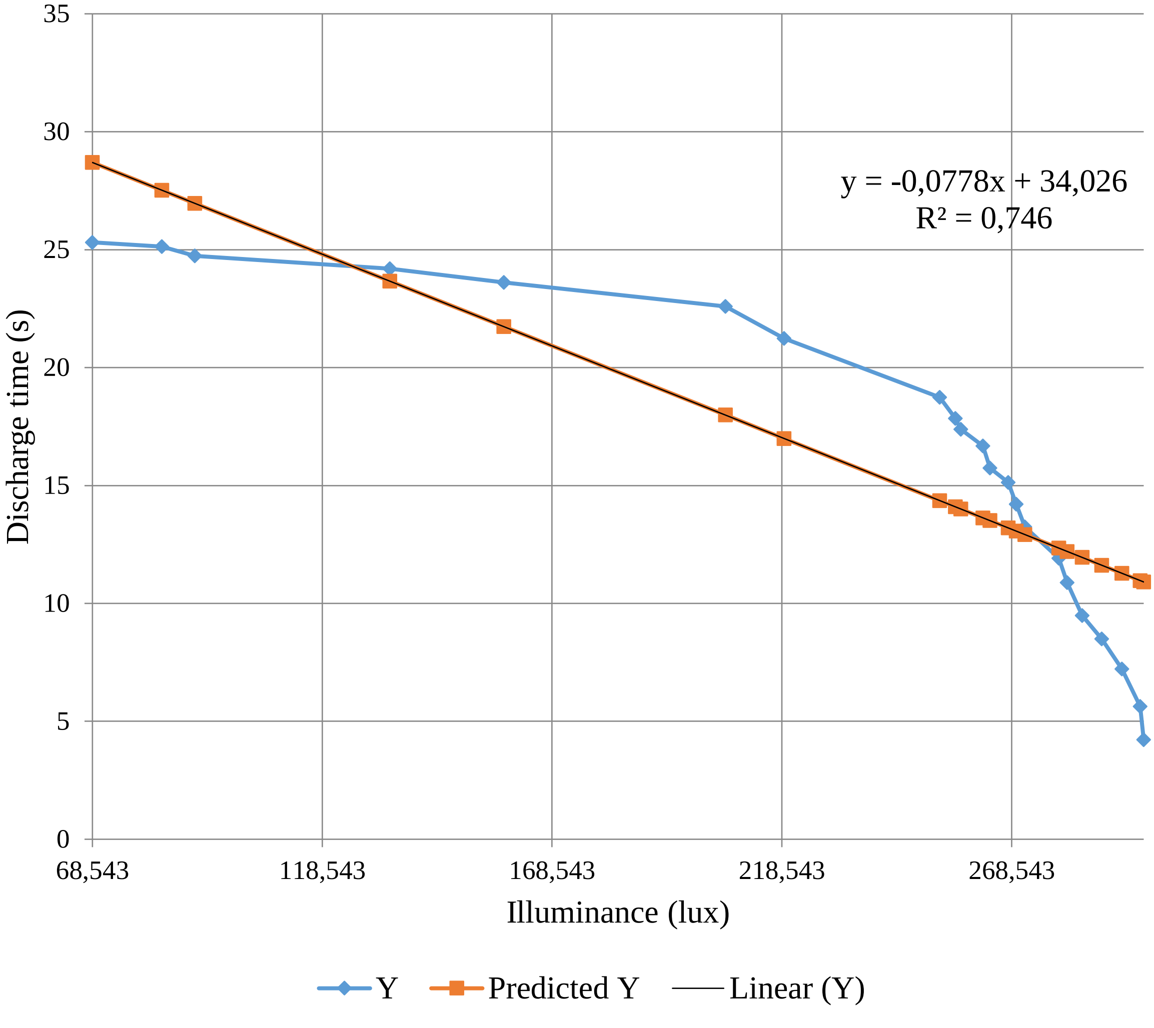

Figure 4.15. Discharge time to 63 % of the maximum voltage versus illumination (lux) (0-300 lux).

The discharge versus distance plots is more linear in comparison to the discharge time versus illumination linear regression analysis.

Table 4.8. Regression analysis statistics of the discharge time of an OLED detector at illumination (lux) values between 0 and 300 lux.

Regression Analysis Statistics	
Multiple R	0.863731
R Square	0.746031
Standard Error	3.440636

4.7.4 Linear regression analysis for discharge time versus illumination (lux) from 0 to 263 lux.

Linear regression analysis for the discharge time versus illumination (lux) but over a range of 0-263 lux instead of 0-300 lux. These lux measurements correspond to the measurements taken between 0 and 11 cm (Table 4.5). The regression analysis statistics is given in Table 4.9 and the linear regression plot is given in Figure 4.16.

The multiple R value is 0.94221, which is larger than the value of 0.863731 for the illumination from 0-300 lux. Therefore, the data for discharge time versus 0-263 lux is more linear than the data from 0-300 lux. Additionally, the R square value is 0.887781, meaning that approximate 14 % more of the data fits the linear regression model for 0 –263 than 0-300 lux. The standard error for 0-263 lux is more than half of the standard error for 0-300 lux.

Table 4.9. Regression analysis statistics of the discharge time of an OLED detector at illumination (lux) values between 0 and 263 lux.

Regression Analysis Statistics	
Multiple R	0.942221
R Square	0.887781
Standard Error	1.183061

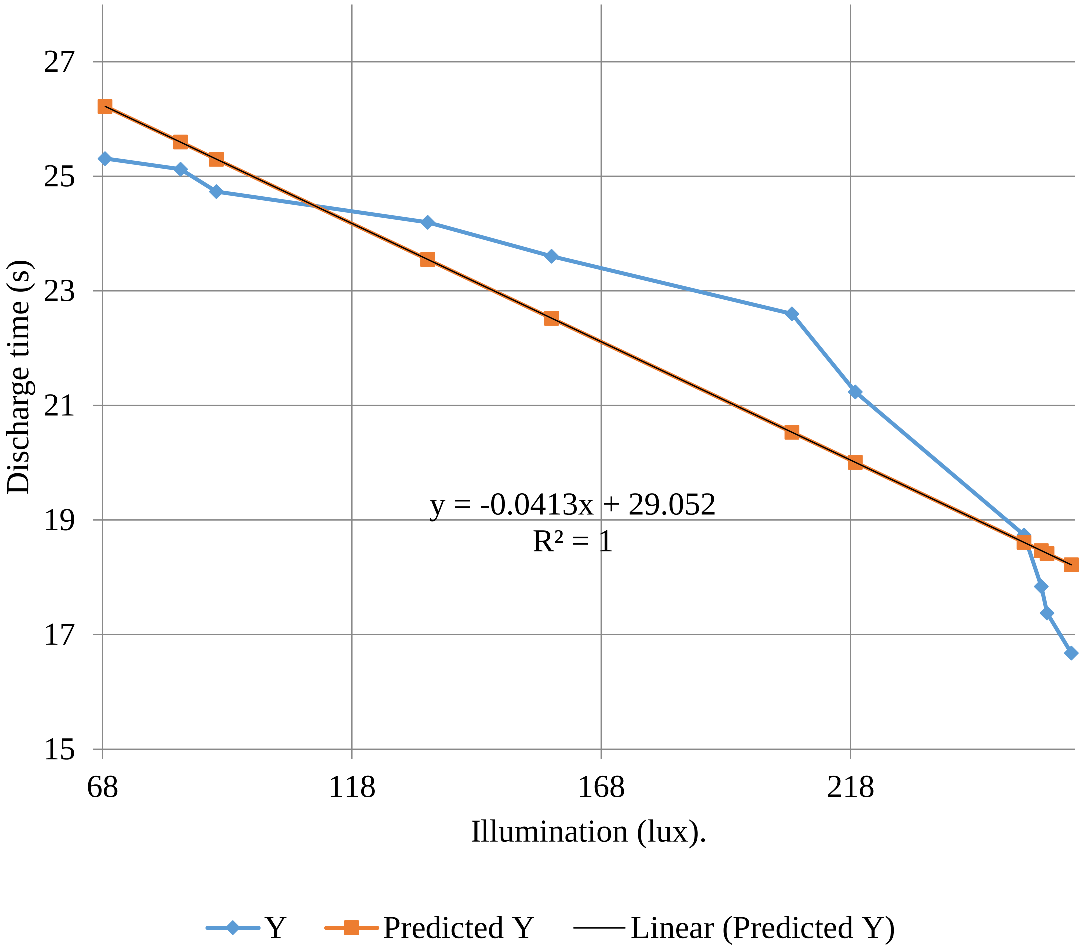

Figure 4.16. Discharge time to 63 % of the maximum voltage versus illumination (lux) (0-263 lux).

4.8 TESTING THE ANGULAR SPECTRAL RESPONSE OF OLEDS

As in the case of LED emitters and detector, the viewing angle was measured from the 0 ° reference angle, which is the viewing angle perpendicular to the panel [7], [103]. The angular response of the emitter and detector OLED was characterized.

4.8.1 Emitter OLED

As in the case of the emitter LEDs, the light spectrum of the emitter is dependent on the angle at which the light is viewed from [103]. The transmittance measurement is measured, using a spectrometer to determine the intensity of the emitted light at different viewing angle. A picture illustrating how the spectrometer measurements were taken, using an AvaSpec spectrometer and a semi-circular block, that has holes for the spectrometer probe at 15 ° degree increments is shown in Figure 4.6. The spectral response of the OLED panel at a 75 ° viewing angle to the panel is shown in Figure 4.18.

A spectrometer measured signal is the product of the integration time (seconds), spectrometer sensitivity (counts·Watt^{-1}seconds^{-1})) and optical power (Watts) and is given as a "count" value as the Watts and second units cancel out. The sensitivity of the spectrometer is dependent on the ADC size of the spectrometer [101]. As in the case of the OLED panel at a 0 ° (Figure 4.7), an ADC count value of 300000 is measured over majority of the visible spectrum, however the amplitude is significantly smaller.

Table 4.10 summarizes the various parameters, measured with the AvaSpec spectrometer, at different viewing angles. The irradiance and luminous intensities were converted from polar form to rectangular form for plotting purposes. The luminous intensity (Candela) versus viewing angle (Figure 4.19) and irradiance (μWatt/cm^2) versus viewing angle (Figure 4.20) illustrates that the magnitude of both luminous intensity and irradiance between a 0 ° and 45 ° viewing angle is approximately equal. There is also not a dip in the irradiance plot at a 0 ° viewing angle, as in the case of the white LED irradiance plot (Figure 4.17). This is because OLED panels are not packaged in a light dispersing packaging as in the case of LEDs, and therefore have a more consistent angular response.

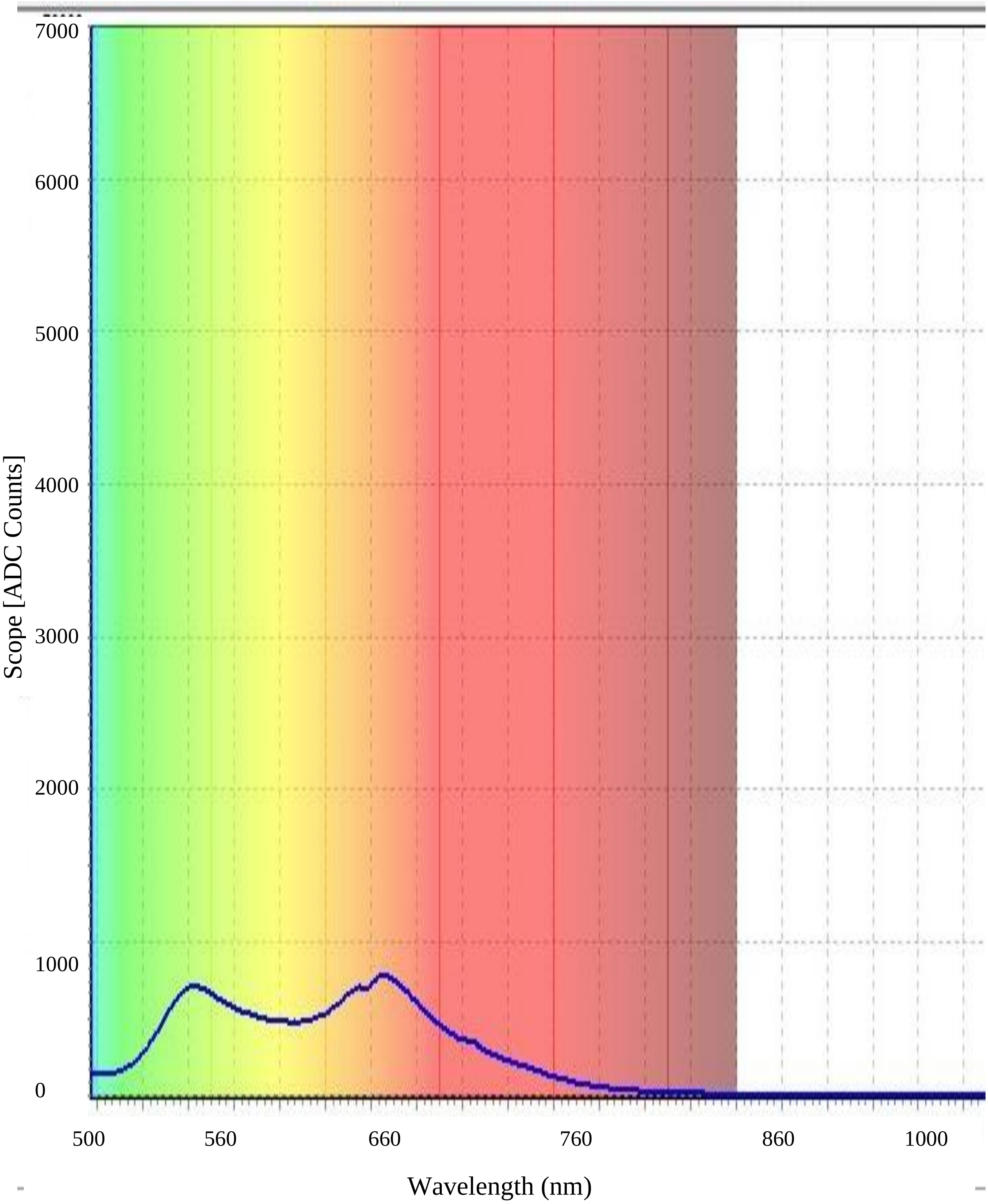

Figure 4.18 Spectral response of a flexible OLED panel measured at a 75 ° viewing angle to the panel.

4.8.2 Detector OLED angular response

As in the case of LEDs, the angular response was measured by changing the viewing angle between the light emitting OLED and the light detecting OLED [7]. The angular response test setup was performed in an optically isolated laboratory, where the only light present was from the emitter OLED. The detector OLED was placed, with its centre point 15 cm away from the emitters centre point. The OLED panels were ensured to be inline and parallel, using tape measures. The OLEDs were both kept exactly perpendicular to the desk by attaching them to the side of boxes, which were perpendicular to the desk. The detector OLED panel was then rotated about the starting position, using a protractor. The centre of the protractor was ensured to be kept in line with the centre of the OLED panel. The test setup is shown in Figure 4.21. The discharge time of the light detecting OLED panel was measured at each viewing angle. The results are shown in Table 4.11 and are plotted in Figure 4.23.

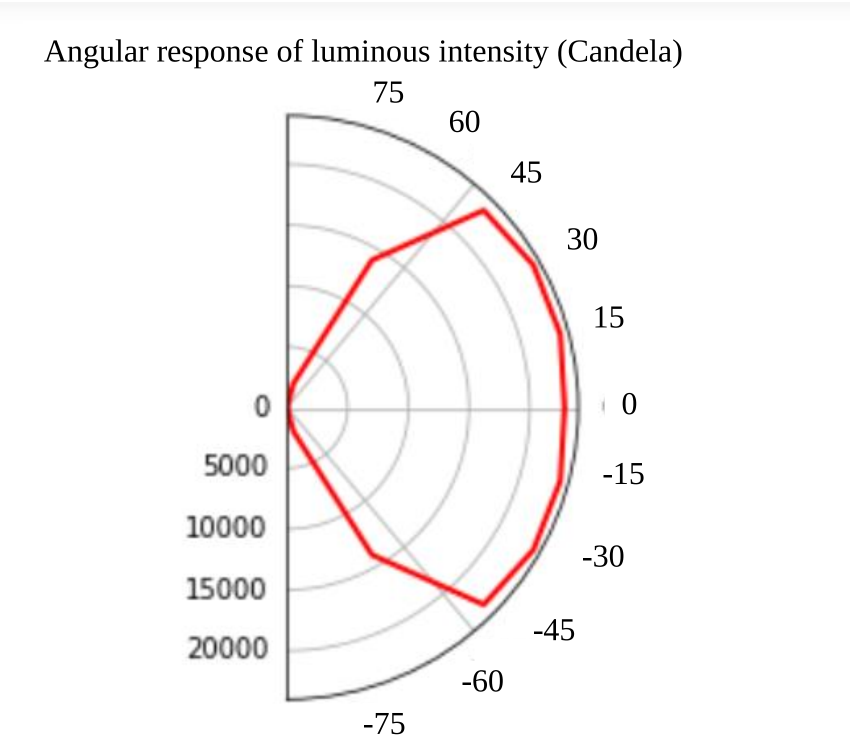

Figure 4.19 Luminous intensity (Candela) angular response of an OLED panel plotted in Python.

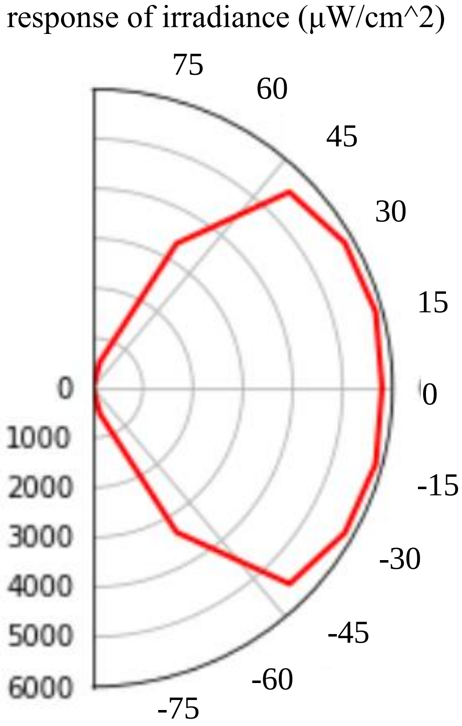

Figure 4.20 Irradiance (µWatt/cm^2) angular response of an OLED plotted in Python.

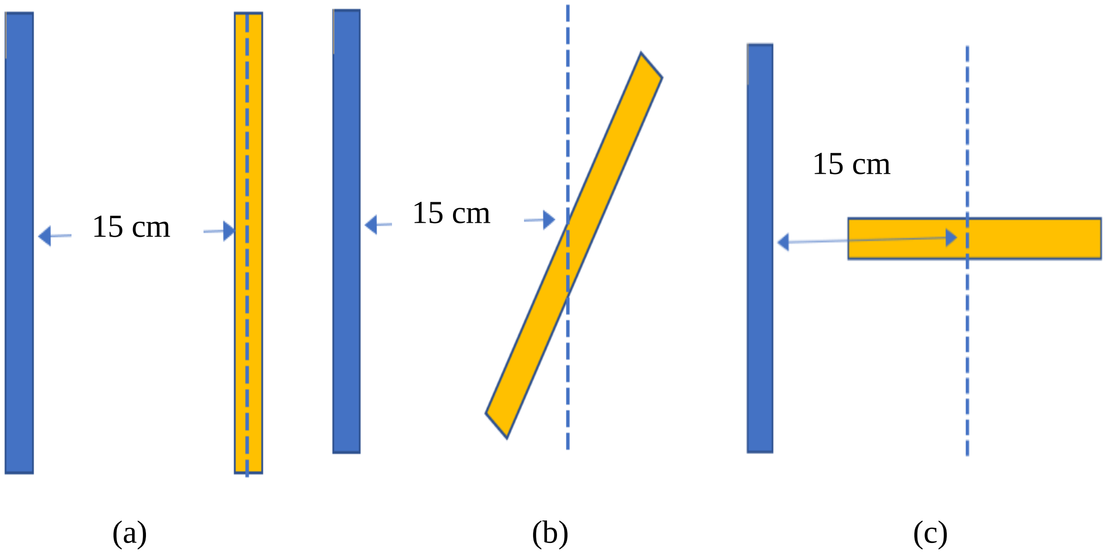

Figure 4.21. Test setup 1 to test the angular response of the discharge time.

(a) Starting position (0 ° viewing angle). (b) Detector OLED panel at altered viewing angle. (c) Detector OLED panel at a 90 ° viewing angle.

Table 4.10 Angular spectral response of a flexible OLED panel.

Parameter	**75 °**	**60 °**	**45 °**	**30 °**	**15 °**	**0 °**
Dominant wavelength (nm)	582.11	581.62	581.31	581.74	581.95	581.96
Irradiance (μWatt/cm^2)	540.36	3345.6	5565.1	5823.0	5862.6	5788.2
Irradiance (μWatt/cm^2) in rectangular form.	139.86 + 521.95*j*	1672.80 + 2897.37*j*	3935.12 + 3935.12*j*	5042.87 + 2911.50*j*	5662.84 + 1517.35*j*	5788.20 + 0.00*j*
Luminous Intensity (Candela)	2036.1	13989	22923	23433	23310	22865
Luminous Intensity (Candela) in rectangular form.	526.98 + 1966.72*j*	6994.50 + 12114.83*j*	16209.01 + 16209.01*j*	20293.57 + 11716.50*j*	22515.73 + 6033.07*j*	22865.00 + 0.00*j*
Luminous Flux (Lumens)	5.287E-5	3.632E-4	5.952E-4	6.084E-4	6.052E-4	5.937E-4
Centre wavelength (nm)	1096.8	591.04	595.95	599.15	600.58	600.79
Amplitude of centre wavelength	5.3035	16.040	31.932	32.610	32.740	32.740

From the angular response plots (Figure 4.22), it can be seen that from a 45 ° viewing angle to a 90 ° viewing angle there is an increase in discharge time. This is because when the detector OLED panel gets rotated beyond a 45 ° viewing angle, less light falls on the detector OLED and the discharge time of the detector OLED panel increases. From the x-y plane plot Figure 4.23b, the discharge time at a 0 ° viewing angle is larger than at viewing angles between 15 ° and 45 ° and that the discharge time decreases between 0 ° and 45 °. This is because a half the detector OLED panel moves closer towards the emitter OLED panel, causing more light to fall of the detector OLED between 15 ° and 45 ° than at a 0 ° viewing angle.

A second test setup to measure the angular response of the light detecting OLED panel was built, so that portions of the detector OLED panel did not move closer to the emitter OLED panel, when the viewing angle was adjusted.

Table 4.11. Angular response of the discharge time keeping the centre point 15 cm away and pivoting it on the centre axis.

Viewing angle (°)	**Discharge time (s)**
0	18.828
15	18.363
30	18.164
45	17.833
60	19.79
75	20.513
90	24.552

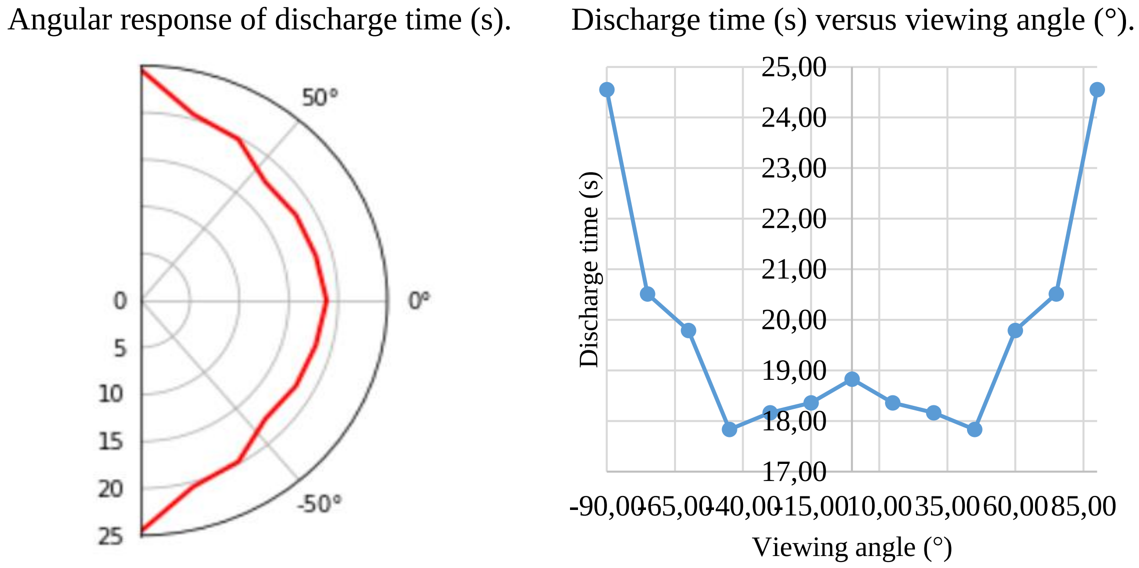

(a) (b)

Figure 4.22. Angular response of the discharge time keeping the centre point 15 cm away and pivoting it on the centre axis. a. polar plot. b. x-y axis plot.

(a) Polar plot. (b) x-y plane plot.

This was done placing the OLED panels 5 cm away from each other and by fixing the bottom of the light detecting OLED panel. The centre of the protractor was then placed at the bottom of the light detecting OLED panel and was rotated about that point. The test setup can be seen in Figure 4.23. As in the case of test setup 1, the angular response test setup was performed in an optically isolated laboratory, where the only light present was from the emitter OLED and the OLEDs were both kept exactly perpendicular to the desk by attaching them to the side of boxes, which were perpendicular to the desk.

The discharge time of the light detecting OLED panel, at different viewing angles, are given in Table 4.12 and the results are plotted in Figure 4.25.

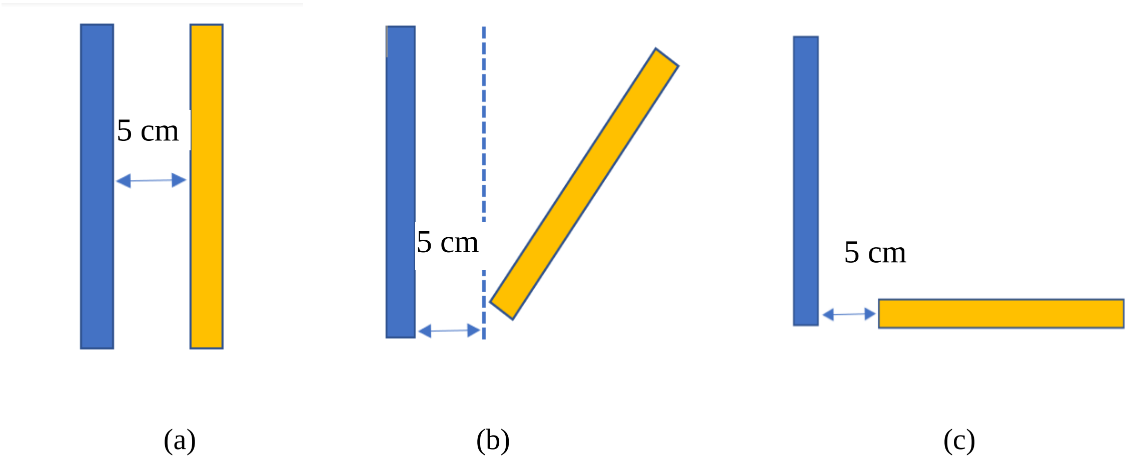

Figure 4.23. Test setup 2 to test the angular response of the discharge time.

(a) Starting position (0 ° viewing angle). (b) Detector OLED panel at altered viewing angle. (c) Detector OLED panel at a 90 ° viewing angle.

4.8.3 OLED emitter with coloured filters

In order to detect light in different wavelength regions, coloured universal Speedlite light filters were bought. The filters did not cover the entire length of the OLED panel, so the side areas, around the coloured filter, was covered with optically isolating tape, as can be seen in Figure 4.26. The width of both the panel and the filter is 40 mm but the panel length is 190 mm, and the filter lengths is 80 mm, therefore approximately 110 mm of the panel was concealed by the tape, and only the section of the panel with the filter over it was exposed.

The emission spectra of the OLED panels, with the different coloured filters over them, were measured using the AvaSpec Spectrometer and the test setup in Figure 4.18, with a 0 ° viewing angle, and the emission spectra are shown in Figure 4.27. The yellow and white filters allow all the wavelengths of emitted light, from the OLED panel, to be emitted through the filter. The light green and pink filters filter out some of the wavelength components but allows majority of the light to pass through.

Table 4.12. Angular response of the discharge time keeping the point closest to the detector 5cm away from the detector.

Viewing angle (°)	**Discharge time (s)**
0	10.0
15	12.736
30	14.318
45	15.803
60	18.573
75	21.268
90	21.768

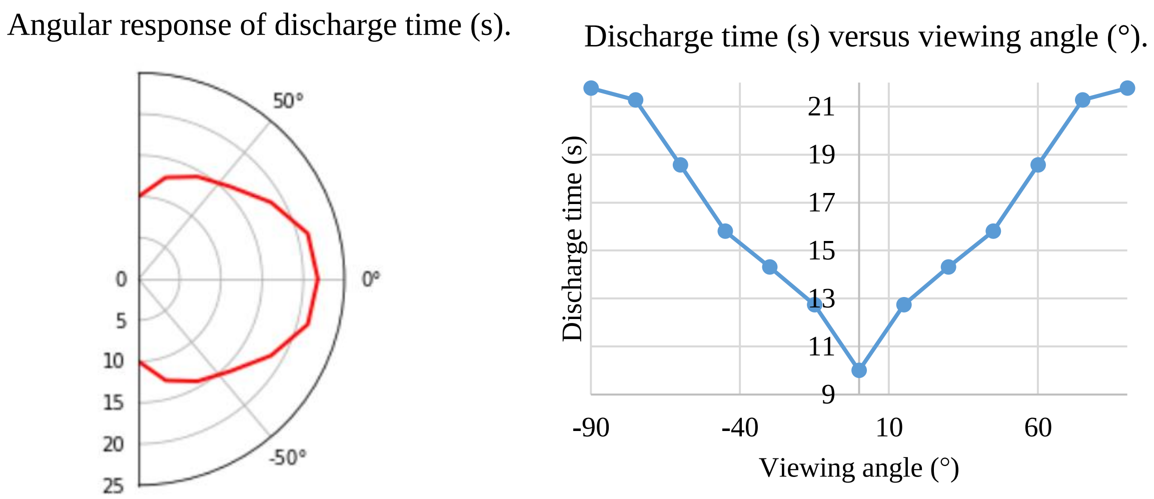

(a) (b)

Figure 4.24. Angular response of the discharge keeping the point closest to the detector 5cm away from the detector.

(a) polar plot (b) x-y axis plot

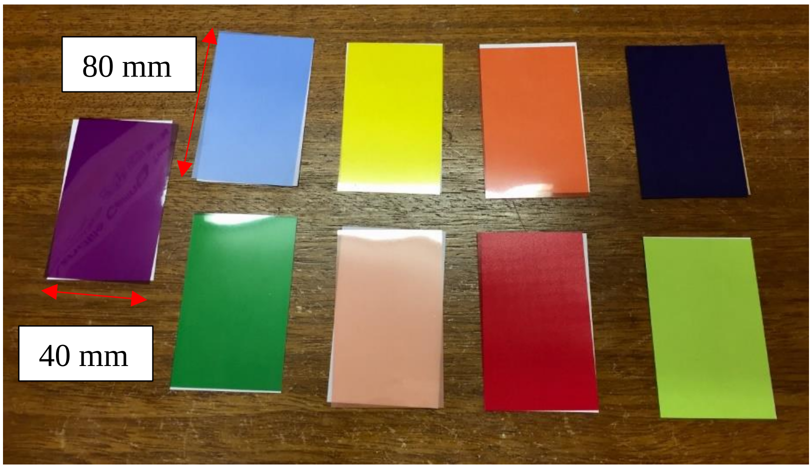

Figure 4.25. Coloured universal Speedlite light filters.

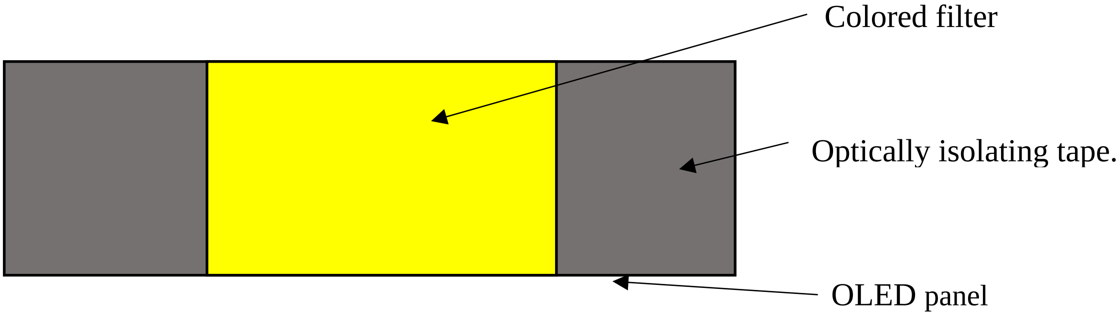

Figure 4.26. OLED panel, with coloured filter, test setup.

The dark green, purple, and orange filters have narrow bandwidths of light wavelengths which pass through the filter and the rest of the wavelengths get filtered out. A table of photometric measurements of the OLED panel, with each of the light filters placed over it, is summarized in Table 4.13.

The luminous intensity values for the white, pink, yellow and light green filters are the largest because the filters allow the most light to pass through them. On the other hand, the dark blue, dark green and purple filter have the smallest luminous intensity values because they allow the least amount of light to pass through.

Table 4.13. Table of photometric measurements for emitter OLED panel, with different colour filters.

Filter	**Dominant wavelength (nm)**	**Irradiance (µWatt/cm^2)**	**Luminous Intensity (Candela)**	**Luminous Flux (Lumens)**	**Illuminance (lux)**
Dark blue	465.64	4086.0	2323.6	6.033E-5	1920.3
Light blue	580.72	5776.7	10076	2.616E-4	8327.5
Dark green	545.52	5350.3	9837.2	2.554E-4	8129.9
Light green	580.63	7496.9	16978	4.408E-4	14031
Yellow	580.63	7776.0	16979	4.408E-4	14032
Orange	596.13	5427.2	6851.9	1.779E-4	5662.7
Red	NA	6165.0	5135.2	1.333E-4	4244.0
Purple	NA	5207.4	3538.2	9.187E-5	2924.2
Pink	586.75	7429.6	14960	3.884E-4	12363
White	583.70	7906.6	17683	4.591E-4	14614

4.9 COLOURIMETRIC ANALYSIS

OLED light emitters and light detectors were tested to see whether they can be used for colourimetric analysis. OLEDs with a purple, dark green, yellow filter and no filter were use as the light detecting OLEDs. The purple and dark green filter were selected as they both have narrow bandwidths of wavelengths that they filter (Figure 4.27). The dark green filter filters light in the lower wavelength region, while the purple filter filters out light in the higher wavelength region.

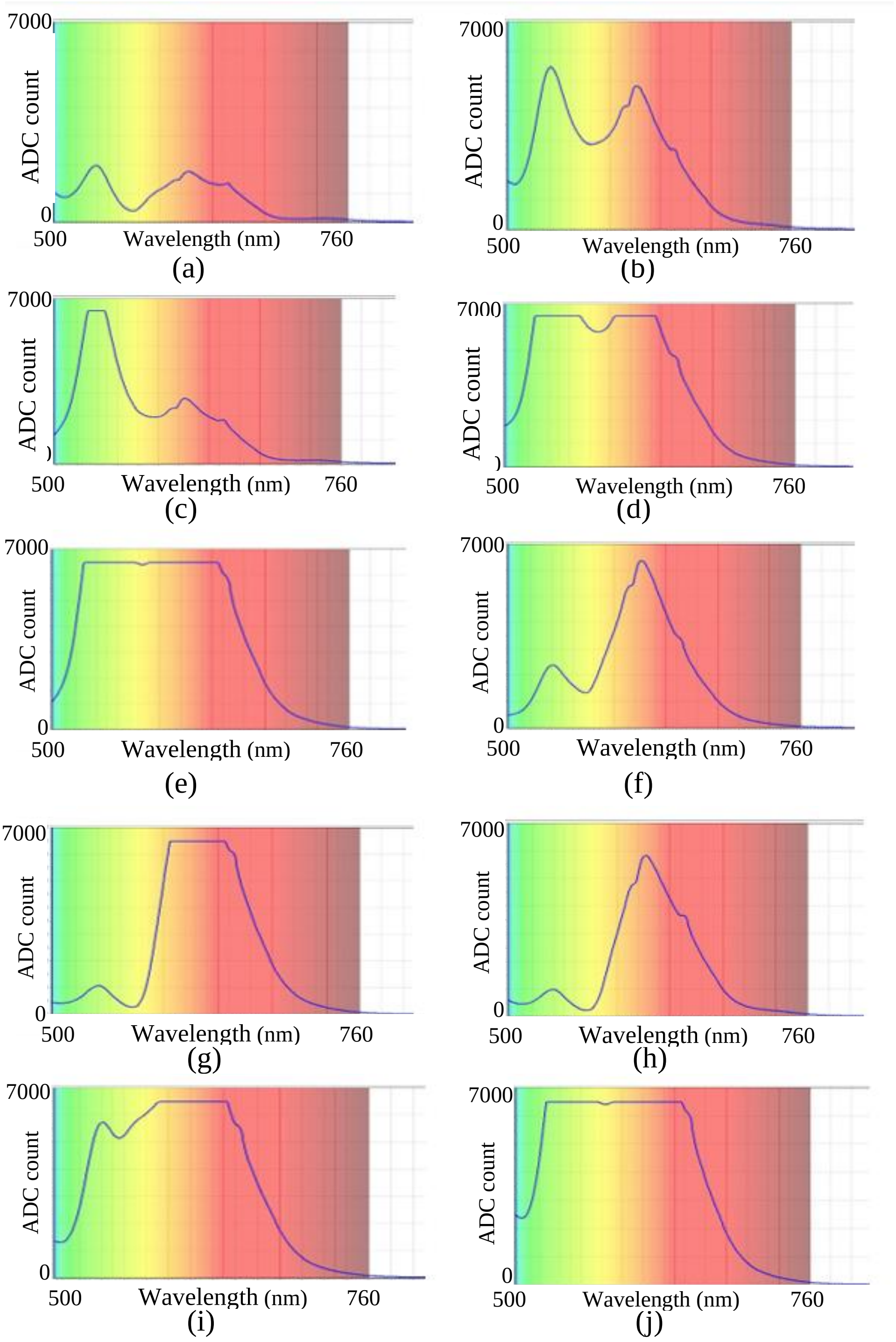

Figure 4.27. Emission spectra of OLED panel, with different coloured light filters.

(a) Dark blue filter (b) Light blue filter (c) Dark green filter (d) Light green filter (e) Yellow filter (f) Orange filter (g) Red filter (h) Purple filter (i) Pink filter (j) White filter

This allows for light detection in two distinct wavelength ranges. The yellow filter was also selected as it has a large bandwidth and can be used to detect light across a large range of wavelengths. A detector OLED with no filter was also used, for comparison purposes.

Due to the expense of the pH reagent, used for the LED colourimetric tests (Section 3.7), food colouring was used to colour samples for colourimetric analysis. Food colouring was added to 2 litres of water, and the quantity of food colouring is given in Table 4.14. The colours of each food colouring sample was matched to the pH tests as close as possible using the eye, as a colour meter was not available. The food colouring was added to the water, using a 0.5 ml injection syringe. Although this was not a very accurate manor of matching colours, it was sufficient to determine whether or not OLEDs can be used to distinguish between different colour liquid samples and can therefore be implemented for future colourimetric analysis.

A transparent, square, plastic, 2.5 litre container was used for the OLED colourimetric test. The filters were attached to the OLED panels as shown in Figure 4.26. Each side of plastic container was 11 cm long and the length of the coloured filters is 8 cm long. Therefore, the entire length of the filter attached to the OLED panel could be stuck at the centre of each side of container, using sellotape around the edges.

The linearity of illuminance versus discharge time between 1 and 11 cm from the OLED emitter was investigated in Section 4.2.4. The illumination was to be seen to relatively linear, with a R square value of 0.887781 for distances between 1 and 11 cm, which is the same size as the container used.

A detector OLED panel was places opposite an emitter OLED to measure the transmitted light, a detector OLED panel was placed perpendicular to an emitter OLED in order to measure the light refracted and a detector OLED panel was place directly above an emitter OLED in order to measure the light reflected.

The OLED panels were ensured to be centred, stuck flat against the container, and placed in line with each other, using measuring tapes. The test setup was performed in an optically isolated laboratory, where the only light present was from the emitter OLED.

Instead of using the discharge time, a variable “count” was incremented each time the ADC value was measured and sent the serial port. The maximum and minimum “count” variable values for each pH sample, using each colour filter for the OLED detector was recorded and is summarized in Table 4.15.

As in the case of the LEDs (Section 3.8), even a small deviation in light affected the discharge time. Therefore, to ensure accuracy, a test was setup which ran consecutive tests for 20 minutes and determined the maximum and minimum detected “count” variable value for each sample, was performed. 20 minutes of consecutive test measurements were performed because OLED detectors have discharge times up until 25 seconds. There at least 40 “count” variable measurements were measured. Sufficient time to recharge the detector OLED panels, between test measurements was ensured.

The maximum and minimum “count” variable values for an OLED detector with a purple filter, detecting transmitted light through each sample is given in Figure 4.29.

Although the pH values were not tested with the OLED panel tests, due to the large volume of liquid that needed to be tested to span the dimensions of the OLED panel, food colouring was matched to the colour of the pH test kit.

The pH value that represents the colour of the food colouring pH sample is given on the x-axis of the plot. It can be seen in Figure 4.29 that for an OLED detector with a purple filter detecting transmitted light, the “count” variable ranges for each sample fall into 4 distinct groups. Group 1 falls below a “count” value of 155000 and the only sample in that range is a sample with only clear water in it and no reagents. The clear water sample is used as a reference point and to calculate relative transmission, reflection, and refraction values.

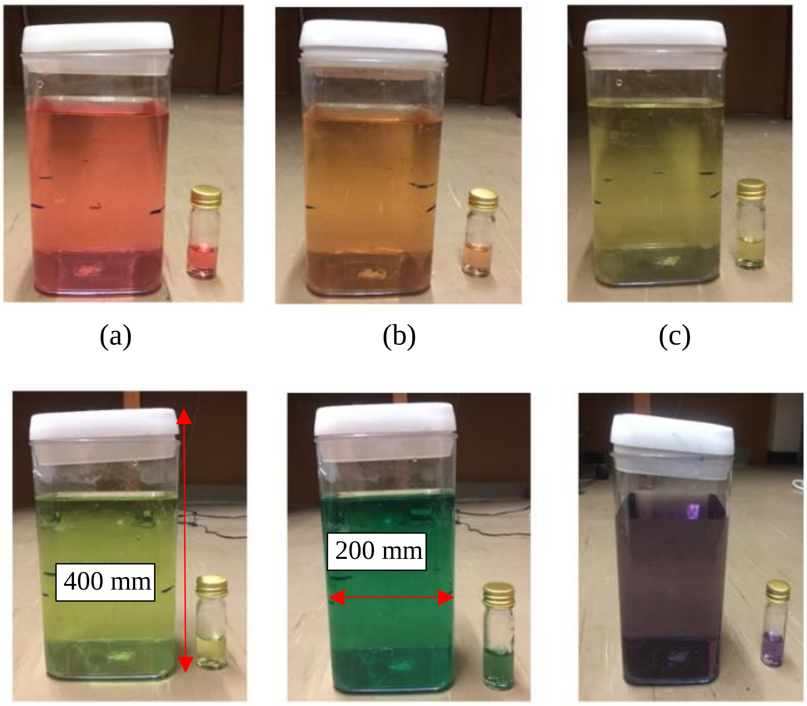

(a) (b) (c)

(d) (e) (f)

Figure 4.28. pH test samples, and their corresponding 2 litre food colouring samples. (a) Pink (pH 4) (b) Orange (pH 5) (c) Yellow (pH 6) (d) Light green (pH 7) (e) Dark green (pH 8) (f) Purple (pH 9)

Group 2 falls between 170000 and 175500 and both a pH of 4 and 5 falls in that range. Group 3 falls between 155000 and 170000 and a pH of 6 and 9 fall into that range.

Lastly, group 4 falls above a “count” value of 175500 and a pH of 7 and 8 fall in that range. In order to differentiate between the pH samples in the same groups in Figure 4.30 the transmission maximum and minimum “count” values for an OLED detector, with a green filter (Figure 4.30) and no filter (Figure 4.31) were used as well as the reflection maximum and minimum “count” values for an OLED detector with no filter Figure 4.32.

Table 4.14. Food colouring added to 2 litres of water in order to match the colour to different pH colourimetric test colours.

Colour of water	pH representative	Food colouring per 2 litres
Pink	4	0.5 ml of pink food colouring.
Orange	5	0.02 ml red food colouring and 1 ml yellow food colouring.
Yellow	6	0.45 ml yellow food colouring.
Light Green	7	0.45 ml yellow food colouring and 0.1 ml of blue food colouring.
Dark green	8	0.45 ml of yellow food colouring and 0.35 ml of blue food colouring.
Purple	9	0.015 ml of blue food colouring and 0.05 ml of red food colouring

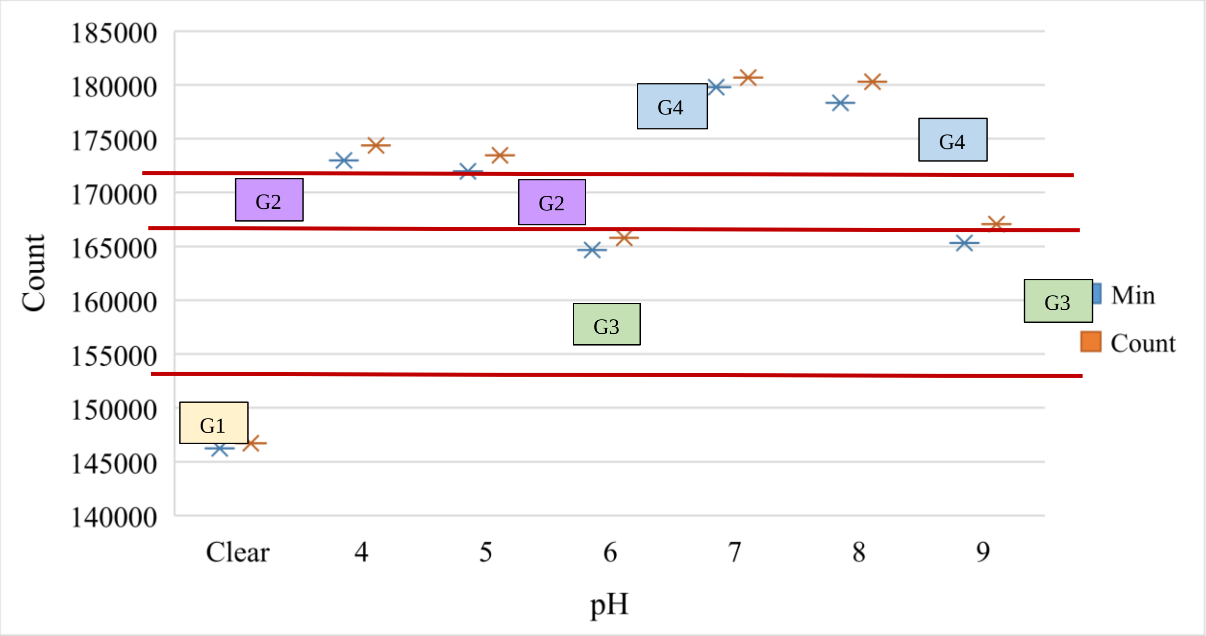

Figure 4.29. Maximum and minimum ADC count values, for OLED with a purple filter, detecting light transmission through samples.

Table 4.15. Maximum and minimum ADC count values for OLED detects, with different colour light filters and detector orientations, for each of the coloured water samples.

LED detector colour	**Detector orientation**	**pH**						
		Water	**4**	**5**	**6**	**7**	**8**	**9**
No filter	Reflect	162694-164477	174162-175782	177476-178449	177967-179802	177003-178856	184618-186836	176172-176819
	Refract	158333-159460	175043-176875	172259-174278	171799-175548	178026-180254	181188-186430	171035-172488
	Transmit	122481-122845	159545-160070	158426-160756	160925-165581	170506-171686	171796-172955	156172-157249
Purple	Reflect	166304-166988	172418-173733	176012-177990	178466-181323	178143-178961	180126-182527	179132-179551
	Refract	162978-164201	175931-178493	175130-180711	175901-177916	180042-181819	179957-181386	174710-176398
	Transmit	1460235-146712	172994-174371	171982-173458	177190-179190	179779-180671	178337-180288	165309-167075
Green	Reflect	165349-166784	172661-173911	174641-177721	178671-180722	177404-179146	180010-181550	174733-176863
	Refract	164406-165554	177659-179281	176343-178310	175996-177661	178919-180479	181024-182293	173944-175293
	Transmit	153073-153940	178972-181861	173902-175363	168007-169027	178179-177866	178951-180265	169004-169969
Yellow	Reflect	166512-167626	173515-174147	178302-181184	178416-179939	177812-178927	178140-179323	176198-178116
	Refract	164134-165608	176175-178251	178586-180727	175832-177963	179188-180617	181065-182424	174201-175622
	Transmit	154367-155864	179522-180353	173415-176311	167193-168503	179620-181981	178350-179568	170002-171409

The transmission maximum and minimum “count” values for an OLED detector, with a green filter (Figure 4.30) is used to differentiate between the samples in group 2. A pH of 4 “count” range falls above 177000 and a pH of 5 “count” range falls below 177000 when a green filter is used to measured light transmission. This is indicated by A and B in Figure 4.30.

The transmission maximum and minimum “count” values for an OLED detector, with a no filter (Figure 4.31) is used to differentiate between the samples in group 3. A pH of 6 “count” range falls above 164000 and a pH of 9 “count” range falls below 164000 when no filter is used to measured light transmission. This is indicated by C and D in Figure 4.31.

Lastly, the reflection maximum and minimum “count” values for an OLED detector, with a no filter (Figure 4.31) is used to differentiate between the samples in group 4. A pH of 7 “count” range falls below 183000 and a pH of 8 “count” range falls below 183000 when no filter is used to measured light transmission. This is indicated by F and E in Figure 4.32.

Therefore, an array of 4 OLED detectors, one with a purple filter detecting light transmission, one with a dark green filter detecting light transmission, one with no filter detecting light transmission and one with no filter detecting light reflection can be used to differentiate between different coloured water samples that represent the colours of a colourimetric pH test between a pH of 4 and 10.

The groups and letter used to classify each water samples colour and therefore pH, is summarized in Table 4.16.

The maximum and minimum “count” values for the different coloured filters detecting light transmission, refraction and reflection and were not used for the given analysis are shown in Figure 4.33 and Figure 4.34. While different combinations of these plots and results can also be used to differentiate between the different coloured water samples, the chosen identification method made use of the minimum number of filters and tests. The additional plot, can however, be used as verification and confirmation of the identified pH sample.

The largest count range in Table 3.13 is 175130-180711, which is a range of 5581. There is 3.13 % deviation from the measured mean. Although there is some deviation in the measured results, the measurements are quite accurate and fall within 3.13 % of the mean.

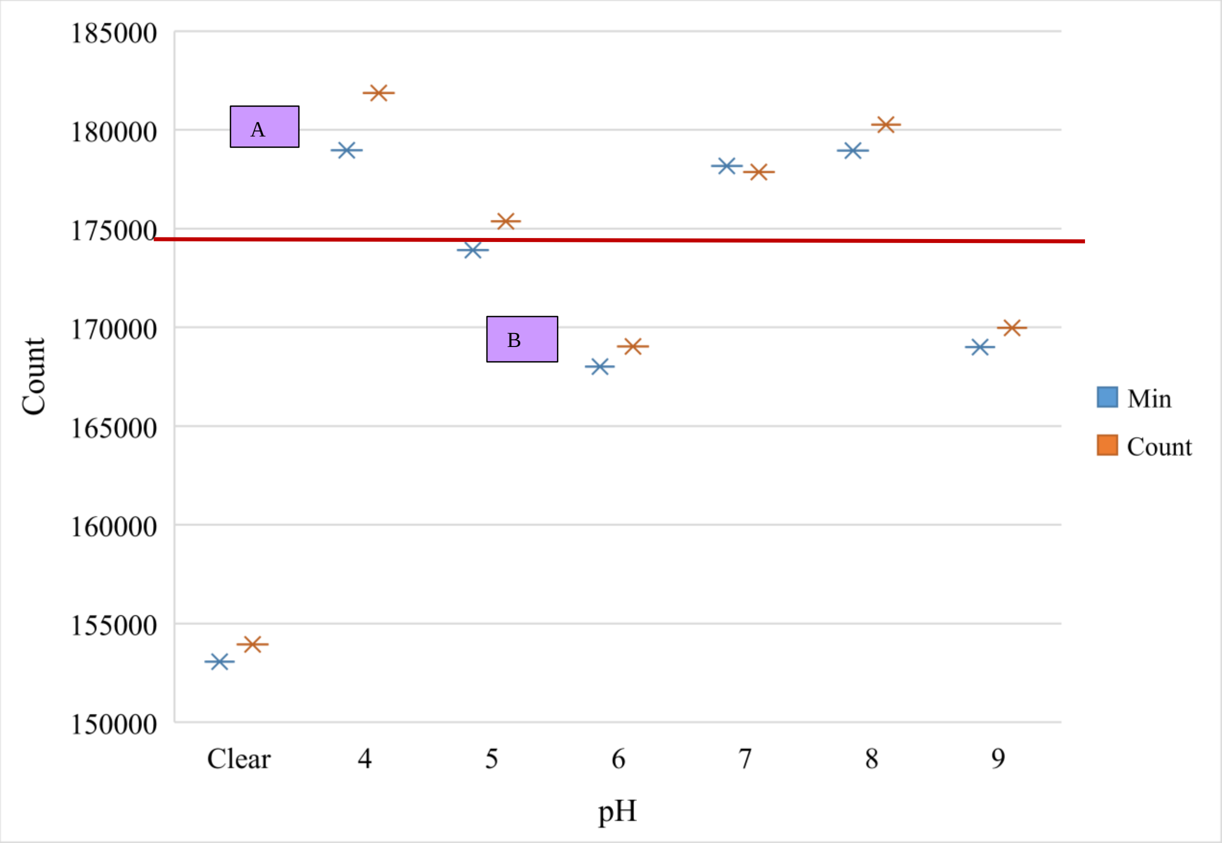

Figure 4.30. Maximum and minimum ADC count values, for OLED with a green filter, detecting light transmission through samples.

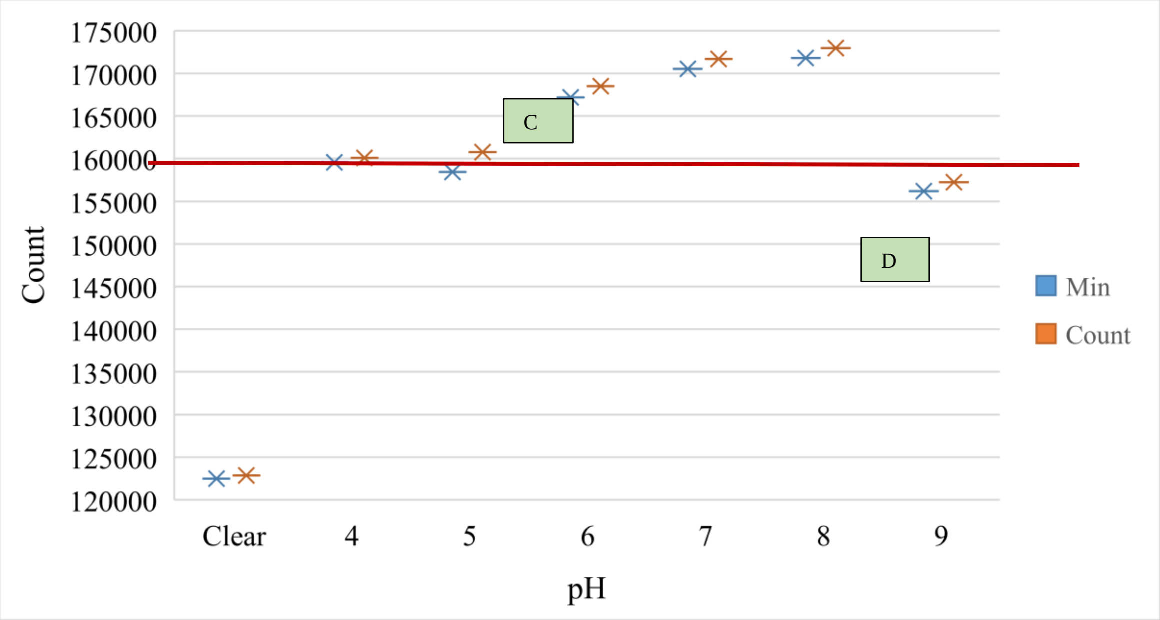

Figure 4.31. Maximum and minimum ADC count values, for OLED with no filter, detecting light transmission through samples.

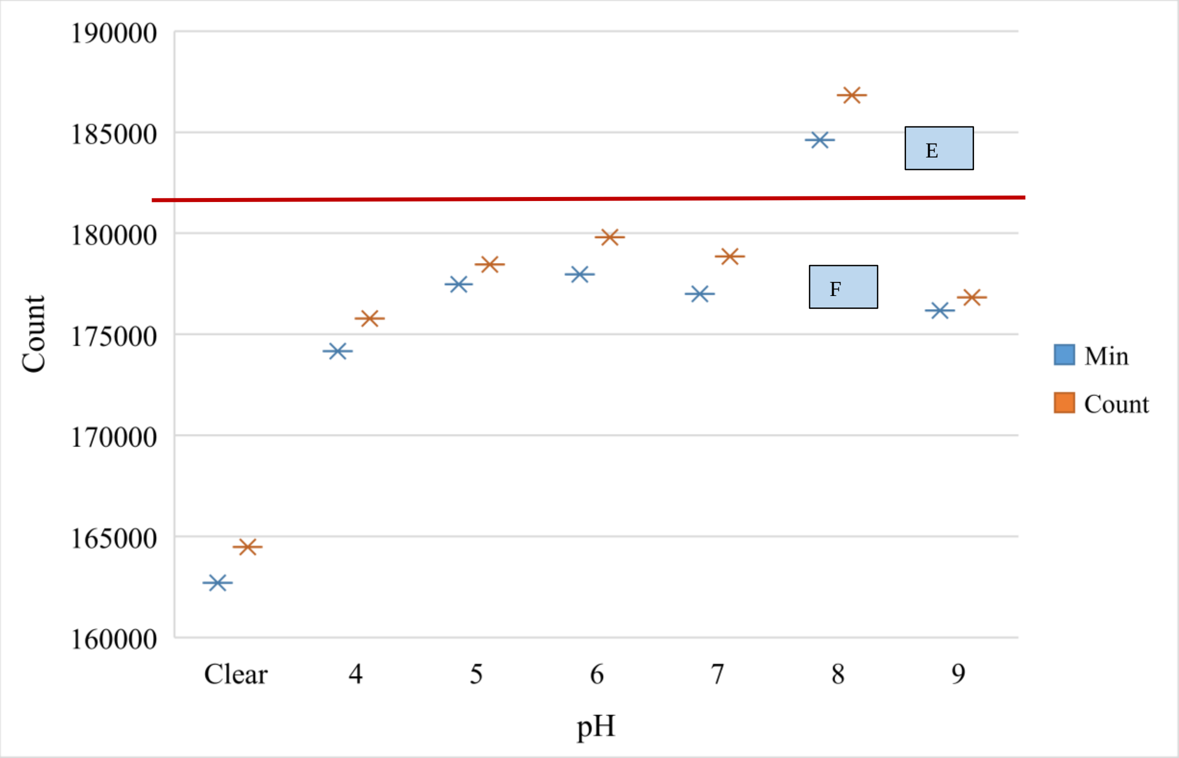

Figure 4.32. Maximum and minimum ADC count values, for OLED with no filter, detecting light reflection through samples.

Table 4.16. Groups and letter used to classify each water samples.

pH level	Identification
Clear	G1
4	G2 and A
5	G2 and B
6	G3 and C
7	G4 and F
8	G4 and E
9	G3 and D

The relative “count” transmission, reflection and refraction value ranges were calculated using (3.4) [33]. The minimum relative “count” values were calculated by taking the minimum “count” value of the sample (Table 4.15) and the maximum “count value of the clear water reference sample (Table 4.15) as can be seen in (4.2). Similarly, the maximum relative “count” values were calculated by taking the maximum “count” value of the sample (Table 4.15) and the minimum “count value of the clear water reference sample (Table 4.15) as can be seen in (4.2).

$$\boldsymbol{Relative\ count}\ (\%) = \frac{\boldsymbol{Count_{sample} - Count_{clear\ water0}}}{\boldsymbol{Count_{sample}}} \times \mathbf{100}\ \Omega \qquad (4.2)$$

The minimum and maximum calculated relative transmission, reflection and refraction values are given in Table 4.17. These results can also be used to identify the colour (pH) of the water samples. The advantage of using the relative values, is that it can be recalibrated for any reference samples and therefore any container can be used if it is recalibrated for it.

The relative transmission values using a purple and green filter as well as the relative reflection ranges using no filter are plotted in Figure 4.35, Figure 3.36 and Figure 4.37 respectively.

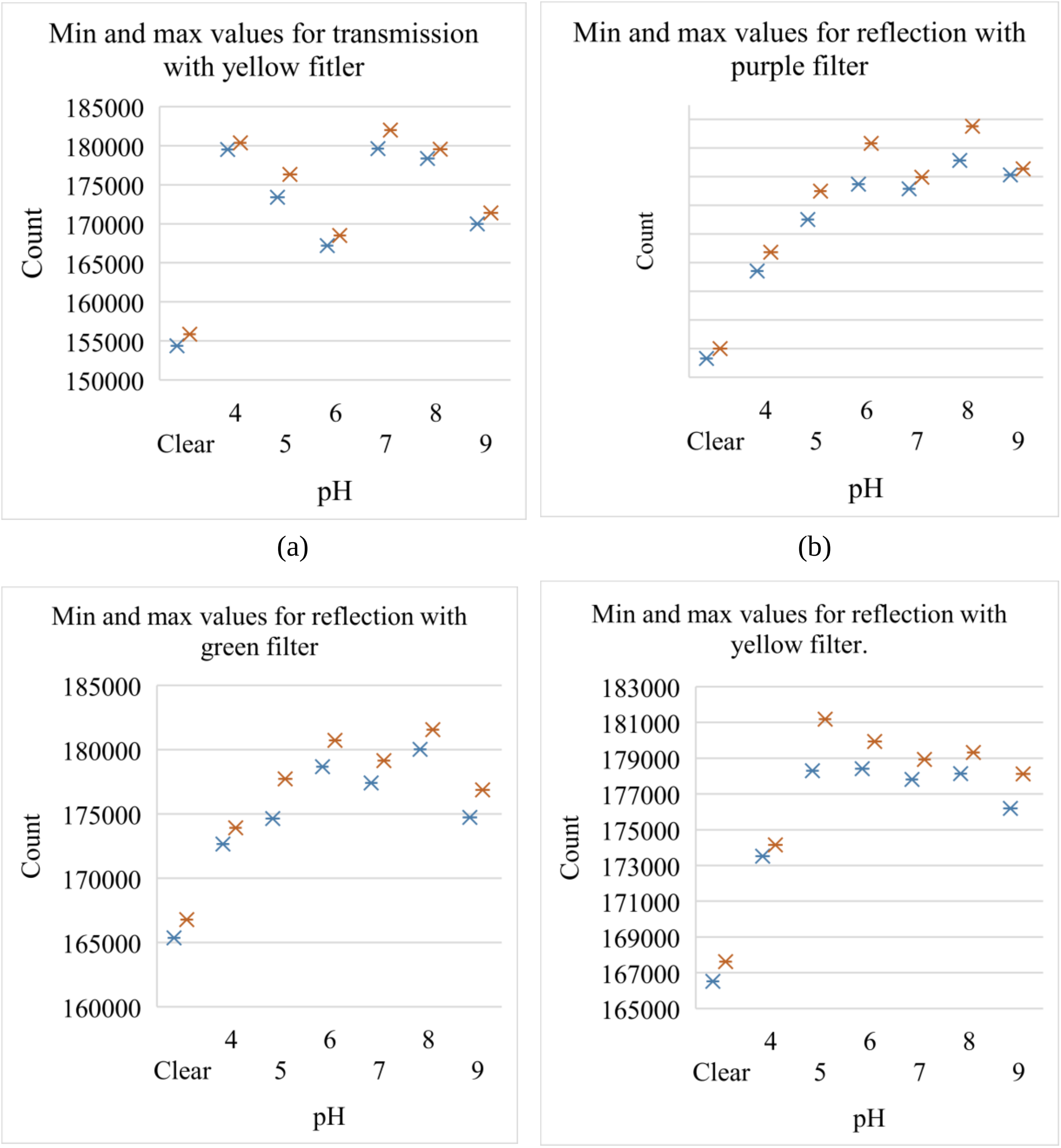

(a) (b)

(c) (d)

Figure 4.33. Maximum and minimum ADC count values, for OLEDs with different light filters, measuring light transmission and reflection, through water samples.

(a) Yellow filter, measuring light transmission. (b) Purple filter, measuring light reflection. (c) Green filter, measuring light reflection. (d) Yellow filter, measuring light reflection.

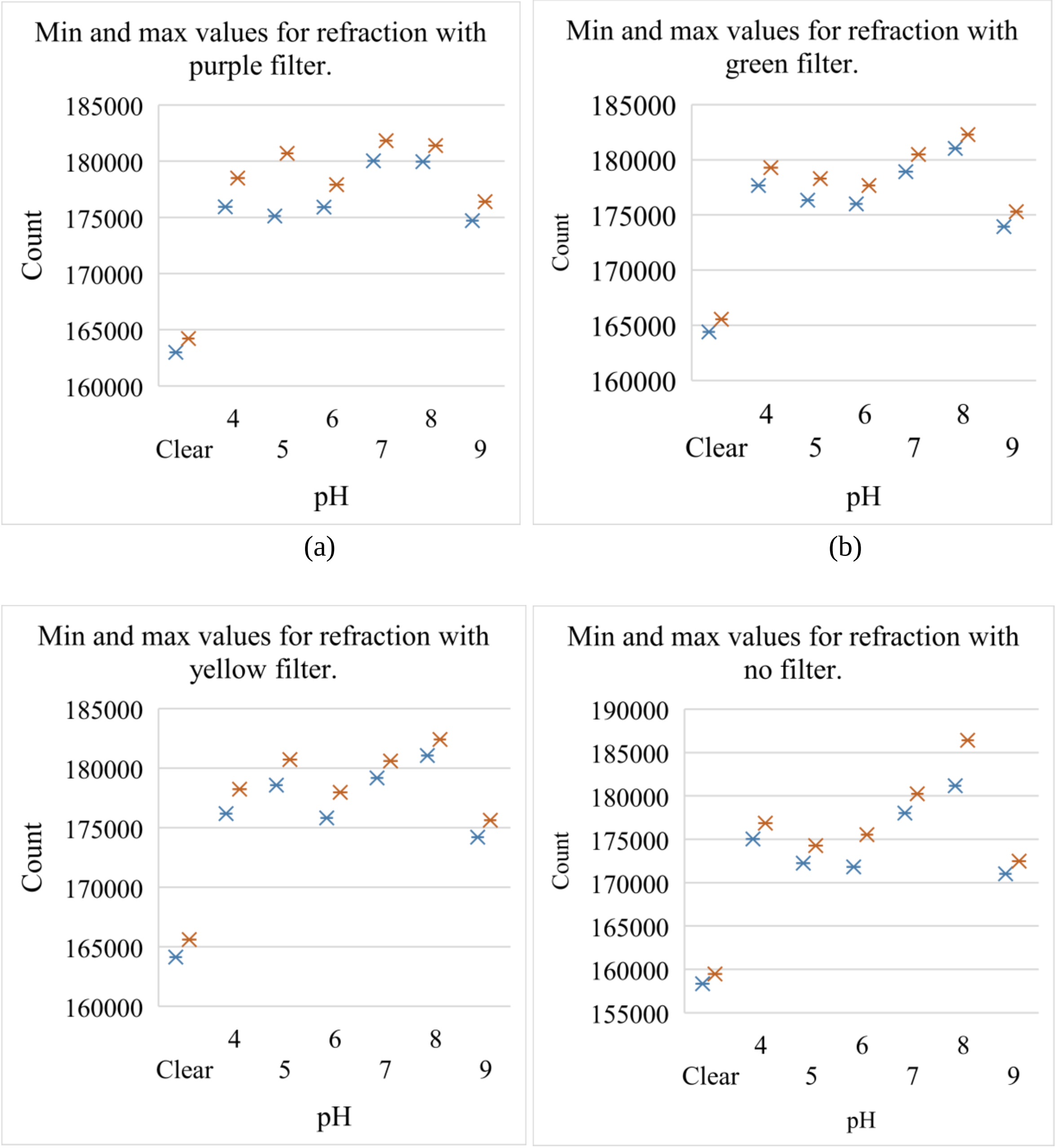

(a) (b)

(c) (d)

Figure 4.34. Maximum and minimum ADC count values, for OLEDs with different light filters,

measuring light refraction, through water samples.

(a) Purple filter, measuring light refraction. (b) Green filter, measuring light refraction. (c) Yellow filter, measuring light refraction. (d) No filter, measuring light refraction.

It can be seen from Figure 4.35 that the data ranges fall into 3 distinct groups, indicated as G1, G2 and G3. G1 are data ranges that fall above 20, G2 are data ranges that fall above 15 and below 20 and G3 are data ranges that fall below 15. In order to differentiate between pH (coloured water samples that represent a given pH) samples that fall in the same group in Figure 4.35, the relative transmission values with a green filter (Figure 4.36) and the relative reflection values with no filter (Figure 4.37) are used.

In Figure 4.35 a pH of 4 and 5 fall into group 1 but can be differentiated, using Figure 4.36. In Figure 4.36 a pH of 4 falls above 15.5 % and a pH of 5 falls below 15.5 %. Similarly, in Figure 4.35 a pH of 6, 7 and 8 fall into group 2 but a pH of 6 can be differentiated from a pH of 7 and 8, using Figure 4.36. In Figure 4.36 a pH of 6 falls below 15.5 % and a pH of 7 and 8 falls above 15.5 %.

Lastly, to differentiate between a pH of 7 and 8, which fall in group 2 in Figure 4.35 and group A in Figure 4.36, Figure 4.37 is used. In Figure 4.37 a pH of 7 falls below 11.5 % and a pH of 8 falls above 11.5 %.

The groups and letter used to classify each water samples colour and therefore pH, using relative “count” values, are summarized in Table 4.18.

Therefore, an array of 3 OLED detectors, one with a purple filter detecting light transmission, one with a dark green filter detecting light transmission and one with no filter detecting light reflection can be used to differentiate between different coloured water samples that represent the colours of a colorimetric pH test between a pH of 4 and 10, using relative “count” values. It can also be seen that 1 less OLED emitter and detector pair is required when using the relative “count” values than the original “count” values.

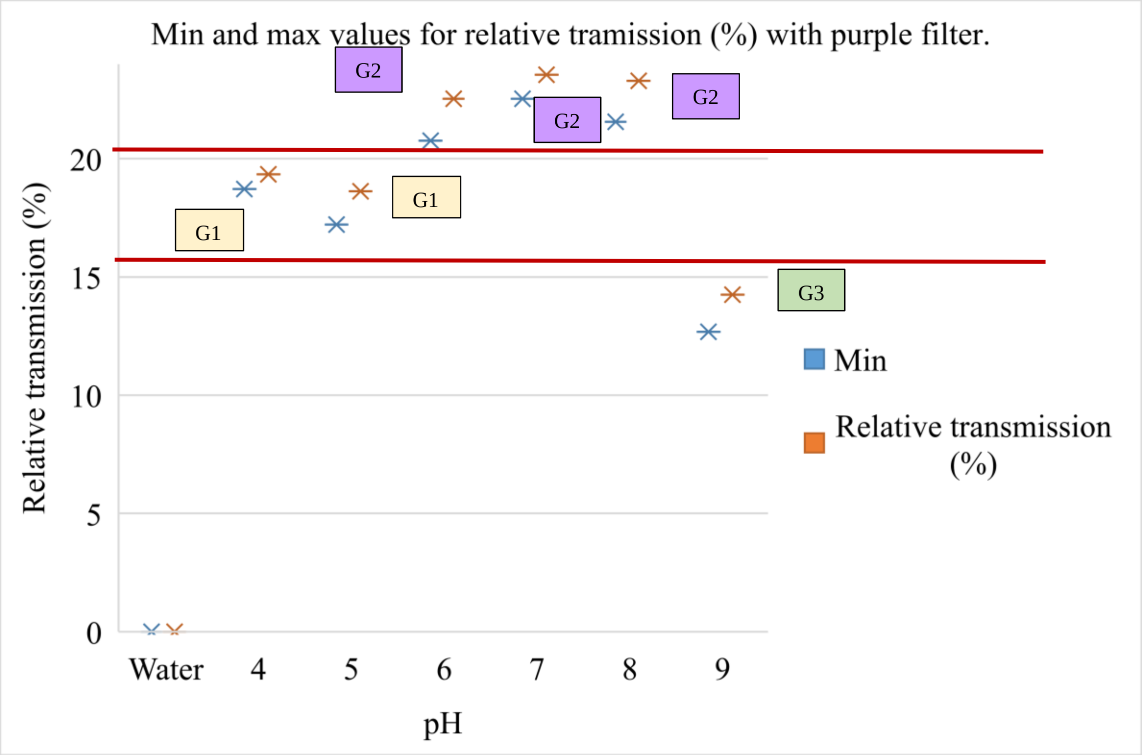

Figure 4.35. Minimum and maximum values for relative transmission (%) with a purple filter.

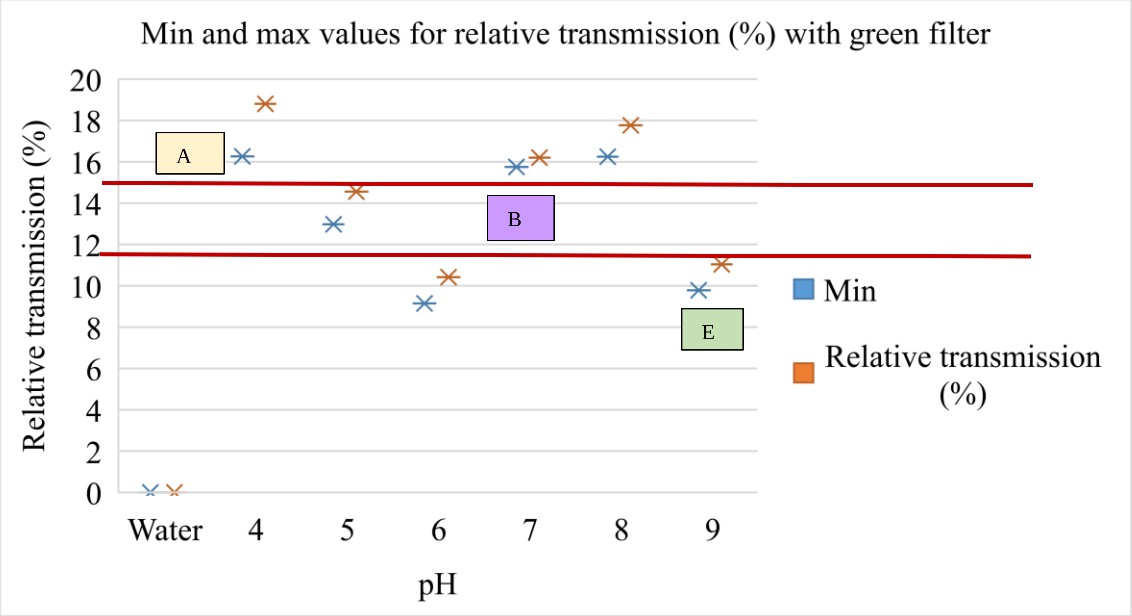

Figure 4.36. Minimum and maximum values for relative transmission (%) with a green filter.

Table 4.17. Relative absorbance values (%) for OLED detects, with different colour light filters and detector orientations, for each of the coloured water samples.

LED detector colour	**Detector orientation**	**pH**						
		Water	**4**	**5**	**6**	**7**	**8**	**9**
No filter	Reflect	0	5.89-8.04	7.90-9.68	8.20-10.52	7.62-9.93	12.25-14.84	7.11-8.68
	Refract	0	9.77-11.71	8.03-10.07	7.74-10.87	11.64-13.84	13.63-17.75	7.26-8.94
	Transmit	0	29.88-30.69	28.96-31.25	31.00-35.19	38.80-40.17	39.85-41.21	27.13-28.39
Purple	Reflect	0	3.25-4.47	5.40-7.03	6.87-9.03	6.68-7.61	7.87-9.76	7.27-7.97
	Refract	0	7.14-9.52	6.66-10.88	7.13-9.17	9.65-11.56	9.60-11.29	6.40-8.23
	Transmit	0	18.72-19.34	17.22-18.62	20.77-22.54	22.54-23.55	21.56-23.29	12.68-14.25
Green	Reflect	0	3.52-5.18	4.71-7.48	7.13-9.30	6.37-8.34	7.93-9.80	4.77-6.96
	Refract	0	7.31-9.05	6.52-8.46	6.31-8.06	8.07-9.78	9.34-10.88	5.07-6.62
	Transmit	0	16.26-18.81	12.97-14.56	9.14-10.42	15.75-16.20	16.25-17.76	9.79-11.04
Yellow	Reflect	0	3.51-4.59	6.37-8.81	6.44-8.06	6.08-7.46	6.27-7.69	5.11-6.97
	Refract	0	6.38-8.60	7.84-10.11	6.17-8.43	8.20-10.04	9.33-11.14	5.19-7.00

	Transmit	0	15.18-16.83	11.26-14.22	7.27-9.16	15.24-17.89	14.43-16.33	9.07-11.04

Table 4.18. Groups and letter used to classify each water samples, using relative “count” values.

pH level	**Identification**
Water	0
4	G1 and A
5	G1 and B
6	G2 and C
7	G2 and E
8	G2 and D
9	G3

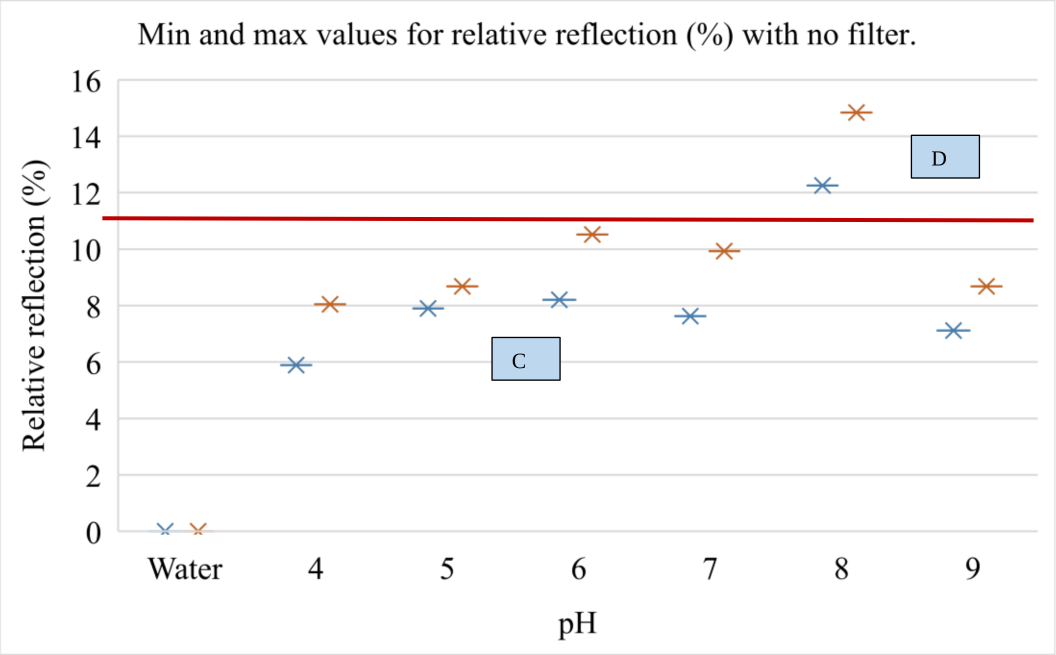

Figure 4.37. Minimum and maximum values for relative transmission (%) with a no filter.

CHAPTER 5 INKJET PRINTED OLED SIMULATIONS

5.1 CHAPTER OVERVIEW

An OLED structure was designed, simulated, and optimized in this chapter. The OLED structure was designed to be fully inkjet printable. Inkjet printing is advantageous as there is little material wastage, it can be printed on numerous flexible substrates and high printing resolutions are attainable.

In in the case of most OLED structure, not all the layers in the structure are inkjet printable. This is because some of the chosen materials are not inkjet printable, or other printing methods for a layer increases the device performance. A partially ink-jet printable OLED display structures is discussed in Section 5.2 and is simulated and analysed in Section 5.5.

Each layer of the OLED structure influences the overall performance of the OLED structure. The emission spectra and refraction indexes of the various layers in an OLED structure is discussed in Section 5.3. The electrical properties of an OLED structure was simulated and discussed in Section 5.4.

In Section 5.6, a fully inkjet printable OLED structure was proposed. OLED structures with different inkjet printable cathodes were discussed, simulated, and compared in terms of device performance and light emission.

A fully inkjet printable OLED structure's layers were optimized for light emission and is discussed in Section 5.7. The affect that layer thickness has on photon density, is also discussed.

The designed and simulated OLED structure was not manufactured due to the cost and availability of inks and inkjet printers. However, the fully inkjet printable flexible OLED structure can be manufactured and integrated into microfluidic devices for future research and application.

5.2 PARTIALLY INKJET PRINTABLE OLED

Before designing a fully inkjet printable OLED structure two OLED structures, from literature, were explored that were partially inkjet printable. The first partially inkjet printable OLED structure has mostly inkjet printed layer, except the EML [66]. The second partially inkjet printable OLED structure has inkjet printable layers, except the conductive anode and cathode [106].

5.2.1 Al:ZnO:PEI interlayer OLED

An OLED consisting of only 4-layers, namely a cathode, EIL, EML and transparent anode was manufactured using inkjet printed manufacturing techniques for all of the layers, except the EML, and was seen to emit light up until 16000 cdm^2. A summary of the inks, manufacturing methods and suppliers of each layer is summarized in Table 5.1. The Al:ZnO:PEI EIL interlayer can be replaced with two separate layers consisting of an aluminium doped zinc oxide (Al:ZnO) layer and a PEI layer. A single Al:ZnO:PEI layer does, however, have a lower work-function than two separate layers, which increases the device performance [106].

Table 5.1 Materials for the interlayer OLED illustrated in Figure 5.1 [106].

Layer	**Ink**	**Manufacturing method**	**Ink supplier**
Cathode	AgNWPEDOT:PSS	Inkjet	Heraeus Clevios GmbH and Clevios PEDOT HY
Interlayer	Al:ZnO:PEI	Inkjet	Self-made
EML	SuperYellow LEP dissolved in toluene	Spin-coating	Merck KGaA
Transparent anode	PEDOT:PSS	Inkjet	Clevios PEDOT HY

5.2.2 B. Small molecule OLED (smOLED)

Small molecule OLEDs are a subclass of OLEDs that are categorized by the chemical makeup of the organic semi-conductive materials in the device. A smOLED structure that can be manufactured with an inkjet printed EML, HTL and HIL layer in between a Li/ Al cathode and indium tin oxide (ITO) anode that was deposited by an evaporation process is shown in Figure 5.1 [66]. The materials used for each of the inkjet printed layer, and the manufacturer of the materials are shown in Table 5.2 [66]. The device was attempted on a glass substrate using a Dimatix DMP2800 inkjet printer. It was seen that the quality of each layer heavily influenced the device performance. Although the device was functional, it was not very efficient due to intermixing between the EML and HTL [66].

5.3 OLED LAYER SPECTRA AND REFRACTION INDEX

The emission spectra of emissive materials and refraction index of the different materials used for each layer of the OLED structure is simulated and analysed in this section.

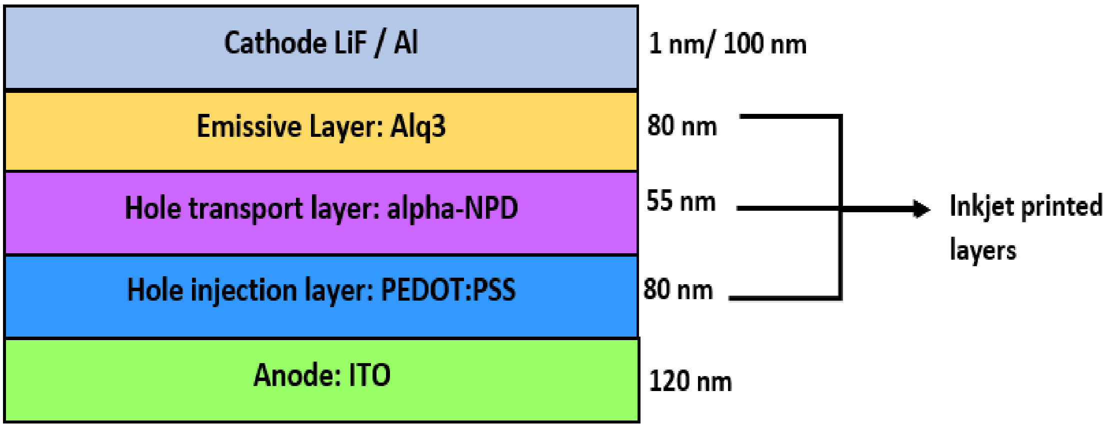

Figure 5.1 The structure of a smOLED, with inkjet printable EML, HTL and HIL layers, Adapted from **[66]**, with permission.

5.3.1 Emission spectra

The emission spectra of various emissive materials, that are inkjet printable, are simulated in Fuxim Setfos simulation software. The emission spectra for Alph-NPD and Alq3, which are used in the OLED display from literature (Figure 5.1) , are shown in Figure 5.2 and Figure 5.3 respectively. The peak intensity wavelength of the simulated materials, as well as the colour of light emission is shown in Table 5.3. The emission spectra of other material that can be used in OLED manufacturing are given in addendum E.

5.3.2 Refraction index.

If a material has a very large refraction index, it can cause the light emitted by the emissive material to not exit the device. This is known as the total internal reflection (TIR) [107]. The refraction index of a material is typically described as a complex number and can be used to calculate the amount of reflected light in a light-emitting structure [108].

Table 5.2 Ink composition of each inkjet printed layer of the smOLED illustrated in Figure 5.1 [66].

Layer	Ink	Ink composition
EML	Alq3	10 mg Alq3 per ml of a mixture of benzylalcohol (purchased from Aldrich) and THF (purchased from Merck).
HTL	α-NPD	Composed from 5mg of α-NPD per ml of the solution. Solution: A mixture of tetralin (1,2,3,4tetrahydronaphthalene) (purchased from Merck) and indane (purchased from Aldrich).
HIL	PEDOT:PSS	Clevios™ CH8000 (purchased from Heraeus) or Orgacon HIL1005 (purchased from Agfa)

The difference in refraction index at layer interfaces in OLED displays can decrease the efficiency of the OLED because light gets internally reflected when there is a change in refraction index. Typically, 20 % of the light emitted by the EML is reflected back into the OLED. Extraction layers can be added to the OLED to reduce the difference in refraction index of adjacent layers. There is a difference in refraction index between the air surrounding the OLED and the OLED display itself that also needs to be considered [109]. The complex refraction index of ITO and Alq3 is shown in Figure 5.4 and Figure 5.5. The complex indexes of materials at their dominant wavelengths are compared in Table 5.4. The refraction indexes are measured at 540 nm as this is the wavelength with the largest light intensity (Figure 5.3). The index plots of other materials that can be used in OLED manufacturing are given in addendum F.

As can be seen from Table 5.4, the EML materials refraction indexes have larger real parts and smaller imaginary parts than the anode and cathode materials, which can lead to decreased device efficiency. The HIL and HTL layers have refraction indexes are seen to be in between the EML material values and the anode and cathode values, allowing for a more gradual difference in refraction index between layers of the OLED and thus improved device efficiency.

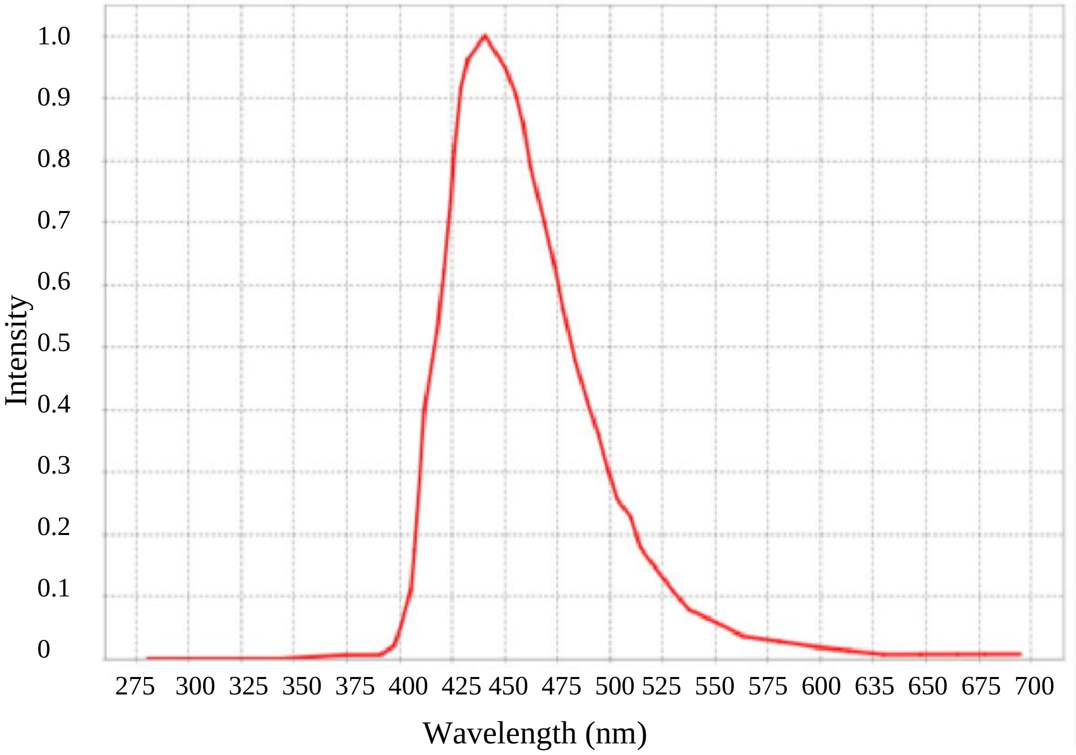

Figure 5.2. Emission spectrum of Alpha-NPD

Table 5.3. Peak intensity wavelength and light emission colour of various materials simulated in Fluxim Setfos.

Material	Peak intensity wavelength	Colour of light emission
Alpha-NPD	440 nm	Dark blue
Alq	530 nm	Green
Alq3	540 nm	Green
DOO-MEH-PPV	575 nm	Yellow
Super yellow [38].	550 nm	Yellow-green

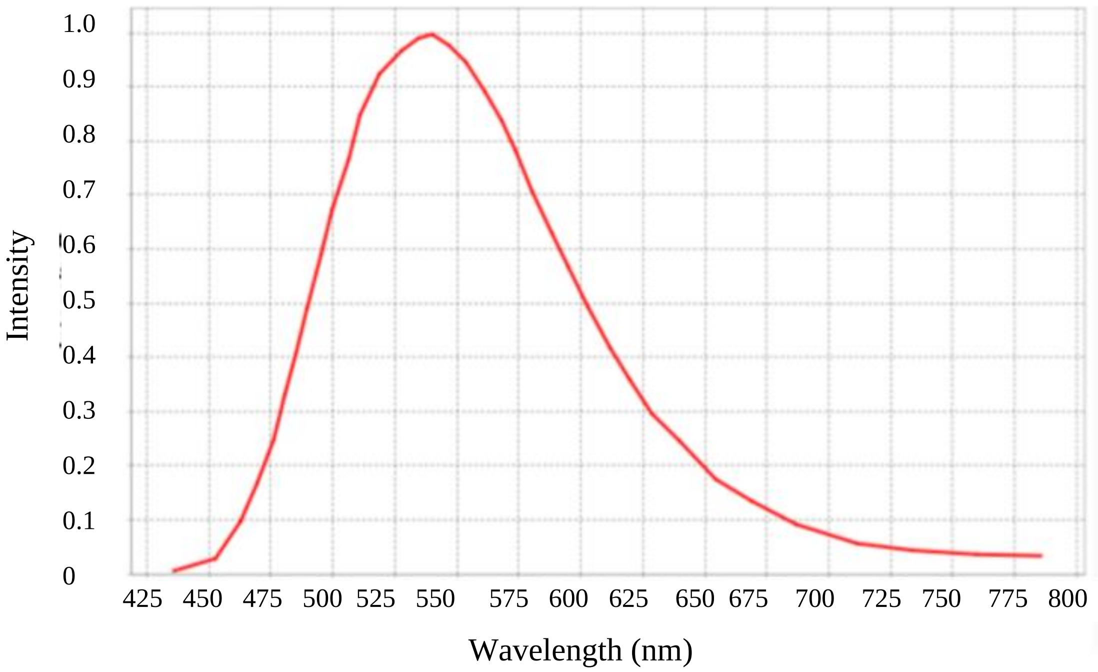

Figure 5.3. Emission spectrum of Alq3.

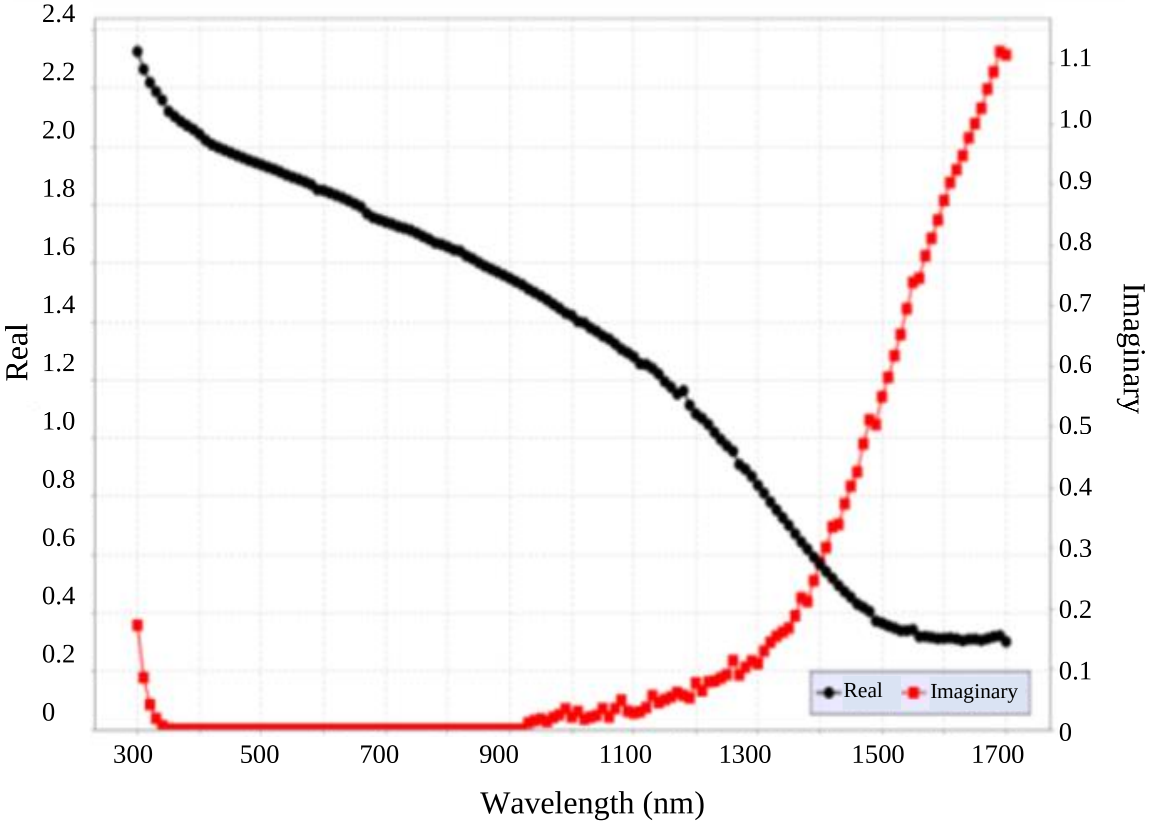

Figure 5.4. Refraction index of ITO.

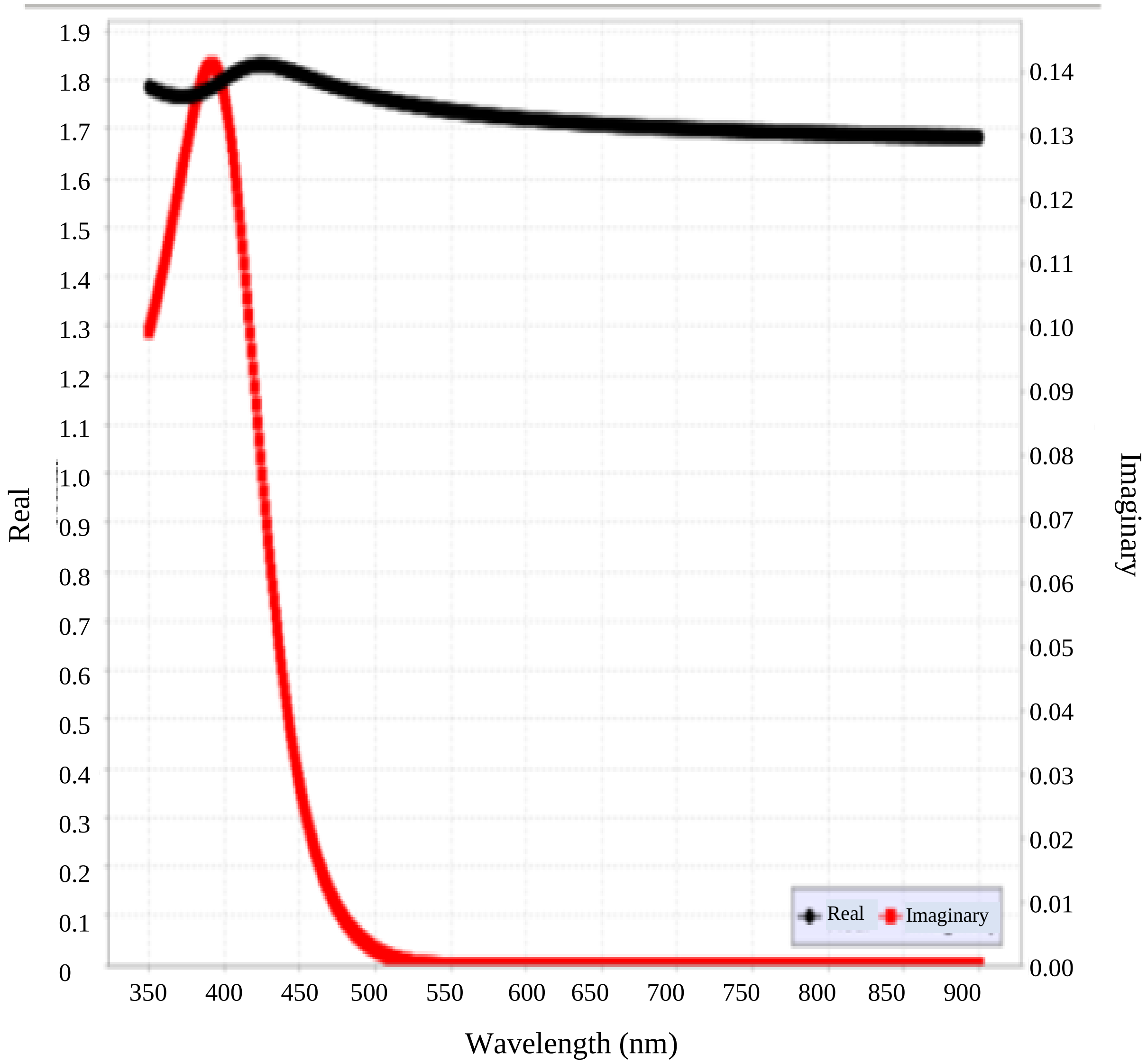

Figure 5.5. Refraction index of Alq3.

5.4 ELECTRICAL PROPERTIES OF AN ITO/ALQ3/AL OLED STRUCTURE IN SETFOS FLUXIM

The electrical properties of an ITO/Alq3/Al OLED was investigated in Setfos Fluxim. The Alq3 layer was made thicker than in previous simulations for testing purposes. The energy level diagram of the OLED structure in shown in Figure 5.6. The electrical properties of a structure with more than 3 layers cannot be simulated in the free version of the Setfos Fluxim simulation environment.

Table 5.4. Refraction index of materials at 540 nm and the layer that the material can be used for.

Material	Layer	Refractive index (n)
Ag	Cathode	0.12 + i0.8
Au	Cathode	0.4 + i2.5
Cu	Cathode	0.3 + 10.5j
Alpha-NPD	HTL	1.08 + i3.5E-9
Alq	EML	1.75 + i0
Alq3	EML	1.74 + i0
LiF	EML	1.4 + i0.76
ZnO	EML	2 + i0
ZnS	EML	2.4 + i0.17
PEDOT Bayron CH8000	HIL	1.53 + i0.46
ITO	Anode	1.9 + i0

The current transient, transfer curve and electrical power density of the ITO/Alq3/Al OLED structure is shown in Figure 5.7, Figure 5.7 and Figure 5.8 respectively and can be used to calculate the electric field across the structure. The relationship between the electric field (E), applied voltage (V) and layer thickness (L) can be expressed as shown in (5.1) [72].

$$E = \frac{V}{L} \tag{5.1}$$

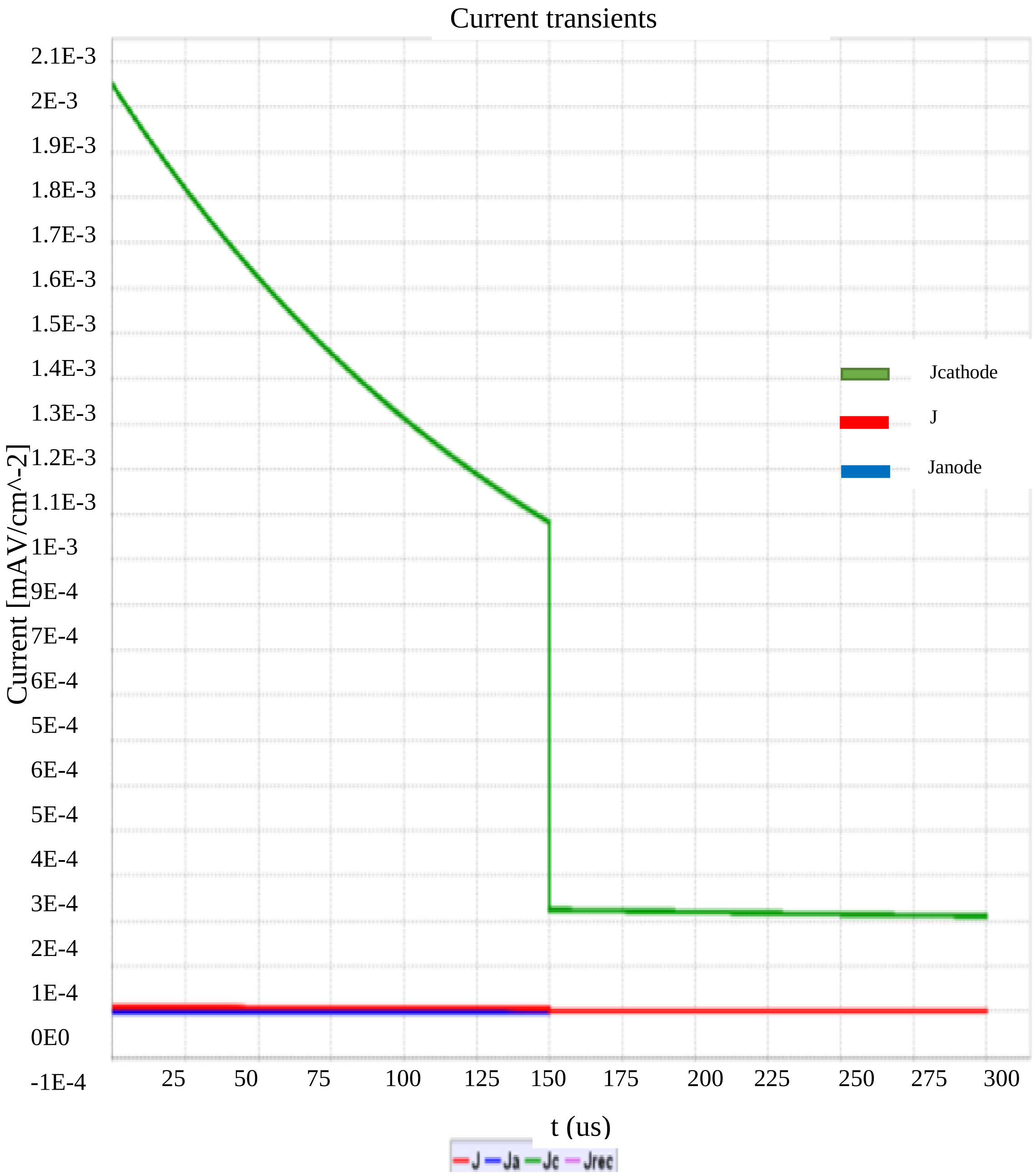

Figure 5.7. Current transient plot of an ITO/Alq3/Al OLED structure.

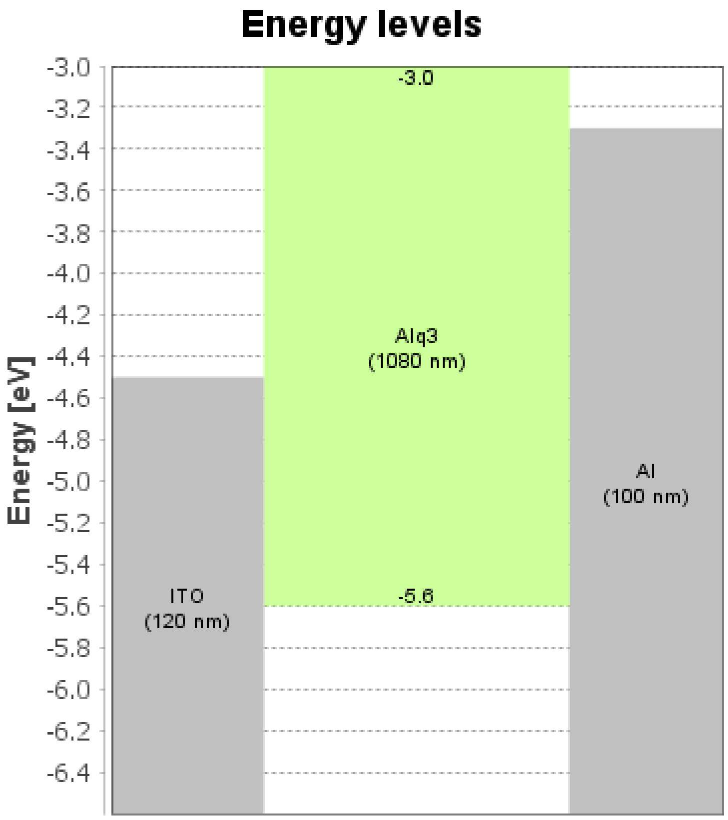

Figure 5.66. Energy level diagram of an ITO/Alq3/Al OLED structure.

5.5 ITO/PEDOT:PSS/ALPHA-NPD/ALQ3/ALO SIMULATION

The OLED from literature as seen in Figure 5.1 was simulated in Setfos Fluxim simulation software, with the same materials and layer thickness as described in literature [66]. The layer thicknesses and materials of the OLED that was setup in the software is shown in Figure 5.9 and Figure 5.10**.**

The emission spectrum of the ITO/PEDOT:PSS/Alpha-NPD/Alq3/Al OLED that was simulated in Setfos Fluxim is shown in Figure 5.11 and the colour diagram is shown in Figure 5.12**.** It can be seen in Figure 5.12 that the dominant wavelength of the OLED is 557 nm. This will give rise to a yellow-green light emission (Table 5.5).

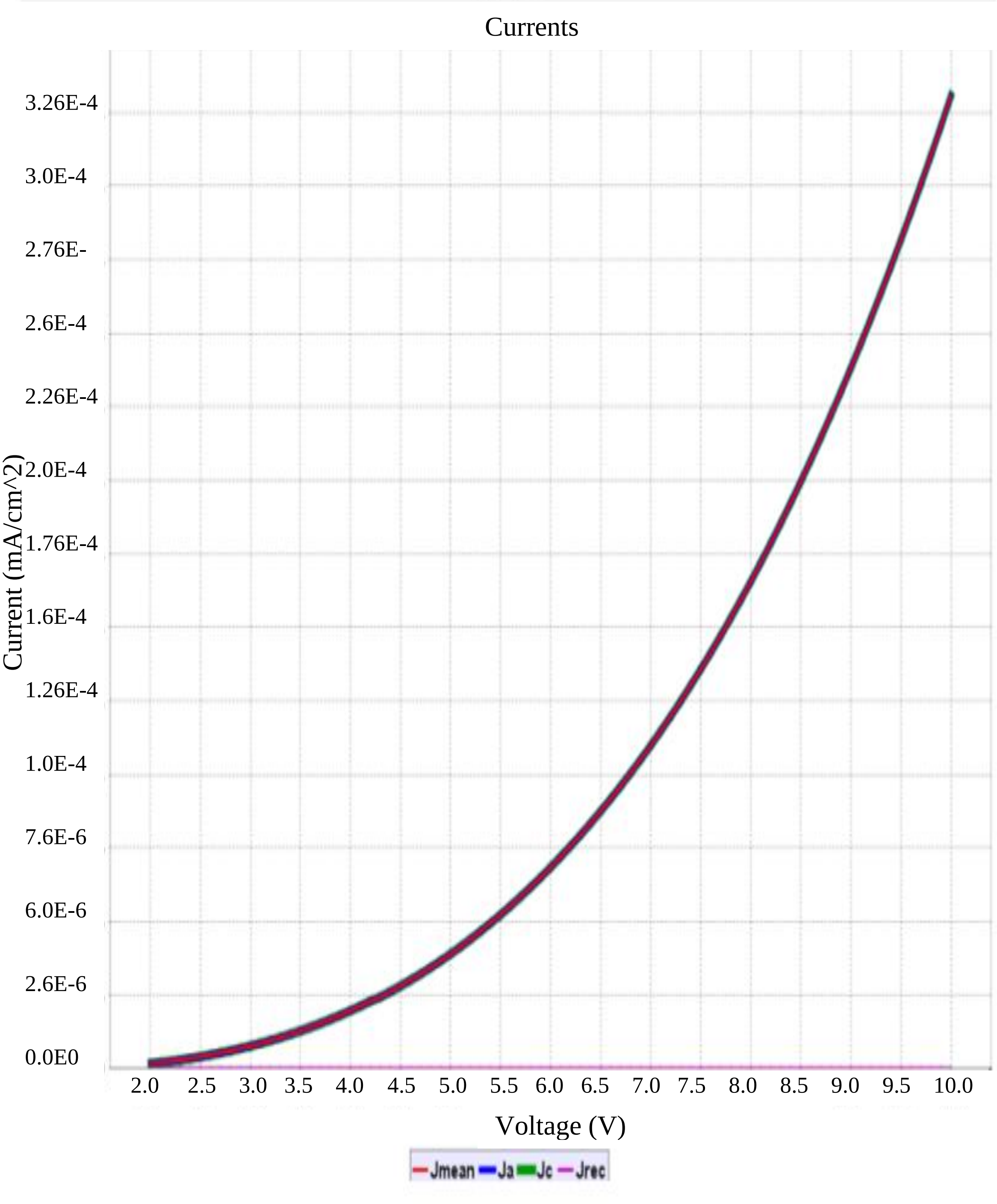

Figure 5.7. Transfer curve of an ITO/Alq3/Al OLED structure.

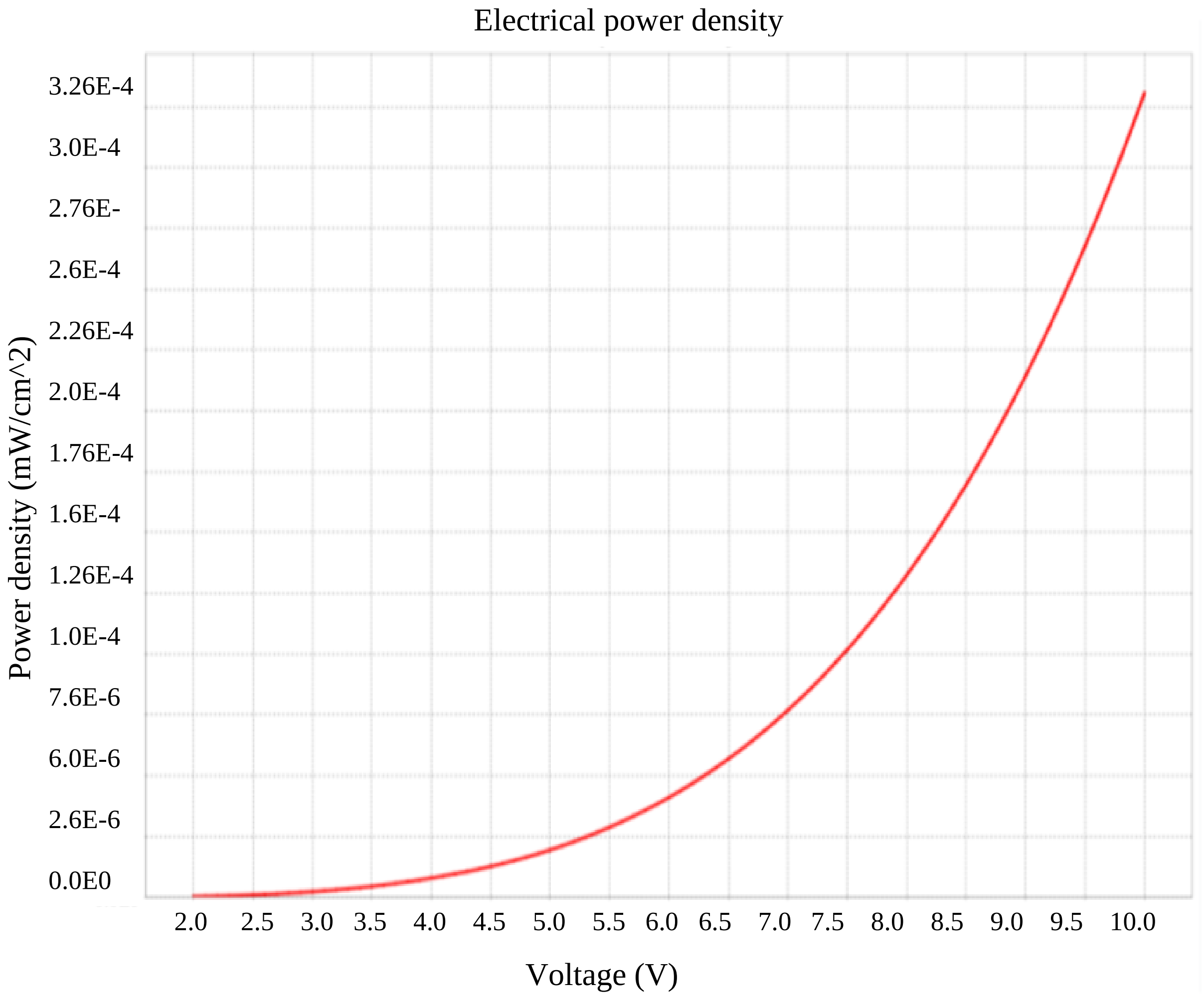

Figure 5.8. Electrical power density versus applied voltage of an ITO/Alq3/Al OLED structure

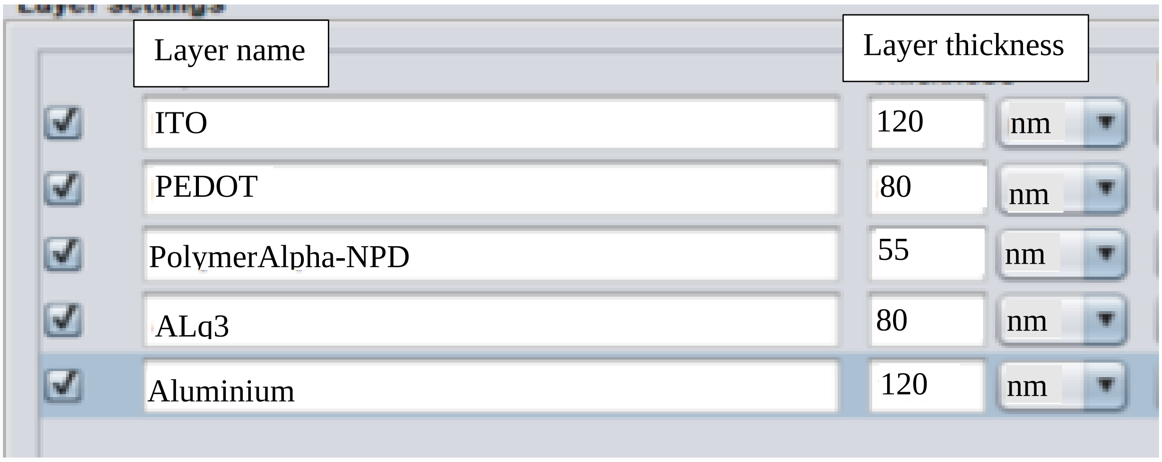

	Layer name	Layer thickness	
☑	ITO	120	nm
☑	PEDOT	80	nm
☑	PolymerAlpha-NPD	55	nm
☑	ALq3	80	nm
☑	Aluminium	120	nm

Figure 5.9. Layer setup in Setfos Fluxim for an ITO/PEDOT:PSS/Alpha-NPD/Alq3/AlO.

5.5.1 Effect of HTL and HIL layer

The ITO/PEDOT:PSS/Alpha-NPD/Alq3/Al OLED that is shown in Figure 5.10 was simulated with and without the HTL and HIL layers and their emission characteristics that their dominant wavelengths are compared in Table 5.5. Figure 5.11 illustrates the p-polarized (green), s-polarized (blue) and total light emission (red). The simulated plots of the OLEDs emission characteristics are given in addendum G.

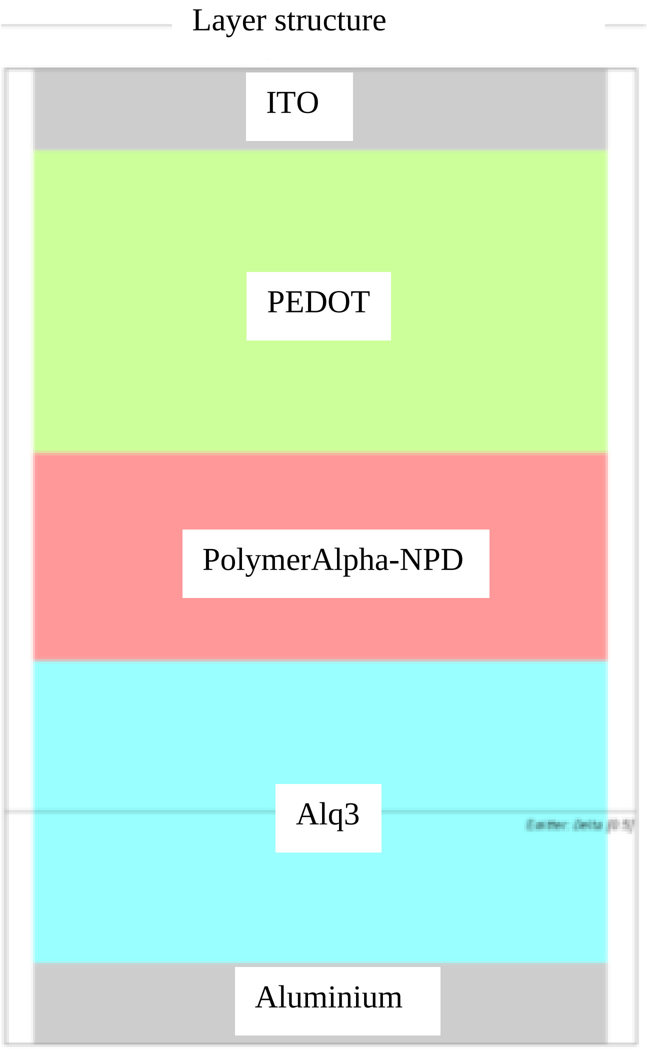

Figure 5.10. Illustration of the ITO/PEDOT:PSS/Alpha-NPD/Alq3/Al OLED in Setfos Fluxim.

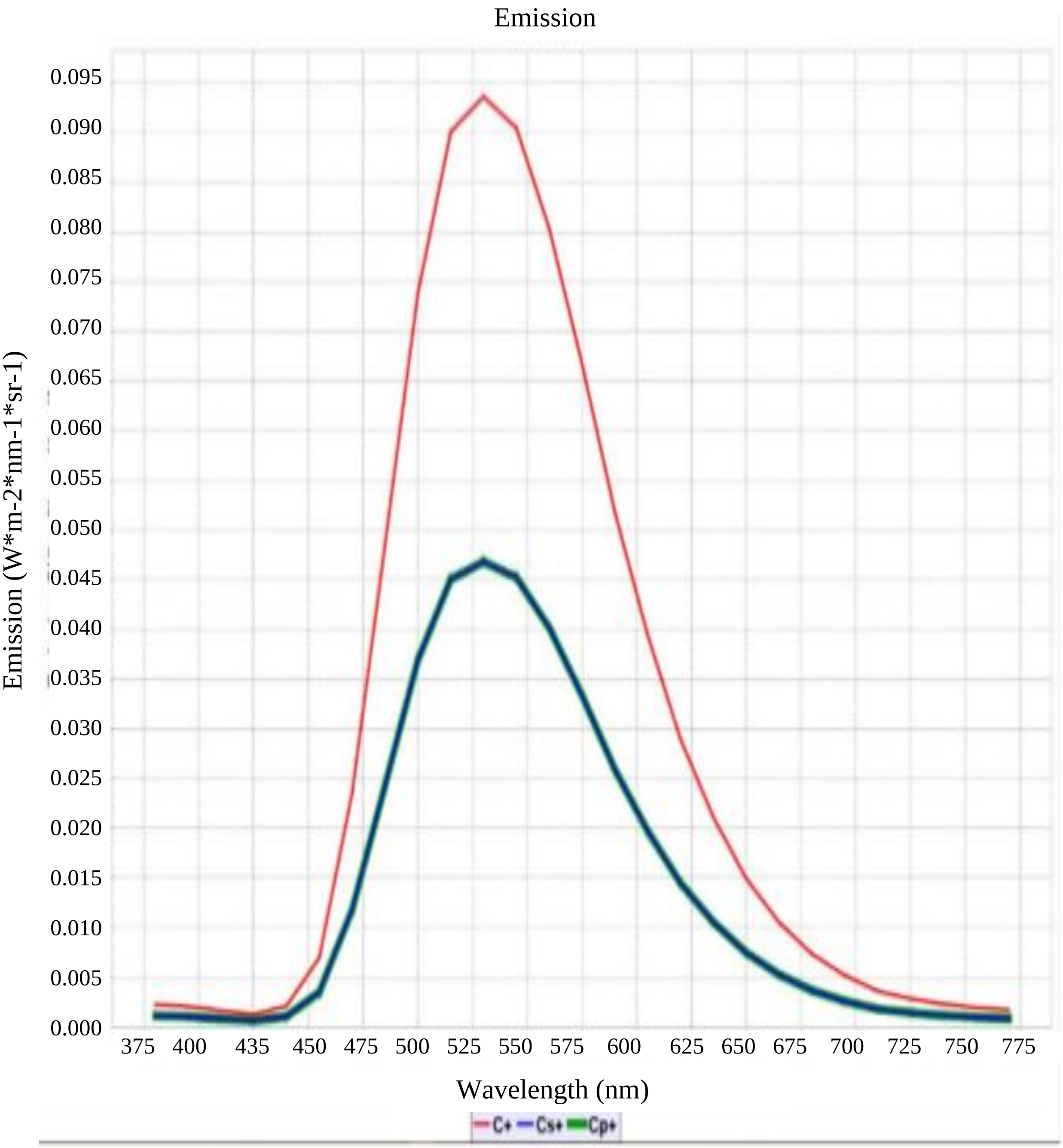

Figure 5.11. Light emission spectrum of ITO/PEDOT:PSS/Alpha-NPD/Alq3/Al OLED.

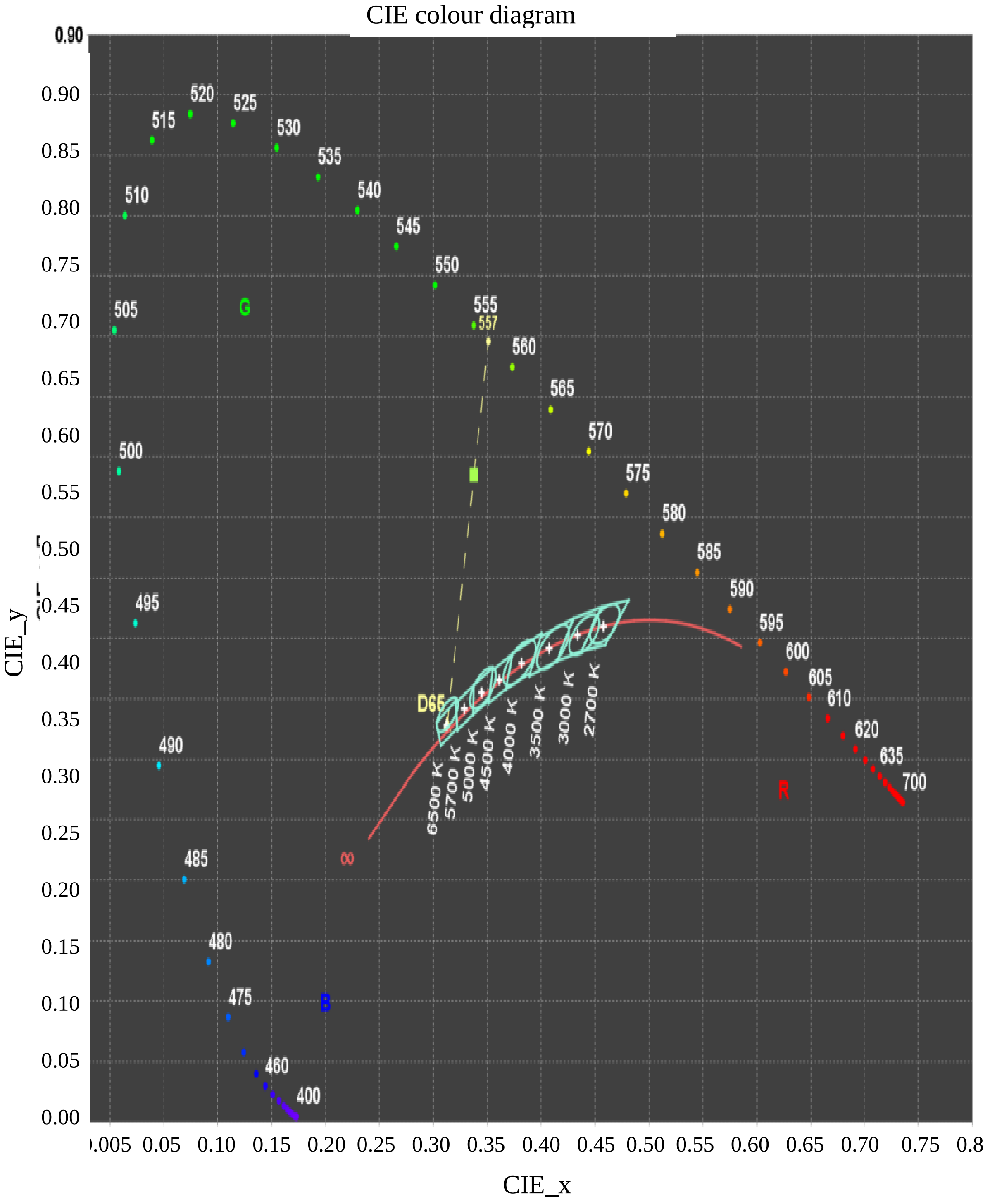

Figure 5.12. Colour diagram of a Light emission spectrum of ITO/PEDOT:PSS/AlphaNPD/Alq3/Al OLED.

It can be seen from Table 5.5 that the light emission at the dominant wavelength increases by 30.77 % when HIL and HTL layers are added to the OLED structure. Although the absorbance of the OLED increases when the HIL and HTL is added, the reflectance decreases. It can also be seen that the exciton density of the OLED increases. The added HIL and HTL also increases the dominant wavelength by 3 nm which will cause the emitted light to be slightly more yellow in colour.

Table 5.5. Electrical properties of an ITO/Alq3/Al and ITO/PEDOT/Alpha-NPD/Alq3/Al OLED at its dominant wavelength.

Property	**ITO/ALQ3/AL**	**ITO/PEDOT/ALPHANPD/ALQ3/AL**
Dominant wavelength	554 nm	557 nm
Emission	0.065 $Wm^{-2}nm^{-1}sr^{-1}$	0.085 $Wm^{-2}nm^{-1}sr^{-1}$
Absorbance	0	0.0119
Reflectance	0.949	0.884
Transmittance	0.056	0.104
White emission	2.15E-2 $Wm^{-2}nm^{-1}sr^{-1}$	0.0275 $Wm^{-2}nm^{-1}sr^{-1}$
Exciton density	7.5E20 m^{-3}	1.55E21 m^{-3}
Radiating dipole density	1.55E29 $m^{-3}s^{-1}$	1.55E29 $m^{-3}s^{-1}$
Radiative rate profile	2.5E8 s^{-1}	1E8 s^{-1}

5.5.2 Electrical properties of ITO/PEDOT:PSS/NPB/Alq3/Al in GPVDM.

The electrical properties of OLED structures, with more than 3 layers, can be simulated in GPVDM. GPVDM does not however have an alpha-NPD material that was used as the HTL in the previous simulation of the device in Figure 5.1 [66]. In Table 2.4, however, it can be seen that NPB [65], TPD, PC [59] and α-NPD [66] can be used as the HTL in devices that have PEDOT:PPS HIL. Alpha-NPD was therefore substituted with NPB for the HTL layer in the OLED for the GPVDM simulations. The layer setup is shown in Figure 5.13 and the material parameters that can be edited in GPVDM is shown in Figure 5.14.

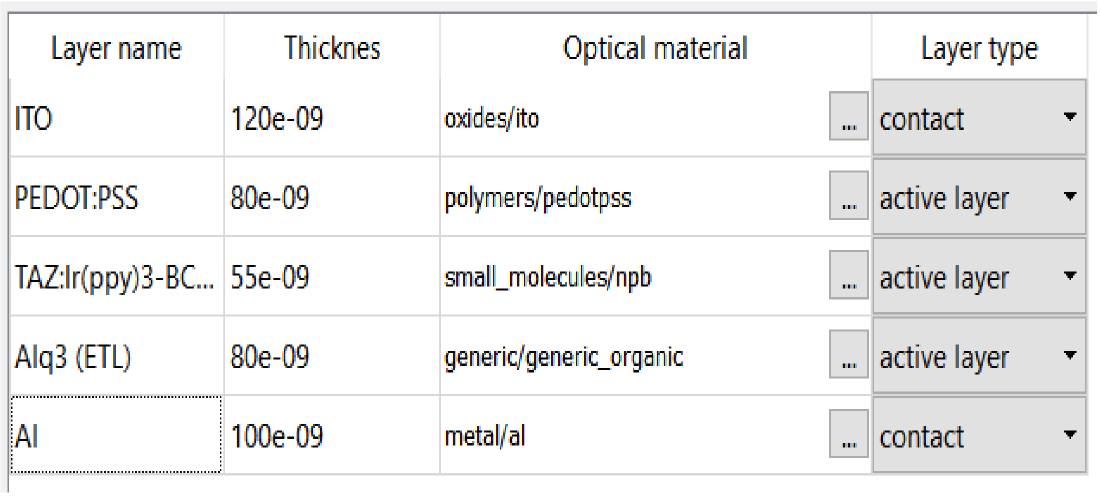

Layer name	Thicknes	Optical material	Layer type
ITO	120e-09	oxides/ito ...	contact
PEDOT:PSS	80e-09	polymers/pedotpss ...	active layer
TAZ:Ir(ppy)3-BC...	55e-09	small_molecules/npb ...	active layer
Alq3 (ETL)	80e-09	generic/generic_organic ...	active layer
Al	100e-09	metal/al ...	contact

Figure 5.13. Layer setup in GPVDM.

5.6 ELECTRICAL PROPERTIES OF OLEDS WITH DIFFERENT CATHODE MATERIALS IN GPVDM

The OLED from literature [66] (Figure 5.1) was simulated with an aluminium, gold and silver anode. Aluminium is not inkjet printable, while gold and silver nanoparticles inks are. The simulated OLED structures that illustrate the light beams emitted from the device are shown in Figure 5.15, Figure 5.16 and Figure 5.17 respectively. The internal light reflections at the interfaces between layers can also be seen in the diagrams. It can be seen that less light is emitted in a narrower beam when a silver anode is used and the most light is emitted with the largest beam width when an aluminium anode is used.

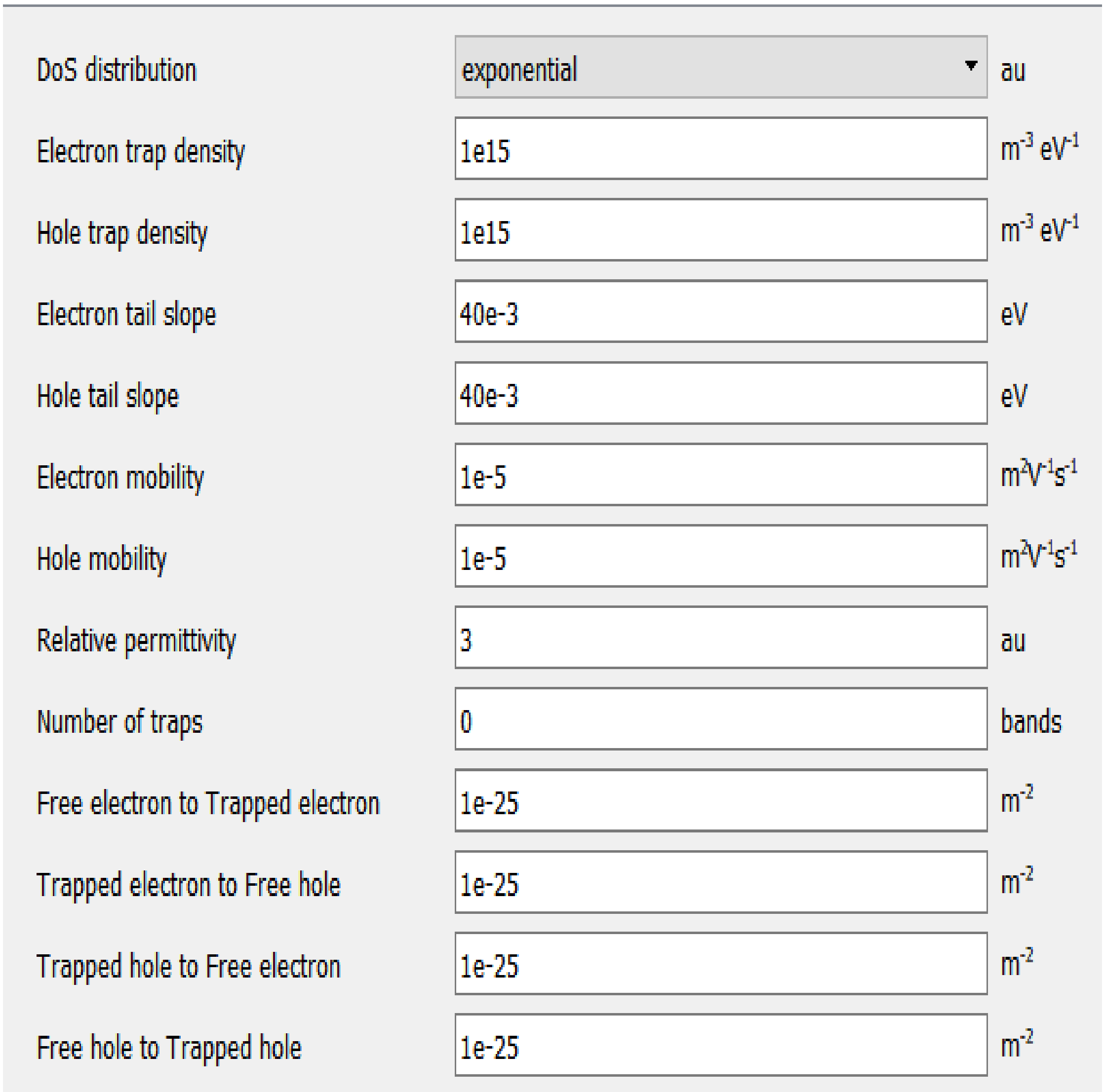

DoS distribution	exponential	au
Electron trap density	1e15	m^{-3} eV^{-1}
Hole trap density	1e15	m^{-3} eV^{-1}
Electron tail slope	40e-3	eV
Hole tail slope	40e-3	eV
Electron mobility	1e-5	$m^2V^{-1}s^{-1}$
Hole mobility	1e-5	$m^2V^{-1}s^{-1}$
Relative permittivity	3	au
Number of traps	0	bands
Free electron to Trapped electron	1e-25	m^{-2}
Trapped electron to Free hole	1e-25	m^{-2}
Trapped hole to Free electron	1e-25	m^{-2}
Free hole to Trapped hole	1e-25	m^{-2}

Figure 5.14. Material property editor in GPVDM.

5.7 LAYER MATERIAL OPTIMIZATION FOR LIGHT EMISSION

The electrical properties of the OLEDs with the aluminium, gold and silver anodes are shown in Tables 5.6, 5.7 and 5.8, respectively.

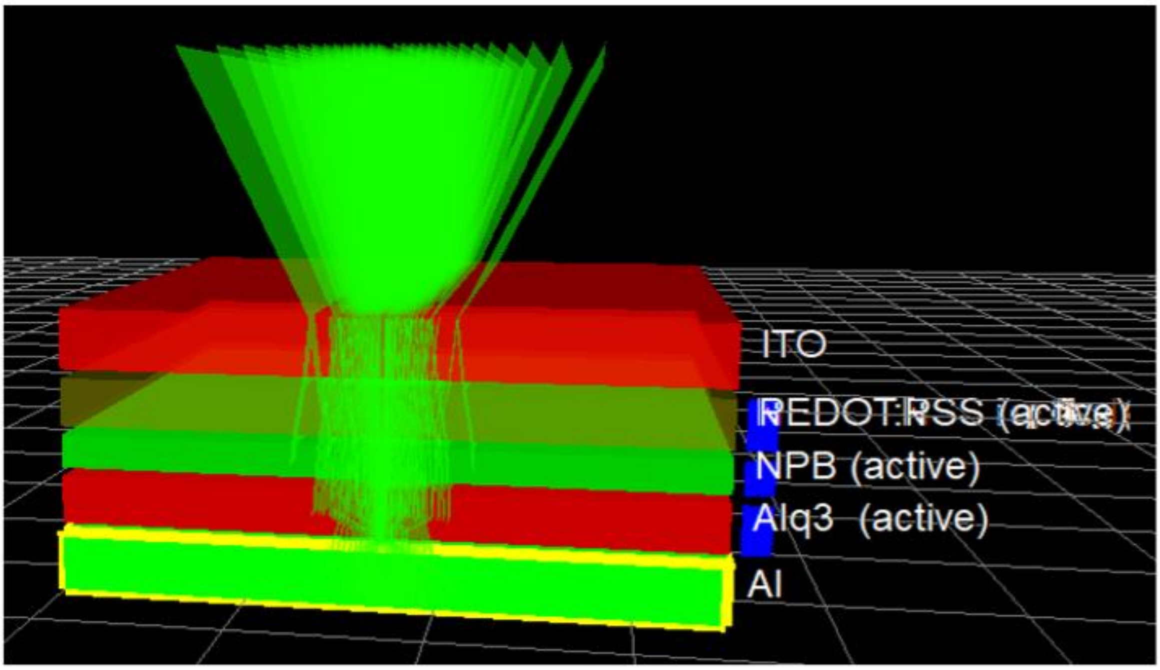

Figure 5.15. Light emission of an Al/Alq3/BCP/PEDOT:PSS/ITO OLED.

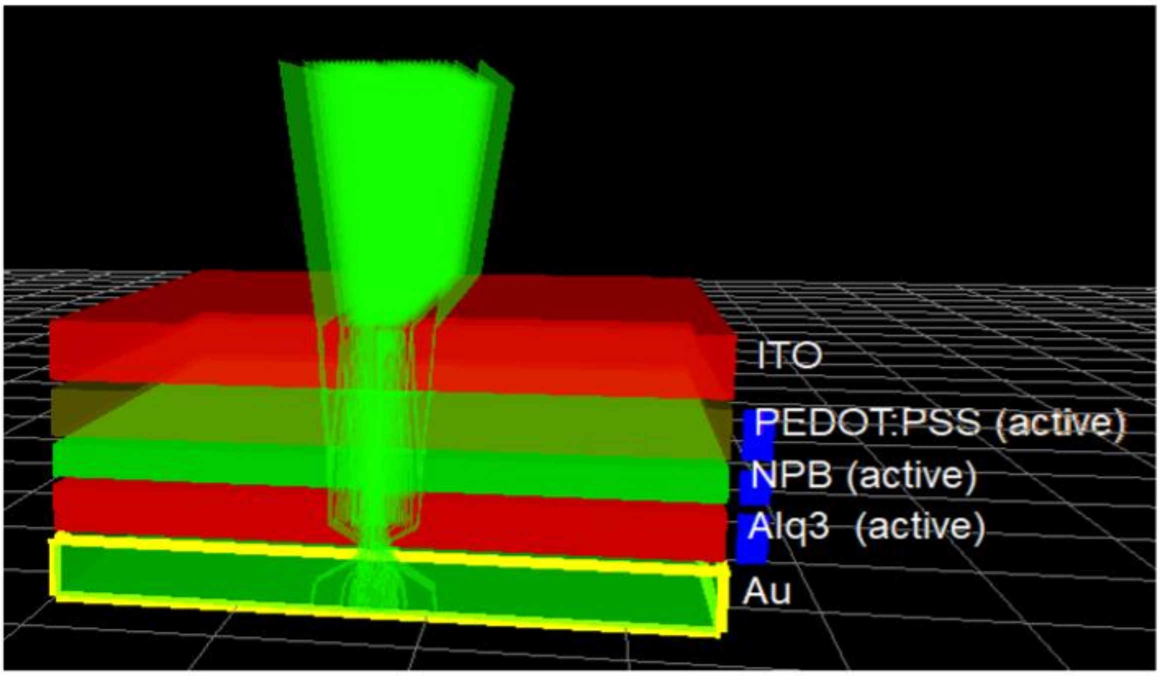

Figure 5.16. Light emission of an Au/Alq3/BCP/PEDOT:PSS/ITO OLED.

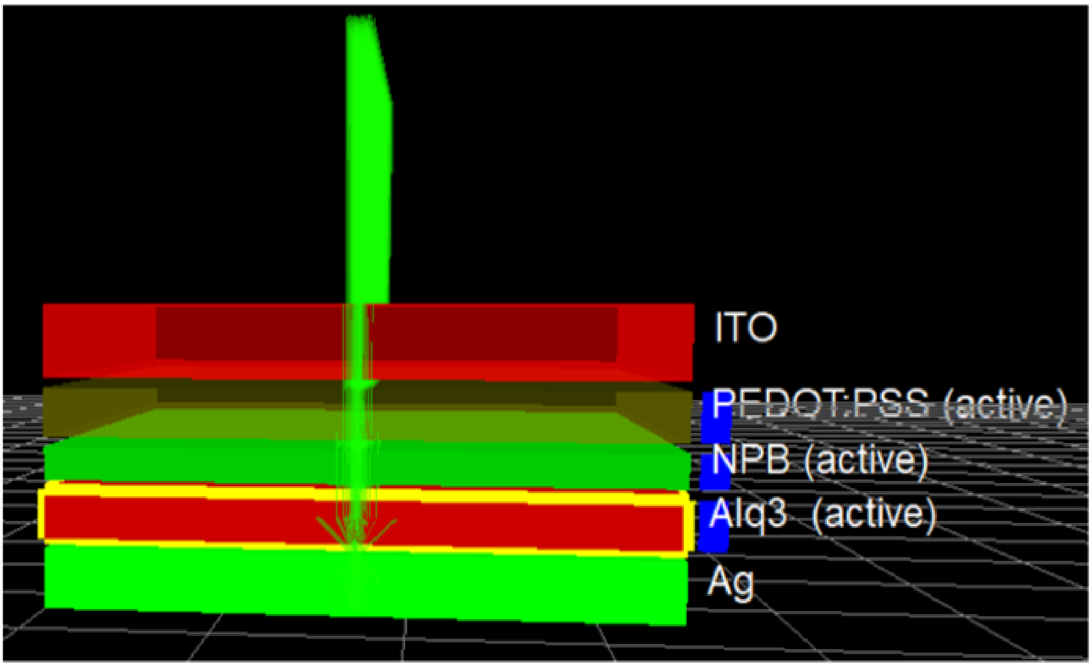

Figure 5.17. Light emission of an Ag/Alq3/BCP/PEDOT:PSS/ITO OLED.

Table 5.6. Al/Alq3/BCP/PEDOT:PSS/ITO

Voltage (V)	**Current (A)**	**Charge density (m^{-3})**	**Current density ($A\ m^{-3}$)**	**Light Flux ($W\ m^{-3}$)**
0	0	0	0	0
0.5	0	2.23E21	0	0
1	0	4.88E21	0	0
1.5	0	6.89E21	0	0
2	0	9.86E21	0	0
2.5	0	1.6E22	0	0
3	0	2.54E22	0	0
3.5	2.89E-8	3.51E22	0.018	3.31E-11
4	2.94E-7	4.45E22	0.025	8.61E-11
4.5	3.00E-6	5.50E22	0.260	10.00E-10
5	2.97E-5	6.42E22	2.471	9.17E-9

Table 5.7. Au/Alq3/BCP/PEDOT:PSS/ITO

Voltage (V)	**Current (A)**	**Charge density (m^{-3})**	**Current density (A m^{-3})**	**Light Flux (W m^{-3})**
0	0	0	0	0
0.5	0	2.35E21	0	0
1	0	4.67E21	0	0
1.5	0	6.47E21	0	0
2	0	1.03E22	0	0
2.5	0	1.52E22	0	0
3	0	2.49E22	0	0
3.5	2.97E-7	3.65E22	0.021	3.50E-12
4	2.38E-7	4.49E22	0.024	9.00E-11
4.5	1.99E-6	5.41E22	0.204	8.31E-10
5	2.99E-5	6.45E22	2.477	7.57E-9

Table 5.8. Ag/Alq3/BCP/PEDOT:PSS/ITO

Voltage (V)	**Current (A)**	**Charge density (m^{-3})**	**Current density (A m^{-3})**	**Light Flux (W m^{-3})**
0	0	0	0	0
0.5	0	2.63E21	0	0
1	0	5E21	0	0
1.5	0	7.87E21	0	0
2	0	1.00E22	0	0
2.5	0	1.79E22	0	0
3	0	2.70E22	0	0
3.5	2.97E-7	3.53E22	0.015	1.29E-11
4	2.38E-7	4.61E22	0.025	2.15E-11
4.5	1.99E-6	5.84E22	0.257	1.48E-10
5	2.99E-5	6.51E22	2.467	1.42E-9

5.8 LAYER THICKNESS OPTIMIZATION FOR LIGHT EMISSION

Aluminium is not inkjet printable, while gold and silver nanoparticles inks are. Since silver nanoparticle ink is inkjet printable [110], readily available and the cheapest nanoparticle ink, the aluminium anode was replaced with a silver anode for further simulation purposes. The ITO/PEDOT:PSS/Alpha-NPD/Alq3/Ag OLED with the silver anode layer thicknesses was optimized using the Setfos Fluxim, layer thickness optimizer. The layer thickness was optimized layer by layer for optimal radiance and light emission. The optimized layer thicknesses are summarized in Table 5.9 and the emission characteristics of the OLED structure before and after layer optimization is summarized in Table 5.10. The simulated plots are given in addendum G. It can be seen in Table 5.10 that by optimizing the layer thicknesses of the OLED structure, the light emission increases by 57.84 %. The dominant wavelength also decreases by 8 nm, which means that the OLED with the optimized layer thickness will be slightly greener than the original yellow-green OLED structure.

Table 5.9. ITO/PEDOT:PSS/ALPHA-NPD/ALQ3/AG OLED optimized layer thicknesses.

Layer	Materials	Original layer thickness (nm)	Optimized layer thickness (nm)
Cathode	Ag	100	99.99
EML	Alq3	80	177.89
HTL	α-NPD	55	234
HIL	PEDOT:PSS	80	14.47
Anode	ITO	120	99.99

The optimized layer thicknesses for the OLED display with a silver anode (Table 5.9) was implemented and the electrical properties were simulated. The plots of the electrical properties in GPVDM can be seen in addendum G. The light emission of the OLED before and after layer thickness optimization is shown in Figure 5.18.

Table 5.10. ITO/PEDOT:PSS/ALPHA-NPD/ALQ3/AG OLED emission characteristics before and after layer thickness optimization.

Property	Original layer thicknesses	Optimized layer thickness
Dominant wavelength	556 nm	548 nm
Emission	0.102 $Wm^{-2}nm^{-1}sr^{-1}$	0.161 $Wm^{-2}nm^{-1}sr^{-1}$
Absorbance	0.0157	0
Reflectance	0.942	0.937
Transmittance	0.04	0.0635
White emission	0.0325 $Wm^{-2}nm^{-1}sr^{-1}$	0.05175 $Wm^{-2}nm^{-1}sr^{-1}$
Exciton density	1.55E21 m^{-3}	1.55E21 m^{-3}
Radiating dipole density	1.55E29 $m^{-3}s^{-1}$	1.55E29 $m^{-3}s^{-1}$
Radiative rate profile	1E8 s^{-1}	9.5E7 s^{-1}

The electrical properties for the OLED before layer thickness optimization can be seen in Table 5.8 and the OLED with optimized layer thickness can be seen in Table 5.11. It can be seen that the optimized layer thickness OLED display conducts a current at a much lower voltage than the original OLED structure. The current density and light flux (Wm^{-3}) is also less in the optimized OLED, which means that by optimizing the OLED layer thickness, less power can be consumed.

The energy levels and photon density of the OLED before layer optimization can be seen in Table 5.19 and Figure 5.20**.** It can be seen in Figure 5.20 that before layer thickness optimization, many photons are trapped and reabsorbed in the OLED layers before they exit the device. The position -100 nm to 0 nm is the atmosphere region above the OLED display and the positions between 0 and 300 nm is the different layers of the OLED display.

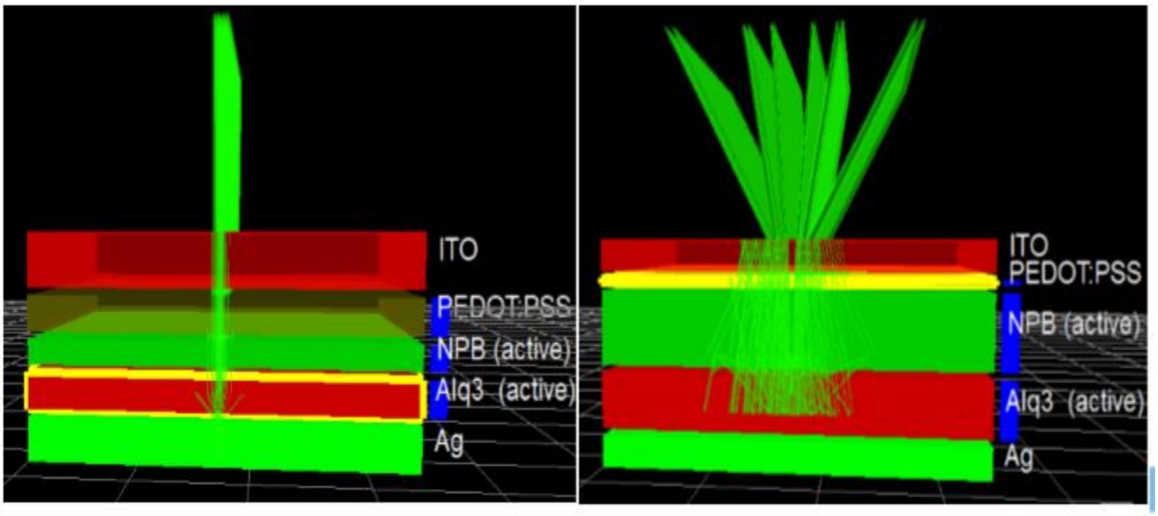

(a) (b)

Figure 5.18. Before and after layer thickness optimization.

(a) Ag/Alq3/BCP/PEDOT:PSS/ITO before layer thickness optimization.

(b) Ag/Alq3/BCP/PEDOT:PSS/ITO after layer thickness optimization.

Table 5.11. Electrical properties of optimized layer Ag/Alq3/BCP/PEDOT:PSS/ITO OLED.

Voltage	**Current (A)**	**Charge density (m^{-3})**	**Current density (Am^{-3})**	**Light Flux (W m^{-3})**
0	0	0	0	0
0.5	1.13E-8	6.37E20	0.0010	0
1	1.35E-8	1.34E21	0.0011	0
1.5	1.50E-8	1.44E21	0.0013	0
2	1.72E-8	2.61E21	0.0014	0
2.5	1.79E-8	3.53E21	0.0015	0
3	1.95E-8	4.75E21	0.0016	0
3.5	2.05E-8	5.80E21	0.0017	9.41E-15
4	2.16E-8	7.19E21	0.0018	2.29E-13
4.5	2.29E-8	8.01E21	0.0019	8.63E-13
5	2.56E-8	9.29E21	0.0021	3.40E-12

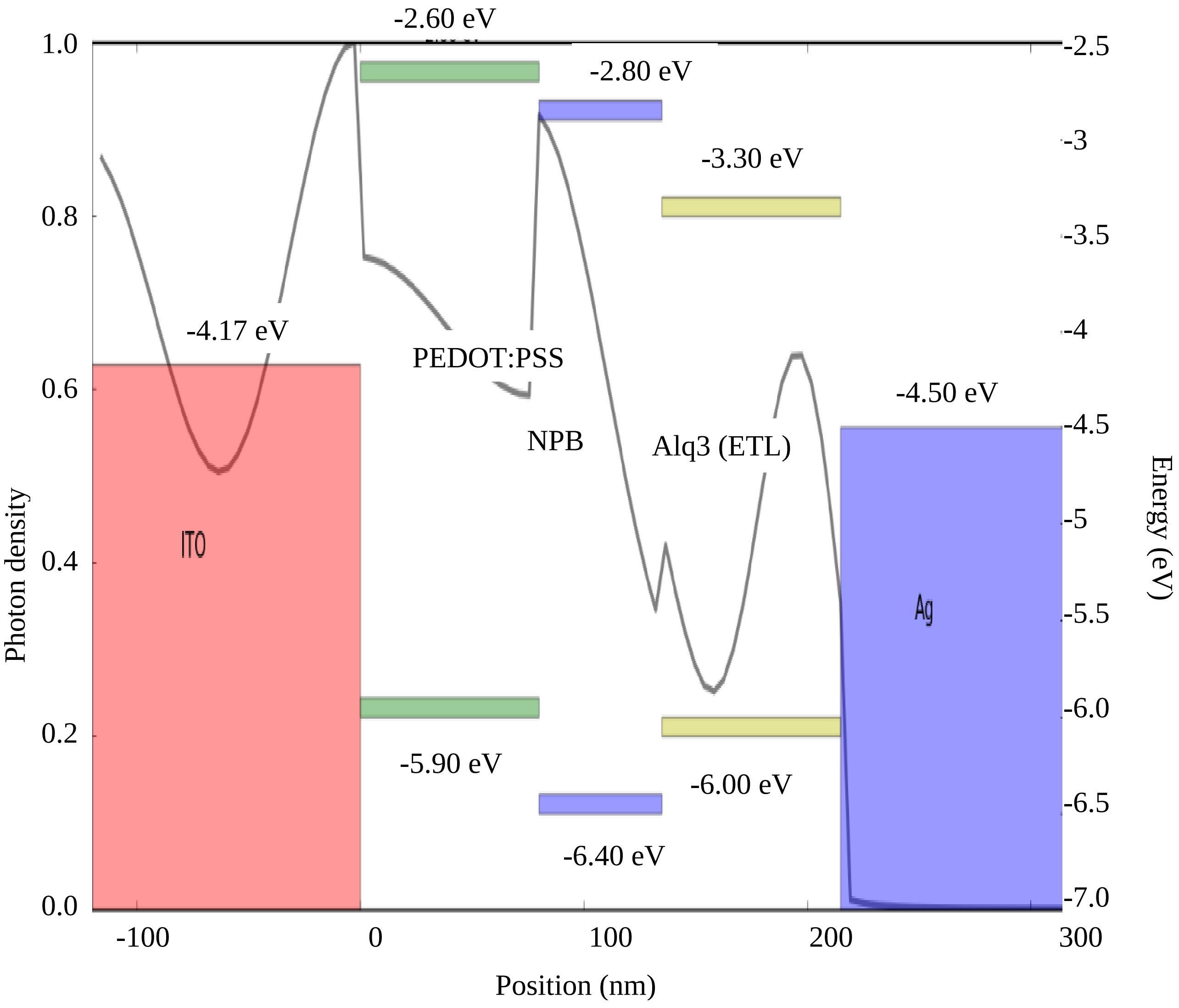

Figure 5.19. Energy levels and photon density of the Ag/Alq3/BCP/PEDOT:PSS/ITO OLED before layer thickness optimization.

The energy levels and photon density of the OLED after optimization can be seen in Figure 5.21 and Figure 5.22. After layer thickness optimization majority of the photons are emitted from the OLED and limited photons are trapped and reabsorbed in the layers of the OLED. The light flux versus current density of the optimized OLED structure is shown in Figure 5.23.

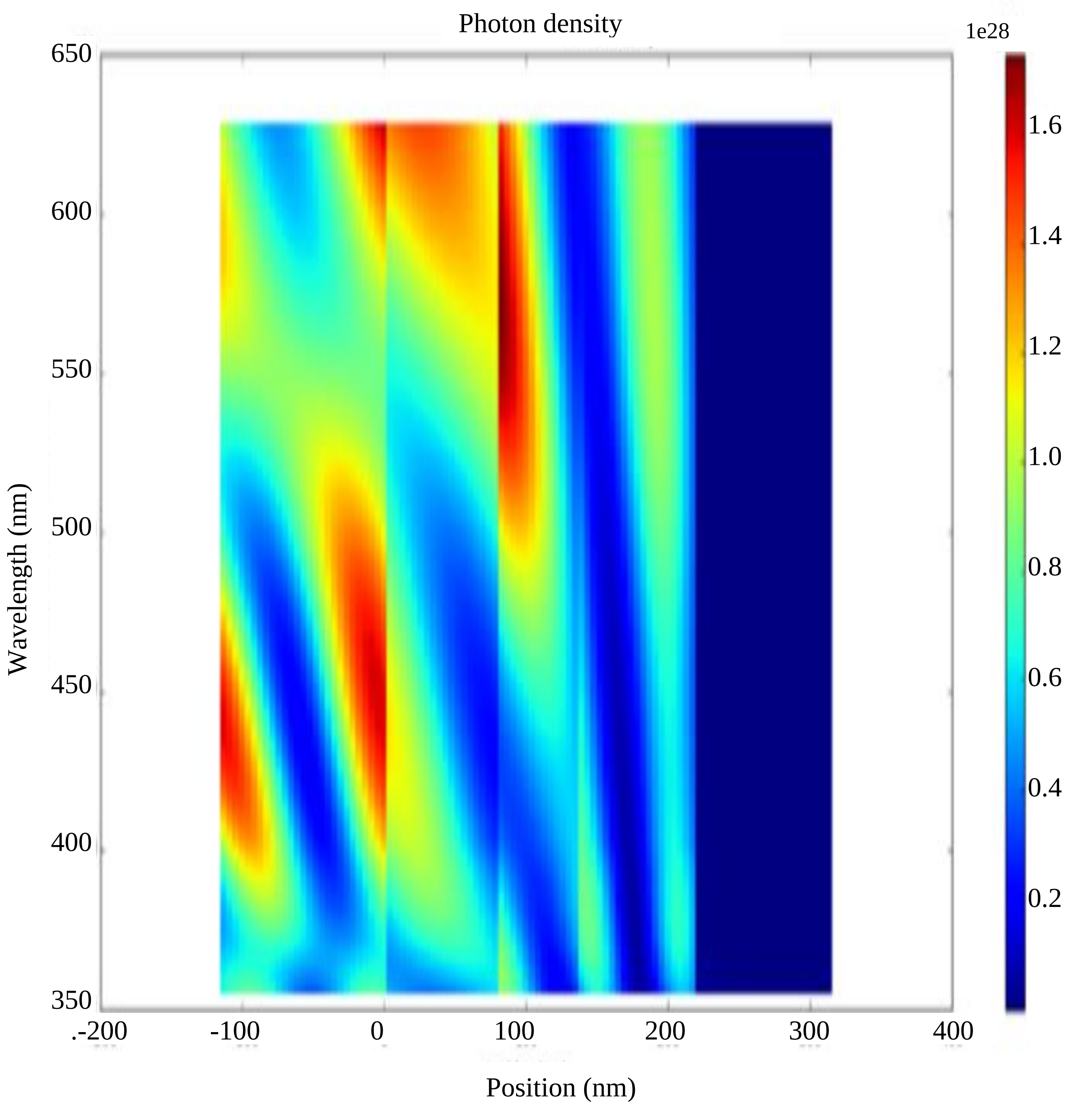

Figure 5.20. Photon density of the Ag/Alq3/BCP/PEDOT:PSS/ITO OLED before layer thickness optimization.

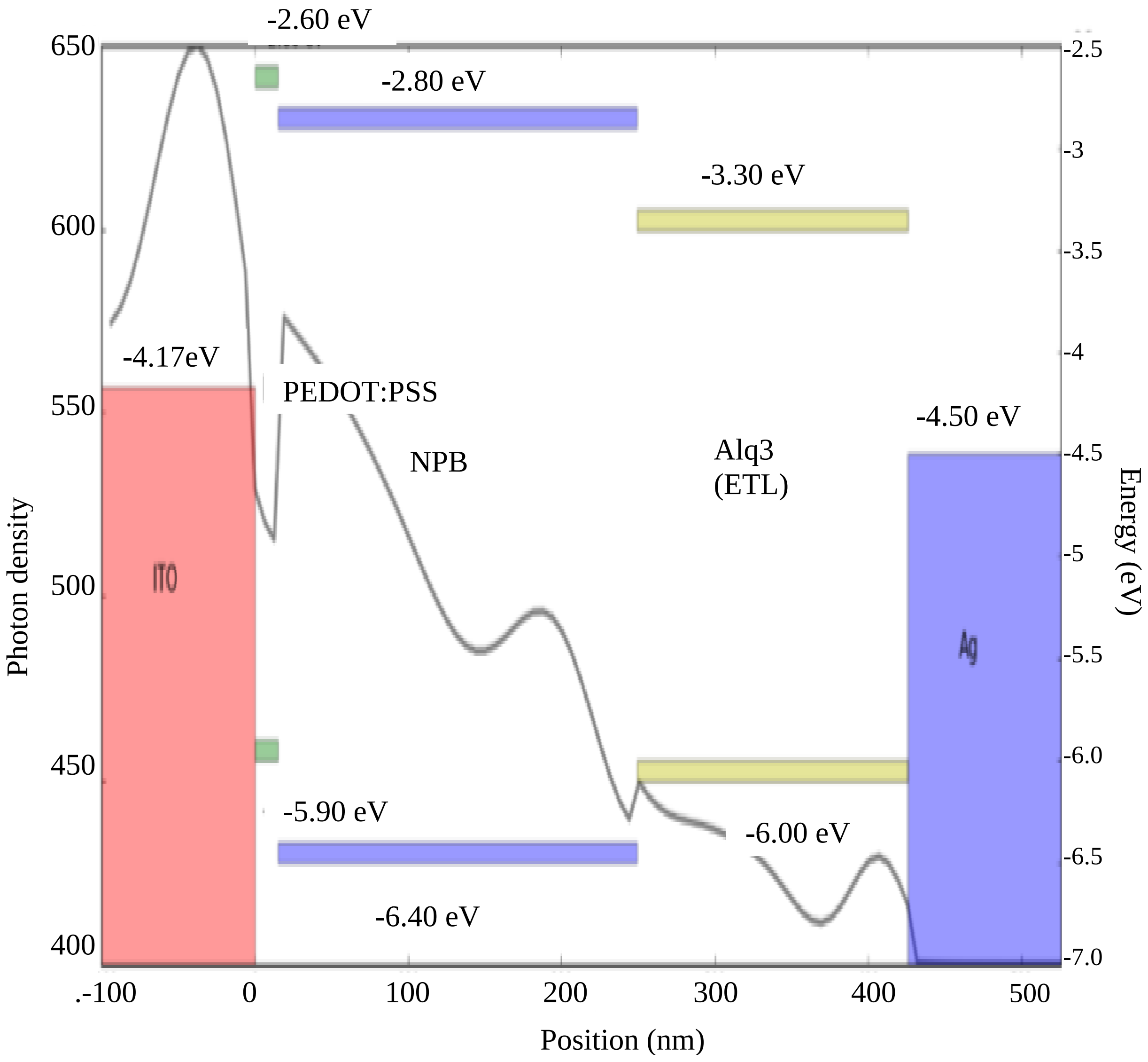

Figure 5.21. Energy levels and photon density of the Ag/Alq3/BCP/PEDOT:PSS/ITO OLED after thickness optimization.

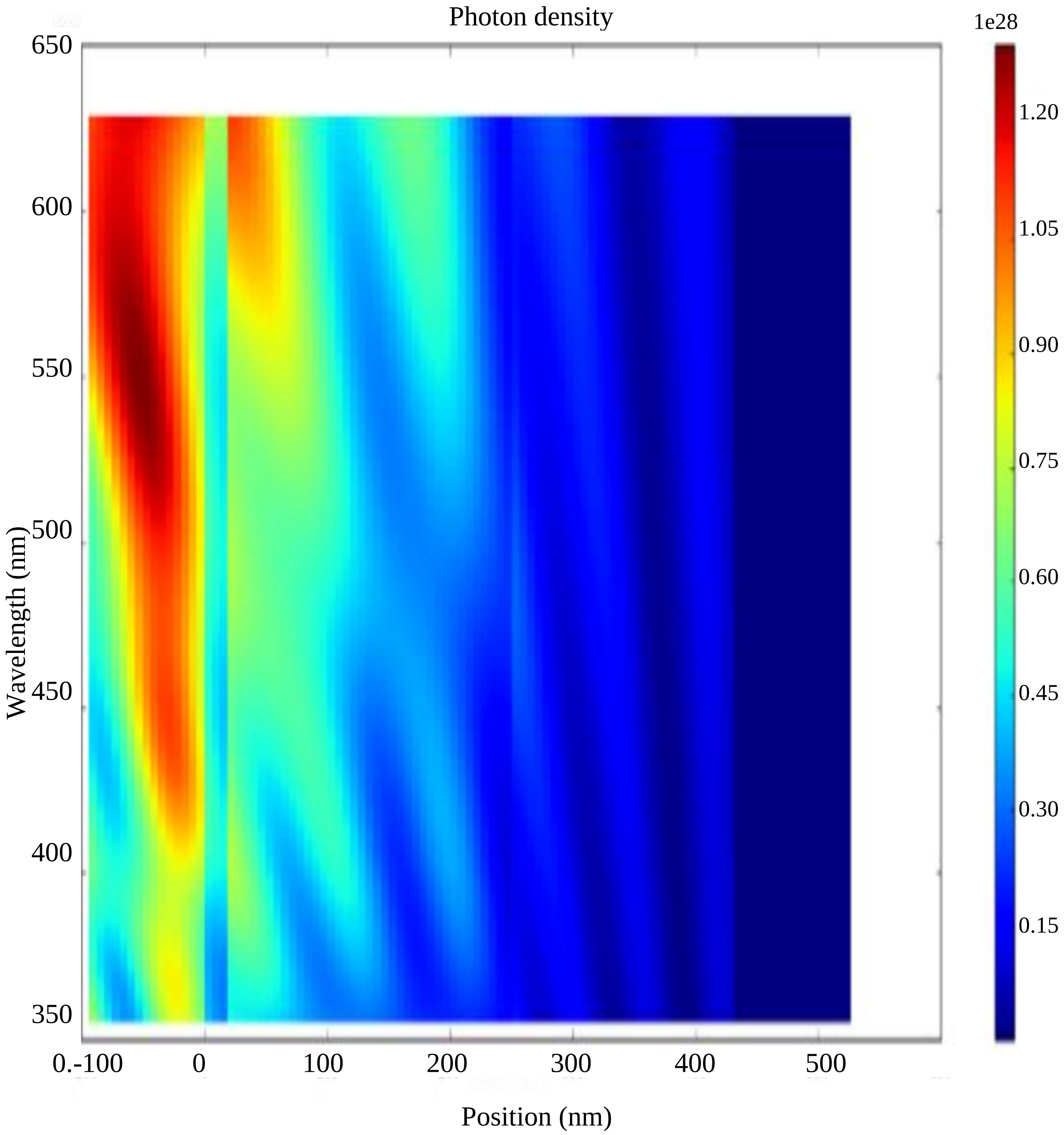

Figure 5.22 Photon density of the Ag/Alq3/BCP/PEDOT:PSS/ITO OLED after layer thickness optimization.

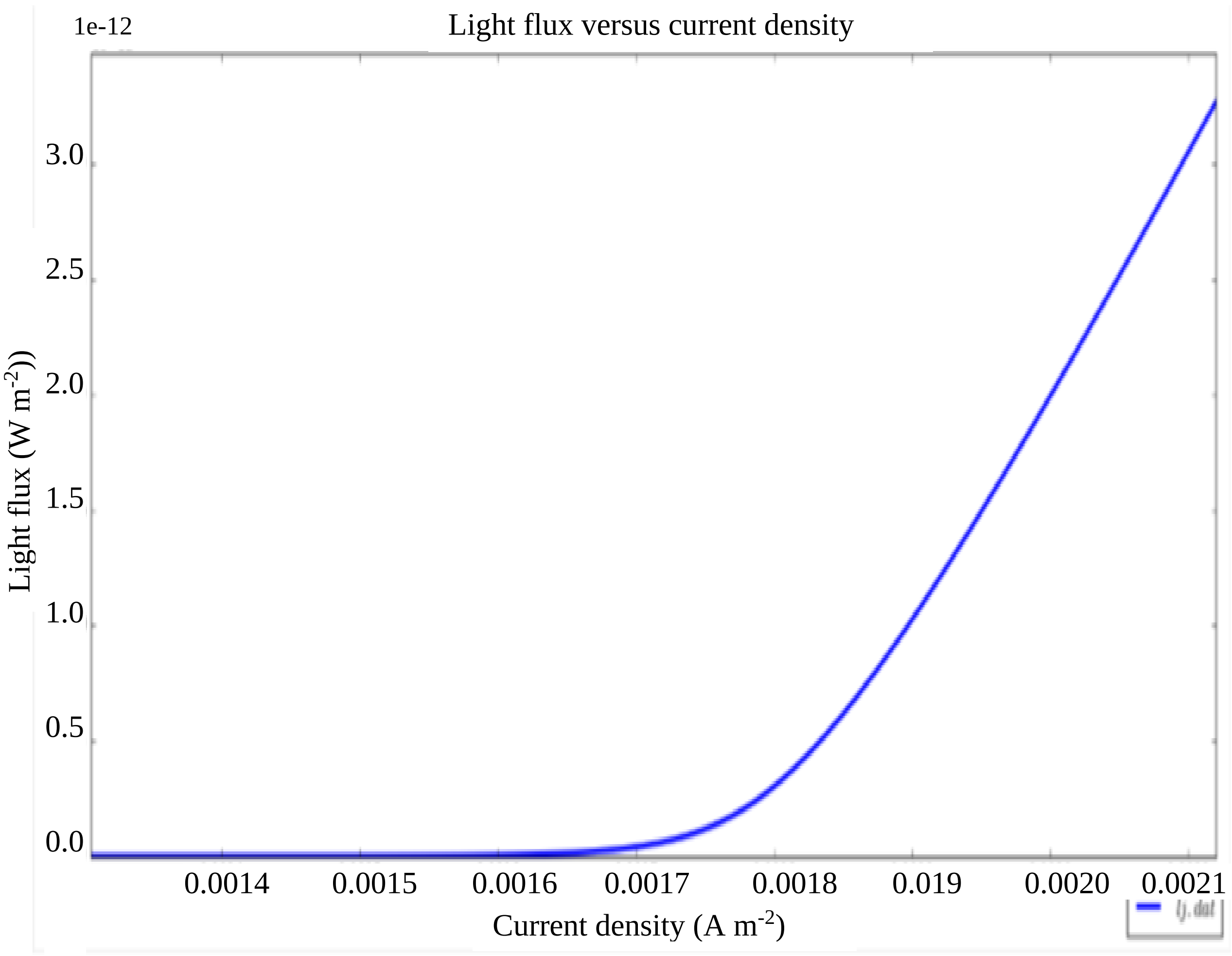

Figure 5.23 Light flux (Wm^{-2}) versus current (Am^{-2}) density of the optimized layer thickness Ag/Alq3/BCP/PEDOT:PSS/ITO OLED.

CHAPTER 6 INKJET PRINTING OF SILVER NANOPARTICLE INK

6.1 CHAPTER OVERVIEW

This chapter describes the inkjet manufacturing techniques for printing silver nanoparticle ink. Silver nano-particle ink can be used as the conductive layer cathode in a printed electronics OLED display.

Although it was not possible to print the entire optimised OLED that is shown in Figure 5.22, due to the cost of inks and the availability of the inkjet printer, only the bottom silver conductive cathode was inkjet printed.

6.2 INKJET PRINTING MANUFACTURING TECHNIQUE

A Fujifilm-Dimatix inkjet printer was used to print the silver cathode. Printing control and curing the ink was a critical aspect of printed electronic manufacturing. The silver cathode to be printed with the Fujifilm-Dimatix inkjet printer was first designed in eMachineShop, which is a free online CAD software. The design was then exported to DesignCAD. In DesignCad the regions where the printer was required to print the ink was hatched. The design was then exported as a DesignCAD file. The file was then converted to a bitmap file using ACE3000, which is a file conversion software. The bitmap file could then be opened in the printers Drop Manager software, where the required printer settings for the design could be set. The process followed to convert an eMachineShop design to a format compatible with the Fujifilm-Dimatix printer is illustrated in a flow chart in Figure 6.1.

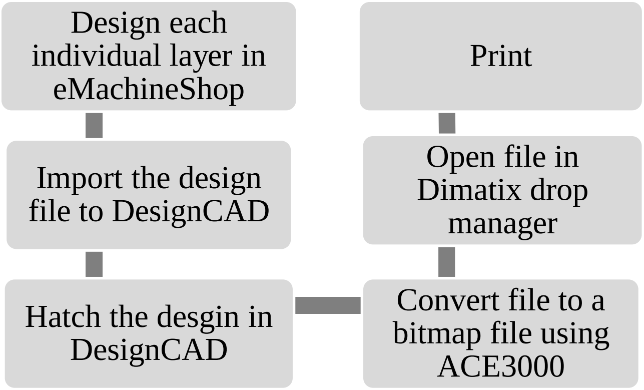

Figure 6.1. Diagram of the file conversion from eMachineShop to the Dimatix Drop Manager.

NPS-J Harima silver conductive ink was used to print the silver conductive cathode and it was cured in an oven, once printed. The silver conductive layer was printed with a drop spacing of 20 μm and with a printer plate temperature of 30 °C.

The printer height was set to 1200 mm above the surface of the substrate. At this height, the drops were seen to print in uniform lines. If the height was set too high or the voltage applied across the piezo element of the printer was too high, satellite droplets formed around the line being printed were seen, as shown in Figure 6.2. Before printing, the drop formation was also checked in the drop watcher to ensure that the nozzle used for printing was not blocked. An image illustrating a drop forming correctly from the nozzle is illustrated in Figure 6.3. A test line was always printed before printing the design to ensure that the printers set up was correct.

NPS-J Harima silver printing procedure:

1. Take the ink out of the fridge where it is stored.
2. Place the ink on an ultrasonic vibrator at room temperature for 2 hours to ensure that the ink is well mixed before printing.

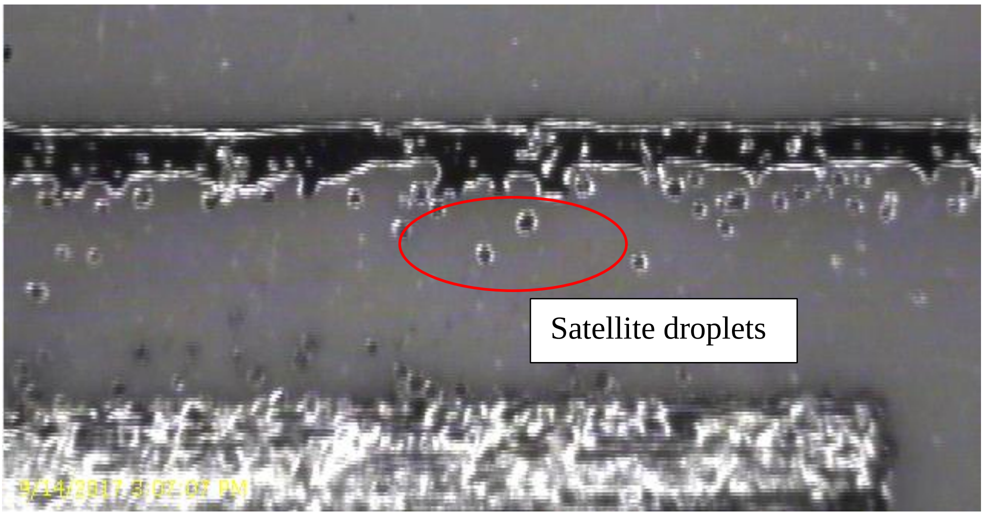

Figure 6.2. Fiducial camera image illustrating satellite droplets.

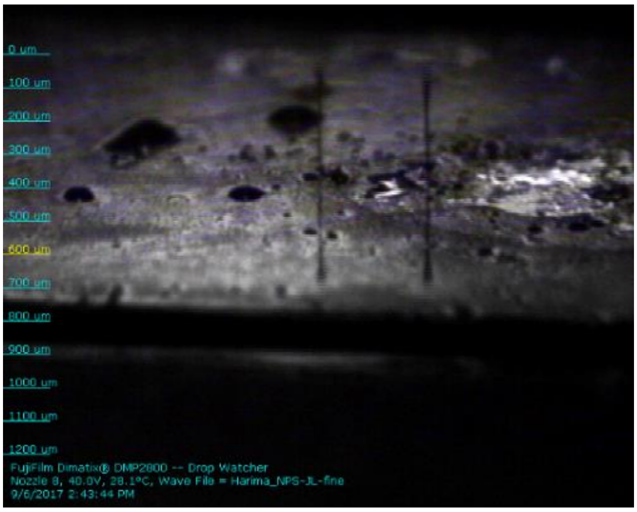

Figure 6.3. Drop watcher showing droplet formation.

3. Load the silver ink into the Fujifilm- Dimatix printer.
4. Open the drop watcher on the printer to ensure that ink droplets are forming as desired and that the printing nozzle is open (Figure 3.5).
5. If the nozzle is blocked and no droplets are forming a cleaning cycle should be run on the printer. The cleaning cycles should be applied from the least aggressive cleaning cycle to the most aggressive cleaning cycle on the printer until the nozzle is unclogged. This is done so that the least amount of ink is wasted.
6. Place substrate on the printer and stick it down with sellotape to avoid it from shifting when printing.

7. Select the design to be printed.
8. Adjust the printer and design settings such as the drop spacing, printer starting point, alignments, number circuits and pitch between circuits.
9. Set the printers bottom plate temperature (Table 3.2).
10. If the silver ink is being printed on top of another layer, print a single line of ink to ensure that the alignment mark corresponds with the alignment marker of the previous layer. The alignment marker can be seen better using the printer's fiducial camera. This camera can also be used to calculate the distance that the printers starting point needs to be adjusted in order for the layers to properly align. Figure 3.6 and Figure 3.7 show the track alignment done using the printer's fiducial camera.
11. Cure the silver ink in an oven as described in subsequence selections. Each of the inks needed to be cured as specified in their datasheets. The Harima silver ink was curved in an oven as specified. Small weights were placed on the corners of the paper substrate when it was placed in the oven to ensure that the paper does not roll up or curve while being heated. Since the available oven's temperature could not be automatically ramped up and down, the ovens temperature was manually ramped. The time that the oven was set at a particular temperature is shown in Table 6.1. After 120 minutes at 120 degrees Celsius, the oven was turned off, but the oven door was left closed so that the oven cooled down slowly. The silver ink was cured in between the first and second layer of the top conductive tracks.

Table 6.1. Temperature ramping for the Harima silver ink.

Temperature (°C)	Time (Minutes)
60	10
80	10
100	10
120	120

Eight rows of silver tracks were printed at a pitch of 500 μm from each other (Figure 6.4). This can serve as the bottom conductive layer of an inkjet printed OLED array. A multi-meter was used to ensure that the conductive tracks did not make contact with adjacent tracks. Due to cost and lab access constraints the rest of the OLED was not printed. But the inkjet printable materials simulated in Chapter 5 could have been used to print the inkjet print a fully function OLED array.

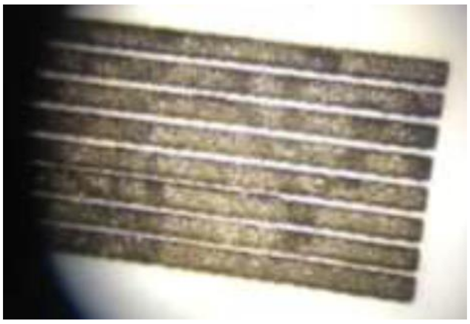

Figure 6.4. Inkjet printed silver conductive tracks.

CHAPTER 7 DISCUSSION

7.1 CHAPTER OVERVIEW

Section 7.2 compares using the reverse biased photocurrent and the reverse biased discharge time to measure illumination. It also states which method is more suitable for future implementation in micro-fluidic devices. Section 7.3 and 7.4 discusses the advantages and disadvantages of LED and OLED based light detectors, respectively. Lastly Section 7.5 discusses the linearity of both LED and OLED emitter-detector pairs.

7.2 PHOTOCURRENT VERSUS DISCHARGE TIME AS DETECTION METHOD

When the photocurrent of the reverse biased LED (Figure 3.6.) and OLED (Figure 3.8) was measured, it was seen that they both had photocurrents in the nano-ampere range or smaller. The LED had a photocurrent in the pico-ampere range and the OLED had a photocurrent in the nano-ampere range. If a revere-biased OLED had to be used as a light detector in a microfluidic channel the size of the OLED would be 10^4 to 10^5 times smaller than the large OLED that was tested. The smaller the OLED surface area, the smaller the measured photocurrent will be.

For an OLED with micrometre dimensions, it can be expected that the photocurrent will be in the pico-ampere range or smaller. Measuring such photocurrents in the pico-ampere range or smaller will require a complex and expensive solution. Noise will also have a bigger influence when measuring currents that are in the pico-ampere range or smaller which can influence the accuracy.

The reverse biased discharge time of an LED and OLED was measured as an alternative to measuring the discharge time. This is a less complex solution and is also very cost affective. A reversed biased LED detector that makes use of the measured discharge time is more sensitive than a reversed biased LED detector that uses the measured photocurrent [17]. This is the same in the case of a reverse biased OLED detector.

In chapter 3 by changing the series resistance of the emitter LED the illumination of the LED decreases. That is an emitter-detector pair, the emitter LED can be used to adjust the sensitivity of the emitter-detector pair.

The time constant for a white LED was calculated as 1.942 seconds and for the OLED panel it was calculated as 35.845 when connected to the 100 MΩ port of the Arduino Uno. The time constant for the OLED is much large than the LED since its capacitance is much larger. This is also since the dimensions of the OLED panel are about 100 times larger than the LED. For future microfluidic application, inkjet printed OLED panel, which small dimensions in the micrometre range is advised.

A discharge time of to 63 % of the maximum discharge voltage was seen to be sufficient to distinguish between different light intensities and was selected as the preferred discharge time. Using a discharge time of 63 % instead of 50 % or 33 % will increase the speed that testing can be done at.

An Arduino Uno was used to measure the discharge times of the LED and OLED detectors, while more sensitive and faster processor could have been used, an Arduino was seen to be sufficient to differentiate between the different pH values. Using an Arduino Uno also kept the cost of the process at a minimum.

The “count” variable value, which was incremented every time the Arduino Uno wrote an ADC value larger than 63 % of the maximum voltage to the serial port, was used to differentiate between samples. The ideal and relative transmission, refraction and reflection values were also investigated.

For an OLED array it was seen that either the “count” value or relative “count” values can be used to differentiate between different coloured water samples. The advantage of using the relative values, is that it can be recalibrated for any reference samples and therefore any container can be used if it is recalibrated for it. Four emitter and 4 detector LED and OLED pairs were needed for colourimetric analysis, using the measured “count” values. However, only three OLED detector pairs were needed when the relative “count” values were used. This saves on materials and costs.

7.3 COMPARISON OF AN LED AN OLED AS A LIGHT DETECTOR

Both the LED emitter-detector pair and the OLED emitter-detector pair has advantages and disadvantages. These advantages and disadvantages are discussed in this section.

7.3.1 Advantages and disadvantages of a reverse biased LED used as a light detector

LEDs are typically enclosed in coloured filters. An LED emitter array and reverse biased LED detector array, using different colour LEDs can easily be implemented using off-the-shelf LEDs. The different colour filters can be used to implement selectivity in colourimetric analysis. The emission spectra of different LEDs (Figure 3.27) also have clear and distinct bandwidths that are filtered out in comparison to the emission spectra of the OLED panels with coloured filters over them **(**Figure 4.27**).**

Off-the-shelf LEDs are not flexible, which makes them non ideal to be implemented inside flexible microfluidic point-of-care colourimetric test equipment. Small surface mount LEDs, such as 603 packaged LEDs can be implemented in an array for larger, non-flexible test equipment.

For LED emitter, the angular response of a white LED for irradiance (Figure 3.23) has a smaller magnitude at a 0 ° viewing angle than at a 15 ° viewing angle due to batwing casing structure. It is also seen to have a sharp decrease in magnitude as the viewing angle gets increased beyond 15 °. This implies that if an LED emitter and LED detector do not remain exactly parallel to each other, inaccuracies in the data can occur.

For a LED detector the discharge time of a LED detector at a 0 ° viewing angle the discharge time is the shortest (Figure 3.25). This is because the most emitted light gets detected by light detecting LED at a 0 ° viewing angle and the more light that is detected, the shorter the discharge time will be. The maximum discharge time is seen to be at a 75 ° angle and not at a 90 °-degree angle. This can be accounted for the fact that at a 90 ° degree viewing angle, light is emitting/detected through the LED packaging perpendicular to the packaging. This causes the light detected at a 90 °-degree angle to be brighter than at 75 ° degree, and therefore the discharge time to be shorter.

For the LED detector the largest count range (Table 3.15) is 2058 - 2186, which has a range of 128. The maximum deviation from the mean value in a range is therefore 6.03 %. For the OLED the maximum deviation from the measured mean value in a “count” range is 3.13 % from the mean, which is almost 3 % less than the LEDs.

7.3.2 Advantages and disadvantages of a flexible reverse biased OLED used as a light detector

The flexibility of a reverse biased OLED panel is advantageous as it can be used in low-cost point-of-care test equipment that make use of a flexible substrates such as paper or flexible polymers.

Although the OLED structure was not completely inkjet printed in practise, simulated results in Chapter 5 shows that an OLED structure, making use on only inkjet printable materials is attainable. An inkjet printable OLED structure is advantageous as it can be inkjet printed on numerous flexible or non-flexible substrate, can be used in low-cost applications, and can attain high resolutions.

A reverse biased OLED structure can be used as a photodetector, as seen in Chapter 4. An inkjet printed OLED emitter-detector pair has the potential of being implemented in flexible microfluidic diagnostic devices.

Although the emission spectra of different LEDs (Figure 3.27) had clear and distinct bandwidths that they filtered out in comparison to the emission spectra of the OLED panels with coloured filters over them (Figure 4.27). The OLEDs, with coloured filters can be implemented for spectral selectivity.

The white LED also has a larger bandwidth than the OLED panel, without a filter. This causes wavelengths in the blue bandwidth to be filtered out by the OLED panel, without a filter needing to be applied. Measuring light emission in the blue wavelength range with a reverse biased OLED therefore did not yield very distinct results. Selectivity in the blue wavelength range is not attainable with the OLED panel tested.

The angular response of an OLED has a similar magnitude (irradiance $\mu W/cm^2$) between a 0 ° and 45 ° viewing angle. The OLED emission is therefore less sensitive to the viewing angle than the LED emission. This is advantageous when implementing an array of OLED emitters and detectors, especially when light from multiple emitters in an array are detected by the same detector OLED.

Colourimetric analysis was performed using a LED and OLED emitter and detector array. The LED based colourimetric analysis was performed on pH samples, while the OLED based colourimetric analysis was performed on food colouring pH samples.

The food colouring samples were matched as closely to the pH samples, with the human eye. This is not a very accurate manor of matching colour but a colour meter was unavailable. Although this is not a very accurate manor of matching colours, it is sufficient to determine whether or not OLEDs can be used to distinguish between different colour liquid samples and can therefore be implemented for future colourimetric analysis.

7.4 LINEARITY

The linearity of the LED and OLED emitter-detector pair was required to be investigated in the initial project proposal. The results, however, gave data that was exponential in nature. A smaller subsection of the data (1 to 11 cm) was therefore analysed as the data in this range could be fitted to a linear plot (Chapter 3 and Chapter 4).

The linearity of the discharge time versus distance and illumination was investigated for a white LED and OLED. The distances between 1 and 50 cm as well as 1 and 11 cm (which is the size of the OLED colourimetric test container) was investigated. The linear regression analysis parameters for all the statistical analysis are summarized in Table 7.1.

Table 7.1 Linear regression parameters for all the linear analysis statistical tests for data between 1 cm and 50 cm.

	LED Distance in the range of 1-50 cm.	**LED Distance in the range of 1-11 cm.**	**LED Illumination (lux).**	**OLED detector at 1-50 cm away**	**OLED detector at 1-11 cm away**	**OLED illumination (lux) values between 0 and 300 lux.**
Multiple R	0.9449	0.9946	0.5725	0.9054	0.9962	0.8637
R Square	0.8928	0.9893	0.3278	0.8198	0.9924	0.7460
Standard Error	0.2383	0.031	0.5969	2.8985	0.3580	3.4406

The linear for the LEDs discharge time versus illumination only has a multiple R value of 0.5725, which means the data is not very accurate. Because the discharge time versus illumination values over a 1-11 cm for an OLED panel is quite linear with a multiple R value of 0.9442 the OLED colourimetric tests in the 11 cm wide container can be said to be linear.

CHAPTER 8 CONCLUSION

There is an increasing demand to develop low cost, biodegradable and flexible rapid diagnostic sensors for water quality monitoring and medical diagnosis [1] - [2]. There is a growing interest in small, low-cost, flexible lab-on-chip devices.

A low cost, colourimetric, light detection method that can be implemented in such devices was investigated. Inkjet printing, which is a low cost additive manufacturing method that can be used to manufacture lab-on-chip devices, was also investigated.

In this report a LED and OLED emitter and detector array was designed that can be used for pH colourimetric analysis of water samples. Using a flexible OLED as a light detecting sensor is a novel concept, so the OLED panel was analyzed and characterized as both a light emitter and detector. An inkjet printable OLED structure was designed and simulated that can be implemented as a fully inkjet printable OLED emitter-detector pair. The OLED panel was also mathematically modelled and simulated in Spice simulation software, in accordance with the research goals.

It was seen that both a LED and a flexible OLED array was able to be used for colourimetric analysis of liquid samples, which can be used for point-of-care or point-of-need applications.

An LED emitter-detector array was implemented and was seen to colourimetrically differentiate between pH samples. The disadvantage of the LED array is that it is not flexible as in the case of the OLED array. Additionally, it cannot be manufactured in micrometer dimensions to be implemented in microfluidic channels. It can, however, be implemented in larger test equipment for colourimetric analysis.

Test setups were designed to characterize the flexible OLED panel in terms of linearity, spectral response, wavelength sensitivity, angular response, capacitive discharge time, dominant wavelength and photocurrent. In regards to the spectral sensitivity of the OLED; it was seen that the OLED is most sensitive in the visual spectrum between 550 nm and 650 nm (Figure 4.1). The angular response of the OLED was plotted in Figure 4.20. It was found that the irradiance of the emitter OLED is approximately constant between a 0 ° and 40 ° viewing angle. Similarly the decharge time of a OLED detector was approximately constant between a 0 ° and 40 ° vieing angle.

However, in the case of an LED the irradiance peaks at a 15 ° viewing anagle and has a 37 % drop from the peak irradiance at a 0 % viewing anagle. This is due to the lense that is placed on LED, to scatter light more broadly. The LED emitter and dector pairs angular alignment is therefore more critical than an OLEDs angular alignment.

In answer to the research questions, it was found that a reverse biased OLED can be used as a light detecting sensor. As the illumination on the reverse biased OLED increased, the photocurrent as well as the reverse biased discharge time were seen to increase. The photocurrent of the large OLED panel was seen to be in the pico ampere range, which would require specialized circuitry to distuinguisg between current variations. If the OLED was to be made 10^6 times smaller in order to be placed in a micro-fluidoc channel, the photocurrent would be even smaller and more challenging to monitor. The reverse bias discharge time, however, requires much simpler methods to measure, such as the microcontroller implementation shown in Chapter 4.

The method of colourimetric analysis, using an OLED emitter and detector array does still need to be further optimized.

The grouping method in Chapter 3 and 4, to distinguish between the different colour water samples, was manually performed which is not optimal. Although using relative count values did create a more standardised approach to differentiate between water samples in different containers, a more rubust standardised approach should be considered. A method of doing this can be to make use of calculated spectral wavelengths and optimising the choice in light filters to create a more robust method of differentiating between water samples. An algorithm can be implemented based on spectral wavelengths, and filter characteristics to automatically differentiate between different water samples.

Addressing the research question about the detector OLEDs efficiency and accuracy, while the reverse biased OLED array could accurately differentiate between different colour samples it was not efficient which such large OLED panels. In this research the discharge time of the OLED with each different colour filter was measured one at a time. In future this could be done with a microprocessor and an array of different OLED panels with different filters. Even still, the discharge time of the large panels are in the milli second range which means it will take long to measure all the discharge times in the array. By implementing smaller OLEDs. The discharge time can be shortened, which will decrease the test time.

Manufacturing the fully inkjet printable OLED structure that was designed and simulated and testing it as an emitter-detector pair should be considered in future research. Once tested it can be printed at high resolutions in micrometer dimensions and implemented into microfluidic channels in lab-on-chip devices.

Although the tested OLED structure was not fully inkjet printed, an off-the-shelf OLED emitter-detector pair was analysis and found to be able to be implemented for colourimetric analysis. An inkjet printable OLED panel was simulated and optimised, but it was never fully manufactured and tested in practice. For lab-on-chip devices, OLED in the micro meter range will need to be implemented, and therefore the OLED emitter and detector array should be tested using smaller OLEDs in future research.

The colourimetric analysis can be extended beyond distinguishing between different water pH and can be used to detect other impurities in water samples. Other optical detection methods, such as fluorescence optical detection can also be investigated for lab-on-chip applications.

REFERENCES

[1] Y. Xu, M. Liu, N. Kong and J. Liu, “Lab-on-paper micro- and nano-analytical devices: Fabrication, modification, detection and emerging applications,” Microchim Acta, pp. 1521-1542, 2016.

[2] T. Zhang, “Methods for Fabricating Printed Electronics with High Conductivity and High Resolution,” The University of Western Ontario, 2014.

[3] P. D. Angelo, “Inkjet-Printed Light-Emitting Devices : Applying Inkjet Microfabrication to Multilayer Electronics,” Univ. Toronto, p. 257, 2013.

[4] N. M. M. Pires, T. Dong, U. Hanke and N. Hoivik, “Recent developments in optical detection technologies in lab-on-a-chip devices for biosensing applications,” Sensors, vol. 14, no. 8, pp. 15458-15479, 2014.

[5] K.-T. Lau, W. S. Yerazunis, R. L. Shepherd and D. Diamond, “Quantitative colorimetric analysis of dye mixtures using an optical photometer based on LED array,” Sensors and Actuators, B: Chemical, vol. 114, no. 2, pp. 819-825, 2006.

[6] M. O'Toole, “Photometric detection in flow analysis systems using integrated PEDDs,” Talanta, no. 5, pp. 1340-1344, 2005.

[7] A. Nikolajev, “Evaluation of led as light sensor,” Tallinn University of Technology Master's thesis, 2017.

[8] M. O'Toole and D. Diamond, “Absorbance Based Light Emitting Diode Optical Sensors and Sensing Devices,” Sensors, vol. 8, pp. 2453-2479, 2008.

[9] M. O'Toole, K. T. Lau, R. Shepherd, C. Slater and D. Diamond, “Determination of Phosphate using a Highly Sensitive Paired Emitter-Detector Diode Photometric Detector,” Analytica Chimica Acta , vol. 597, pp. 290-294, 2007.

[10] K. Lau, S. Baldwin and R. Shepherd, “Novel fused-LEDs devices as optical sensors for colorimetric analysis,” Talanta, vol. 63, pp. 167-173, 2004.

[11] “Simulate organic/ Perovskite Solar Cells, OFETs and OLEDs,” GPVDM, [Online]. Available: http://www.gpvdm.com/. [Accessed 13 12 2019].

[12] “Setfos,” Fluxim, [Online]. Available: https://www.fluxim.com/setfos-intro. [Accessed 13 12 2019].

[13] T.-T. Huang and W. Wu, “Inkjet-Printed Wearable Nanosystems for Self-Powered Technologies,” Advanced Materials Interfaces, vol. 7, no. 2, 2020.

[14] F. A. Viola, B. Brigante and P. Colpani, “A 13.56 mhz Rectifier Based on Fully Inkjet Printed Organic Diodes” Advanced Materials 2020.

[15] A. Z. Qamar and M. H. Shamsi, “Desktop Fabrication of Lab-On-Chip Devices on Flexible Substrates: A Brief Review,” Micromachines 2020, no. 11, p. 126, 2020.

[16] N. M. M. Pires, T. Dong, U. Hanke and N. Hoivik, “Recent developments in optical detection technologies in lab-on-a-chip devices for biosensing applications.,” Sensors, vol. 14, pp. 15458-15479, 2014.

[17] M. O'Toole, K. T. Lau, R. Shepherd, C. Slater, and D. Diamond, “Determination of Phosphate using a Highly Sensitive Paired Emitter-Detector Diode Photometric Detector.,” Elsevier Science Direct , vol. 1, pp. 290-294, 2007.

[18] P. Dasgupta, H. Bellamy and H. Liu, “Light emitting diode based flow-through optical absorption detectors,” Talanta, vol. 40, no. 1, pp. 53-74, 1993.

[19] “MQuant pH Test datasheet,” Merck, 2019. [Online]. Available: http://www.merckmillipore.com/ZA/en/product/pH-Test,MDA_CHEM-108027. [Accessed 23 March 2019].

[20] “MColortest TM,” Merck KGaA, 2015. [Online]. Available: www.analytical-test-kits.com. [Accessed 10 April 2019].

[21] “HI 3834 Iron Test Kit,” Hanna instrume nts, 2018. [Online]. Available: https://www.hannainstruments.co.uk/iron-test-kit.html. [Accessed 21 May 2019].

[22] “HI 3846 Chromium Test Kit,” Hanna instruments, [Online]. Available: http://www.hannacan.com/PDF/manHI3846.pdf. [Accessed 21 May 2019].

[23] “Copper Test Kit,” Hanna instruments, [Online]. Available: http://www.hannacan.com/PDF/manHI3847.pdf. [Accessed 21 May 2019].

[24] “HI 3874 Nitrate Test Kit,” Hanna instruments , [Online]. Available: https://www.hannainstruments.co.uk/nitrate-test-kit.html. [Accessed 21 May 2019].

[25] “HI 3873 Nitrite Test Kit,” Hanna instruments, [Online]. Available: https://hannainst.com/downloads/dl/file/id/1416/manhi_3873.pdf. [Accessed 21 May 2019].

[26] “HI 38017 Free & Total Chlorine Low and Medium Range Test Kit,” Hanna instruments, [Online]. Available: https://hanna.co.za/shop/chemical-test-kits/chemical-test-kits/637/hi38017-free-and-total-chlorine-test-kit-low-and-medium-range. [Accessed 21 May 2019].

[27] “114401 Supelco Chloride Test,” Merck, [Online]. Available: http://www.merckmillipore.com/ZA/en/product/Chloride-Test,MDA_CHEM-114401?ReferrerURL=https%3A%2F%2Fwww.google.com%2F. [Accessed 21 May 2019].

[28] “114783 Supelco Nickel Test,” Merck, [Online]. Available: http://www.merckmillipore.com/ZA/en/product/Nickel-Test,MDA_CHEM-114783. [Accessed 21 May 2019].

[29] J. Cho, E. Yoon, H. Kim, Y. Park and J. S. Kwak, "Improved Emission Efficiency in InGaN Light-Emitting Diodes Using Reverse Bias in Pulsed Voltage Operation," in IEEE Photonics Technology Letters, vol. 20, no. 13, pp. 1190-1192, July1, 2008, doi: 10.1109/LPT.2008.924893.

[30] R. J. Berry, J. E. Harris and R. R. Williams, “Light-Emitting Diodes as Sensors for Colorimetric Analyses.,” Applied Spectroscopy, vol. 51, pp. 1521-1524, 1997.

[31] K. Murphy, B. Heery and T. Sullivan, “A low-cost autonomous optical sensor for water quality monitoring,” Talanta, vol. 132, pp. 520-527, 2015.

[32] M. O'Toole, K. T. Lau and D. Diamond, “Photometric detection in flow analysis systems using integrated PEDDs,” Talanta, vol. 66, pp. 1340-1344, 2005.

[33] K.-T. Lau, W. S. Yerazunis and R. L. Sheperd, “Quantitative colorimetric analysis of dye mixtures using an optical photometer based on LED array,” Elsevier Sensors and Actuators B, vol. 114, pp. 819-825, 2005.

[34] A. Kitae, “Luminescent Materials and Applications,” Wiley, no. 1, 2008.

[35] C. Jiang, L. Mu and J. Zou, “Full-color quantum dot active matrix display fabricated by ink-jet printing,” Science China, vol. 60, no. 10, pp. 1249-1355, 2017.

[36] S. Chung, S. Song, K. Yang, S. M. Jeong and B. Choi, “Luminance enhancement of electroluminescent devices using highly dielectric UV-curable polymer and oxide nanoparticle composite,” Opt. Mater. Express, vol. 4, p. 903–908, 2014.

[37] W. Dang, V. Vinciguerra, L. Lorenzelli and R. Dahiya, “Printable stretchable interconnects,” IOP Sci, pp. 1-16, 2017.

[38] P. D. Keir, “Fabrication and characterization of ACTFEL devices,” Oregon State University Doctor Thesis, pp. 1-69, 1999.

[39] H. M. Haverinen, R. A. Myllyla and G. E. Jabbour, “Inkjet printing of light emitting quantum dots,” Appl. Phys. Lett. , vol. 94, no. 7, pp. 7-10, 2009.

[40] L. Lan, J. Zou, B. Jiang, B. Liu, L. Wang and J. Peng, “Inkjet printing for electroluminescent devices : emissive materials, film formation, and display prototype,” 330 Front. Optoelectron, vol. 10, no. 4, pp. 329-330, 2017.

[41] N. Madhaven, “Small-molecule organic semicondcutors,” 1 April 2002. [Online]. Available: https://chemistry.illinois.edu/system/files/inline-files/s02_Madhavan.pdf. [Accessed 4 Sept 2018].

[42] H. Yang, P. H. Holloway and B. B. Ratna, “Photoluminescent and electroluminescent properties of Mn-doped ZnS nanocrystals,” J. Appl. Phys., vol. 93, no. 1, pp. 586-592, 2003.

[43] G. Mauthner, “Inkjet printed surface cell light-emitting devices from a water-based poymer dispersion,” Org. Electron. physics, Mater. Appl, vol. 9, no. 2, pp. 164-170, 2008.

[44] C. Amruth, B. Luszczynska, B. G. Dupont and Z. Sieradzki, “Inkjet printing techniques and its application in organic light emitting diodes,” Display and Imaging, vol. 2, pp. 339-358, 2017.

[45] S. Zhang, S. Jiao, W. Yuan and S. Zhang, “Efficient Top-emitting Quantum Dot Light Emitting Diodes via Inkjet Printing,” 2nd International Conference on Electronics Technologies, pp. 423-426, 2019.

[46] M. Fleuster, M. Klein, P. v. Roosmalen, A. d. Wit and H. Schwab, “Mass Manufacturing of Full COlor Passive-Matrix and Active Matrix PLED Displays,” SID 04 Digest, pp. 1276-1279, 2004.

[47] X. Wu, J. A. Stiles, K. K. Foo and P. Bailey, “Electroluminescent display panel,” United States Patent, June 1997.

[48] J. Heikenfeld, R. A. Jones and A. J. Steckl, “Black Dielectric Electroluminescent 160x80 Pixel Display,” SID 03 Digest, vol. 35, no. 2, pp. 1110-1113, 2003.

[49] B.-Y. Jung and C. K. Hwangbo, “Spectral Characteristics of Organic Light-Emitting Diodes with (SiO2/TiO2) Dielectric Layers,” Journal of the Korean Physical Society, vol. 49, no. 5, pp. 2112-2117, 2006.

[50] P. L. Ward, “On the Planck-Einstein Relation,” [Online]. Available: https://ozonedepletiontheory.info/Papers/Ward2016OnThePlanckEinsteinRelation.pdf. [Accessed 16 12 2019].

[51] H. Degenhardt, “Principles and Applications of ELectroluminescent,” SpringerLink The Science of Nature, vol. 63, pp. 544-549, 1976.

[52] A. Pivrikas, H. Neugebauer and N. Serdar, “Charge carrier lifetime and recombination in bulk heterojunction solar cells,” IEEE journal of selected topics in quantum electronics, vol. 16, pp. 1746-1758, 2010.

[53] J. Verma, S. M. Islam, A. Verma and V. Protasenko, “Nitride LEDs based on quantum wells and quantum dots,” Elsevier Ltd., pp. 377-413, 2018.

[54] C. Amruth, “Inkjet Printing Technique and its Application in Organic Light Emitting Diodes,” Display and Imaging, vol. 2, pp. 339-358, 2017.

[55] P. Görrn, F. Ghaffari, T. Riedl and W. Kowalsky, “Zinc tin oxide based driver for highly transparent active matrix OLED displays,” Solid. State. Electron, vol. 53, no. 3, p. 329–331, 2009.

[56] S. Liu, J. Chang, I. Wu and C. Wu, “Alternating Current Driven Organic Light Emitting Diodes Using Lithium Fluoride Insulating Layers,” Sci. Rep, vol. 4, no. 1, pp. 1-7, 2015.

[57] S. Rankel and D. Mihailović, “Organic Light Emitting Diodes,” University of Ljubljana Seminar, 2004.

[58] F. Varela, E. Armendáriz and C. Wolluschek, “Inkjet printed electronics: The wet on wet approach,” Chemical Engineering and Processing , vol. 50, pp. 589-591, 2011.

[59] Y. Yoshioka, P. D. Calvert and G. E. Jabbour, “Simple modification of sheet resistivity of conducting polymeric anodes via combinatorial ink-jet printing techniques,” Macromol. Rapid Commun, vol. 26, no. 4, p. 238–24, 2005.

[60] Y. Yin, “Sodium triphosphate as an efficient electron injection layer in organic light-emitting diodes,” Synth. Met, vol. 162, no. 1804-1808, 2012.

[61] H. M. Haverinen, R. A. Myllylä and G. E. Jabbour, “Inkjet printing of light emitting quantum dots,” Appl. Phys. Lett, vol. 94, no. 7, pp. 7-10, 2009.

[62] D. M. Small, W. Y. Sanchez, M. J. Hickey and G. C. Gobe, ““Multiphoton fluorescence microscopy of the live kidney in health and disease Multiphoton fluorescence microscopy of the live kidney in health and disease,” J. Biomed. Opt, vol. 19, no. 2, pp. 1-17, 2014.

[63] C. Hinzmann, O. Magen, Y. J. Hofstetter, P. E. Hopkinson, N. Tessler and Y. Vaynzof, ““Effect of Injection Layer Sub-Bandgap States on Electron Injection in Organic LightEmitting Diodes,” Appl. Mater. Interfaces, 2017.

[64] U. Periyayya, J. H. Kang, J. H. Ryu and C. H. Hong, “Synthesis and improved luminescence properties of OLED/ZnO hybrid materials,” Vacuum, vol. 86, no. 3, p. 254–260, 2011.

[65] J. Kim, C. Hwang, H. Woo, E. Song and J. Baek, “Flexible Organic Electroluminescent Displays with Optical Transparency Using Electrically Conducting Polymers,” Mater. Sci, p. 1540–1543, 2009.

[66] H. Gorter, “Toward inkjet printing of small molecule organic light emitting diodes,” Thin Solid Films, vol. 532, p. 11–15, 2013.

[67] M. J. Coenen, T. M. Slaats, T. M. Eggenhuisen and P. Groen, “Inkjet printing the three organic functional layers of two-colored organic light emitting diodes,” Thin Solid Films, vol. 583, no. 1, p. 194–200, 2015.

[68] N. Gupta, R. Grover, D. S. Mehta and K. Saxena, “A simple technique for the fabrication of zinc oxide-PEDOT:PSS nanocomposite thin film for OLED application,” Synth. Met, vol. 221, p. 261–267, 2016.

[69] P. S. Chen and S. Wang, “Transparent Conductive Electrode Based on Hydrogen Doped Zinc Oxide for OLED Application,” SID EuroDisplay , no. 12, p. 79, 2015.

[70] Kunic, S. Kunic and Z. Sego, “OLED Technology and Displays,” IEEE conference paper, 54th International Symposium ELMAR, pp. 31-35, 2012.

[71] B. Zhao, “A new OLED SPICE model for pixel circuit simulation in OLED-onsilicon microdisplay design,” J. Semicond, vol. 33, no. 7, 2012.

[72] S. G. Lee and R. Hattori, “Physics-based OLED analog behavior modeling,” J. Inf. Disp, vol. 10, no. 3, p. 101–106, 2009.

[73] S. M. Alawi, “Detection of lighting Consumers by Correlation of Control Signals and Illuminance,” Metropoloa University of Applied Science Bachelor Thesis, pp. 1-58, 2018.

[74] C. Bouska, “Fabrication and Characterization of ACTFEL Devices,” pp. 1-69, 2004.

[75] “Light Emitting Diode Optical Unit and Calculation Application Note,” Nichia , 15 March 2016. [Online]. Available: https://www.nichia.co.jp/specification/products/led/ApplicationNote_SE-AP00041-E.pdf. [Accessed 15 March 2018].

[76] A. D. Ryer, Light Measurement Handbook, Newburyport: International Light, 1998.

[77] W. Wang, “Optical detectors,” National Tsing Hua University, [Online]. Available: https://depts.washington.edu/mictech/optics/me557/detector.pdf. [Accessed 6 08 2019].

[78] “Optical Unit and Calculation Light Emitting Diode Light Emitting Diode,” Nichia Appl. Note, p. 1–6, 2016.

[79] “The CIE Chromaticity Diagram,” Denbigh Starkey, 2015. [Online]. Available: https://www.cs.montana.edu/courses/spring2005/430/dslectures/CIEdiagram.pdf. [Accessed 06 09 2019].

[80] D. Starkey, “The CIE Chromaticity Diagram,” [Online]. Available: https://www.cs.montana.edu/courses/spring2005/430/dslectures/CIEdiagram.pdf. [Accessed 3 August 2019].

[81] K. Suganuma, Introduction to Printed Electronics, vol. 74, Osaka, Japan: Springer, 2014, p. 2014.

[82] P. Chen, C. L. Chen, L. Tsai, H. Ting, L. Lin and C. Chen, “65-Inch Inkjet Printed Organic Light-Emitting Display Panel with High Degree of Pixel Uniformity,” SID Digest, vol. 30, pp. 396-398, 2014.

[83] “Jettable Fluid Formulation Guidelines,” Fujifilm Dimatix, 16 May 2013. [Online]. Available: https://www.fujifilmusa.com/shared/bin/Dimatix_Materials_Printer_Jettable_Fluid_Formulation_Guidelines_05-13.pdf. [Accessed 23 May 2017].

[84] J. Li, F. Rossignol and J. Macdonald, “Lab on a Chip,” R. Soc. Chem, vol. 15, no. 12, p. 2538–2558, 2015.

[85] “Rheological Characterisation of Ink Jet Fluids,” University of Cambridge, [Online]. Available: https://www.ceb.cam.ac.uk/research/groups/rg-p4g/archive-folder/pfg/inkjet-folder/rheological-characterisation. [Accessed 4 September 2018].

[86] J. Alaman, R. Alicante, J. I. Pena and C. Sanchez-Somolinos, “Inkjet Printing of Functional Materials for Optical and Photonic Applications,” Materials (Basel), vol. 9, no. 910, pp. 1-47, 2016.

[87] K. Suganuma, Introduction to printed electronics, 1st ed., Osaka, Japan: Springer Science+Business Media New York, 2014.

[88] “Application Note : Viscosity measurement of Various Inkjet Inks,” 2006. [Online]. Available: www.rheosense.com. . [Accessed 14 Sept 2018].

[89] “Fujifilm Dimatix Ink Tutorial,” Fujifilm Dimatix, 2008. [Online]. Available: https://www.cnfusers.cornell.edu/sites/default/files/Equipment-Resources/Ink%20formulation%20tutorial.pdf. [Accessed 13 May 2017].

[90] "Processing Guide for DuPont Luxprint Electroluminescent Inks," Dupont , May 2012. [Online]. Available: https://www.dupont.com/content/dam/dupont/products-and-services/electronic-and-electrical-materials/documents/prodlib/EL_Processing_Guide.pdf. [Accessed 9 April 2017].

[91] A. Teichler, Z. Shu, A. Wild and C. Bader, "Inkjet printing of chemically tailored l ight-emitting polymers," Eur Polym J, vol. 49, no. 8, pp. 2186-2195, 2013.

[92] A. J. Grace, K. F. Drain and Y. Sasaki, "Electroluminescent display device and method of making," United States Patent Application Publication, vol. 1, no. 60, 2002.

[93] "Dimatix Materials Printer DMP-2850," Fujifilm Dimatix, [Online]. Available: https://www.fujifilmusa.com/shared/bin/dimatix_materials_printer_dmp-2850.pdf. [Accessed 16 12 2019].

[94] R. Mannerbro, M. Ranlof, N. Robunson and R. Forchheimer, "Inkjet printed electrochemical organic electronics," Synth Met, vol. 158, no. 13, pp. 556-560, 2008.

[95] Z. P. Yin, Y. A. Huang, N. B. Bu, X. M. Wang and Y. L. Xiong, "Inkjet printing for flexible electronics: Materials, processes and equipments," Chinese Sci. Bull, vol. 55, no. 30, pp. 3383-3407, 2010.

[96] C. Martinez-Domingo, S. Conti, L. Teres, H. L. Gomes and E. Ramon, "Novel flexible inkjet-printed Metal-Insulator-Semiconductor organic diode employing silver electrodes," Organic Electronics, vol. 62, pp. 335-342, 2018.

[97] L. To, "High-efficiency dace electroluminescence in ZnS (Mn , Cu)," Journal of Physics D: Applied Physics, pp. 4-7, 1968.

[98] S. A. Lima, M. R. Davolos, W. Legnani, W. G. Quirino and M. Cremona, "Low voltage electroluminescence of terbium- and thulium-doped zinc oxide films," Elsevier, Journal of alloys and compounds, vol. 418, pp. 35-38, 2006.

[99] D. Kouyate and J. Kossanyi, "Electroluminescence of Sm3 + Ions in Semiconducting Polycrystalline Zinc Oxide," J. Mater. Chem, vol. 2, no. 7, pp. 727-732, 1992.

[100] Y. Vaynzof, "Effect of Injection Layer Sub-Bandgap States on Electron Injection in Organic Light-Emitting Diodes," Applied materials and interfaces, vol. 9, pp. 6221-6227, 2017.

[101] J. Gilmore, “Understanding Spectrometer Signal to Noise,” Hamamatsu, June 2020. [Online]. Available: https://hub.hamamatsu.com/sp/hc/resources/webinars/Understanding_Spectrometer_Signal_to-Noise.pdf. [Accessed 17 November 2020].

[102] S. Cheusheva, “Linear regression analysis in Excel,” Ablebits.com, 18 September 2019. [Online]. Available: https://www.ablebits.com/office-addins-blog/2018/08/01/linear-regression-analysis-excel/#regression-analysis-in-Excel. [Accessed 10 October 2019].

[103] B.-Y. Jung and C. K. Hwangbo, “Spectral Characteristics of Organic Light-Emitting Diodes with (SiO2/TiO2) Dielectric Layers,” Journal of the Korean Physical Society, vol. 49, no. 5, pp. 2112-2117, 2006.

[104] J. Huang , H.-C. Kuo and S.-C. Shen, Nitride Semiconductor light-emitting diodes (LEDs) second edition, Woodhead Publishing Series, 2018, pp. 492-527.

[105] K.-F. Hsu, C.-W. Lin and J.-M. Hwang, “High Efficiency Batwaing Thin-Film Design for LED flat planel lighting,” IEEE 9th Internation Microsystems, Packaging, Assembly and Circuits Technology COnference (IMPACT), pp. 480-483, 2014.

[106] Z. Shu, E. Beckert, R. Eberhardt and A. Tünnermann, “ITO-free, inkjet-printed transparent organic light-emitting diodes with a single inkjet-printed Al:ZnO:PEI interlayer for sensing applications,” J. Mater. Chem. C, vol. 5, no. 44, p. 11590–11597, 2017.

[107] D. McKean, “LED Phosphor ink composition for ink-jet printing”. Hong Kong Patent US 8,329,485 B2, 11 12 2012.

[108] A. J. Moul and K. Meerholz, “Interference method for the determination of the complex refractive index of thin polymer layers,” Appl. Phys. Lett, vol. 91, no. 6, pp. 3-6, 2007.

[109] K. H. Kim and S. Y. Park, “Enhancing light-extraction efficiency of OLEDs with high- and low-refractive-index organic-inorganic hybrid materials,” Org. Electron. physics, Mater. Appl, vol. 36, pp. 103-112, 2016.

[110] L. Zhuo, W. Liu, Z. Zhao and E. Yin, “Cost-effective silver nano-ink for inkjet printing in application of flexible electronic devices,” Chemicak Physics Letters, vol. 757, pp. 1-7, 2020.

[111] S. Chandra Singh, “Basics of Light Emitting diodes , Characterizations and Applications,” ResearchGate, pp. 1 - 35, 2009.

[112] S. Olivier, E. Ishow, S. M. Della-gatta and T. Maindron, “Inkjet deposition of a holetransporting small molecule to realize a hybrid solution-evaporation green top-emitting OLED,” Org. Electron, vol. 49, pp. 24-32, 2017.

[113] K. T. L. Lau, S. Baldwin and R. L. Sheperd, “Novel fused-LEDs devices as optical sensors for colorimetric analysis,” Talanta , vol. 63, pp. 167-173, 2004.

[114] R. Stojanovic and D. Karadaglic, “A LED-LED-based photoplethysmography sensor,” Physiological Measurement, vol. 28, no. 6, 2007.

[115] M. O’Toolea, R. Shepherd and G. G. Wallace, “Inkjet printed LED based pH chemical sensor for gas sensing,” Analytica Chimica Acta, vol. 652, pp. 308-314, 2009.

[116] I. M. P. d. Vargas-Sansalvador, C. Fay, M. D. Fernandez-Ramos, D. Diamond, F. Benito-Lopez and L. F. Capitan-Vallvey, “LED-LED portable oxygen gas sensor,” Analytical and Bioanalytical Chemistry, vol. 404, no. 10, pp. 2851-2858, 2012.

[117] E. V. Kvittingen, L. Kvittingen, B. J. Sjursnes and R. Verley, “Simple and Inexpensive UV-Photometer Using LEDs as Both Light Source and Detector,” Journal of Chemical Education, vol. 93, no. 10, pp. 1814-1817, 2016.

[118] Y. Xu, M. Liu, N. Kong and J. Liu, “Lab-on-paper micro- and nano-analytical devices: Fabrication, modification, detection and emerging applications,” Microchim Acta, vol. 183, pp. 1521-1542, 2016.

[119] K.-T. Lau, W. S. Yerazunis and R. L. Shepherd, “Quantitative colorimetric analysis of dye mixtures using an optical photometer based on LED array,” Sensors and Actuators, B: Chemical, vol. 114, no. 2, pp. 819-825, 2006.

[120] “What is the relationship between the band gap of matter and the wavelength it reflects?,” Quora, [Online]. Available: https://www.quora.com/What-is-the-

relationship-between-the-band-gap-of-matter-and-the-wavelength-it-reflects. [Accessed 16 12 2019].

ADDENDUM A LED EMITTER AND DETECTOR PARAMETERS

A.1 BLUE EMITTER AND DETECTOR PAIR

Table A1. Blue LED emitter parameters with corresponding blue LED light detector discharge time.

Re	Luminance (lux)	Luminous Flux Received (Lumens)	Luminous Intensity (Candela)	Time to 63% (ms)	Time to 50% (ms)	Time to 25% (ms)
470	37.657	1.18E-06	45.565	68	68	68
1k	38.801	1.22E-06	46.949	67	71	71
2.2k	35.984	1.13E-06	43.541	102	102	136
4.7k	29.403	9.24E-07	35.577	101	135	237
6.8k	23.61	7.42E-07	28.568	101	169	305
10k	18.596	5.84E-07	22.502	134	202	371
27k	11.134	3.50E-07	13.472	170	270	986
39k	8.8159	2.77E-07	10.667	174	289	1045
47k	8.2738	2.60E-07	10.011	127	290	870
68k	5.6412	1.77E-07	6.8259	139	315	1453
82k	4.4634	1.40E-07	5.4007	159	325	1321
100k	3.4454	1.08E-07	4.1689	173	355	1738
470k	0.4874	1.53E-08	0.5897	177	363	2191
1M	0.1031	3.24E-09	0.1247	150	346	2341

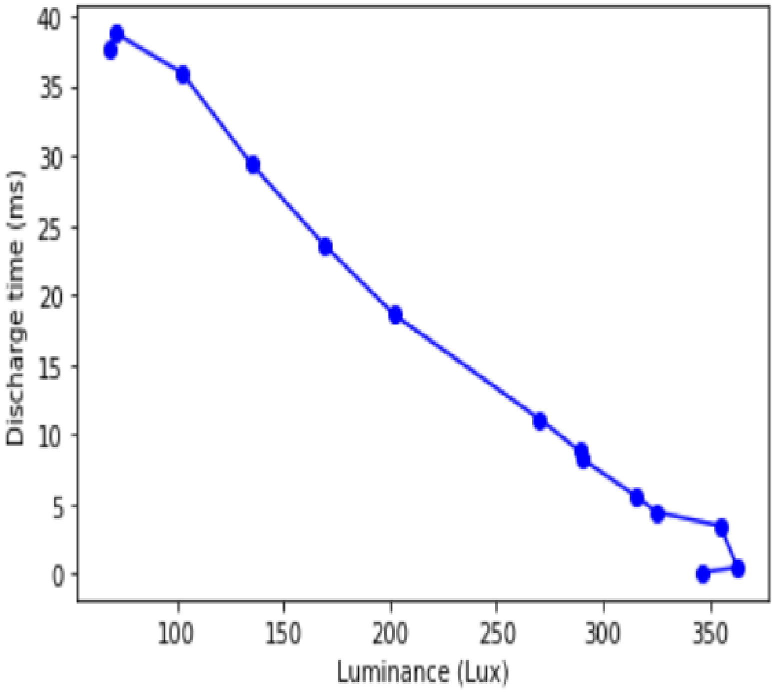

Figure A1. Time to 50 % of capacitive discharge voltage versus luminance (lux) for blue LED detector.

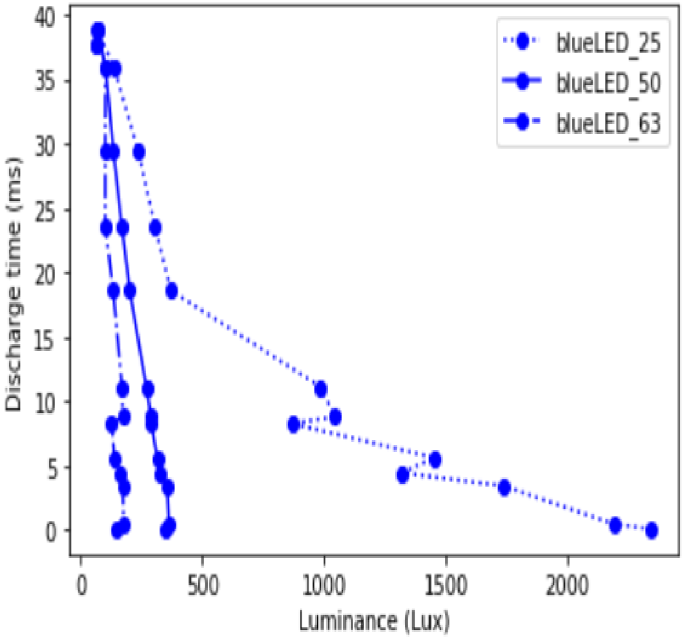

Figure A2. Time to 63 %, 50 % and 25 % of capacitive discharge voltage versus luminance (lux) for blue LED detector.

A.2 RED EMITTER AND DETECTOR PAIR

Table A2. Red LED emitter parameters with corresponding red LED light detector discharge time.

Re	Luminance (lux)	Luminous Flux Received (Lumens)	Luminous Intensity (Candela)	Time to 63% (ms)	Time to 50% (ms)	Time to 25% (ms)	Saturated ?
470	14.887	4.68E-07	17.014	439	576	914	Yes
1k	13.039	4.10E-07	15.777	541	709	1182	Yes
2.2k	11.852	3.72E-07	14.34	743	1016	1727	Yes
4.7k	11.03	3.47E-07	13.346	1046	1418	2500	Yes
6.8k	10.404	3.27E-07	12.589	1180	1618	3006	Yes
10k	9.6319	3.03E-07	11.655	1416	1992	3778	Yes
27k	7.5116	2.36E-07	9.089	1690	2367	5243	Yes
39k	7.1578	2.25E-07	8.661	1689	2398	4957	Yes
47k	6.5737	2.07E-07	7.9542	1754	2439	4940	Yes
68k	6.1433	1.93E-07	7.4334	1704	2439	4937	Yes
82k	5.5722	1.75E-07	6.7424	1734	2475	5015	Yes
100k	4.2674	1.34E-07	5.1635	1734	2464	5026	Yes
470k	1.2986	4.08E-08	1.5713	1771	2501	5078	No
1M	0.2453	7.71E-09	0.2968	1746	2490	5119	No

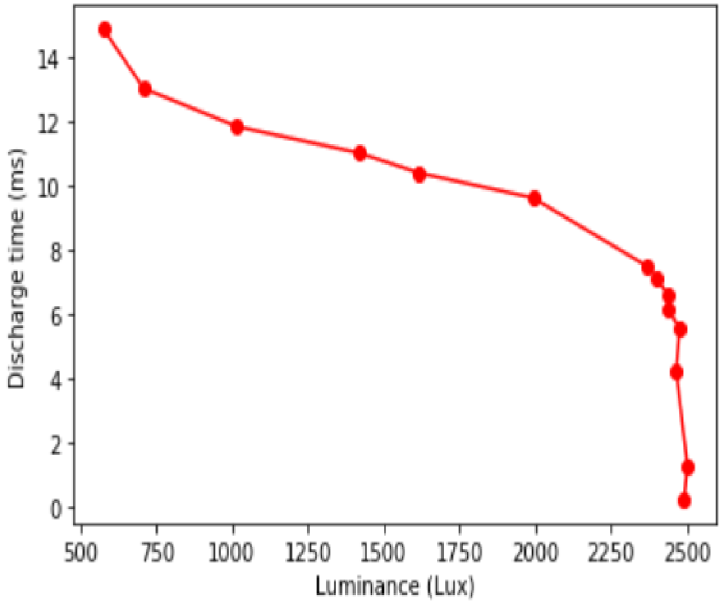

Figure A3. Time to 50 % of capacitive discharge voltage versus luminance (lux) for red LED detector.

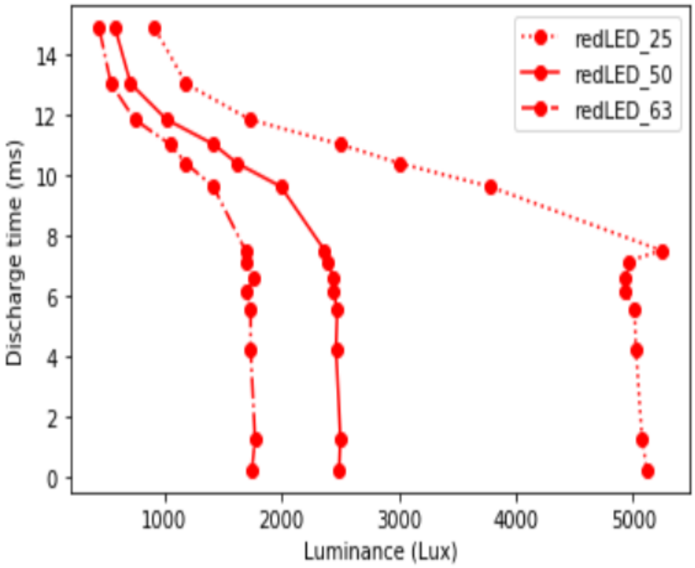

Figure A4. Time to 63 %, 50 % and 25 % of capacitive discharge voltage versus luminance (lux) for red LED detector.

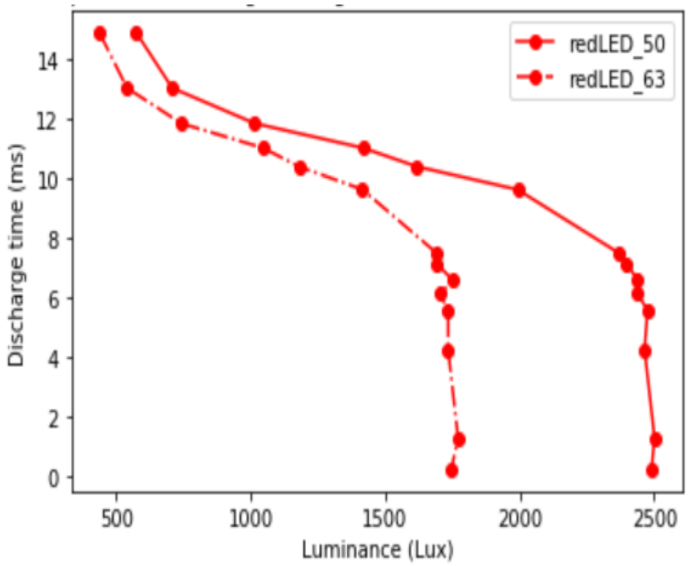

Figure A5. Time to 63 % and 50 % of capacitive discharge voltage versus luminance (lux) for red LED detector.

A.3 YELLOW EMITTER AND DETECTOR PAIR

Table A3. Yellow LED emitter parameters with corresponding yellow LED light detector discharge time.

Re	Luminance (lux)	Luminous Flux Received (Lumens)	Luminous Intensity (Candela)	Time to 63% (ms)	Time to 50% (ms)	Time to 25% (ms)
470	23.601	7.41E-07	28.557	134	168	236
1k	20.097	6.31E-07	24.317	238	283	431
2.2k	14.594	4.59E-07	17.659	457	592	963
4.7k	6.0261	1.89E-07	7.2916	901	1235	2166
6.8k	4.017	1.26E-07	4.8606	1083	1478	2640
10k	2.7095	8.51E-08	3.2785	1247	1725	3329
27k	0.01983	6.23E-10	0.02399	1514	2174	4169
39k	0.01983	6.23E-10	0.02399	399	2213	4382

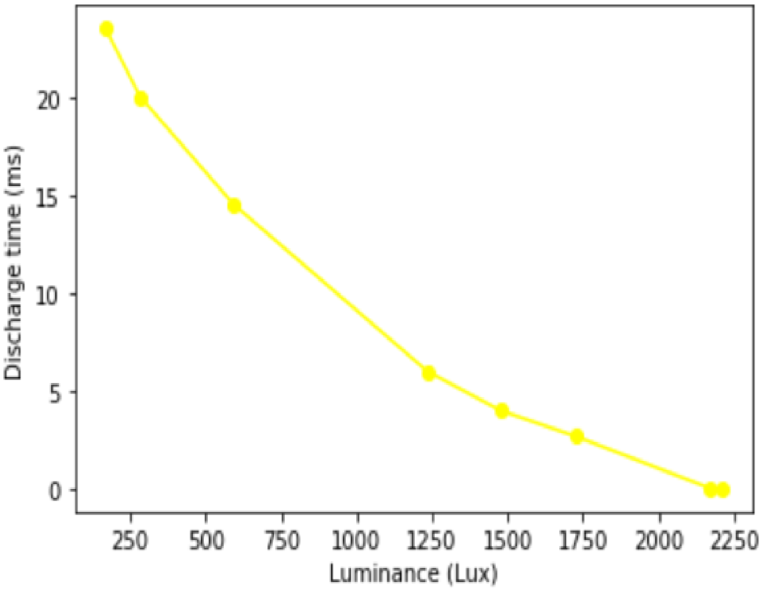

Figure A6. Time to 50 % of capacitive discharge voltage versus luminance (lux) for yellow LED detector.

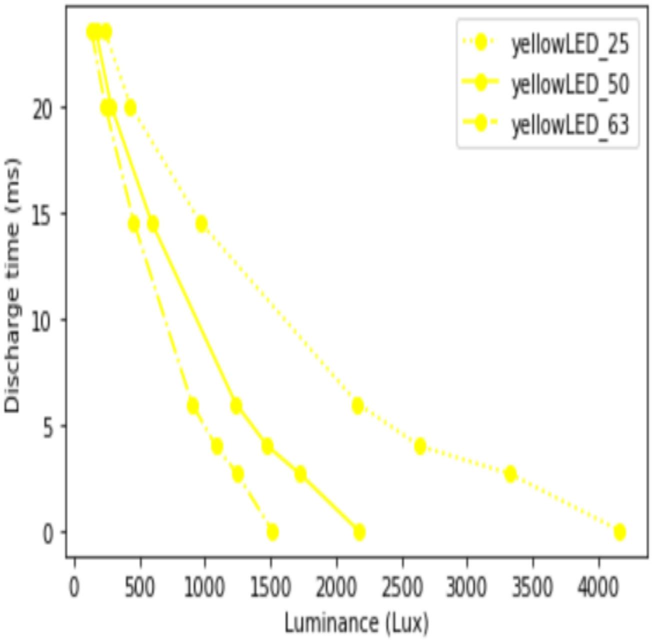

Figure A7. Time to 63 %, 50 % and 25 % of capacitive discharge voltage versus luminance (lux) for yellow LED detector.

A.4 ORANGE EMITTER AND DETECTOR PAIR

Table A4. Orange LED emitter parameters with corresponding orange LED light detector discharge time.

Re	Luminance (lux)	Luminous Flux Received (Lumens)	Luminous Intensity (Candela)	Time to 63% (ms)	Time to 50% (ms)	Time to 25% (ms)
470	9.7571	3.07E-07	11.806	82	123	123
1k	7.6913	2.42E-07	9.3064	113	113	158
2.2k	6.3363	1.99E-07	7.6669	220	257	383
4.7k	5.852	1.84E-07	7.0809	406	514	866
6.8k	4.8008	1.51E-07	5.809	555	786	1280
10k	3.3103	1.04E-07	4.0055	821	1096	1912
27k	0.4816	1.51E-08	0.5828	1242	1688	3181
39k	0.4816	1.51E-08	0.5828	1275	1769	3297

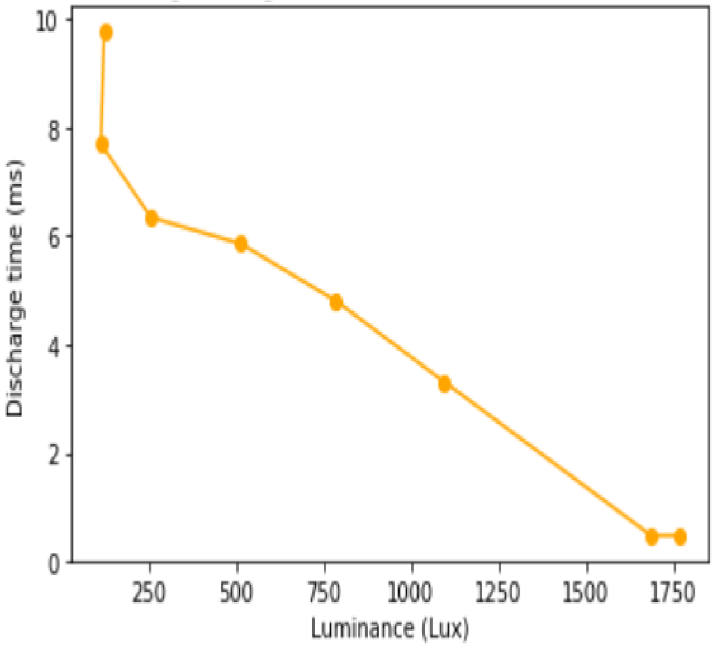

Figure A8. Time to 50 % of capacitive discharge voltage versus luminance (lux) for orange LED detector.

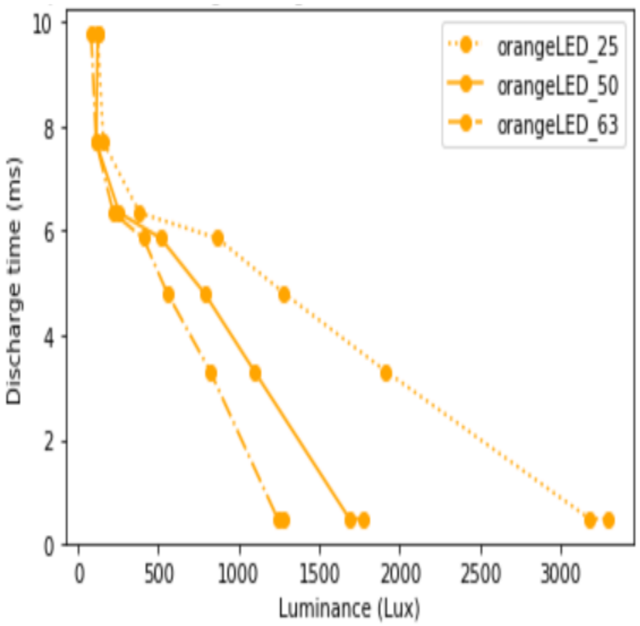

Figure A9. Time to 63 %, 50 % and 25 % of capacitive discharge voltage versus luminance (lux) for orange LED detector.

A.5 WHITE EMITTER AND DETECTOR PAIR

Table A5. White LED emitter parameters with corresponding white LED light detector discharge time.

Re	Luminance (lux)	Luminous Flux Received (Lumens)	Luminous Intensity (Candela)	Time to 63% (ms)	Time to 50% (ms)	Time to 25% (ms)
470	18.456	5.80E-07	22.332	66	100	100
1k	18.961	5.96E-07	22.943	135	135	170
2.2k	19.244	6.05E-07	23.285	171	205	305
4.7k	19.819	6.23E-07	23.981	304	405	609
6.8k	22.611	7.10E-07	27.36	475	645	983
10k	26.907	8.45E-07	32.557	781	1018	1596

27k	39.138	1.23E-06	47.357	1321	1762	3079
39k	39.076	1.23E-06	39.076	2135	2135	3825
47k	38.923	1.22E-06	47.097	1628	2241	4070
68k	38.136	1.20E-06	46.145	1758	2466	4564
82k	37.209	1.17E-06	45.023	1863	2572	4877
100k	35.743	1.12E-06	43.249	1887	2600	5038
470k	35.658	1.12E-06	43.146	2101	2946	5931
1M	35.658	1.12E-06	43.146	2097	2946	5994

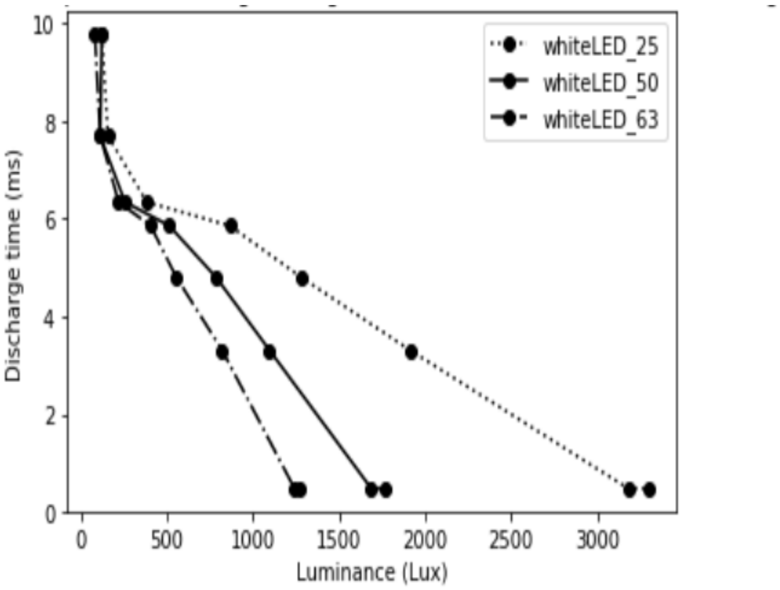

Figure A10. Time to 63 %, 50 % and 25 % of capacitive discharge voltage versus luminance (lux) for white LED detector.

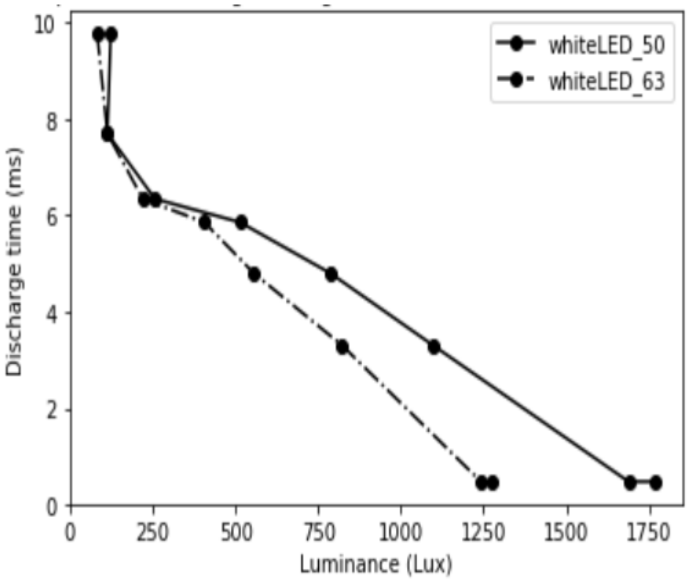

Figure A11. Time to 63 % and 50 % of capacitive discharge voltage versus luminance (lux) for white LED detector.

ADDENDUM B LED RELATIVE ABSORPTION AND REFLECTION

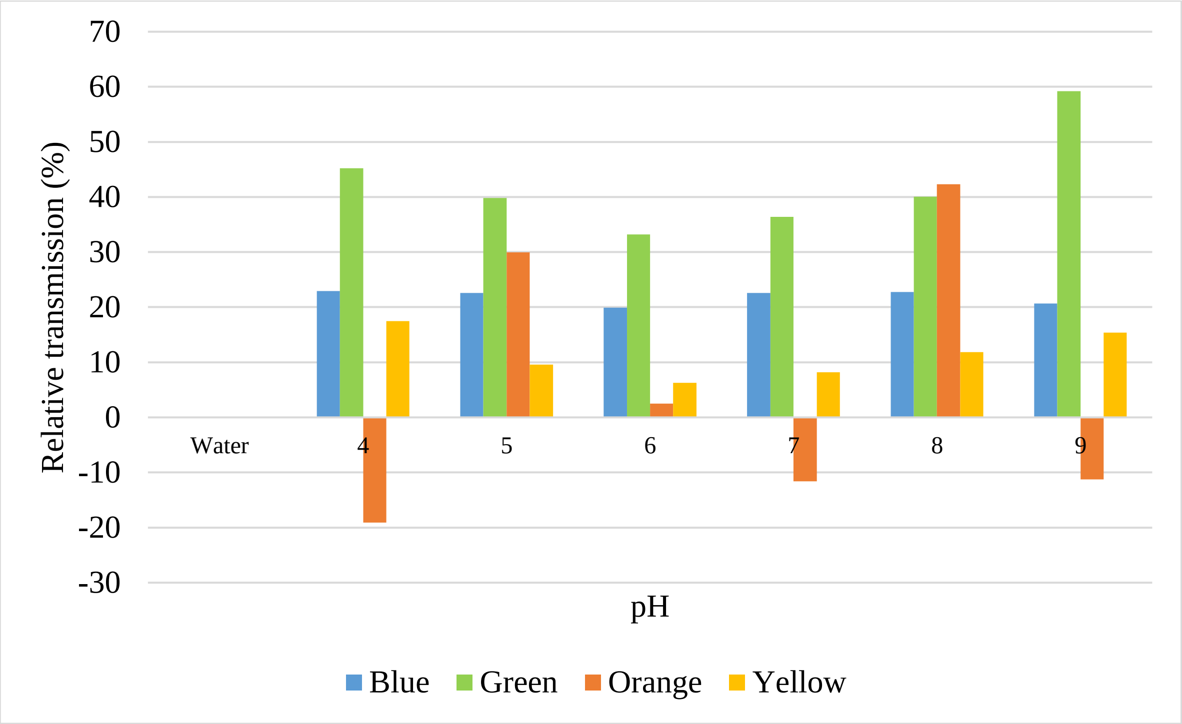

Figure B1. Relative reflection (%) for each of the pH samples.

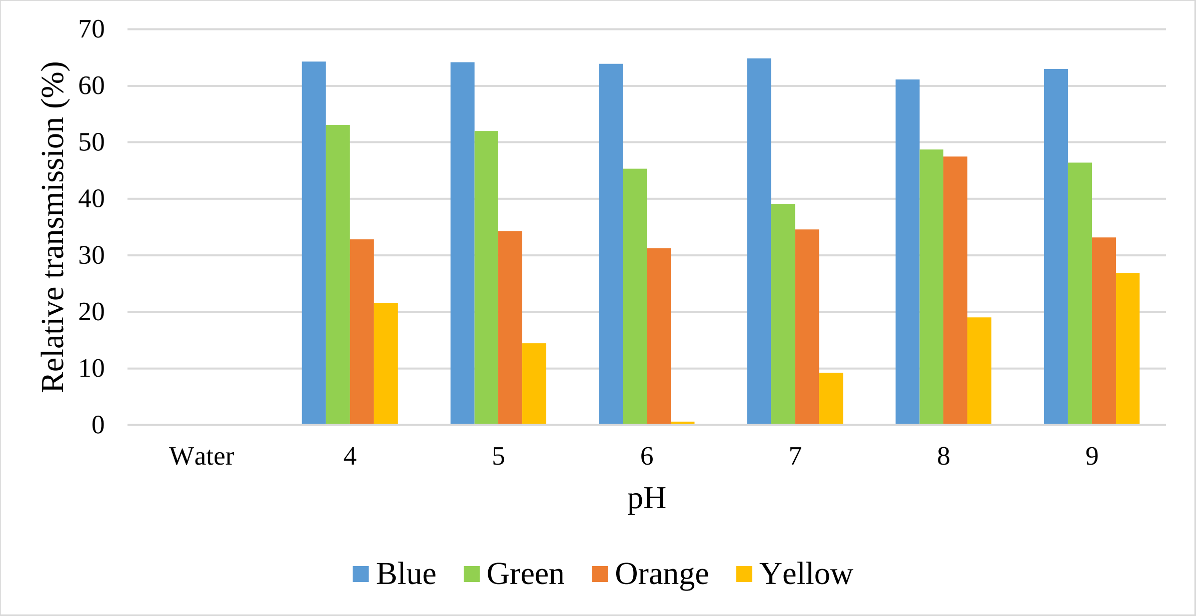

Figure B2. Relative refraction (%) for each of the pH samples.

ADDENDUM C OLED RELATIVE ABSORPTION, TRANSMISSION AND REFLECTION

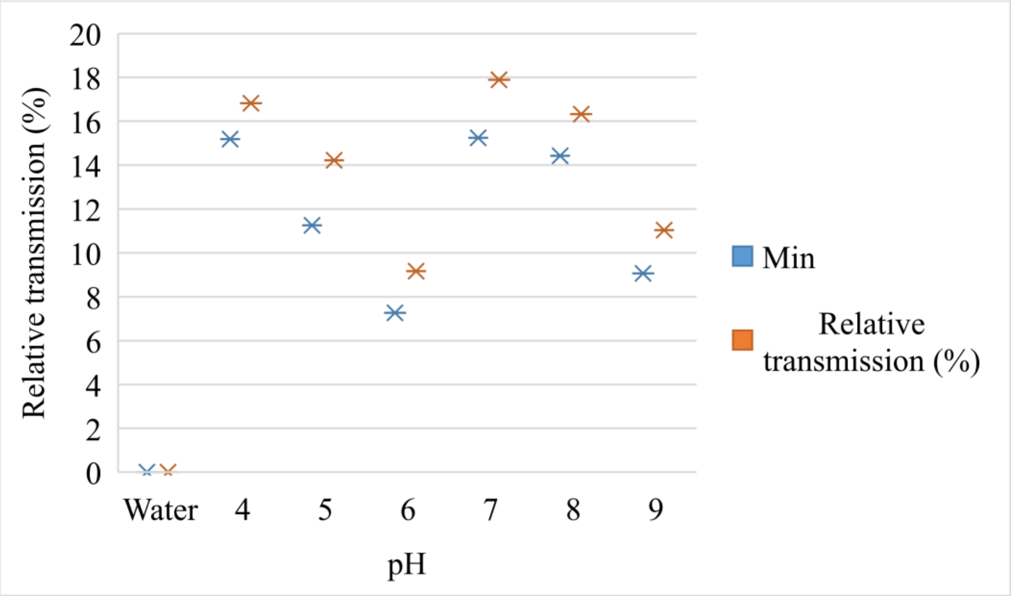

Figure C1. Minimum and maximum values for relative transmission with yellow filter over OLED detector.

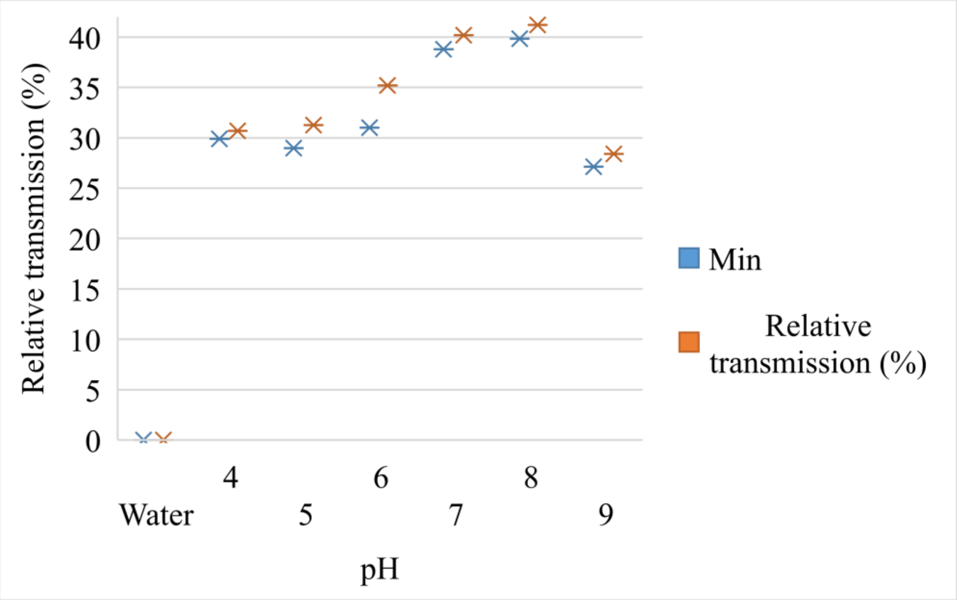

Figure C2. Minimum and maximum values for relative transmission with no filter over OLED detector.

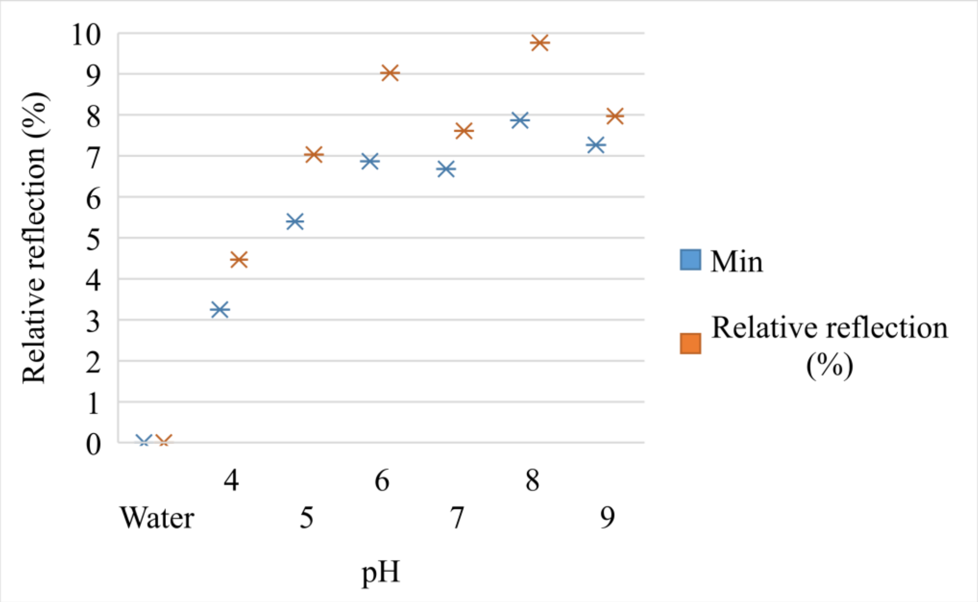

Figure C3. Minimum and maximum values for relative reflection with purple filter over OLED detector.

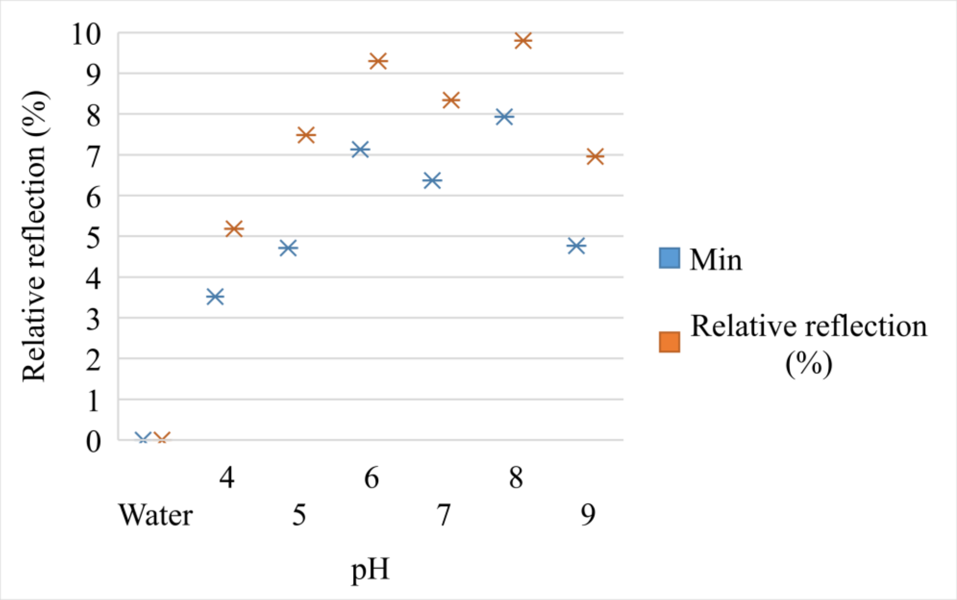

Figure C4. Minimum and maximum values for relative reflection with green filter over OLED detector.

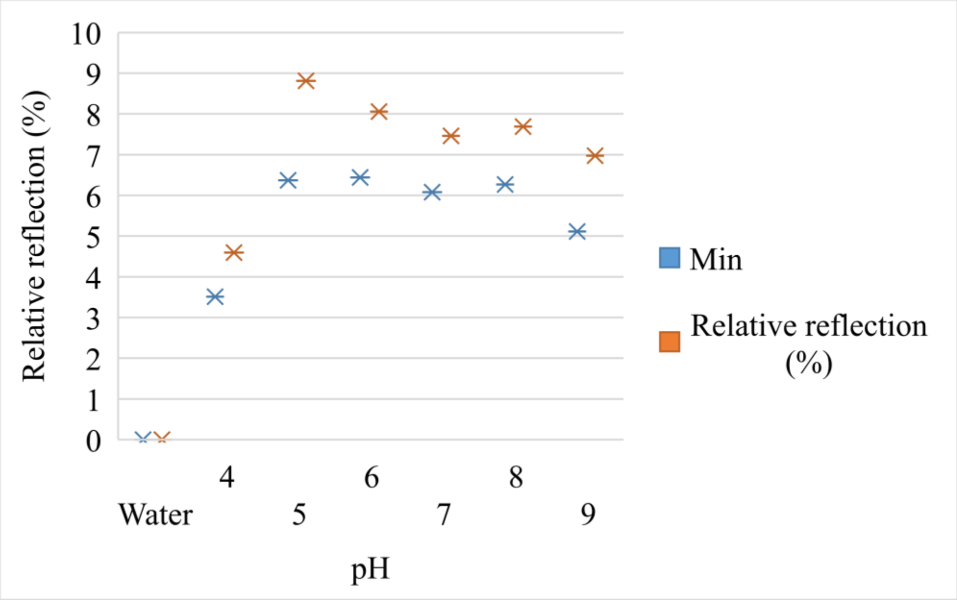

Figure C5. Minimum and maximum values for relative reflection with yellow filter over OLED detector.

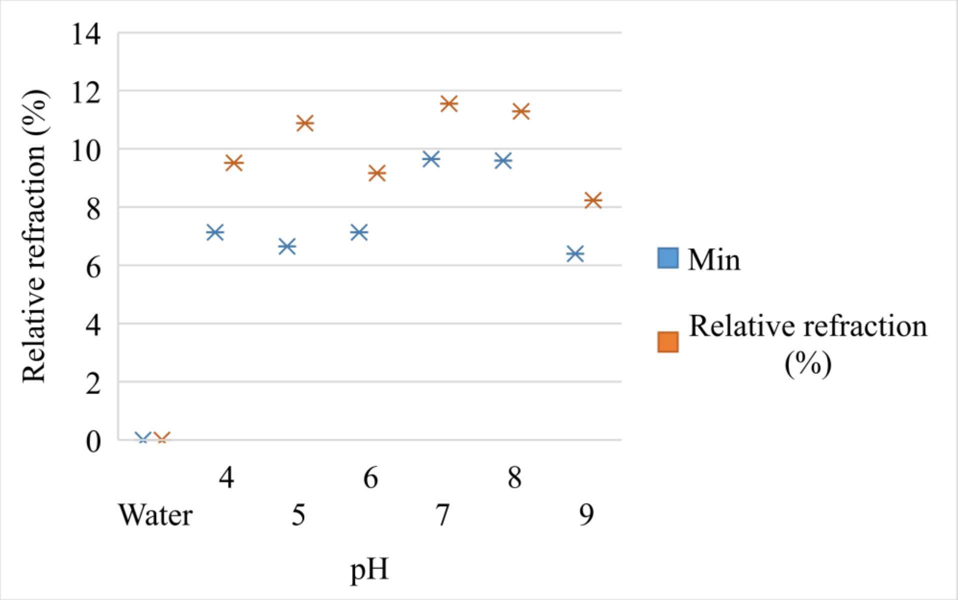

Figure C6. Minimum and maximum values for relative refraction with purple filter over OLED detector.

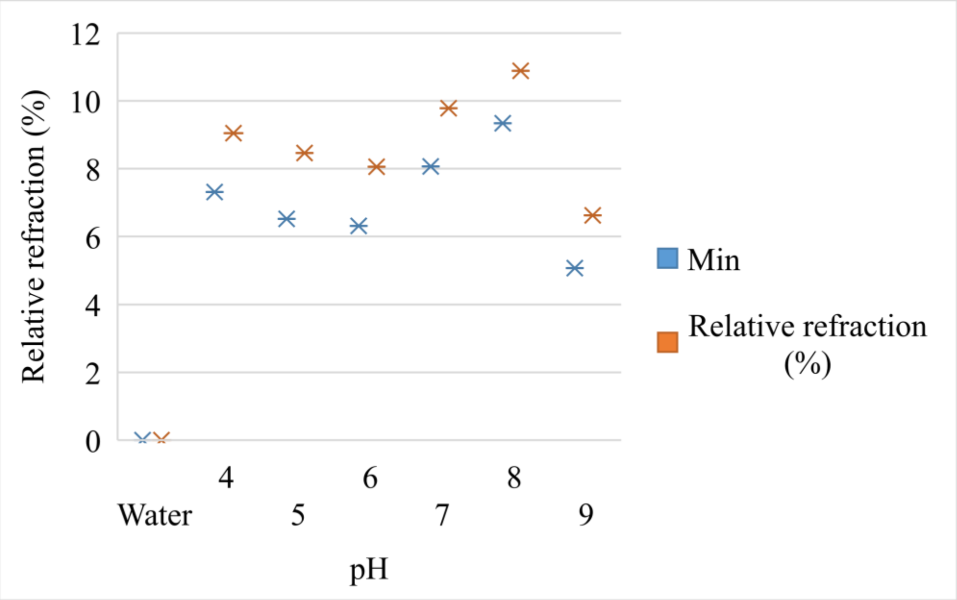

Figure C7. Minimum and maximum values for relative refraction with green filter over OLED detector.

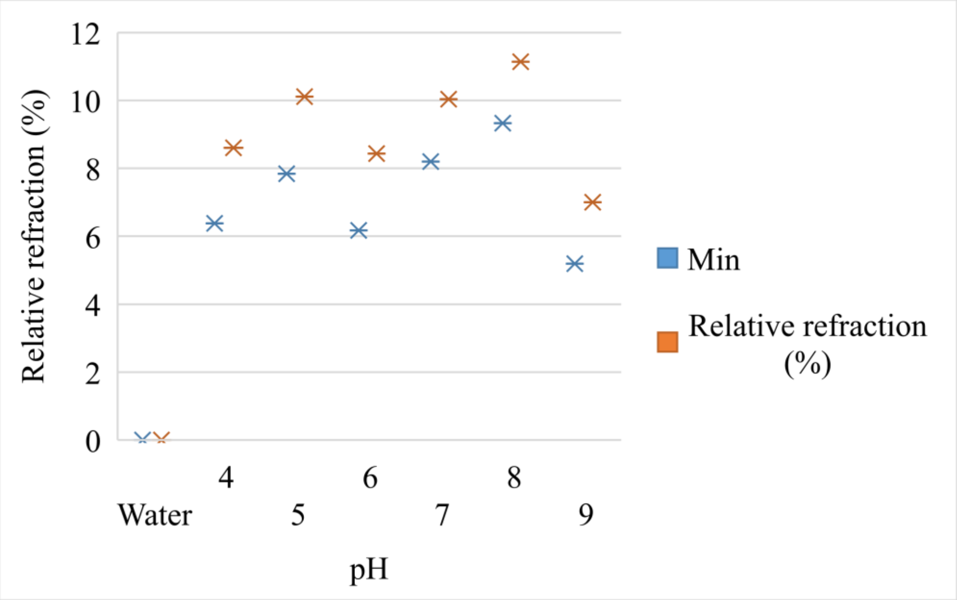

Figure C8. Minimum and maximum values for relative refraction with yellow filter over OLED detector.

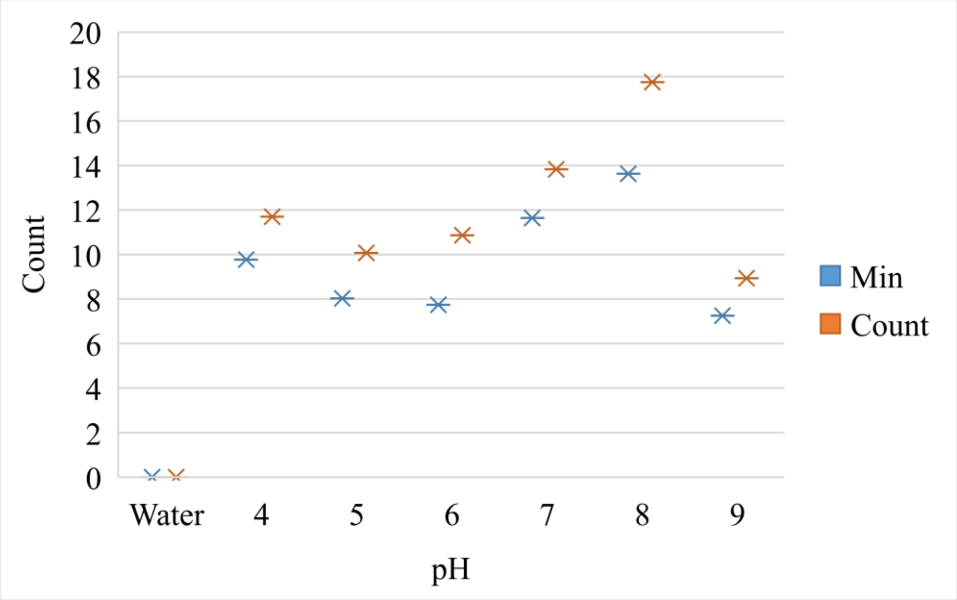

Figure C9. Minimum and maximum values for relative refraction with no filter over OLED detector.

ADDENDUM D ANGULAR SPECTRAL RESPONSE OF WHITE LEDS AND OLEDS

D.1 ANGULAR SPECTRAL RESPONSE OF WHITE LEDS

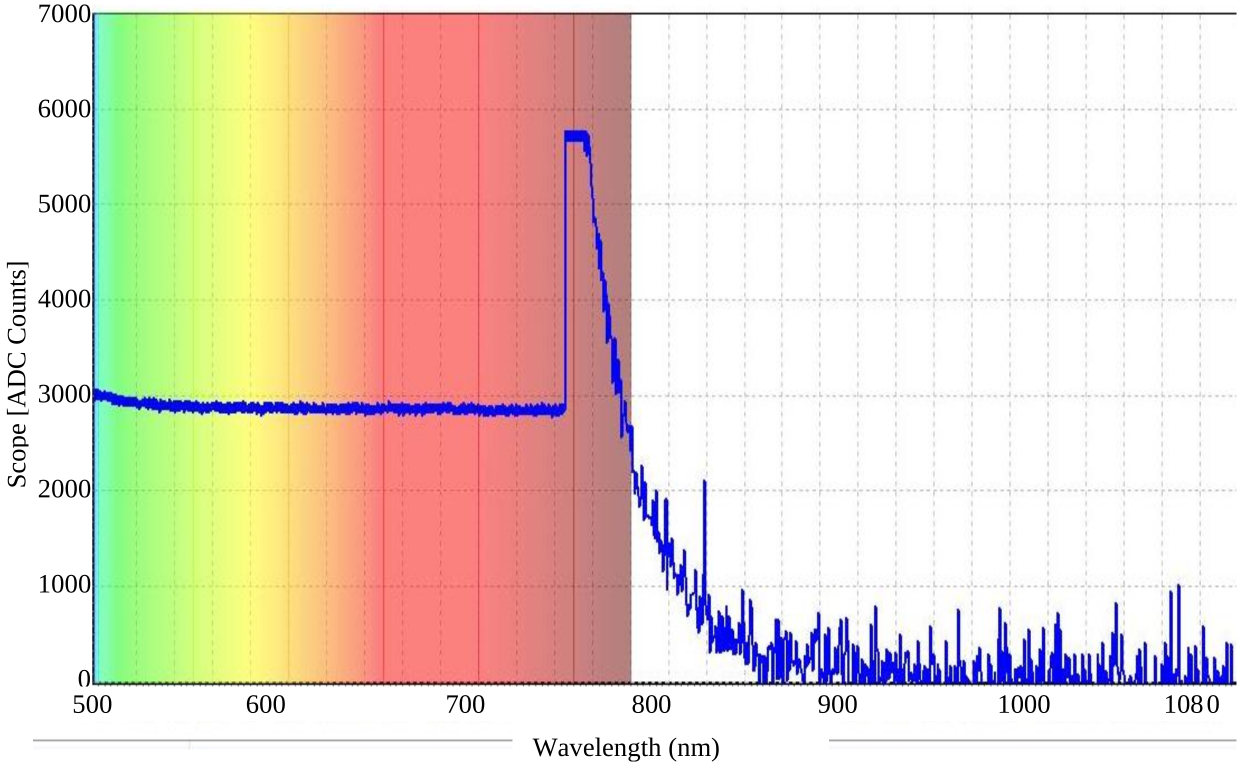

Figure D1. Spectral response of a white LED measured at 75 ° viewing angle

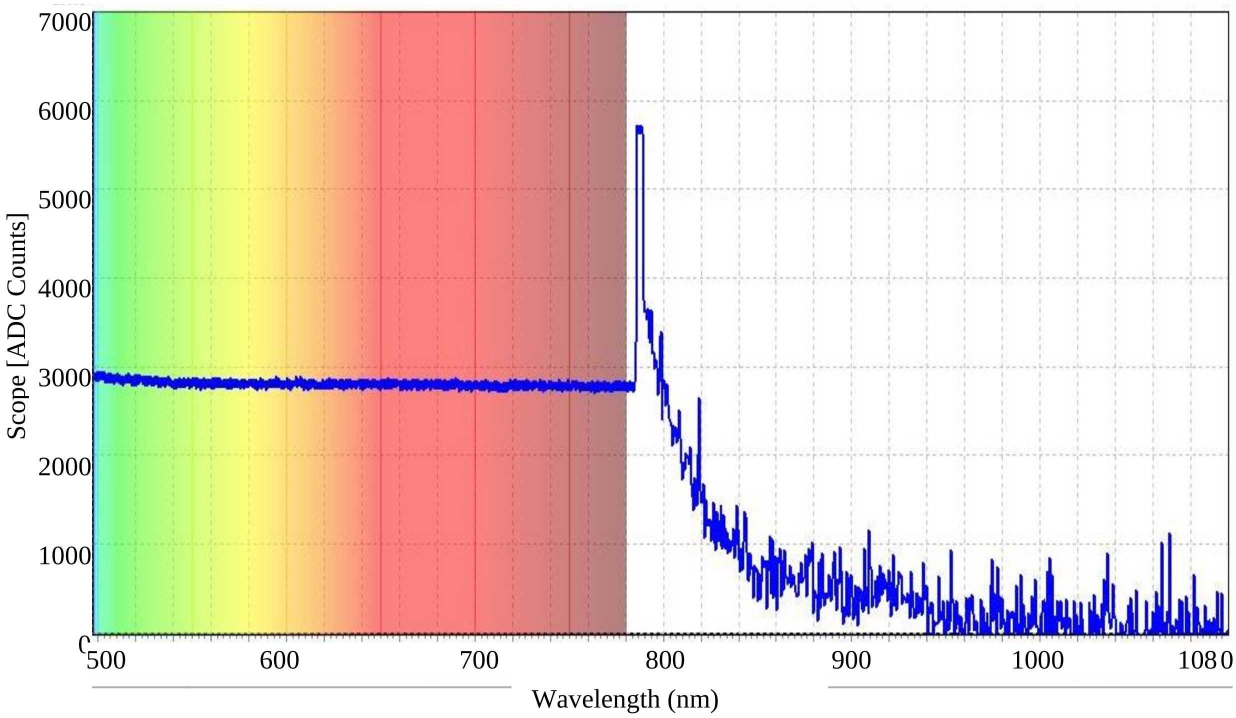

Figure D2. Spectral response of a white LED measured at 60 ° viewing angle.

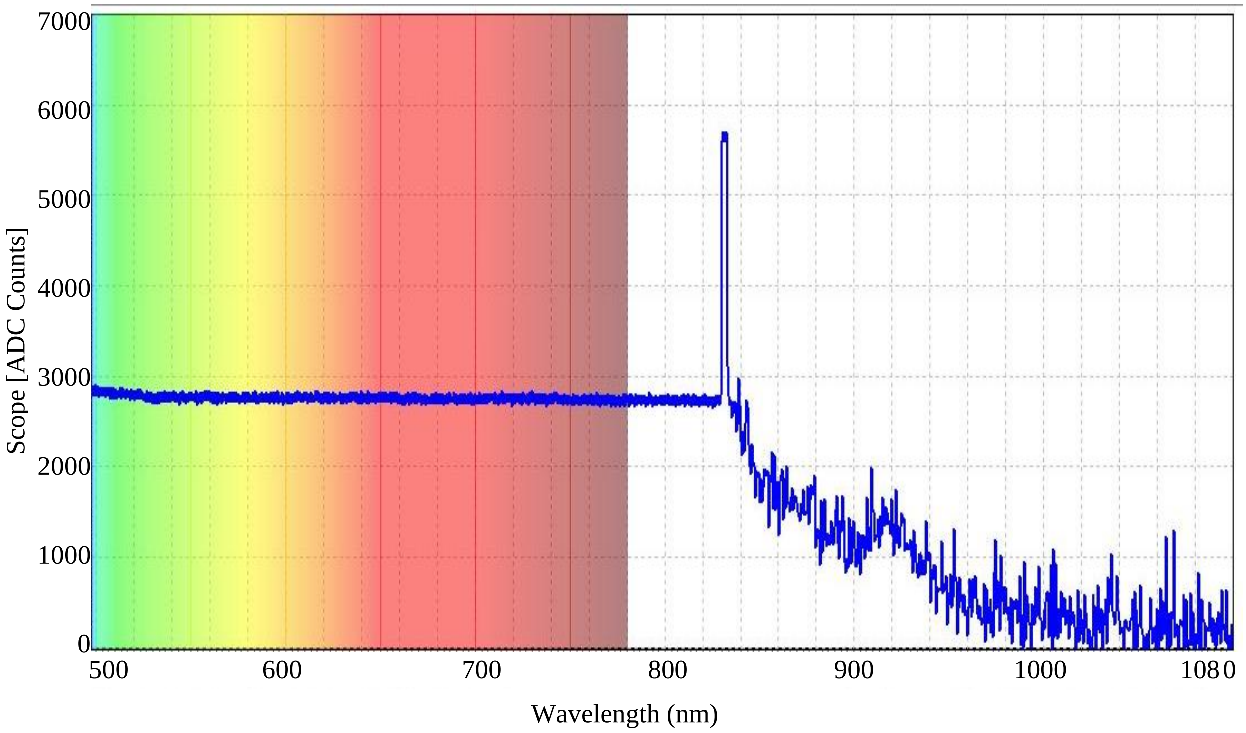

Figure D3. Spectral response of a white LED measured at 45 ° viewing angle.

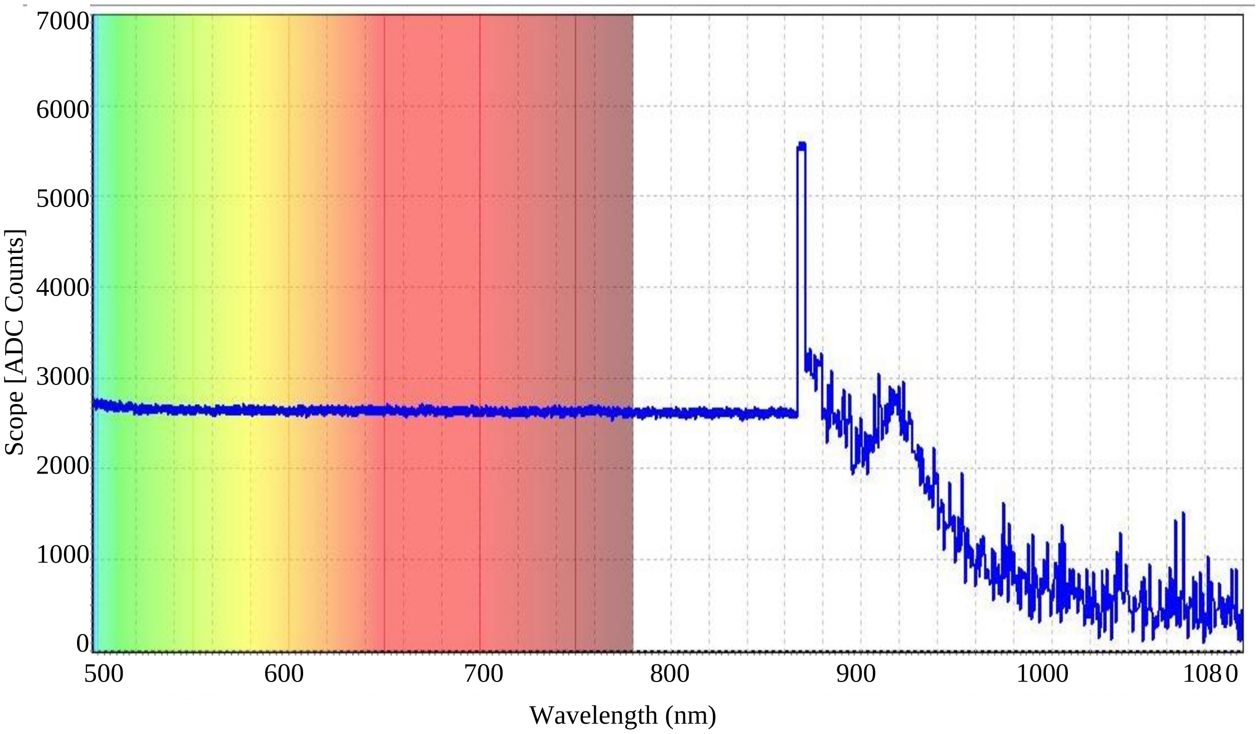

Figure D4. Spectral response of a white LED measured at 30 ° viewing angle.

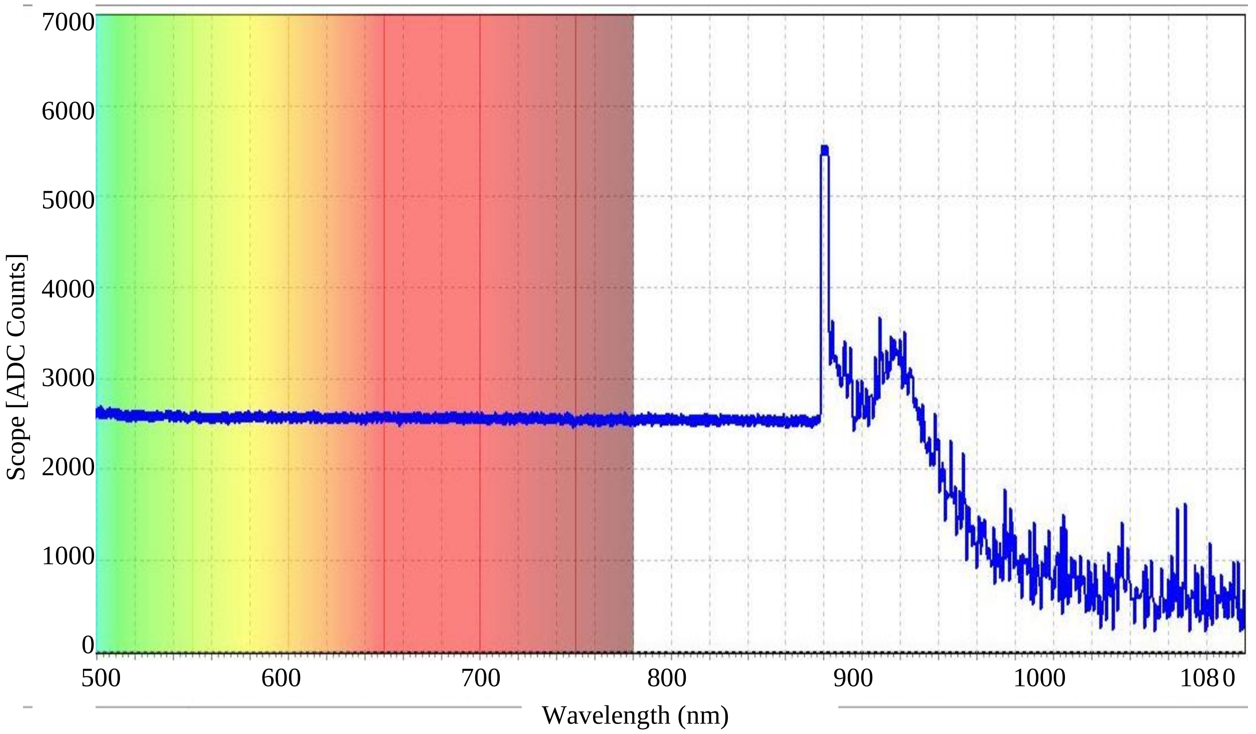

Figure D5. Spectral response of a white LED measured at 15 ° viewing angle.

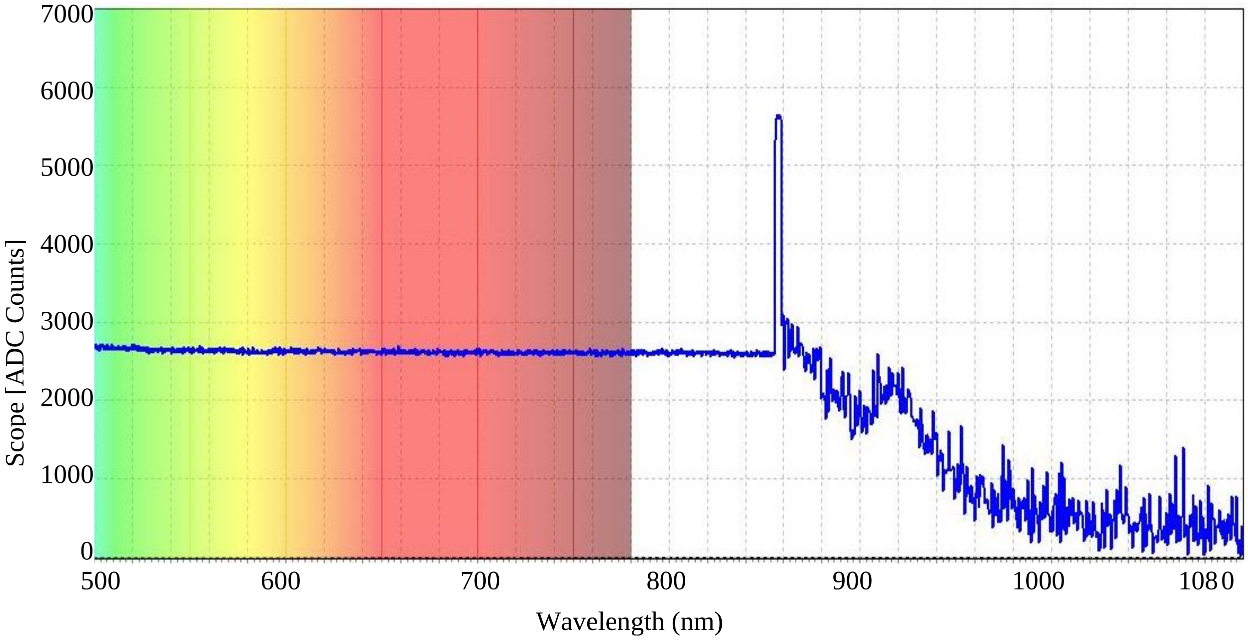

Figure D6. Spectral response of a white LED measured perpendicular to the panel (0 ° viewing angle).

D.2 ANGULAR SPECTRAL RESPONSE OF OLEDS

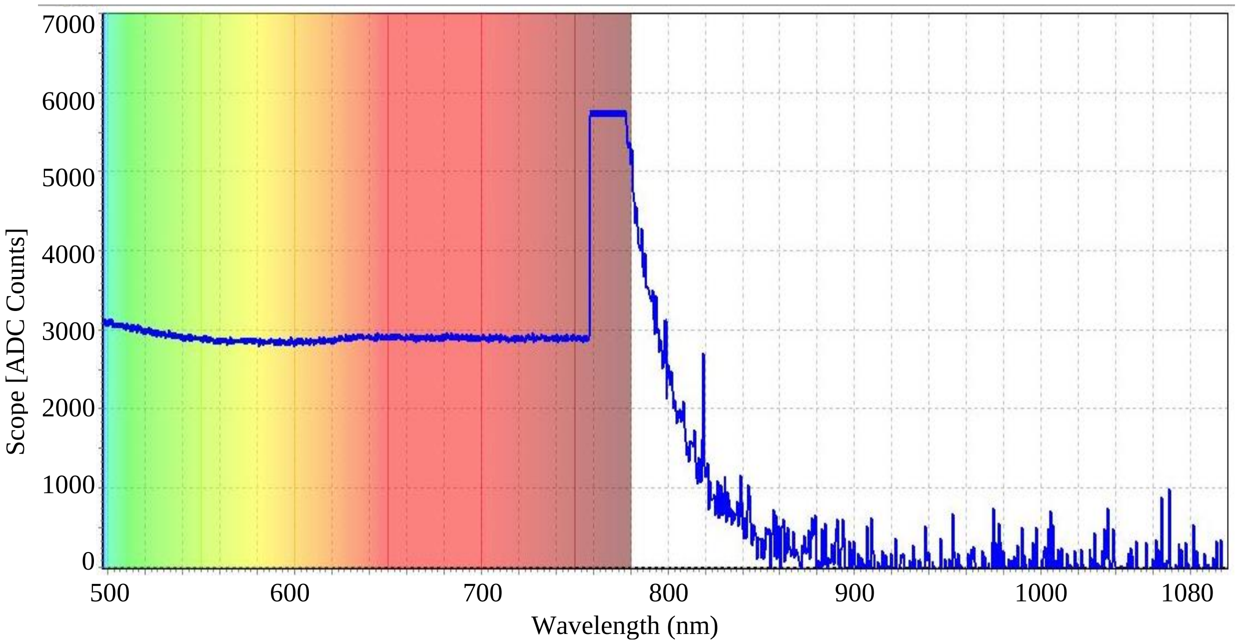

Figure D7. Spectral response of a flexible OLED panel measured at 75 ° viewing angle.

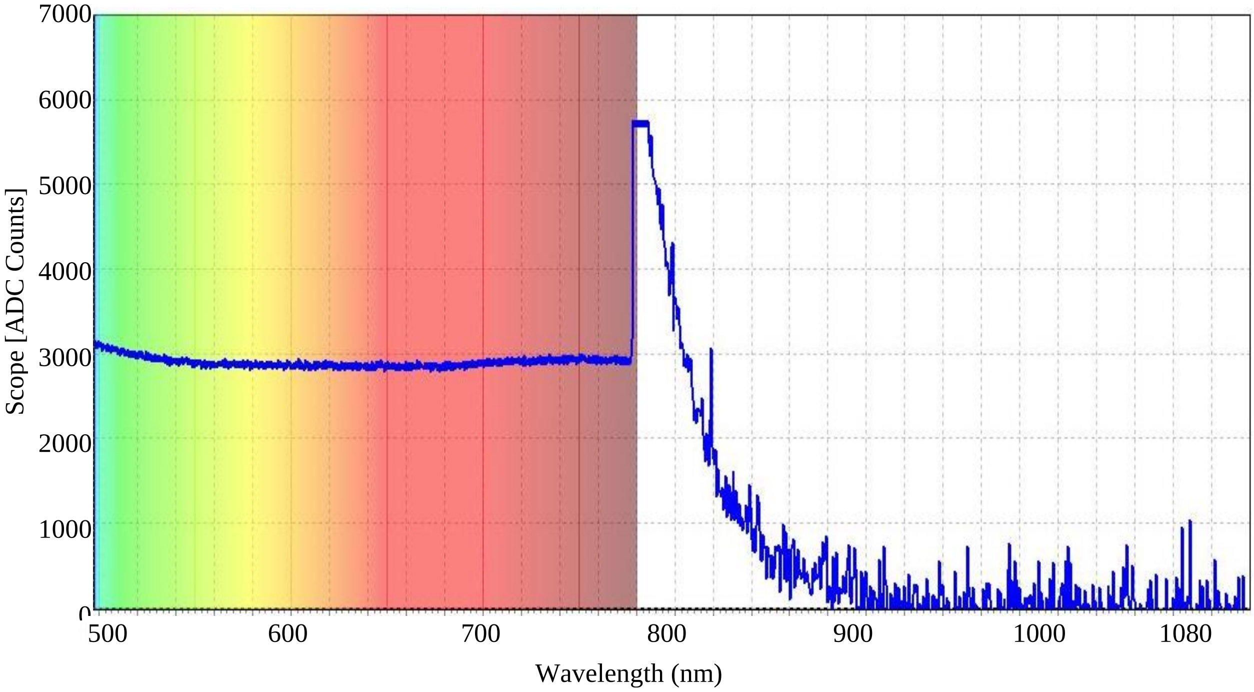

Figure D8. Spectral response of a flexible OLED panel measured at 60 ° viewing angle.

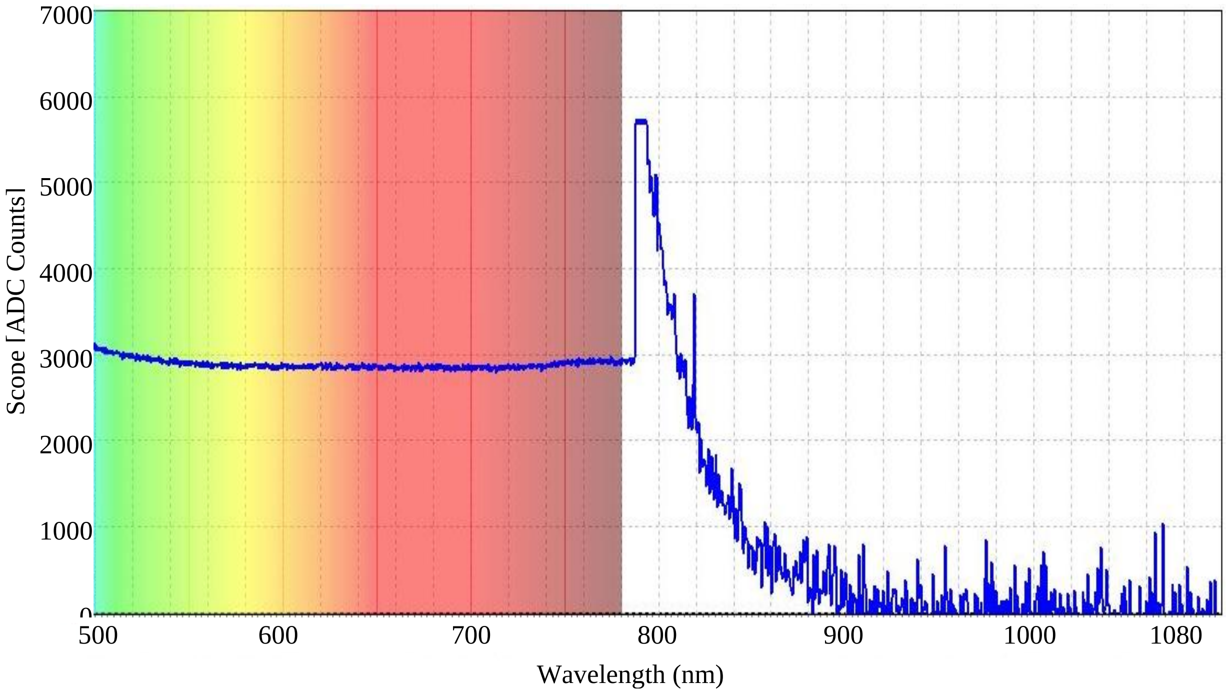

Figure D9. Spectral response of a flexible OLED panel measured at 45 ° viewing angle.

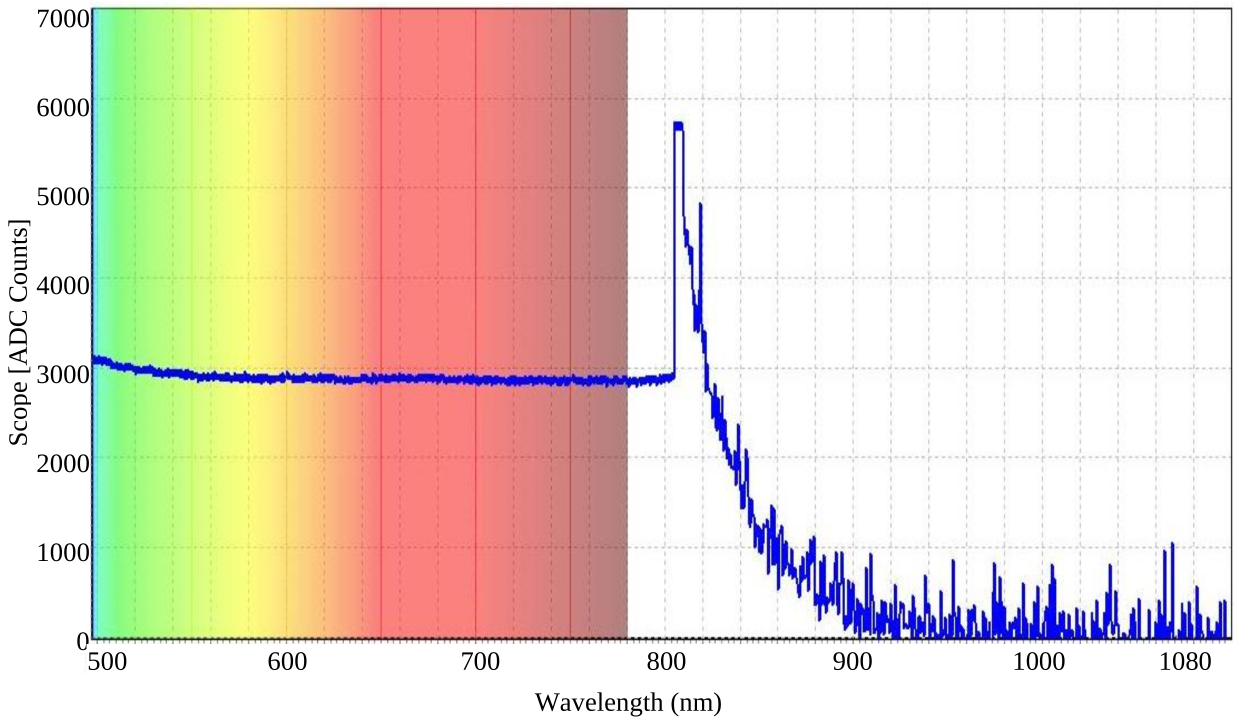

Figure D10. Spectral response of a flexible OLED panel measured at 30 ° viewing angle.

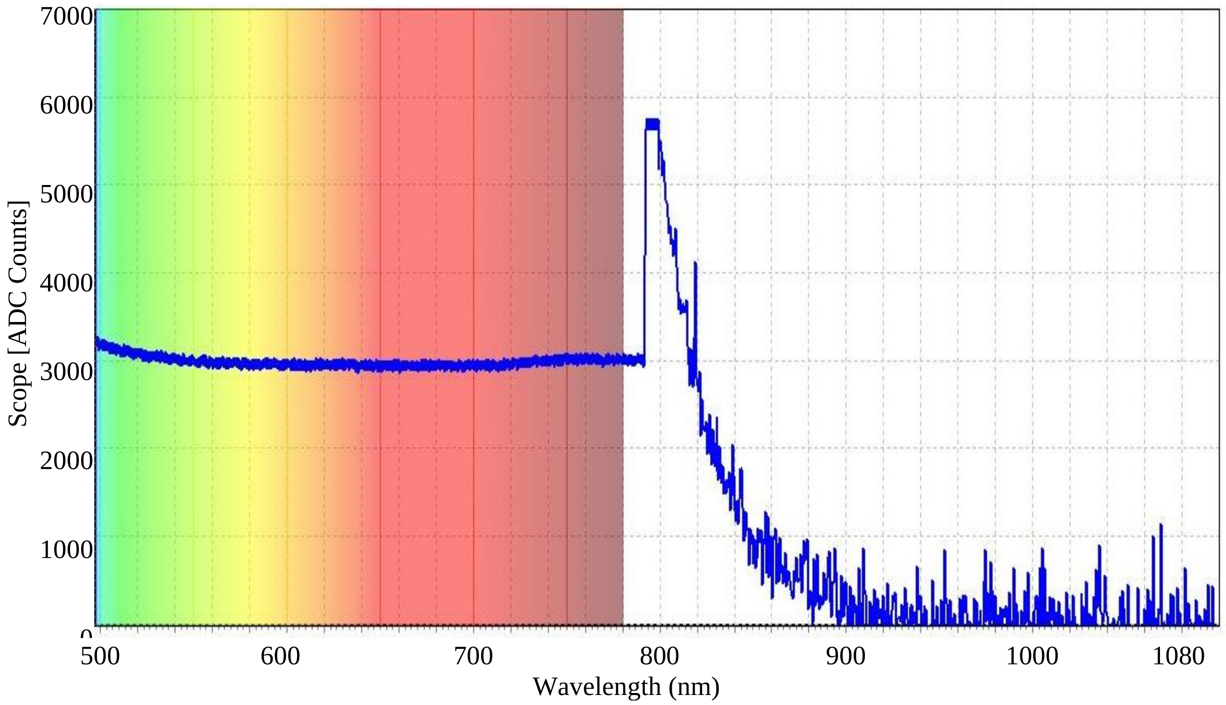

Figure D11. Spectral response of a flexible OLED panel measured at 15 ° viewing angle.

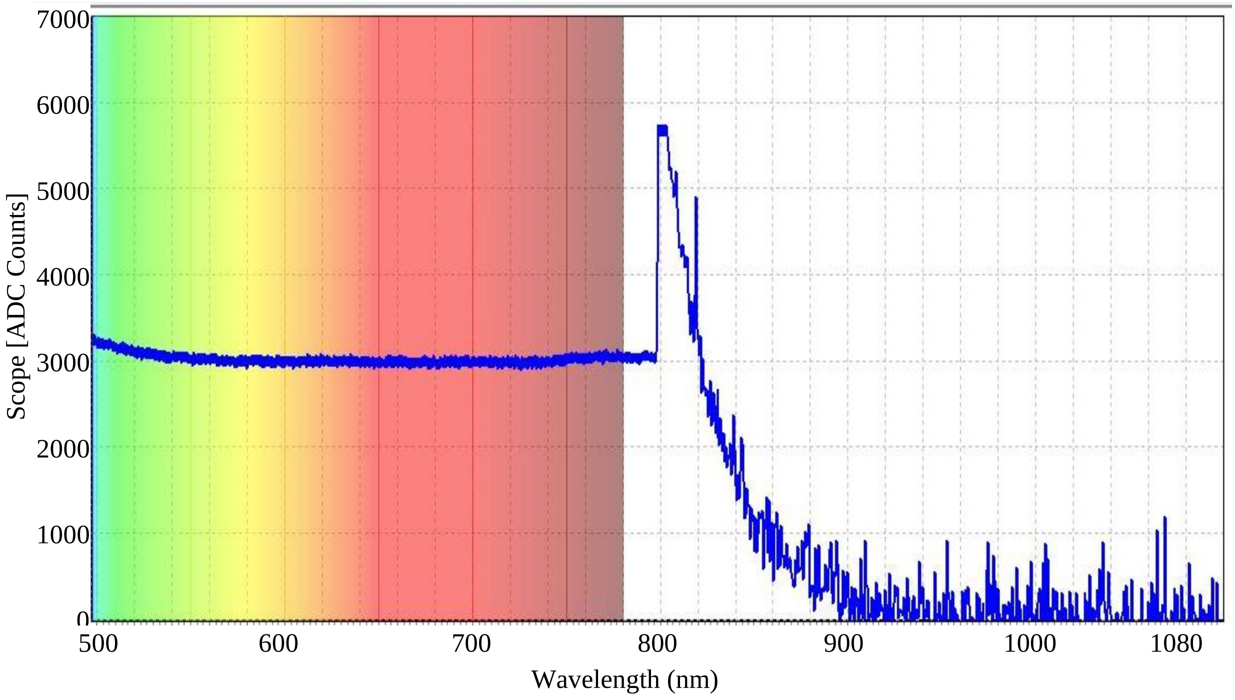

Figure D12. Spectral response of a flexible OLED panel measured perpendicular to the panel (0 ° viewing angle).

ADDENDUM E MATERIAL EMISSION SPECTRA

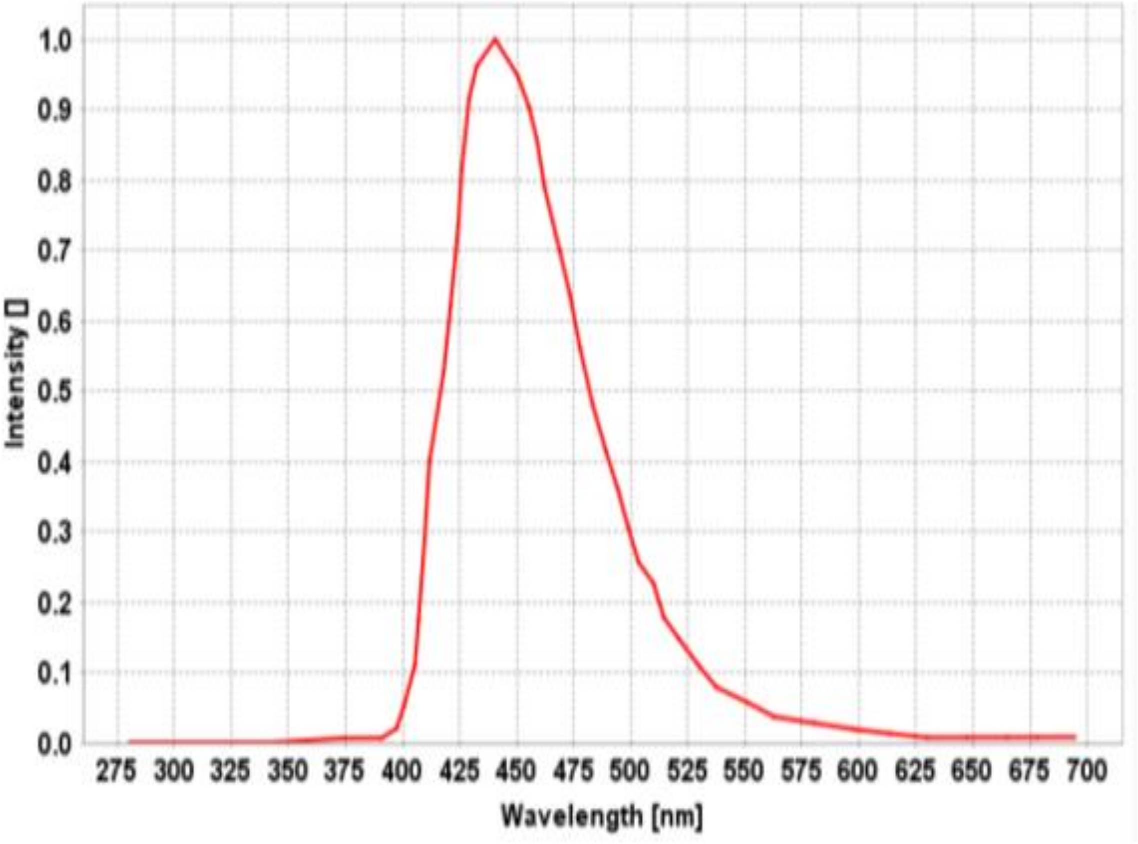

Figure E1. Emission spectrum of Alpha-NPD.

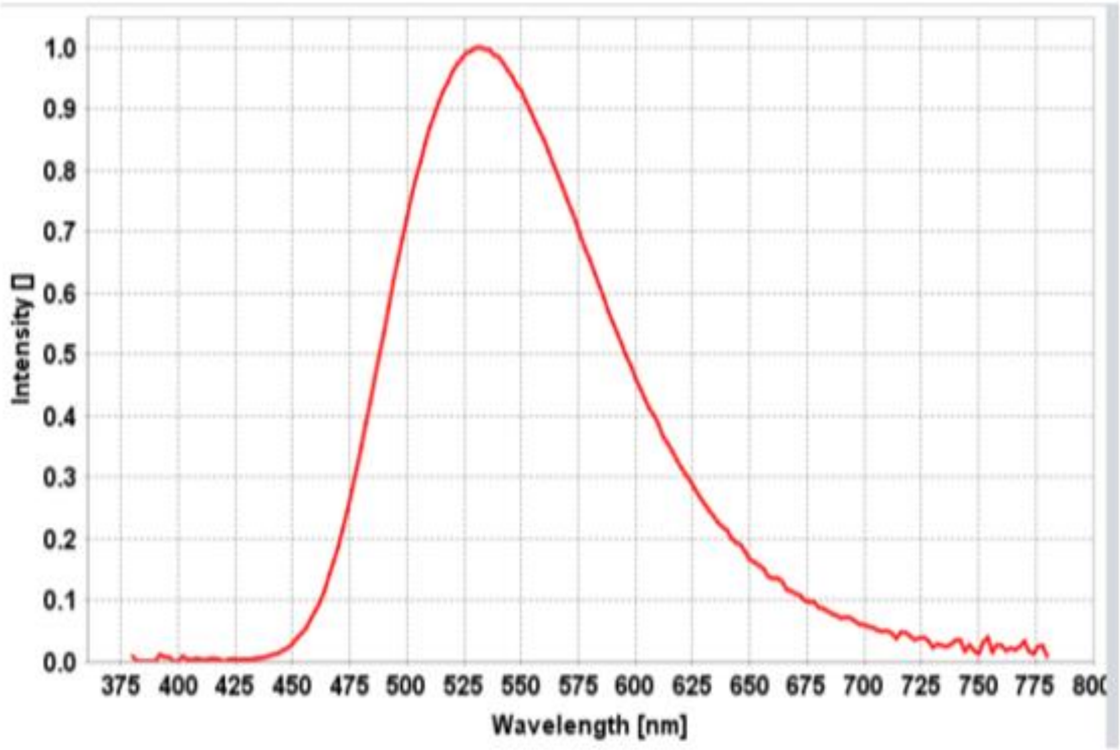

Figure E2. Emission spectrum of Alq.

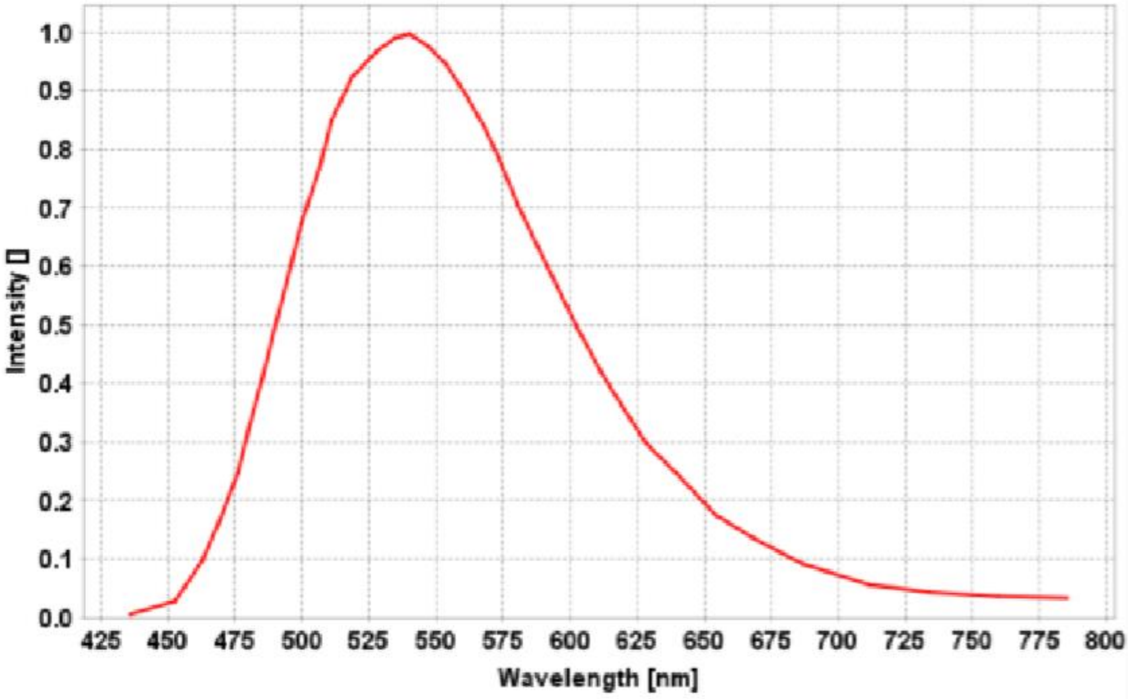

Figure E3. Emission spectrum of Alq3.

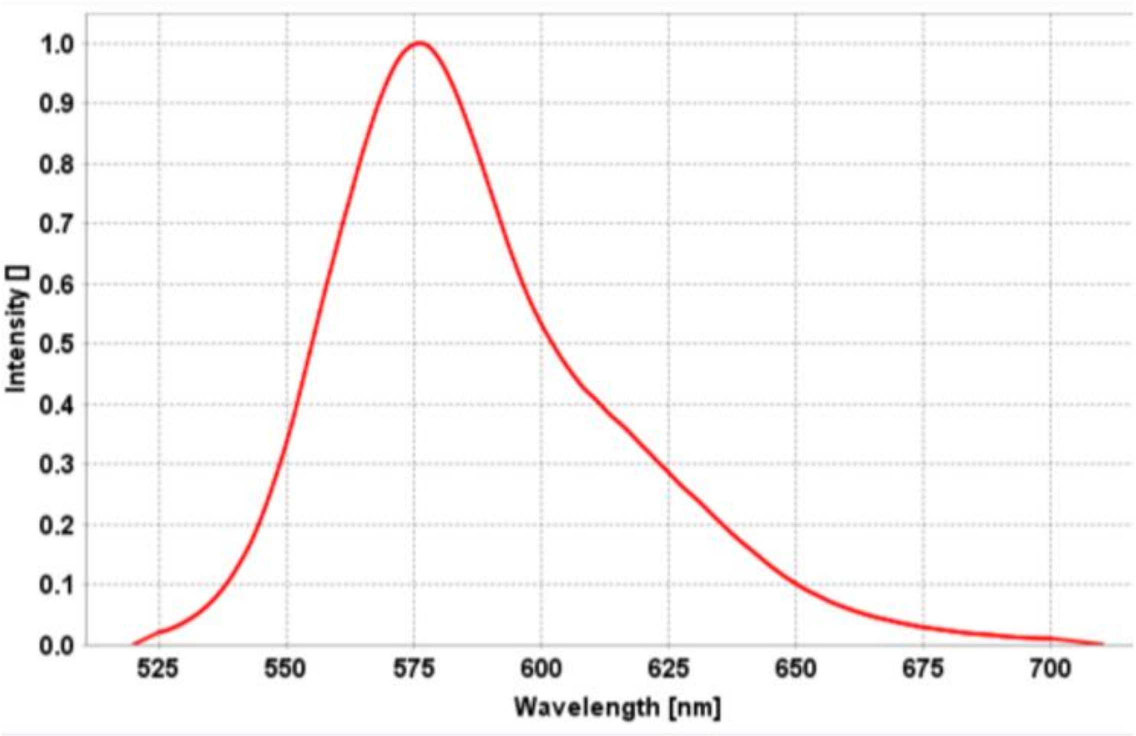

Figure E4. Emission spectrum of DOO-MEH-PPV

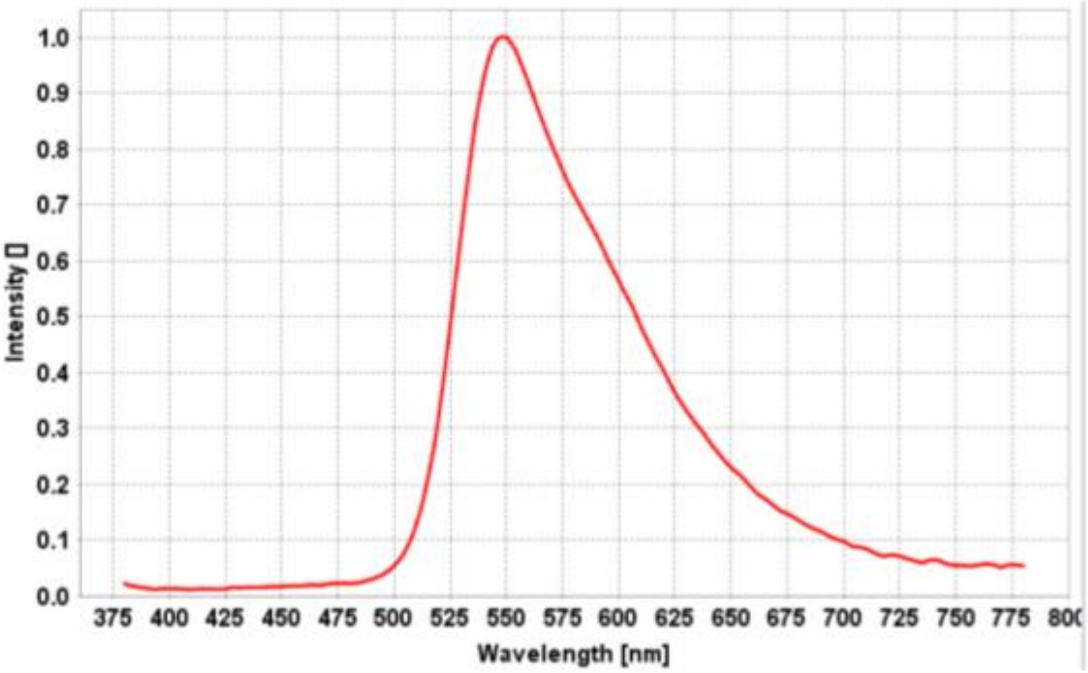

Figure E5. Emission spectrum of Super yellow.

ADDENDUM F MATERIAL REFRACTION INDEX

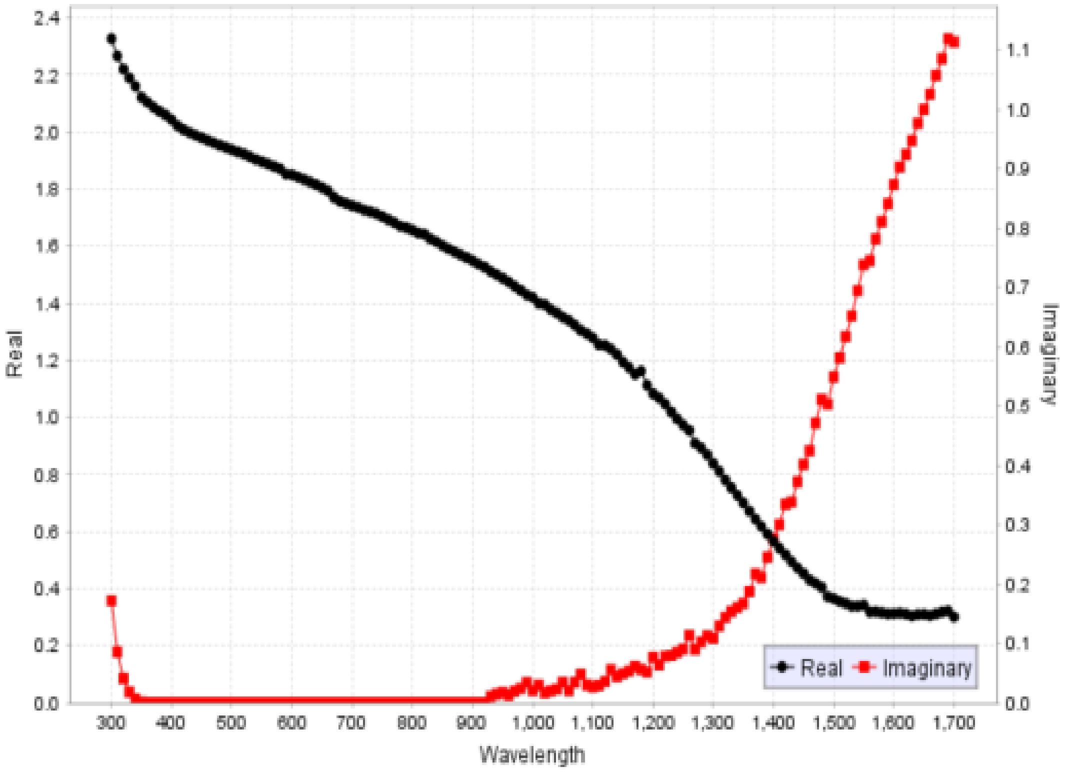

Figure F1. Refraction index of ITO.

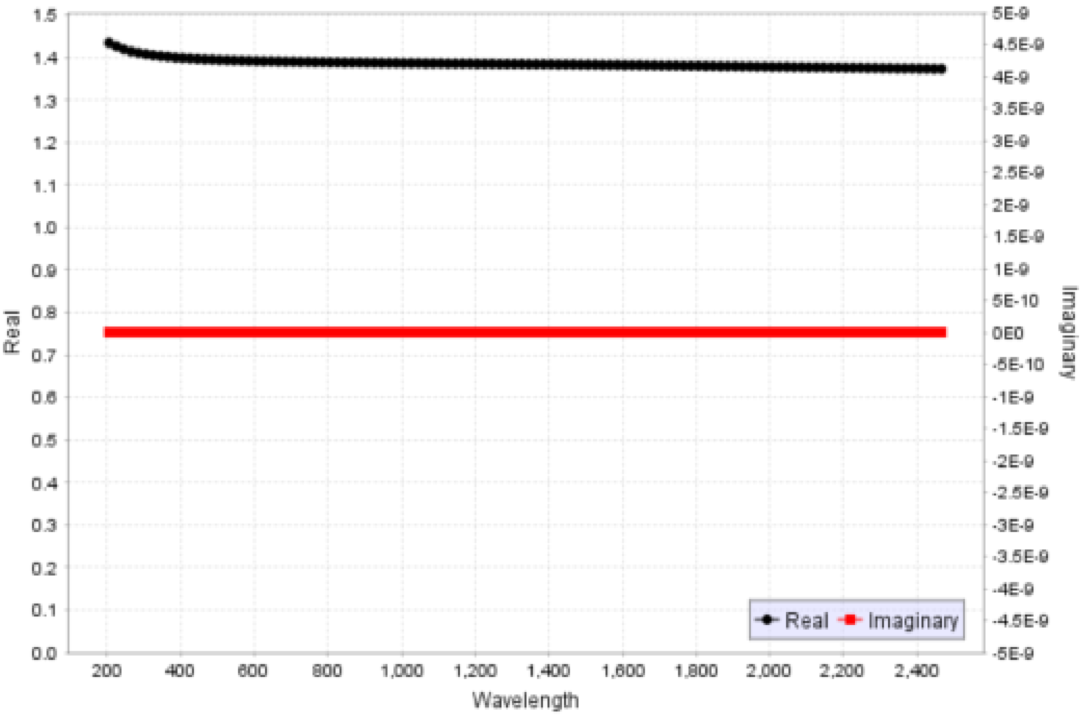

Figure F2. Refraction index of LiF.

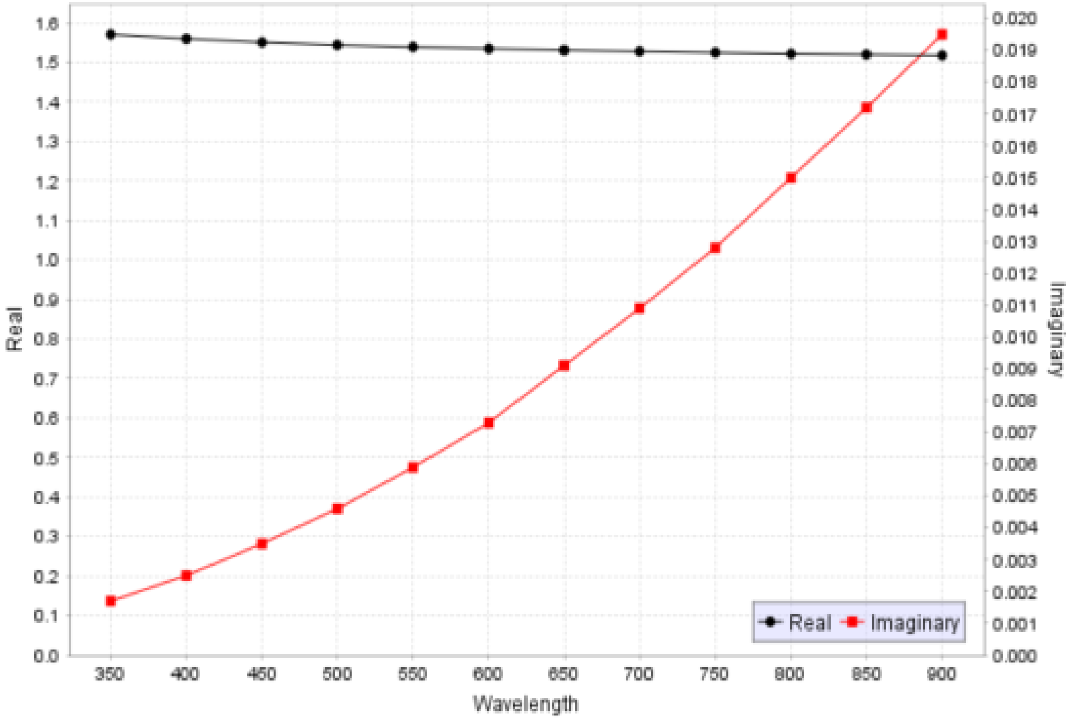

Figure F3. Refraction index of PEDOT BaytronP CH8000.

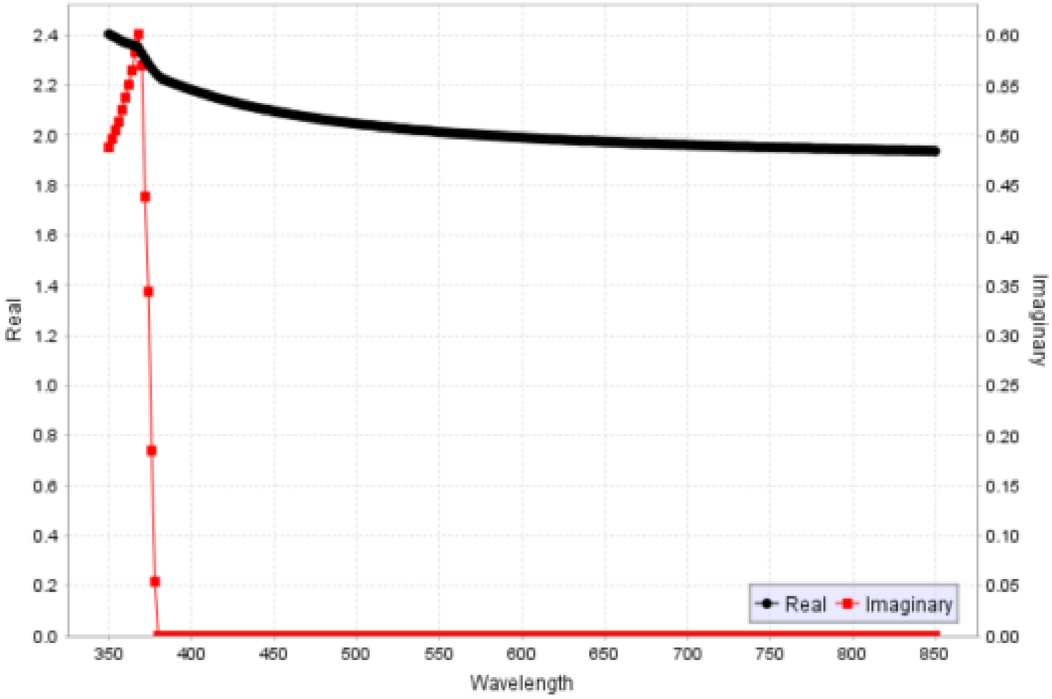

Figure F4. Refraction index of ZnO.

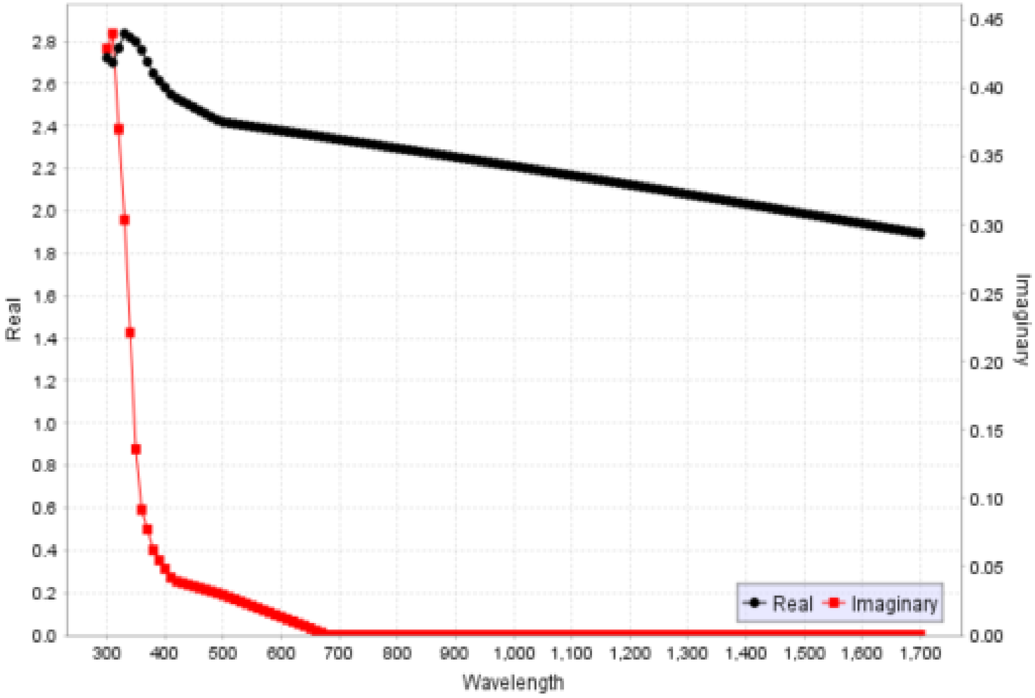

Figure F5. Refraction index of ZnS.

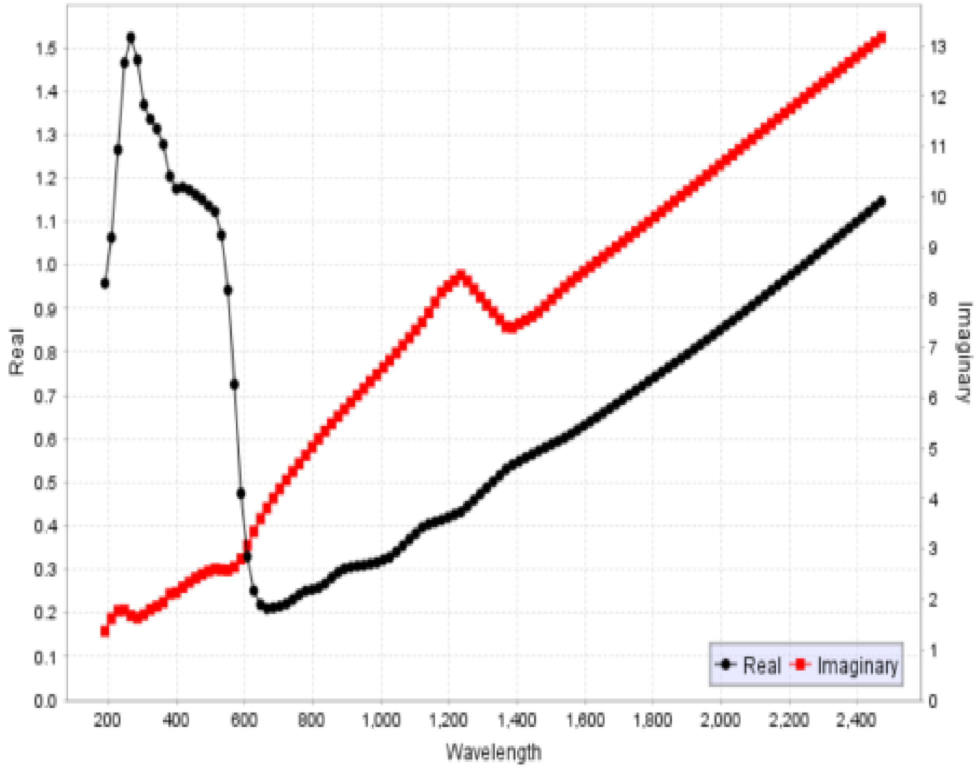

Figure F6. Refraction index of copper (Cu).

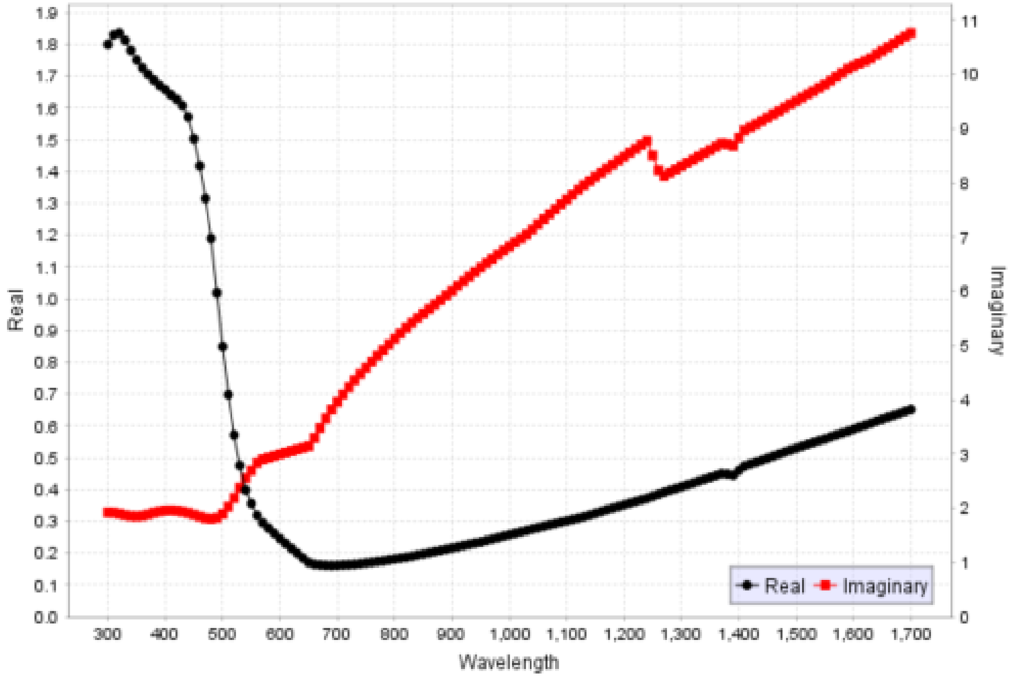

Figure F7. Refraction index of gold (Au).

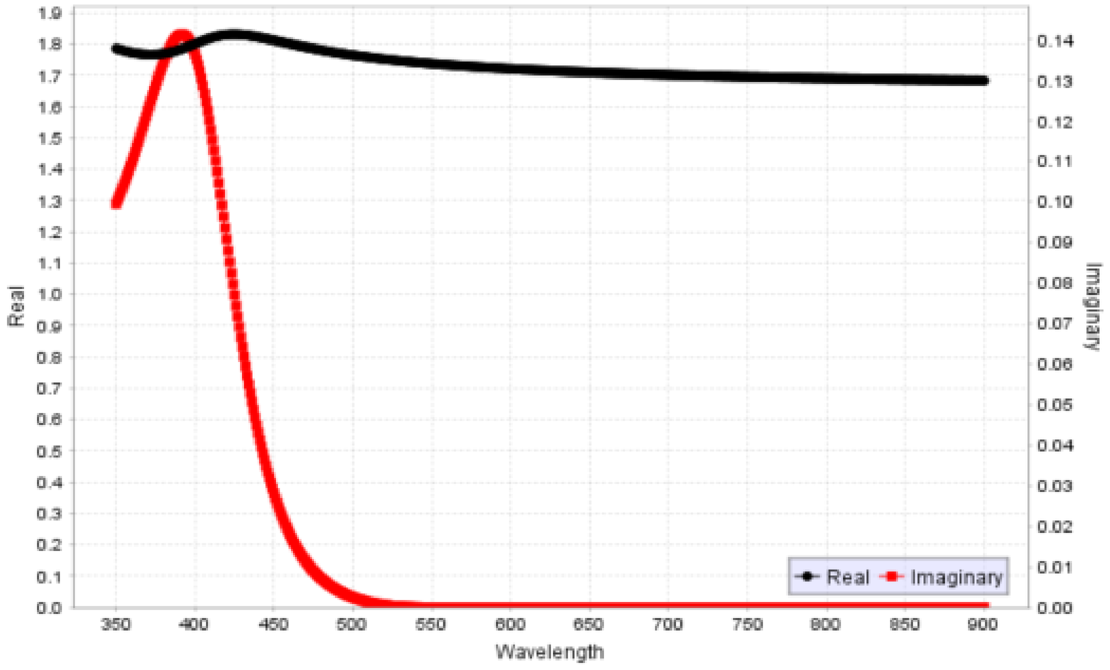

Figure F8. Refraction index of Alq3.

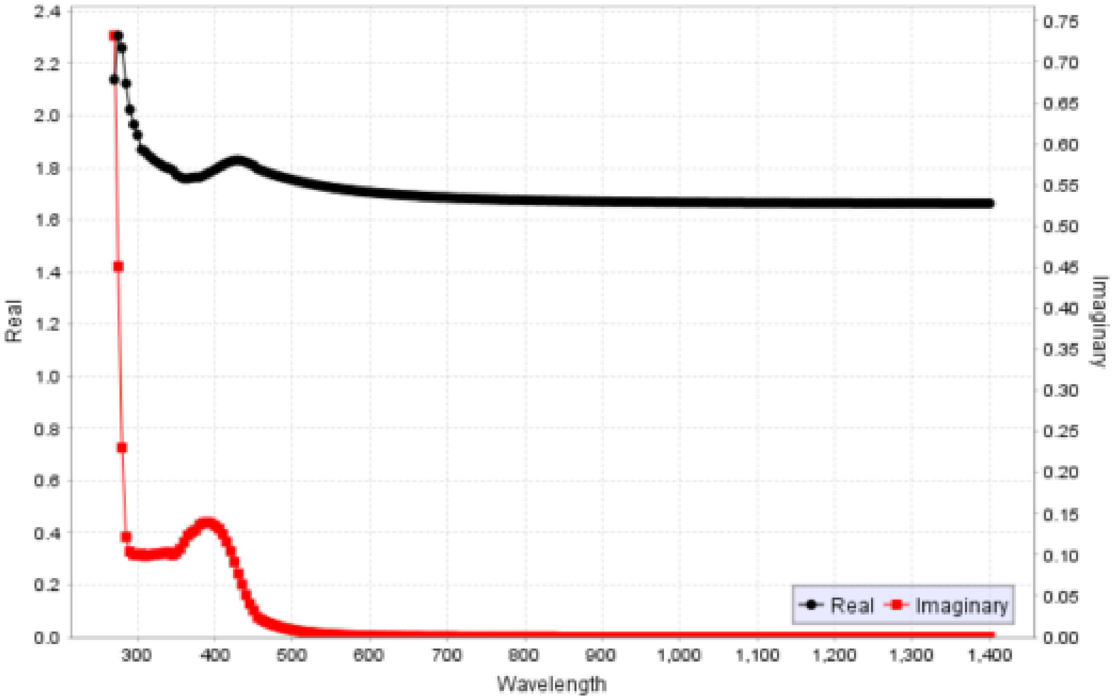

Figure F9. Refraction index of alq.

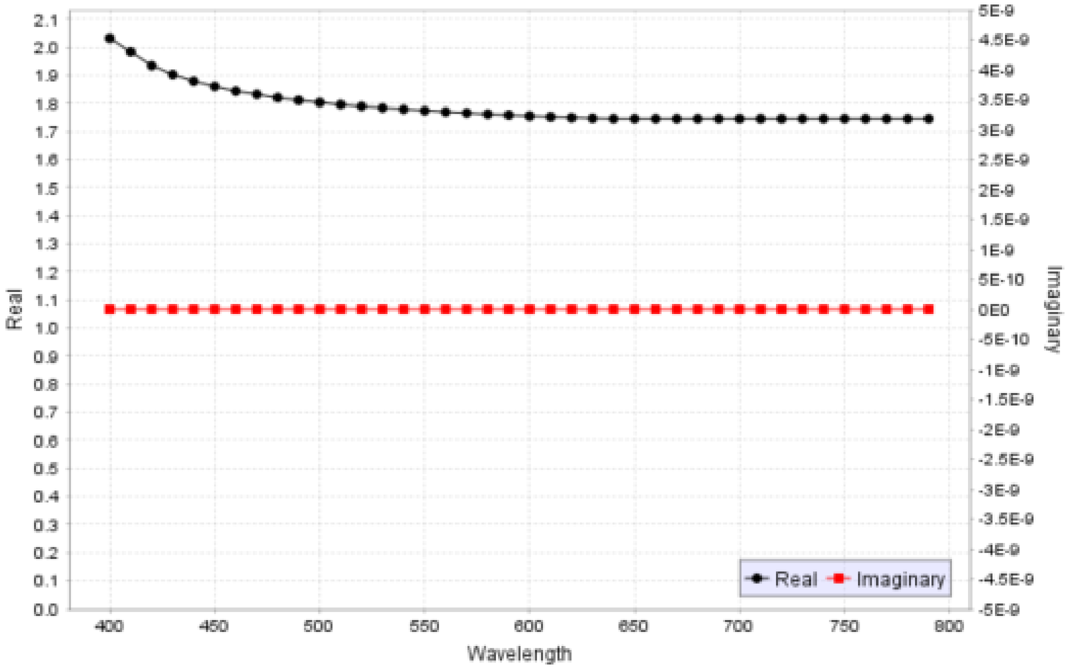

Figure F10. Refraction index of Alpha-NPD.

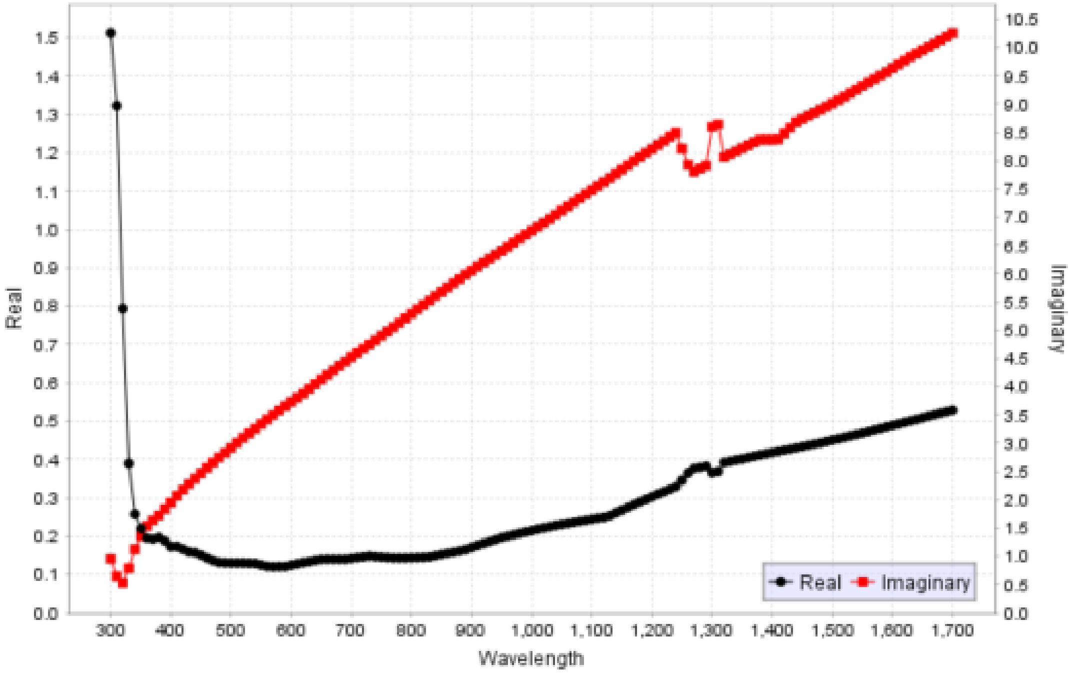

Figure F11. Refraction index of silver (Ag).

ADDENDUM G SIMULATED OLEDS

G.1 ITO/ALQ3/AL OLED

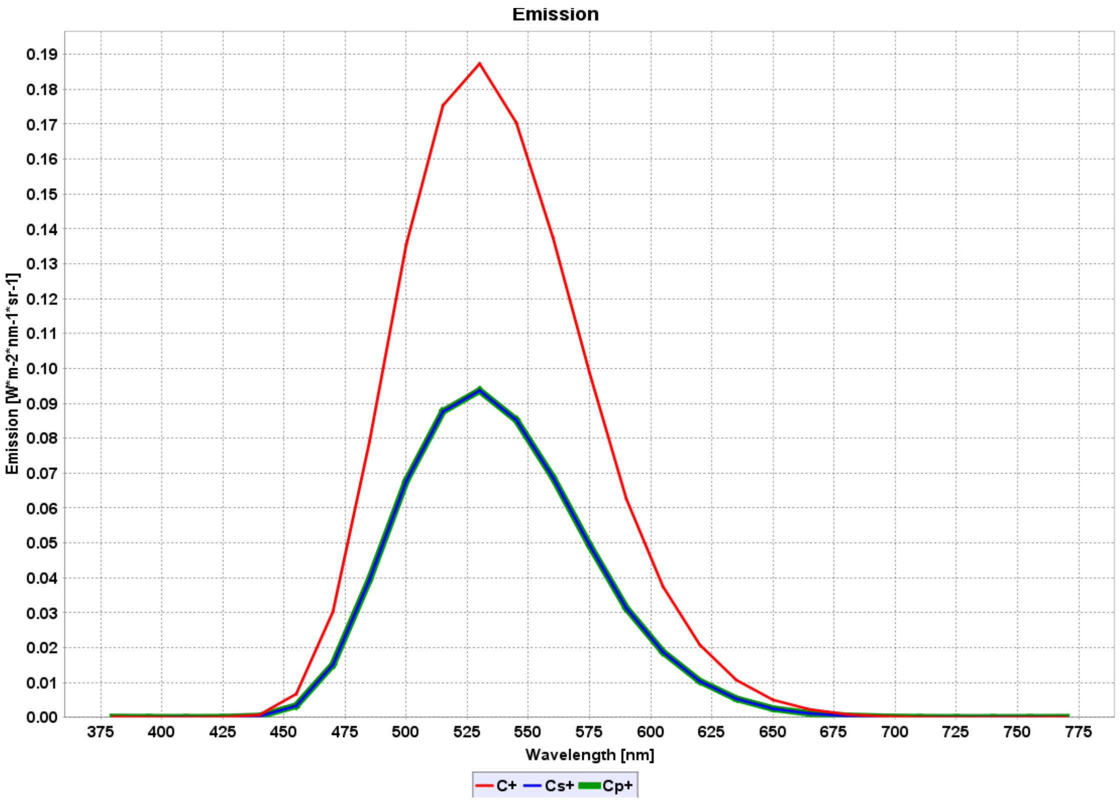

Figure G1. Emission spectrum of an ITO/Alq3/AL OLED.

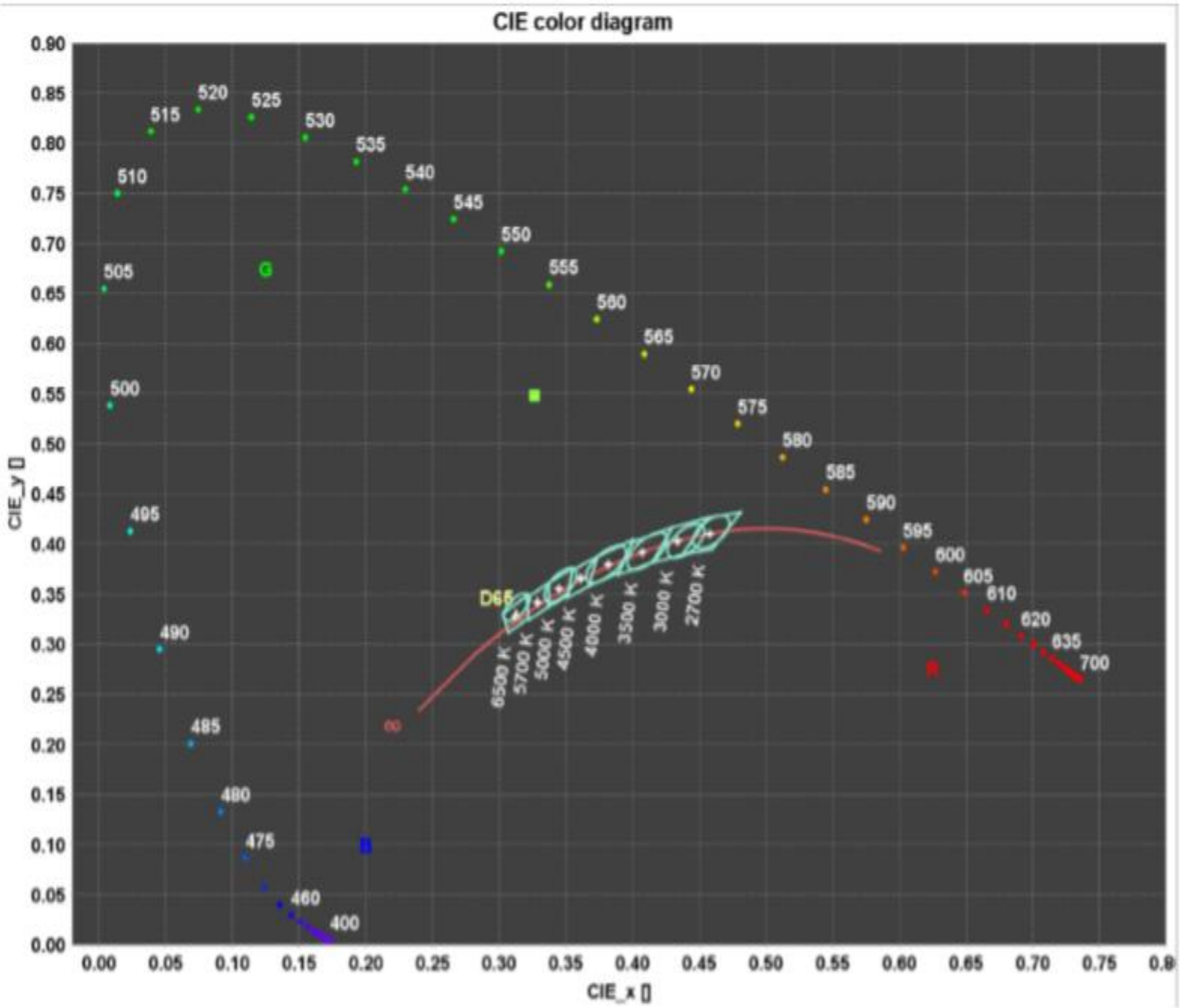

Figure G2. Colour diagram of an ITO/Alq3/AL OLED.

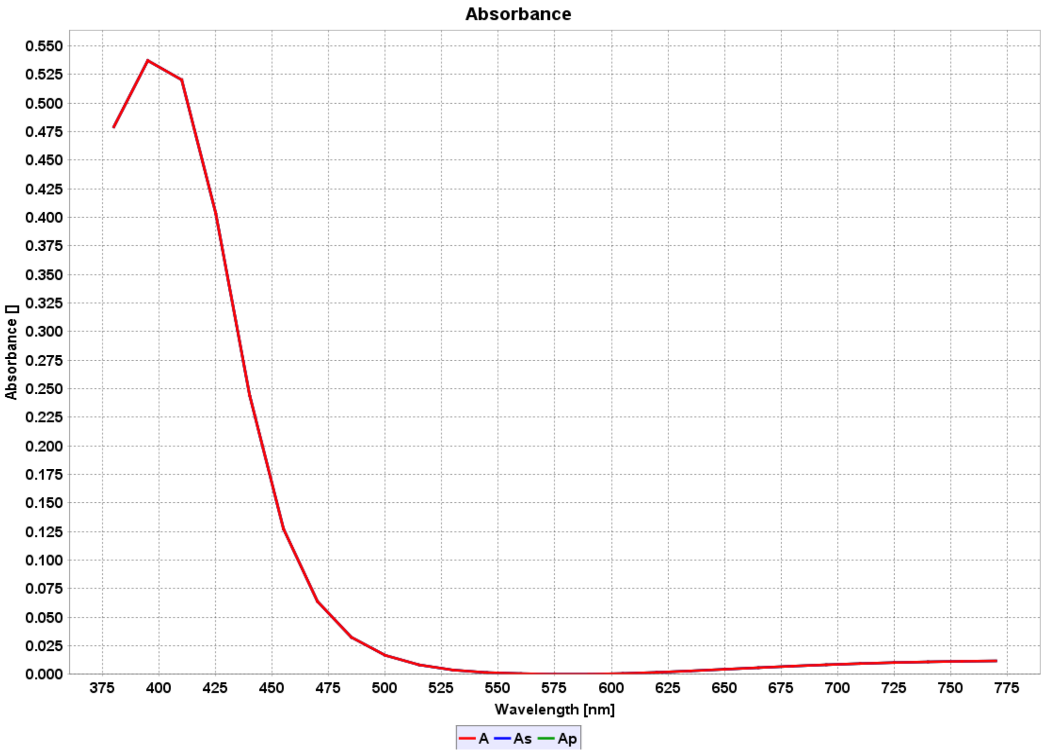

Figure G3. Absorbance of an ITO/Alq3/AL OLED.

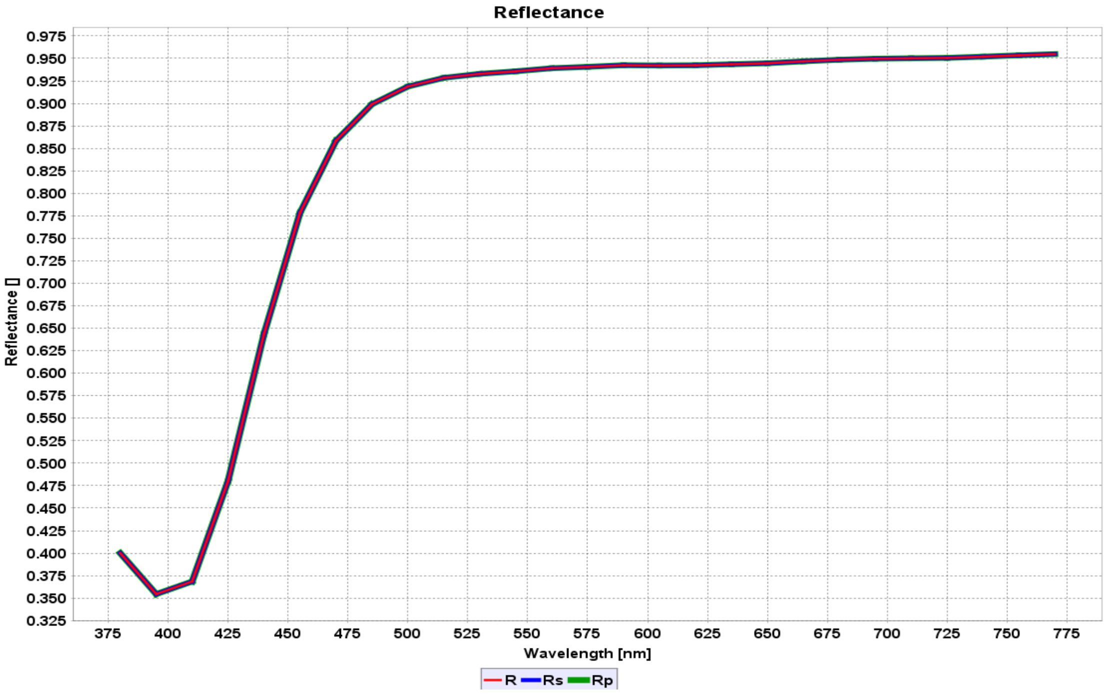

Figure G4. Reflectance of an ITO/Alq3/AL OLED.

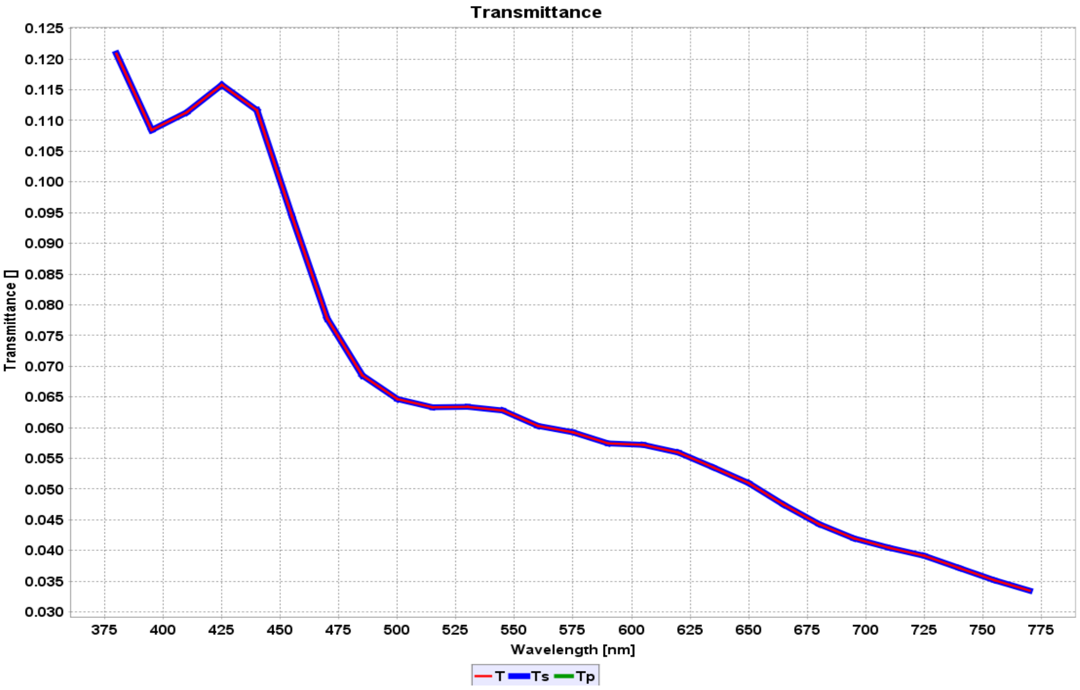

Figure G5.. Transmittance of an ITO/Alq3/AL OLED.

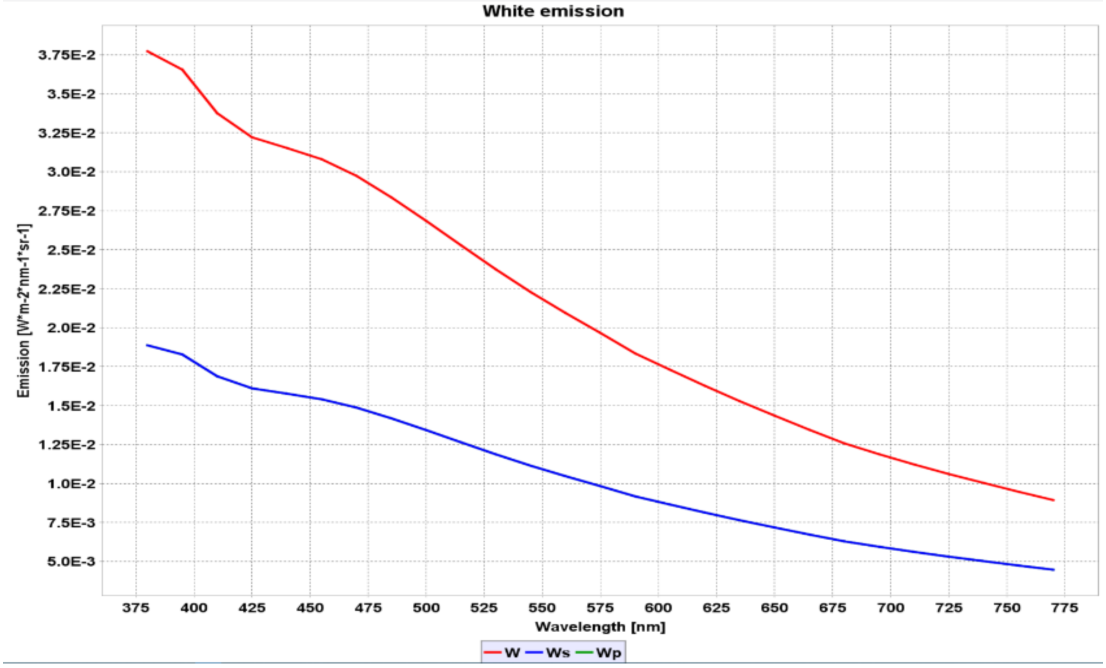

Figure G6. White emission of an ITO/Alq3/AL OLED.

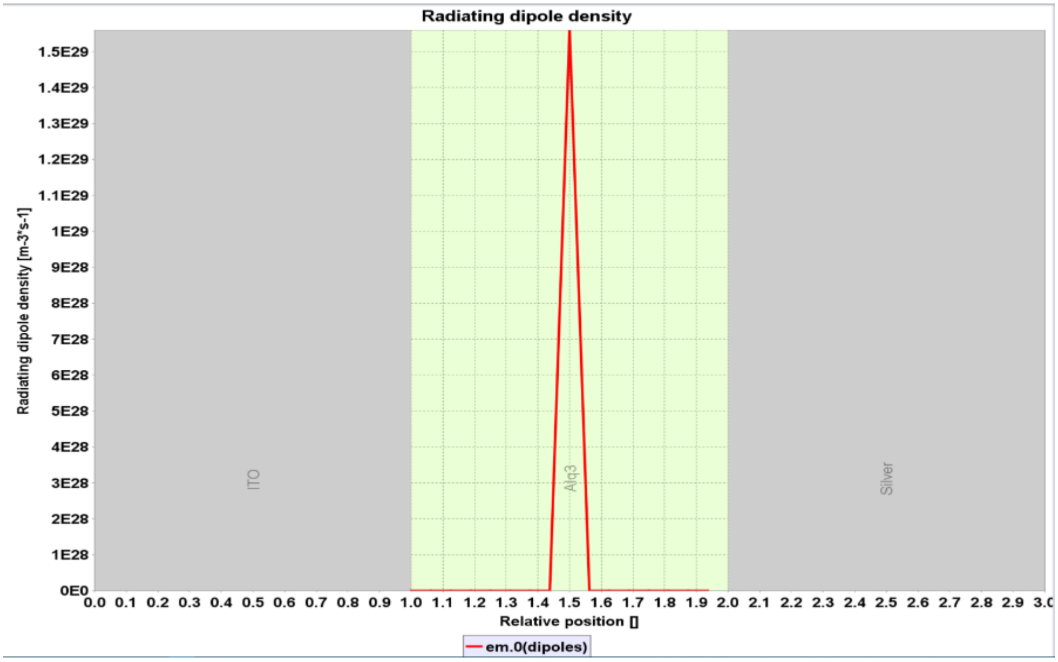

Figure G7. Radiating density of an ITO/Alq3/AL OLED.

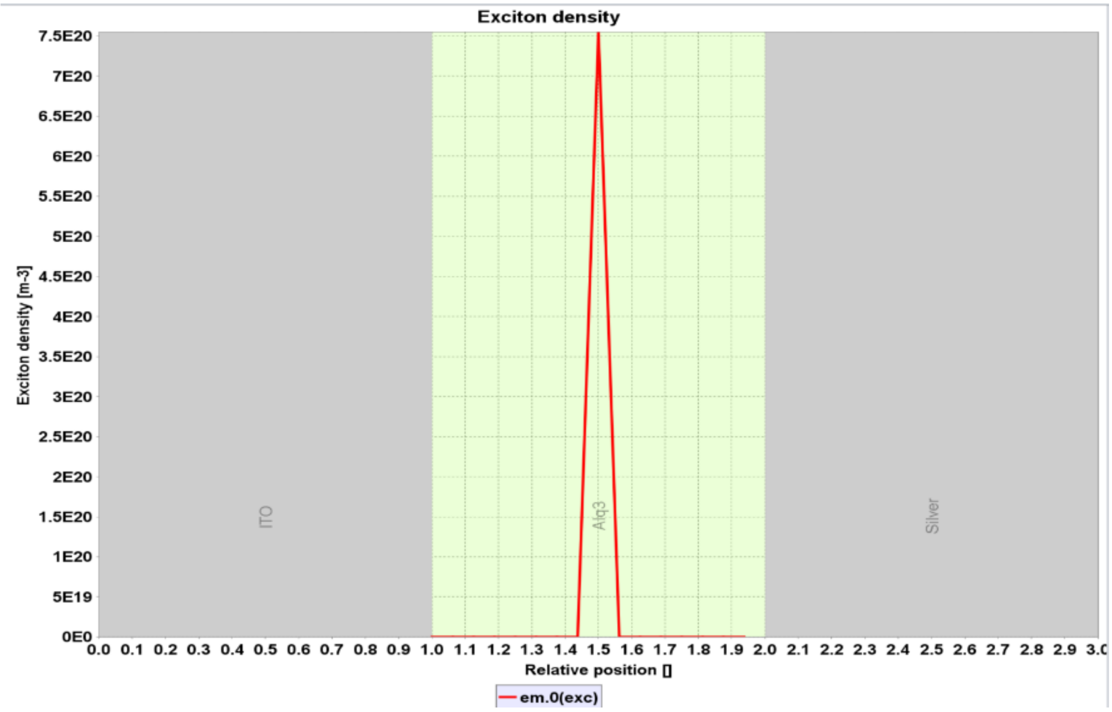

Figure G8. Exciton density of an ITO/Alq3/AL OLED.

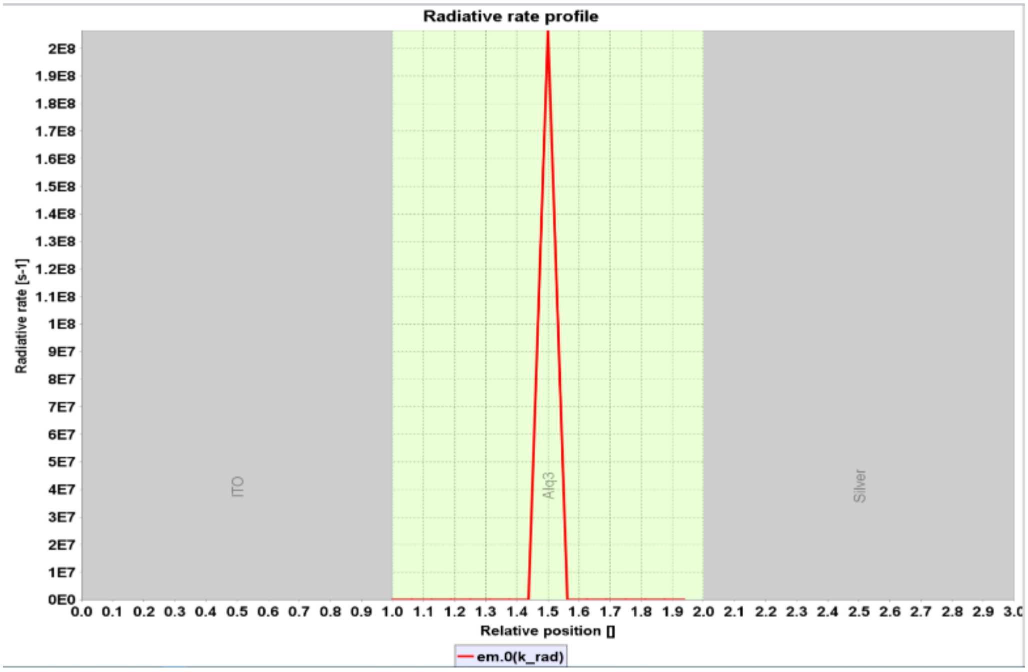

Figure G9 Radiative rate of an ITO/Alq3/AL OLED.

G.2 ITO/PEDOT/ALPHA-NPD/ALQ3/AL OLED

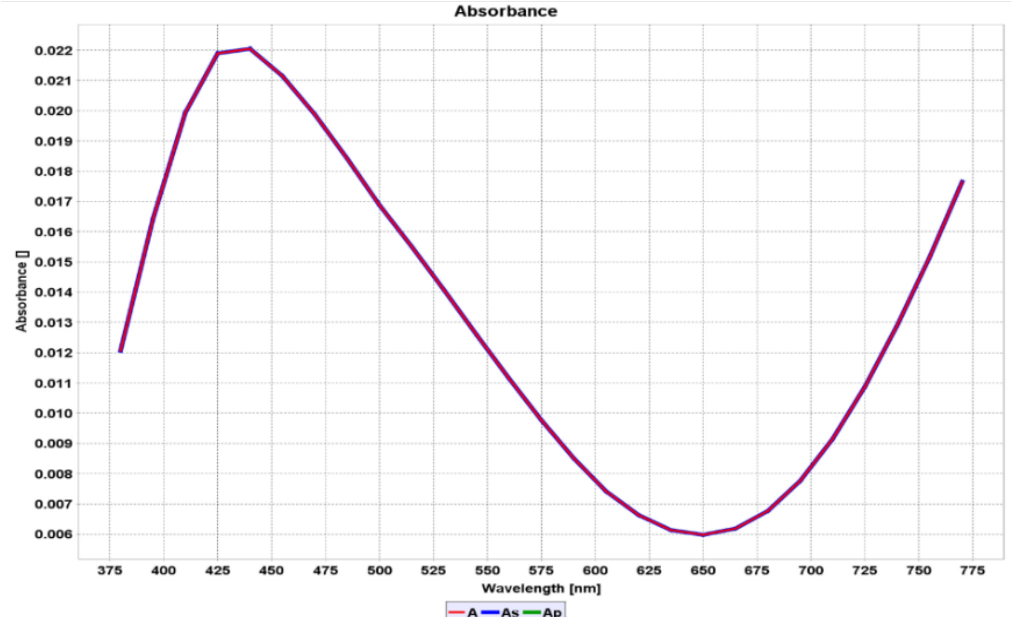

Figure G10. Absorbance spectrum of an ITO/PEDOT/ALPHA-NPD/ALQ3/AL OLED.

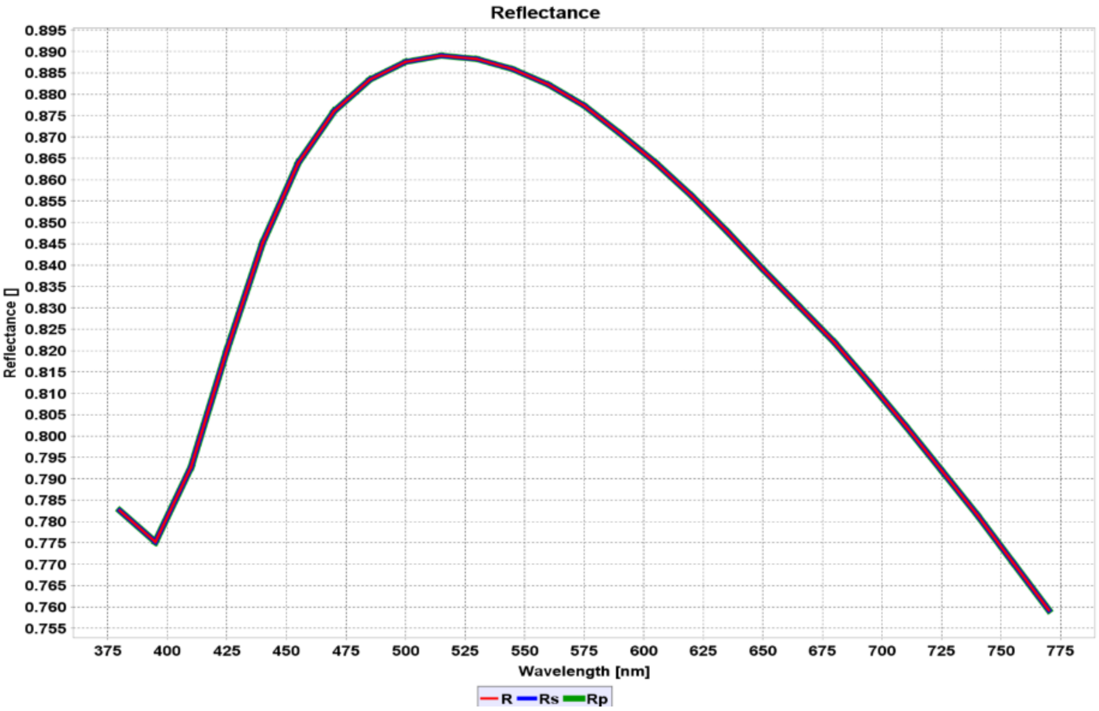

Figure G11. Emission spectrum of an ITO/PEDOT/ALPHA-NPD/ALQ3/AL OLED.

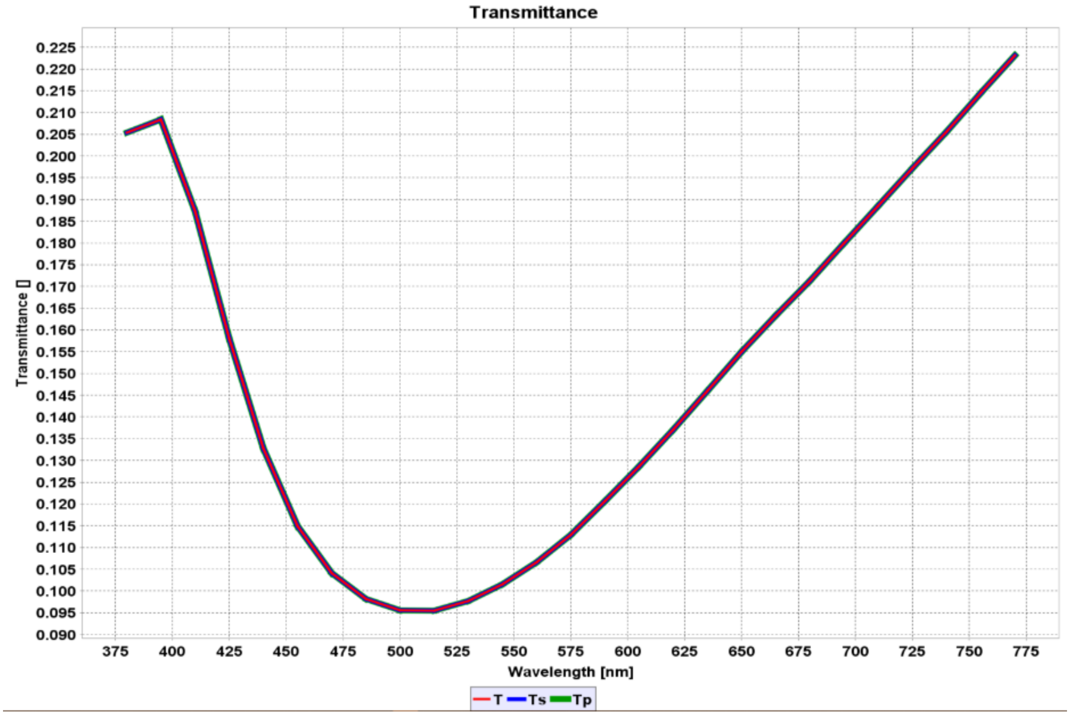

Figure G12. Emission spectrum of an ITO/PEDOT/ALPHA-NPD/ALQ3/AL OLED.

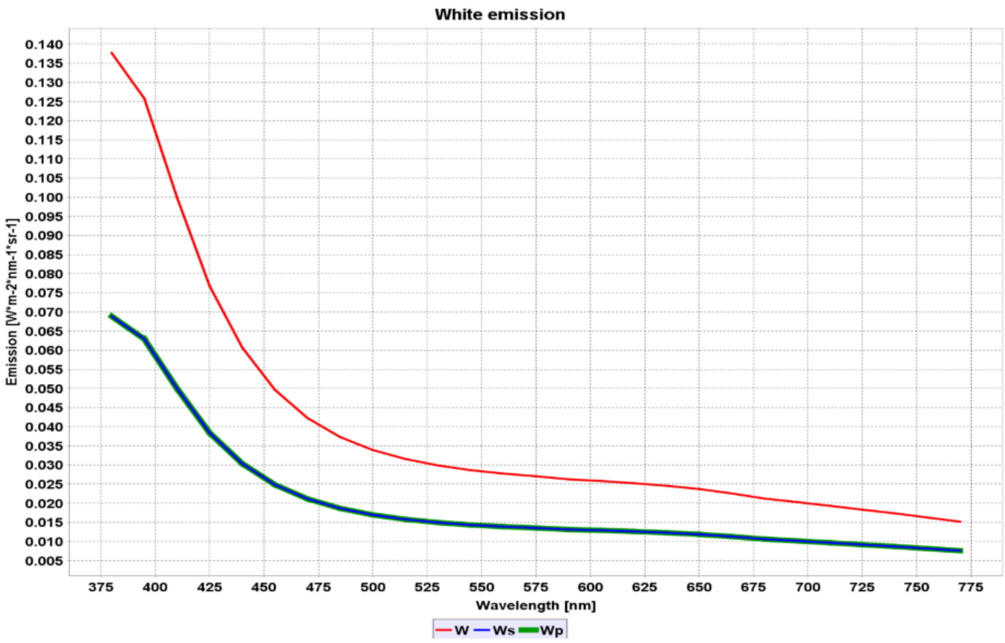

Figure G13. Emission spectrum of an ITO/PEDOT/ALPHA-NPD/ALQ3/AL OLED.

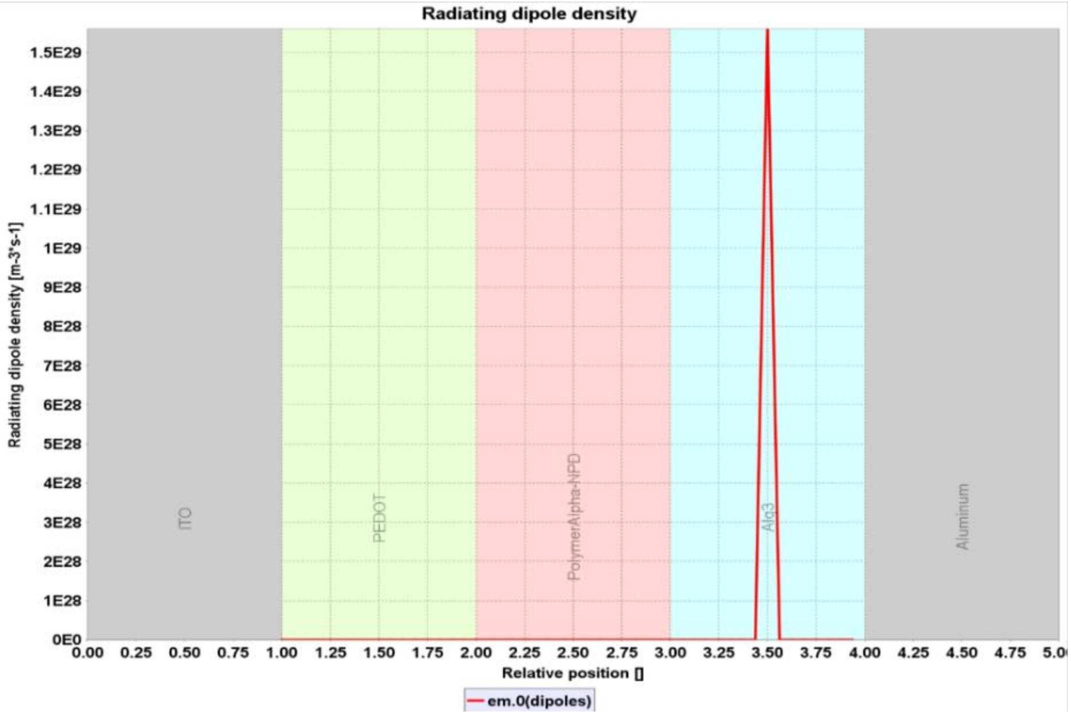

Figure G14. Radiating density of an ITO/PEDOT/ALPHA-NPD/ALQ3/AL OLED.

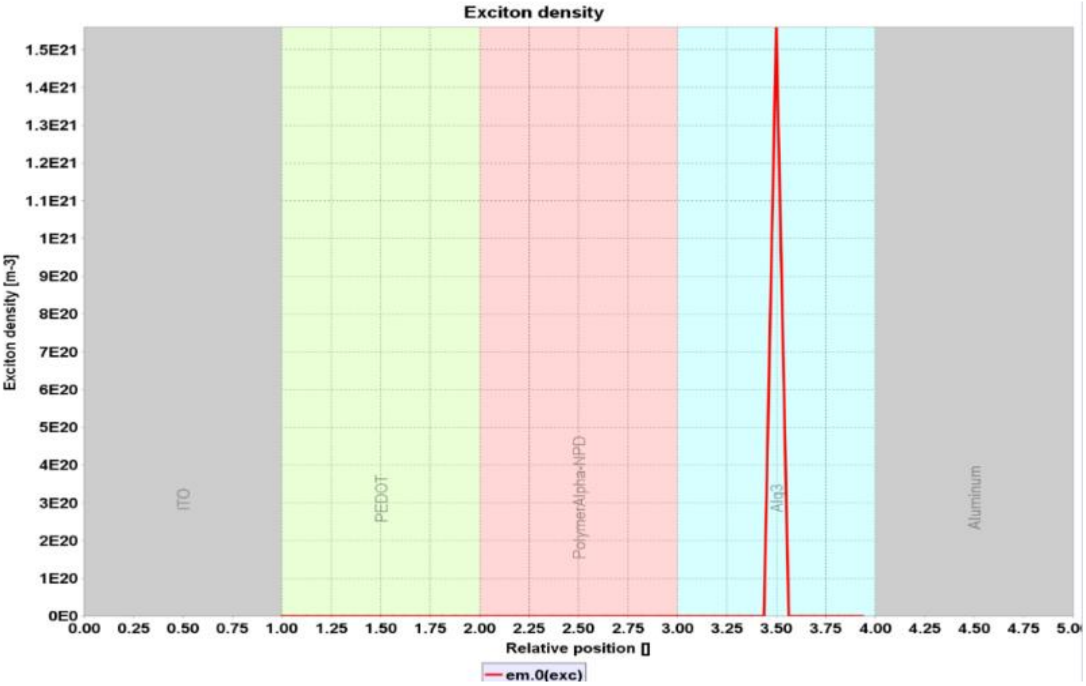

Figure G15. Exciton density of an ITO/PEDOT/ALPHA-NPD/ALQ3/AL OLED.

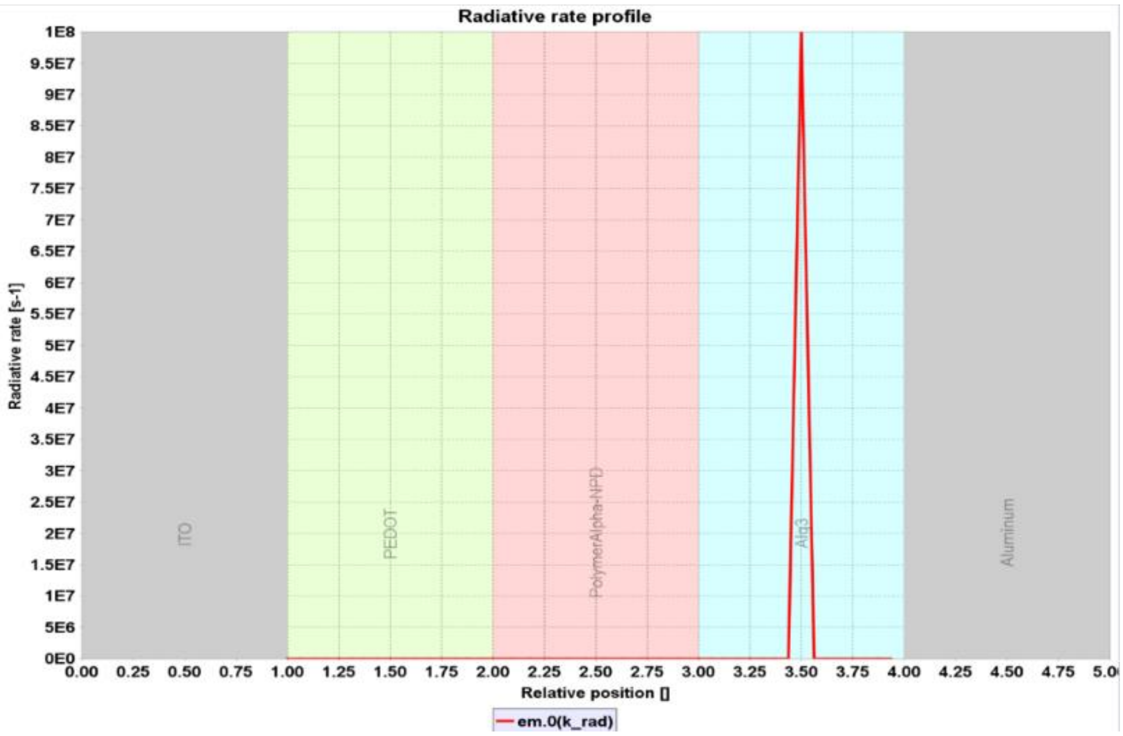

Figure G16. Radiative rate of an ITO/PEDOT/ALPHA-NPD/ALQ3/AL OLED.

G.3 ITO/PEDOT/ALPHA-NPD/ALQ3/AU OLED

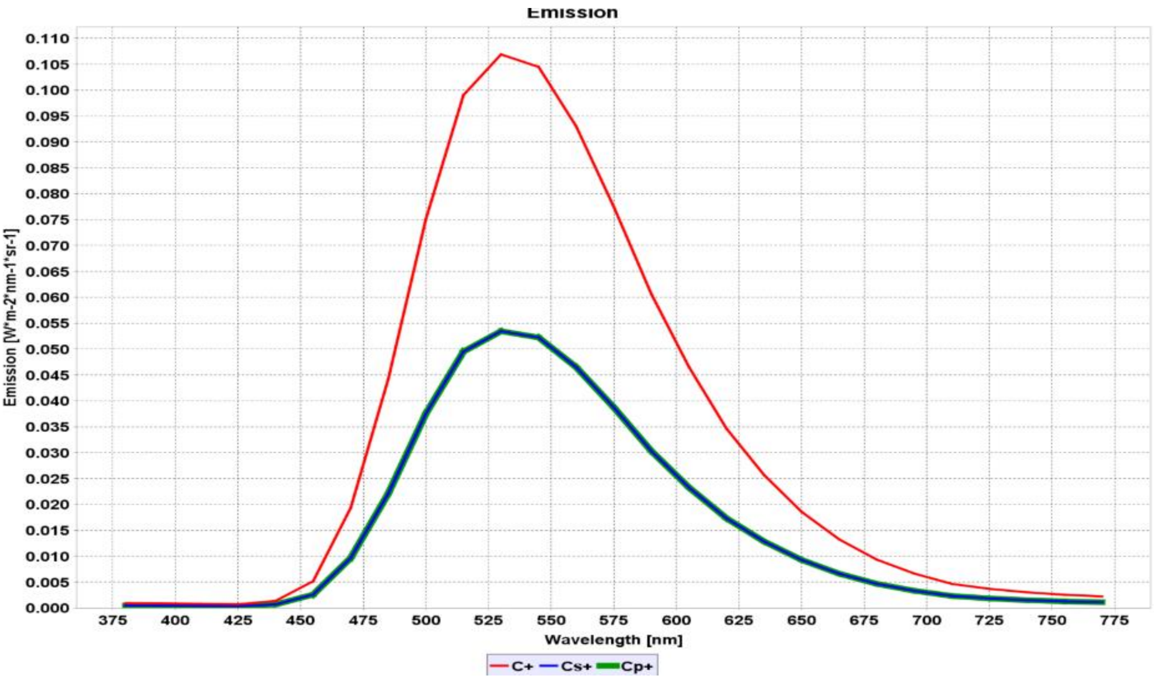

Figure G17. Emission spectrum of an ITO/PEDOT/ALPHA-NPD/ALQ3/AU OLED.

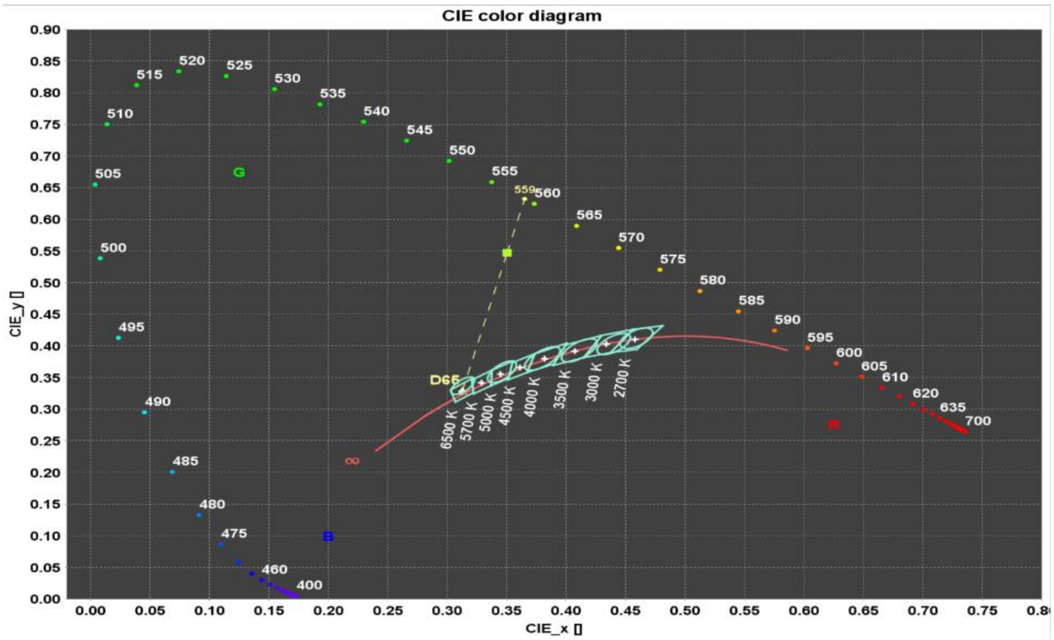

Figure G18. Colour diagram of an ITO/PEDOT/ALPHA-NPD/ALQ3/AU OLED.

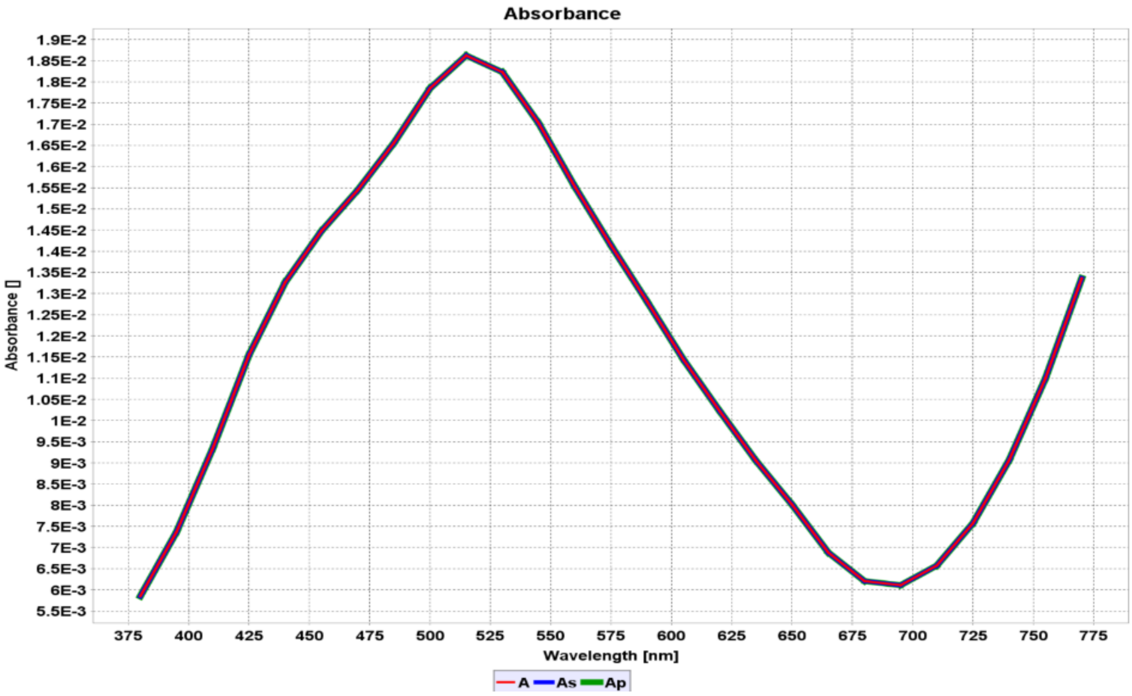

Figure G19. Absorbance of an ITO/PEDOT/ALPHA-NPD/ALQ3/AU OLED.

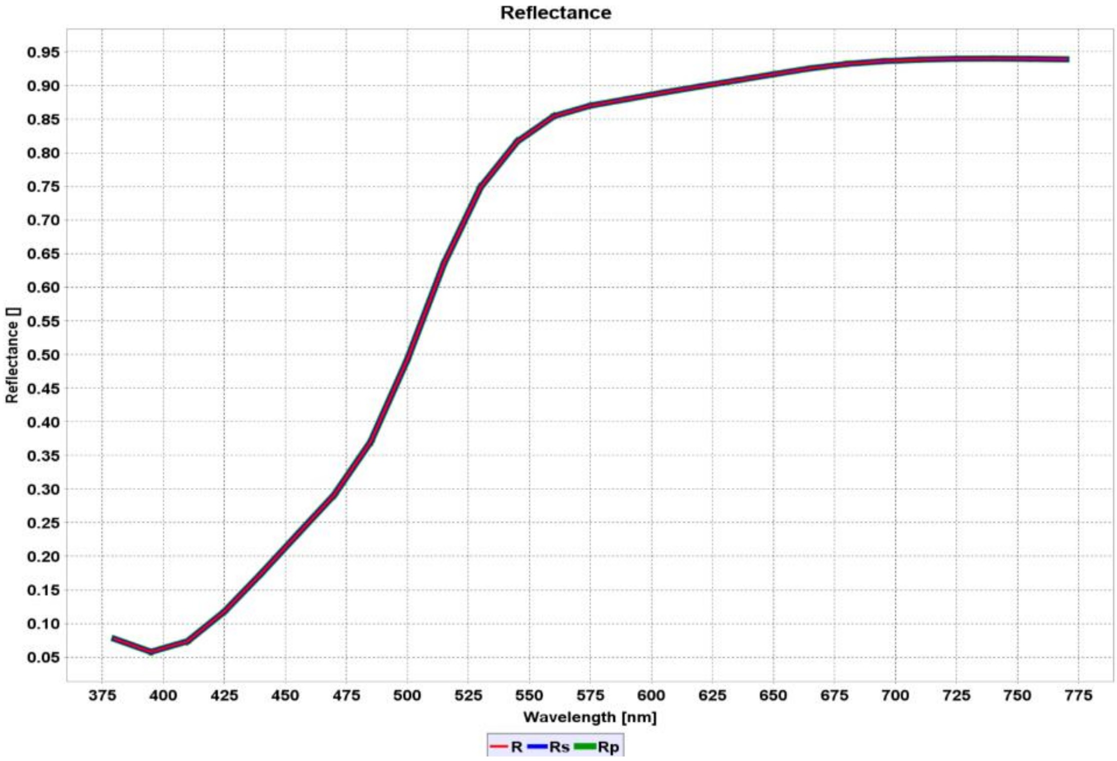

Figure G20. Reflectance of an ITO/PEDOT/ALPHA-NPD/ALQ3/AU OLED.

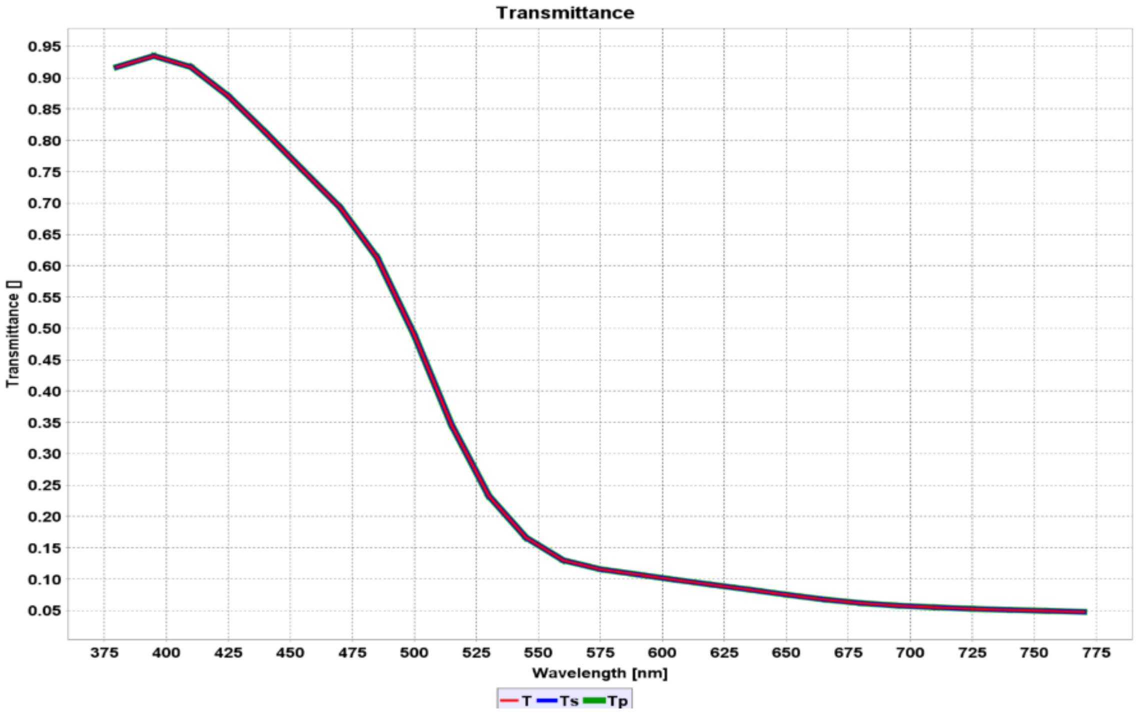

Figure G21. Transmittance of an ITO/PEDOT/ALPHA-NPD/ALQ3/AU OLED.

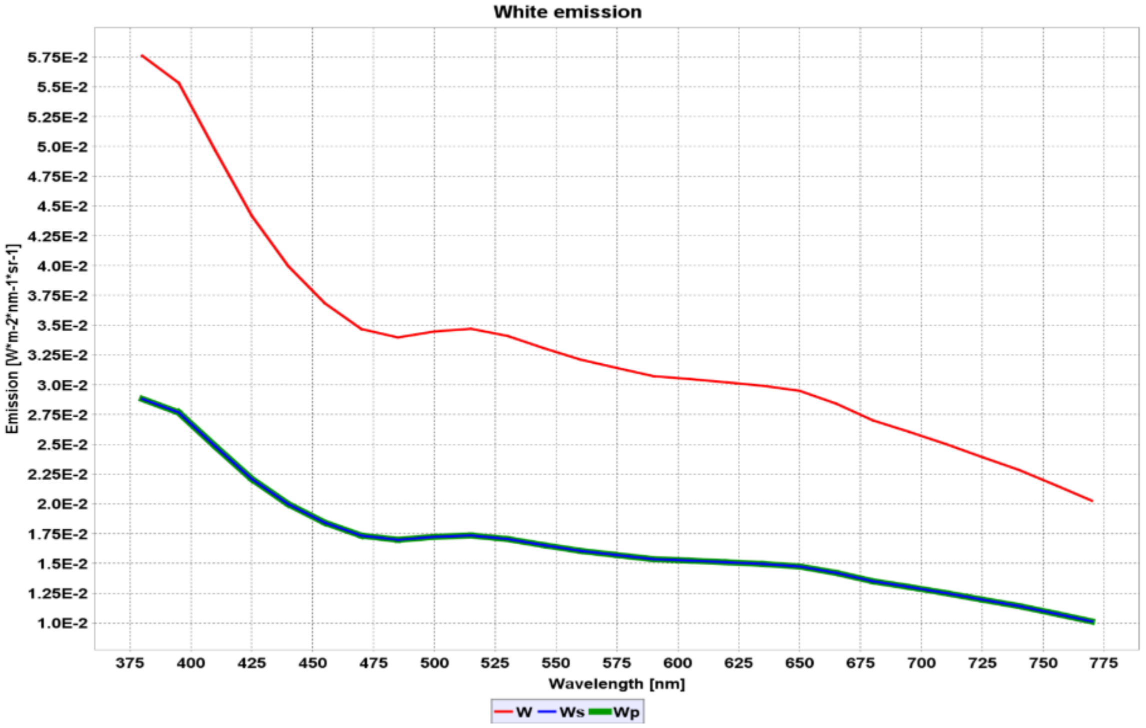

Figure G22. White emission of an ITO/PEDOT/ALPHA-NPD/ALQ3/AU OLED.

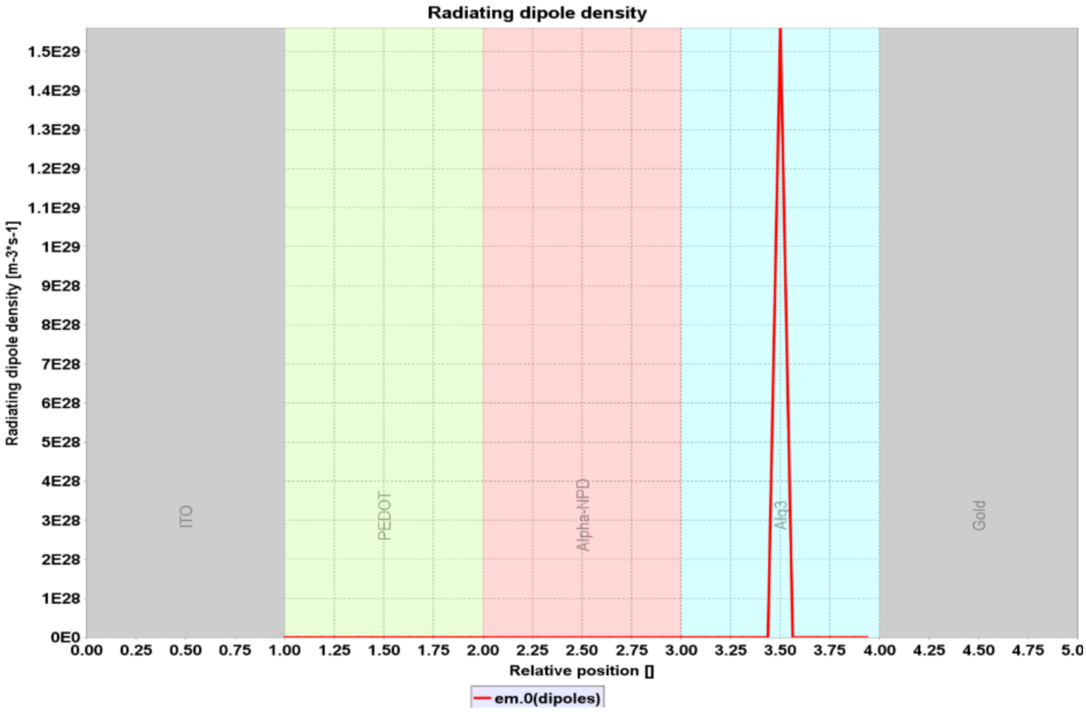

Figure G23. Radiating density of an ITO/PEDOT/ALPHA-NPD/ALQ3/AU OLED.

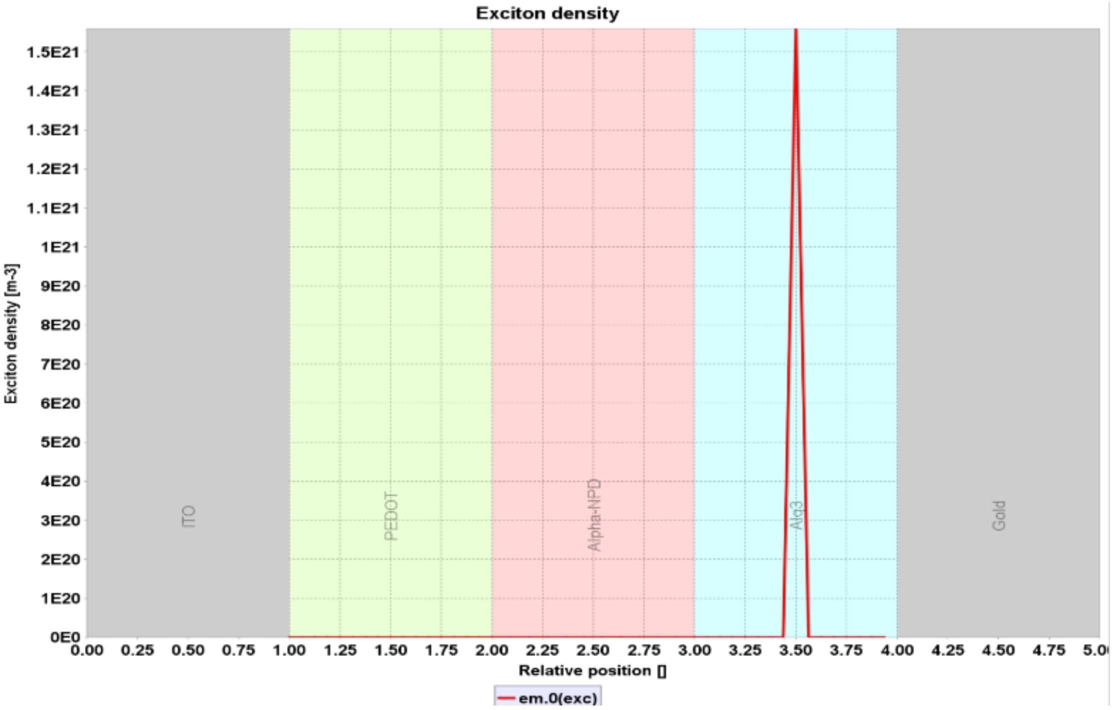

Figure G24. Exciton density of an ITO/PEDOT/ALPHA-NPD/ALQ3/AU OLED.

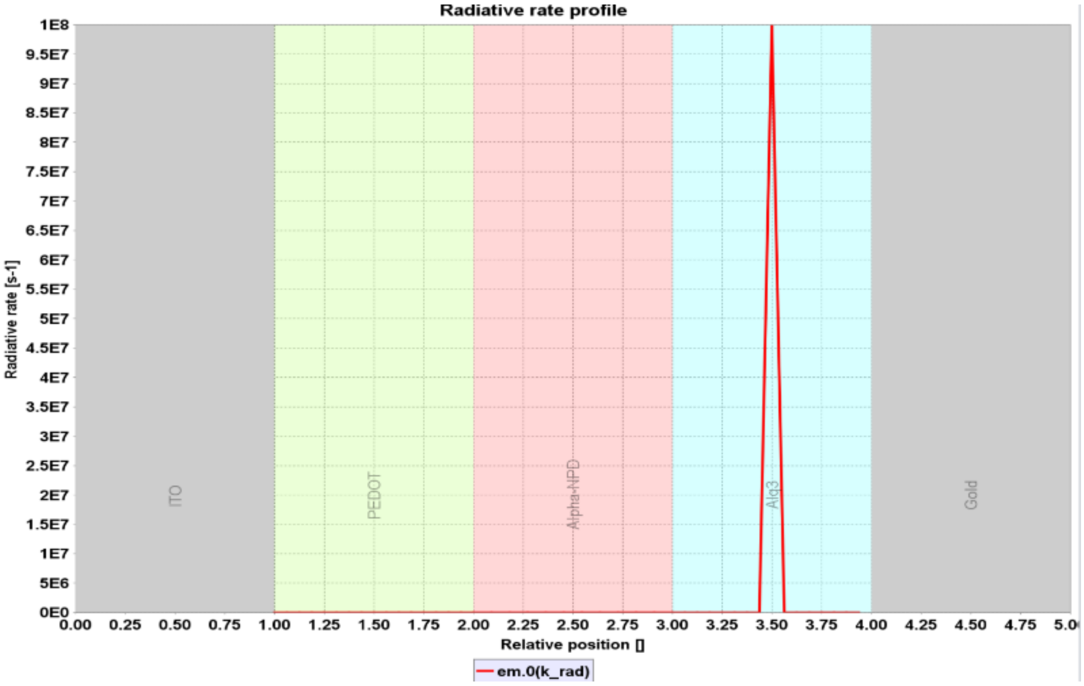

Figure G25. Radiative rate of an ITO/PEDOT/ALPHA-NPD/ALQ3/AU OLED.

G.4 ITO/PEDOT/ALPHA-NPD/ALQ3/AG OLED

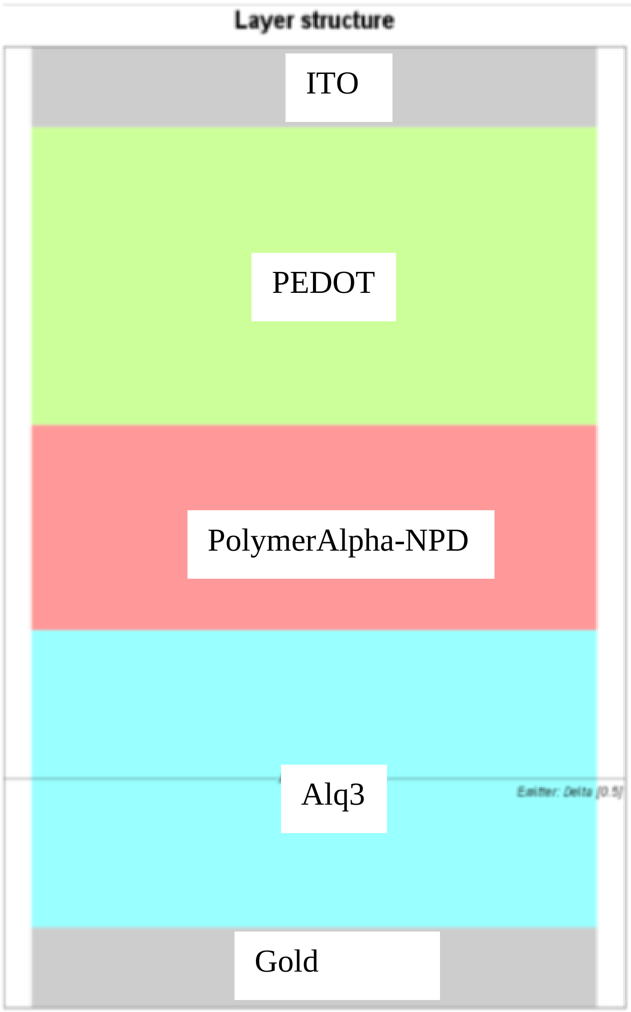

Figure G26. Emission spectrum of an ITO/PEDOT/ALPHA-NPD/ALQ3/AG OLED.

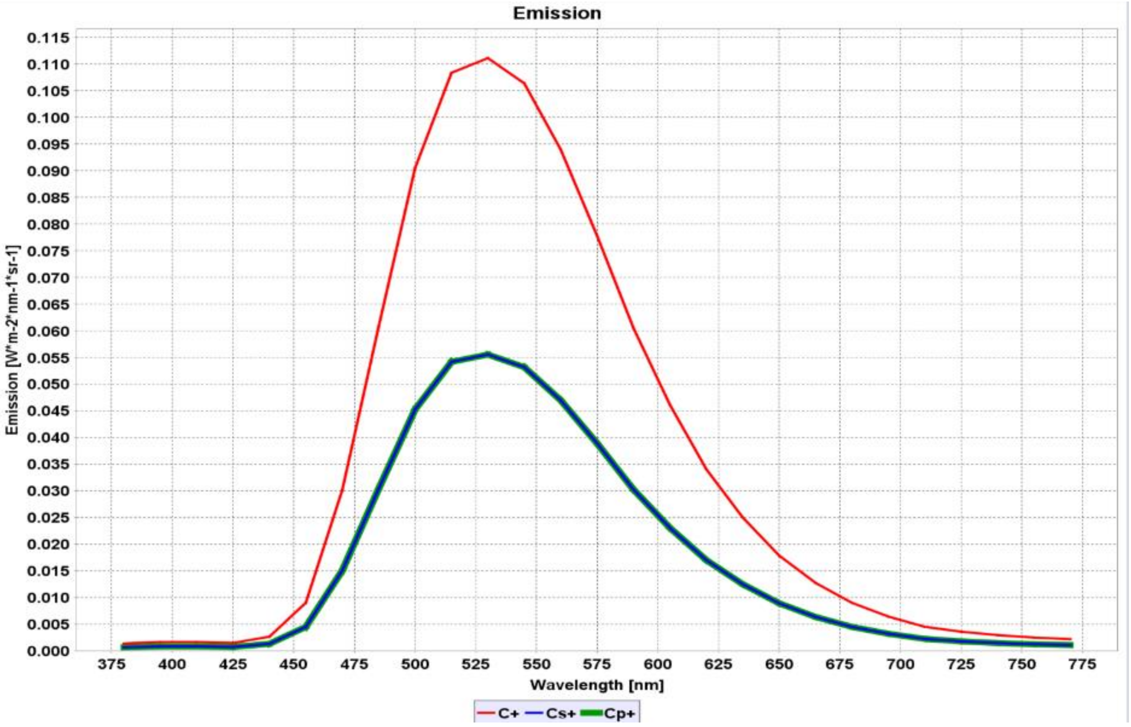

Figure G27. Emission spectrum of an ITO/PEDOT/ALPHA-NPD/ALQ3/AG OLED.

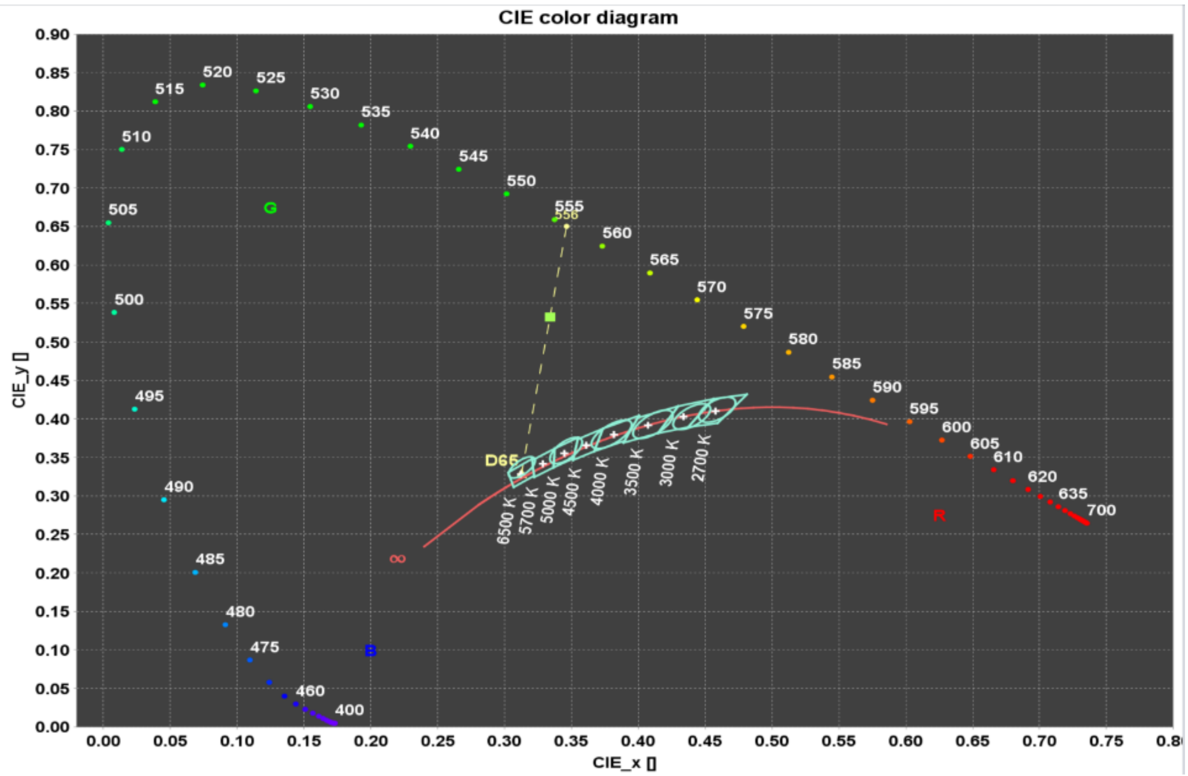

Figure G28. Emission spectrum of an ITO/PEDOT/ALPHA-NPD/ALQ3/AG OLED.

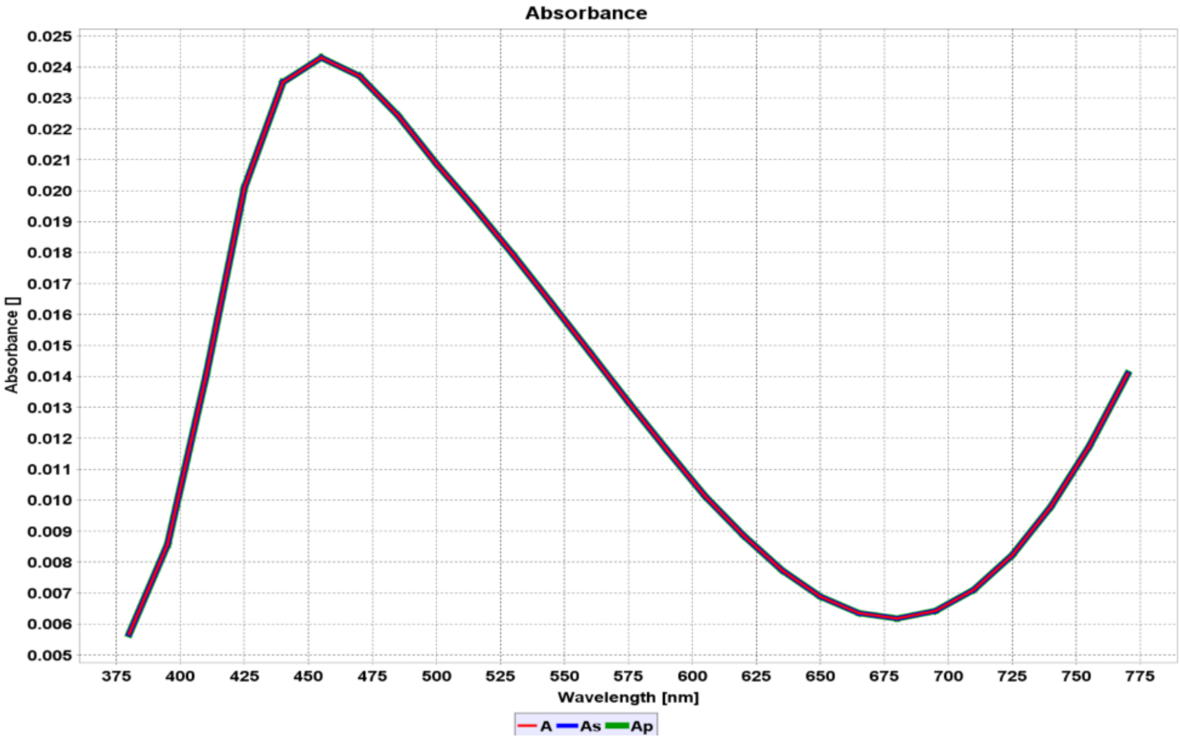

Figure G29. Absorbance of an ITO/PEDOT/ALPHA-NPD/ALQ3/AG OLED.

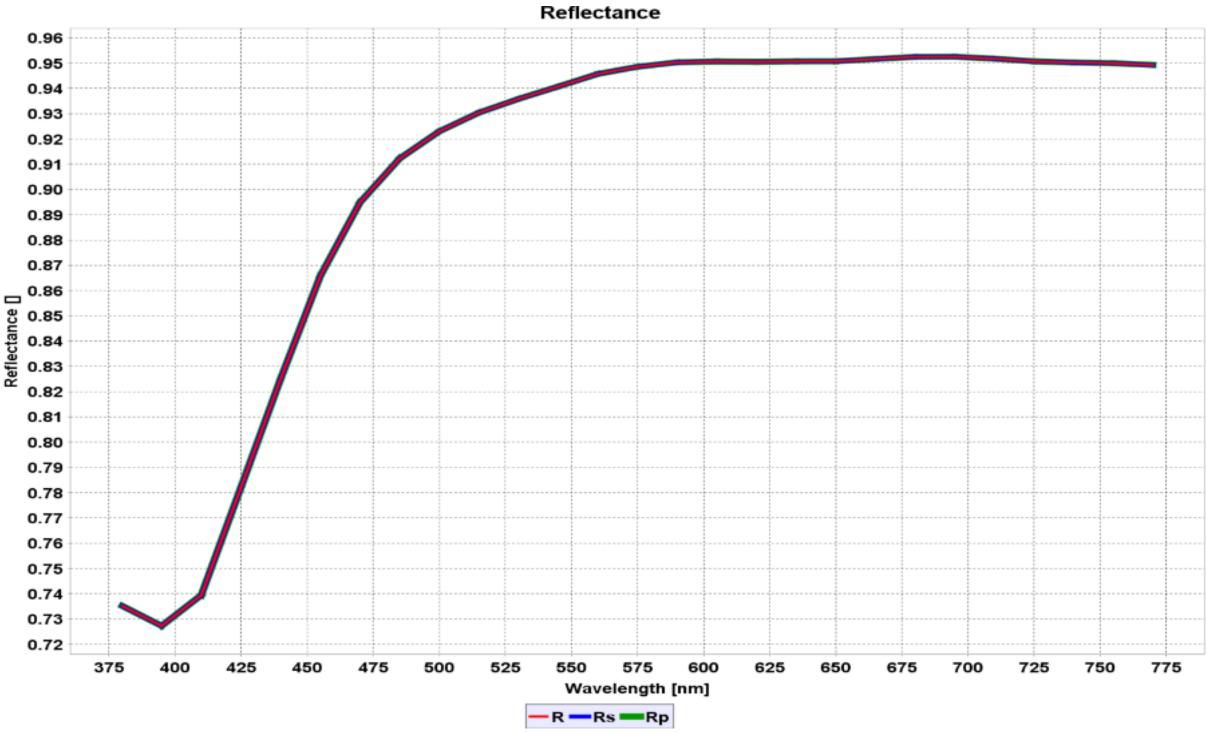

Figure G30. Reflectance of an ITO/PEDOT/ALPHA-NPD/ALQ3/AG OLED.

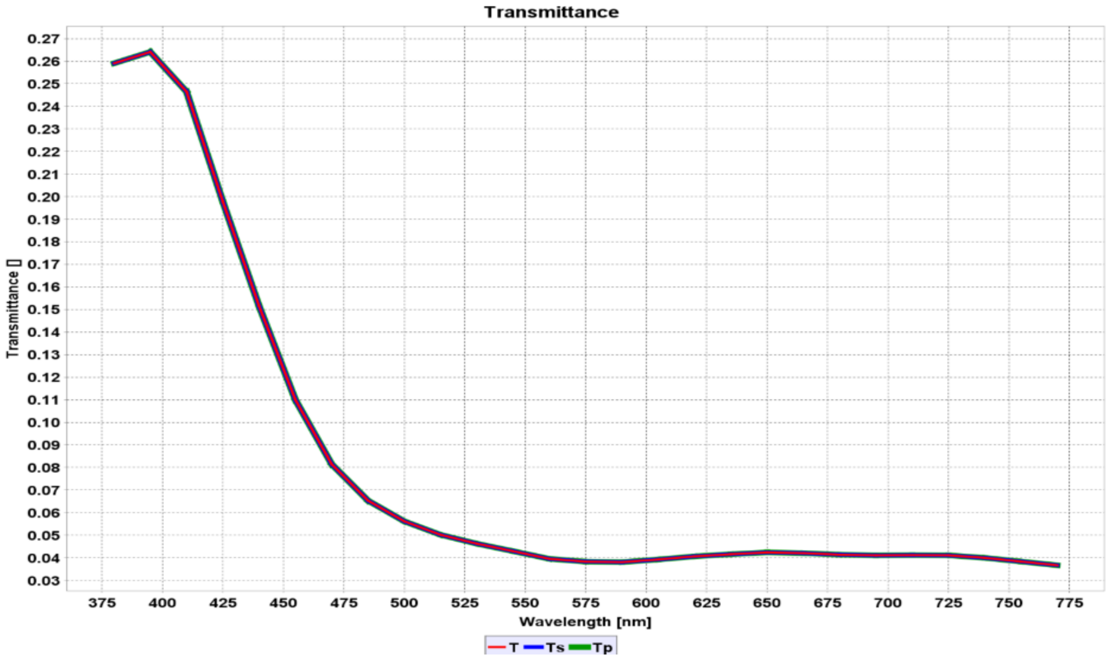

Figure G31 Transmittance of an ITO/PEDOT/ALPHA-NPD/ALQ3/AG OLED.

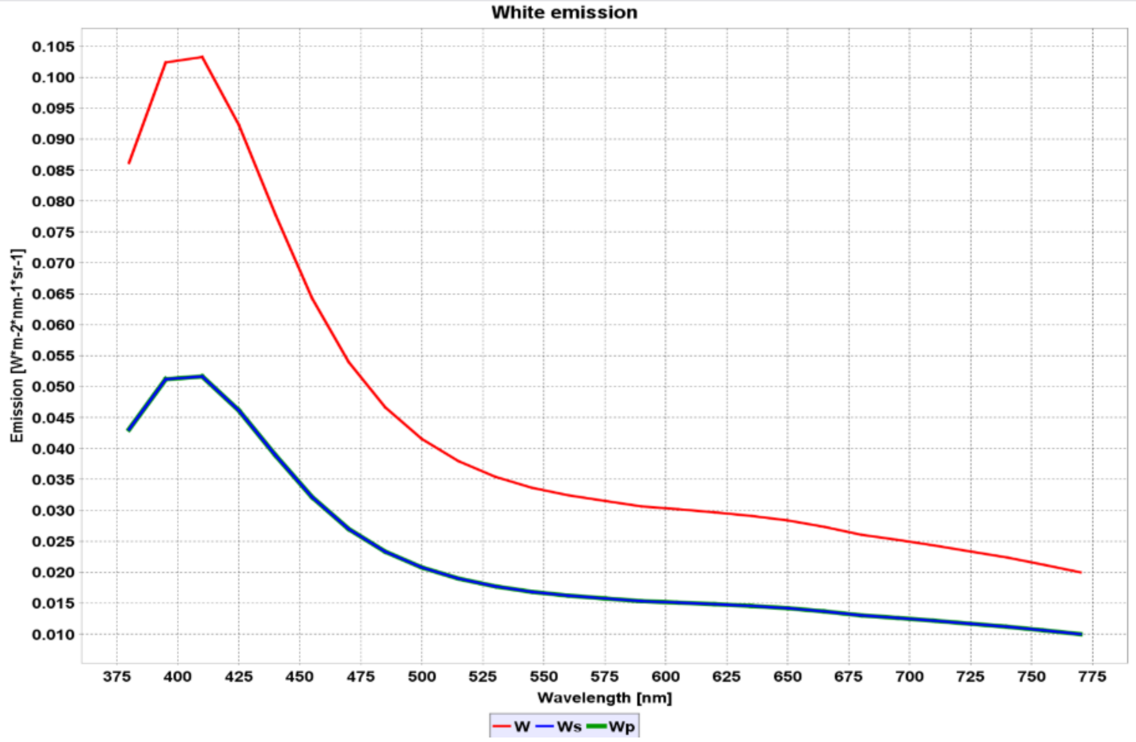

Figure G32 White emission of an ITO/PEDOT/ALPHA-NPD/ALQ3/AG OLED.

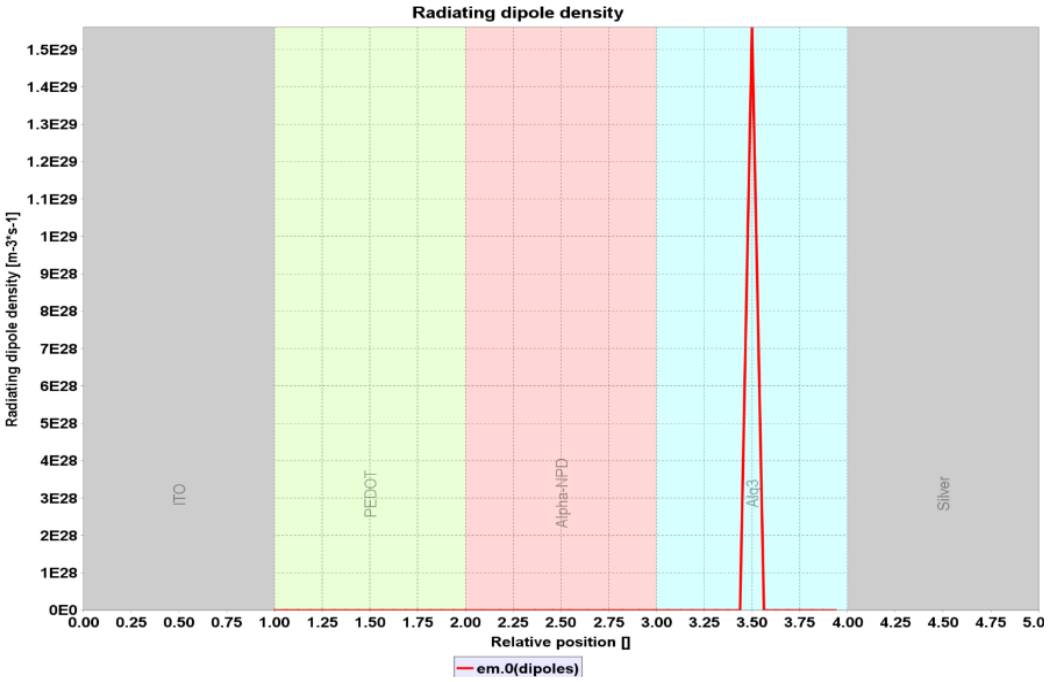

Figure G33. Emission spectrum of an ITO/PEDOT/ALPHA-NPD/ALQ3/AG OLED.

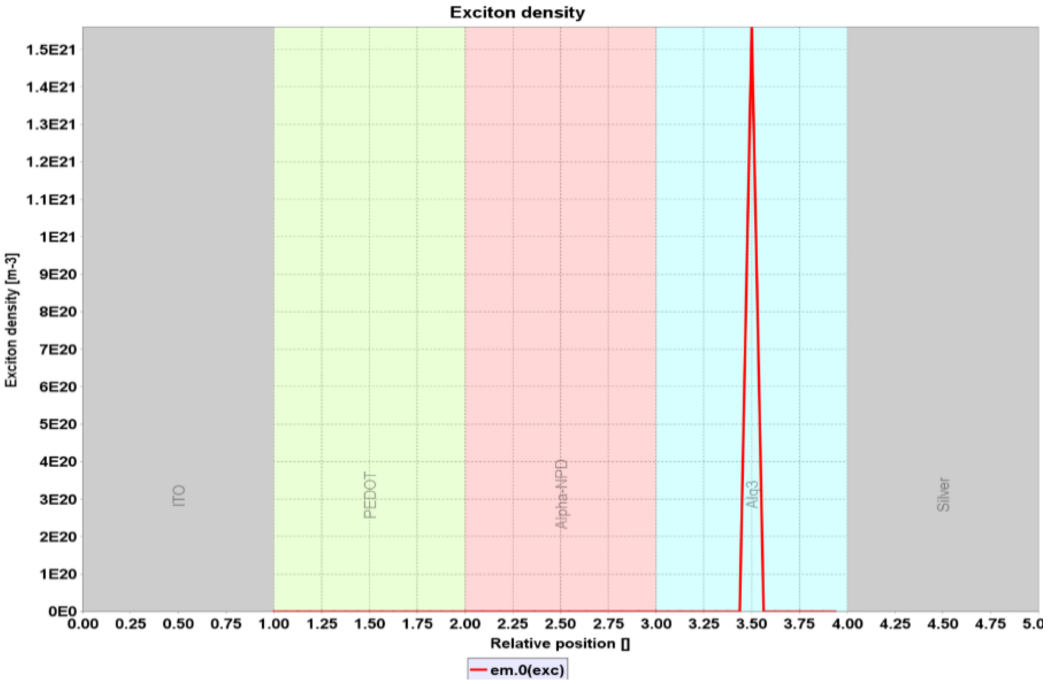

Figure G34. Exciton density of an ITO/PEDOT/ALPHA-NPD/ALQ3/AG OLED.

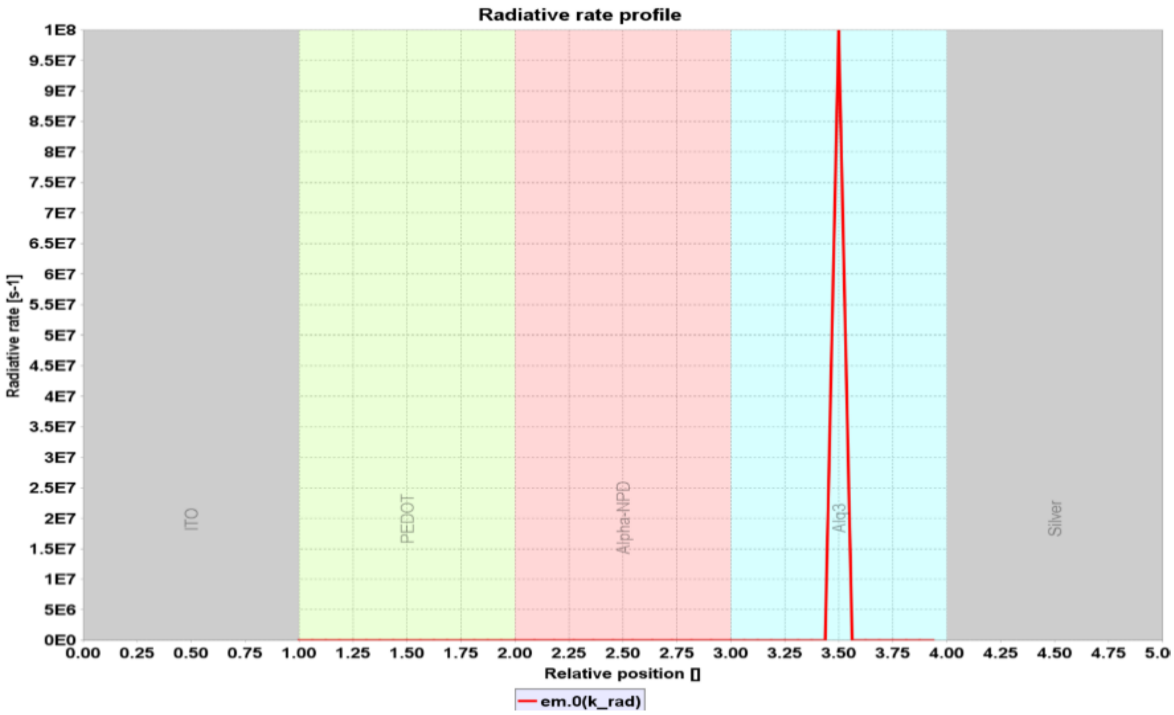

Figure G35. Radiative rate of an ITO/PEDOT/ALPHA-NPD/ALQ3/AG OLED.

G.5 OPTIMIZED ITO/PEDOT/ALPHA-PD/ALQ3/AL OLED

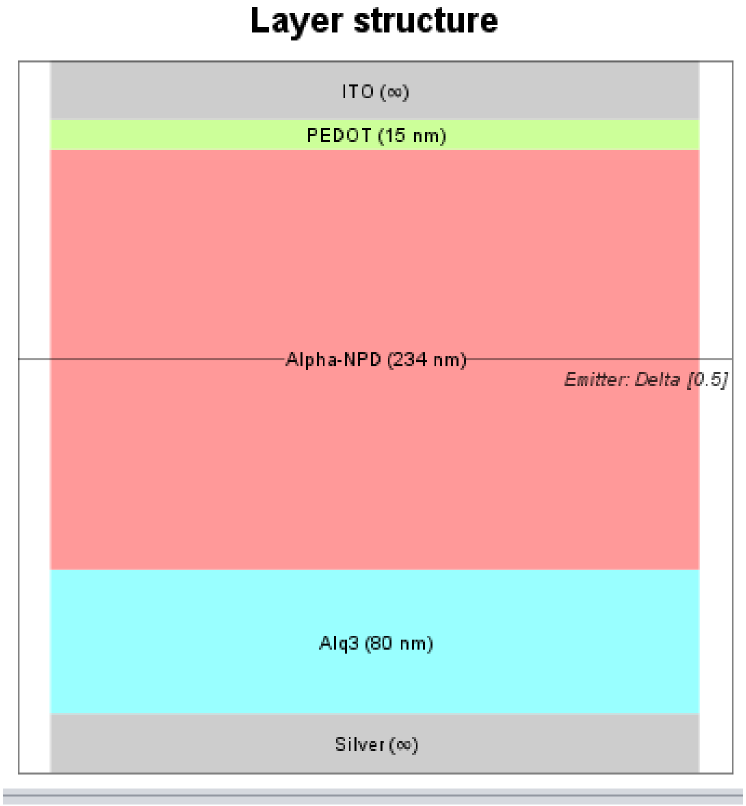

Figure G36. Emission spectrum of an optimized ITO/PEDOT/ALPHA-NPD/ALQ3/AL OLED.

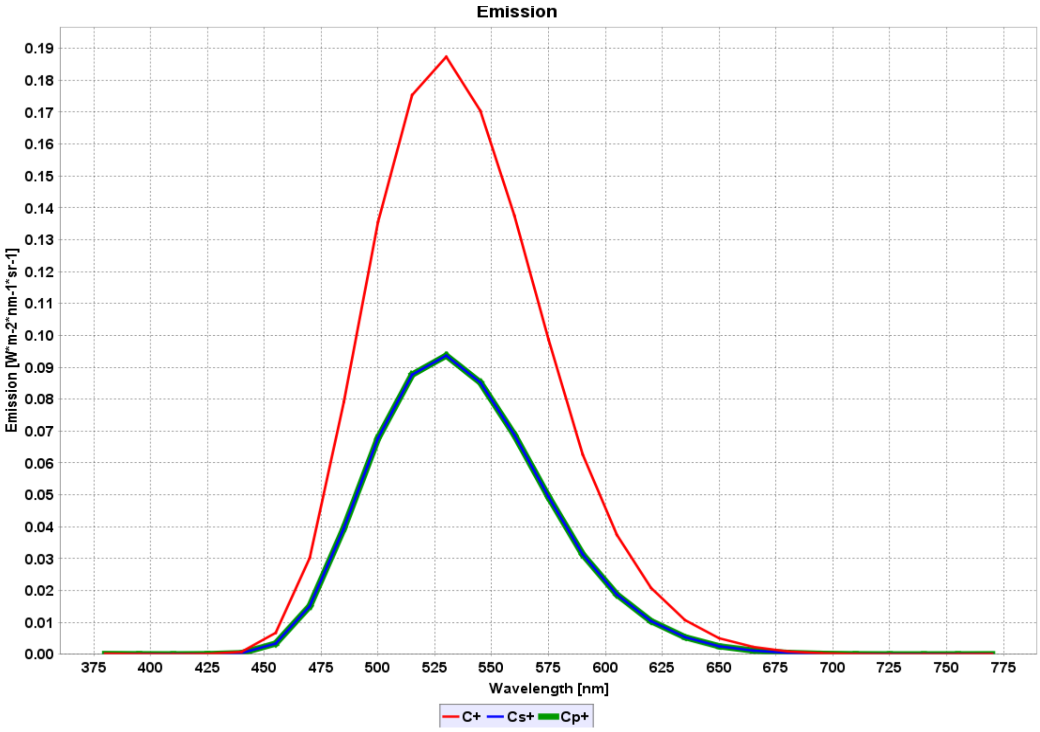

Figure G37. Emission spectrum of an optimized ITO/PEDOT/ALPHA-NPD/ALQ3/AL OLED.

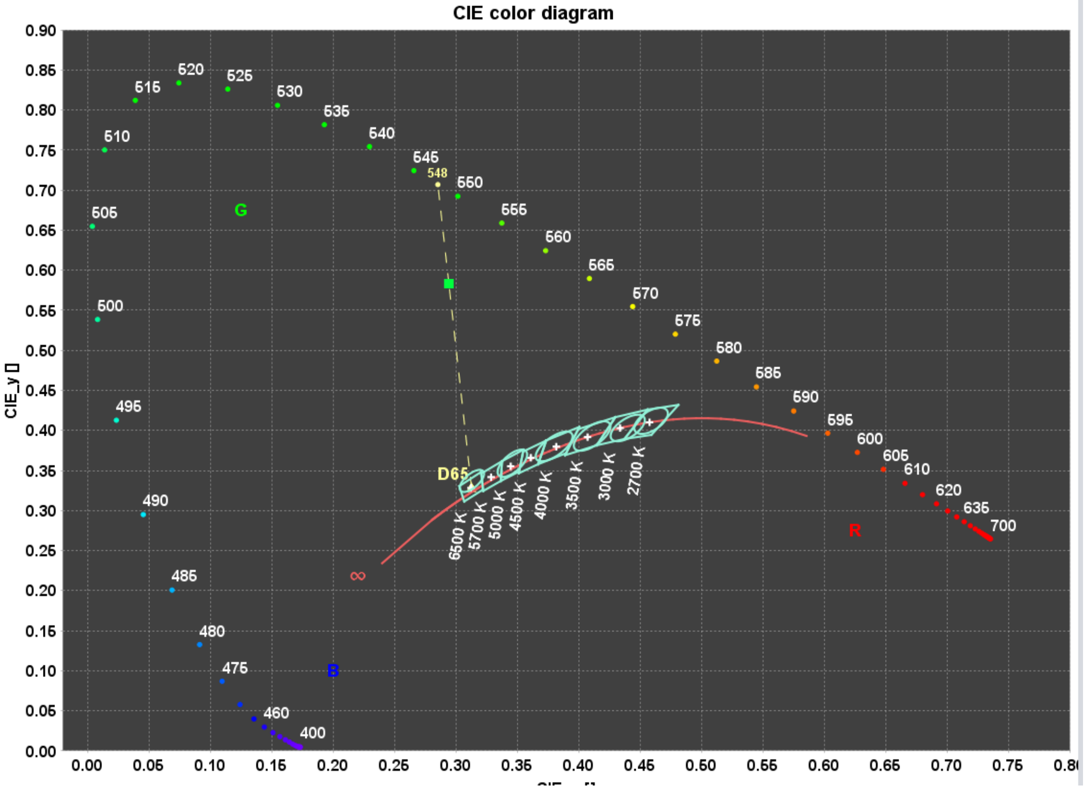

Figure G38. Colour diagram of an optimized ITO/PEDOT/ALPHA-NPD/ALQ3/AL OLED.

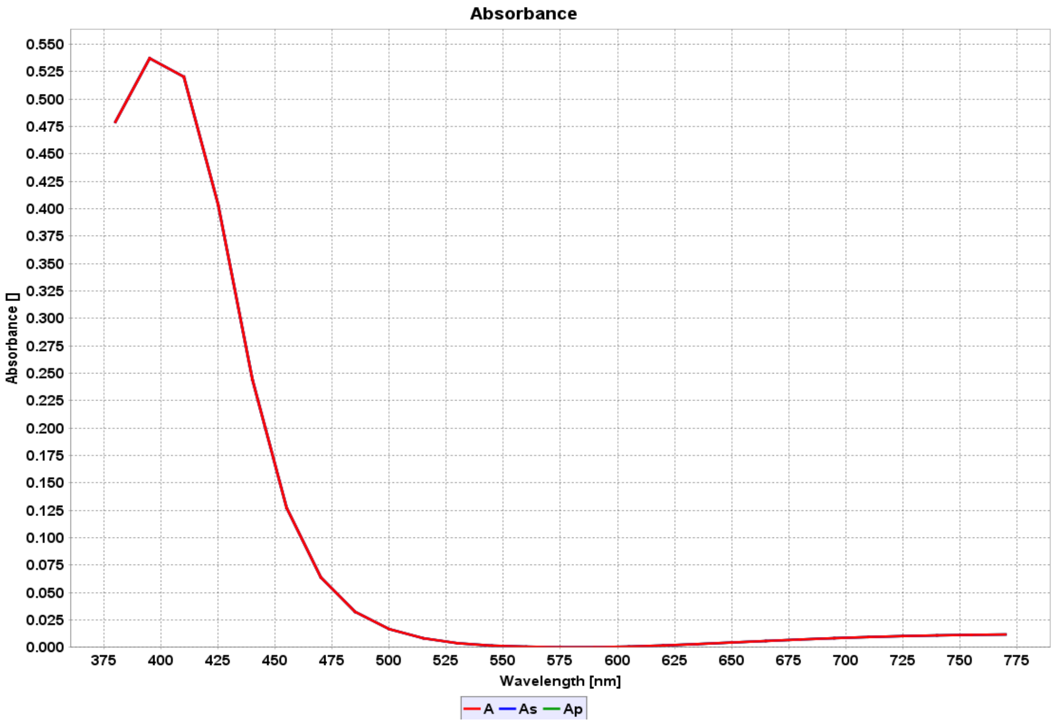

Figure G39. Emission spectrum of an optimized ITO/PEDOT/ALPHA-NPD/ALQ3/AL OLED.

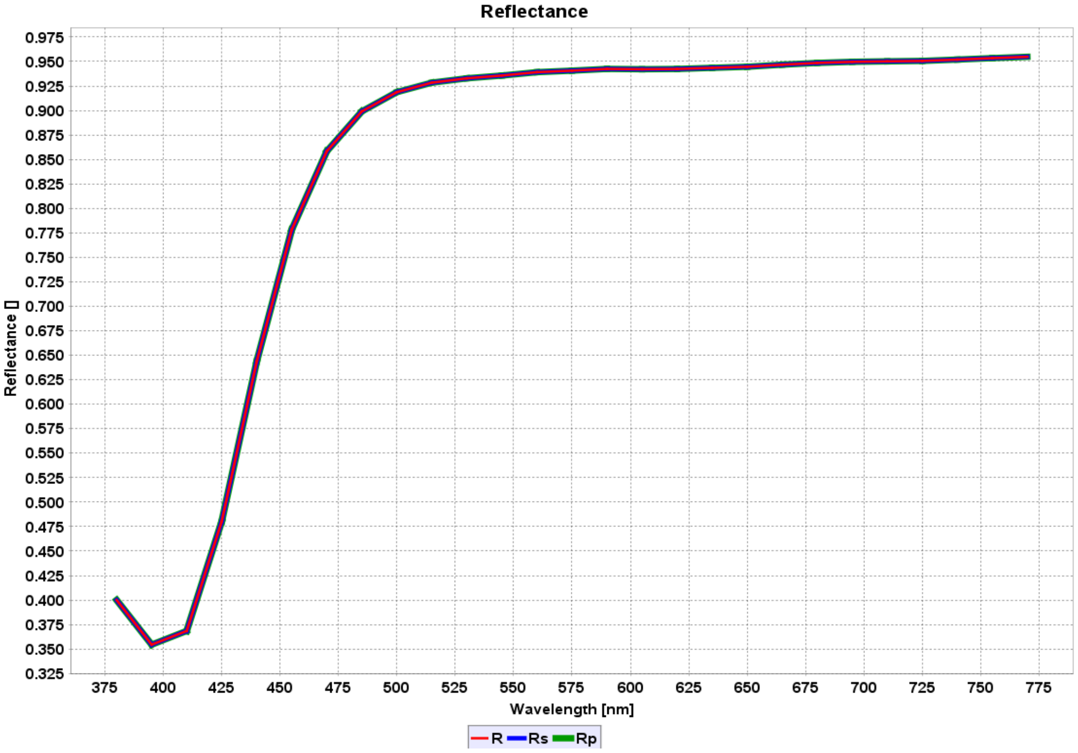

Figure G40. Reflectance of an optimized ITO/PEDOT/ALPHA-NPD/ALQ3/AL OLED.

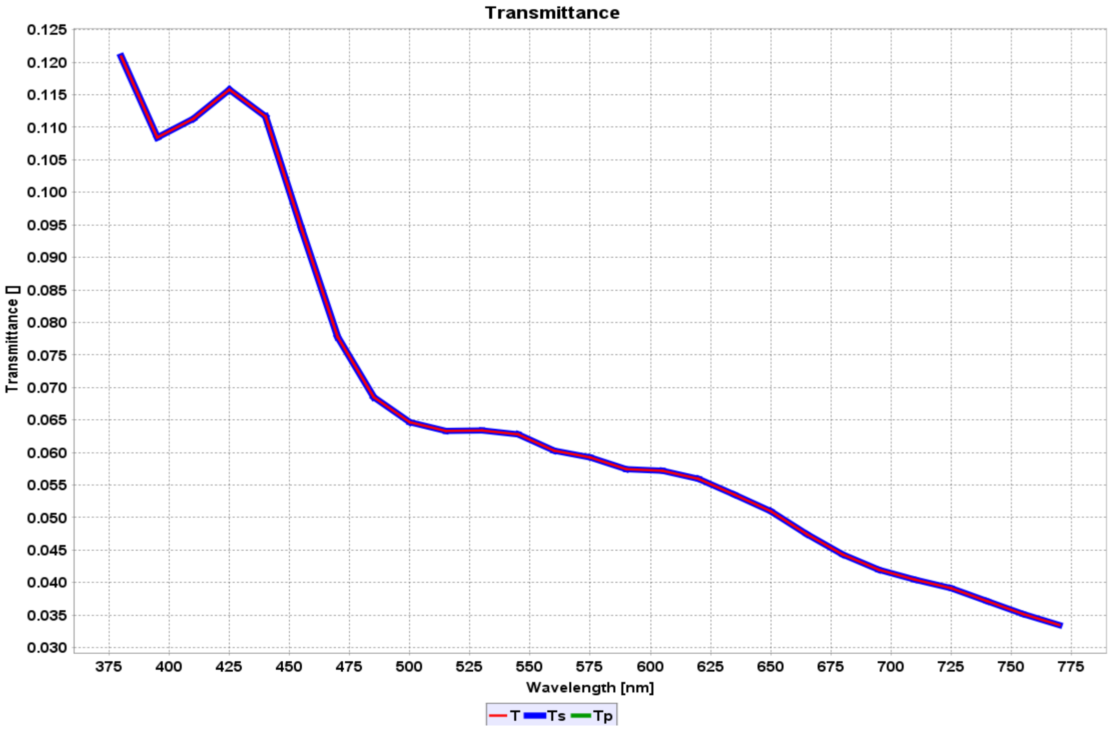

Figure G41. Transmittance of an optimized ITO/PEDOT/ALPHA-NPD/ALQ3/AL OLED.

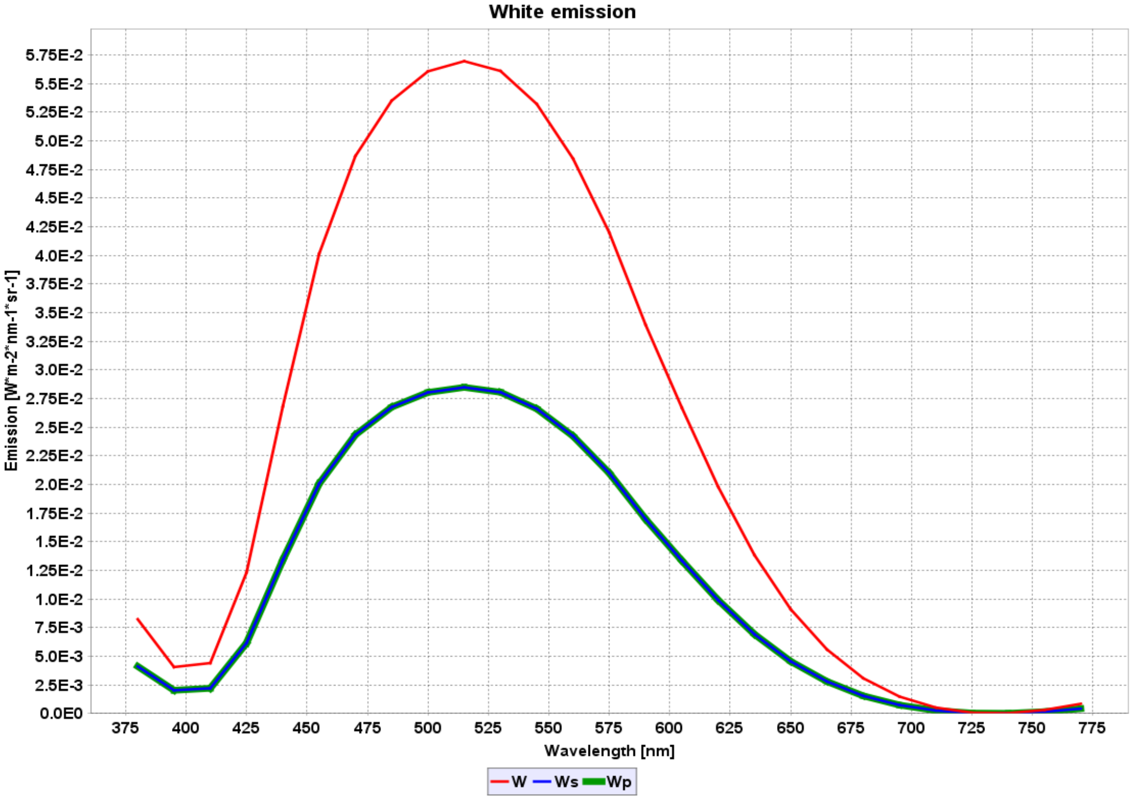

Figure G42. White emission of an optimized ITO/PEDOT/ALPHA-NPD/ALQ3/AL OLED.

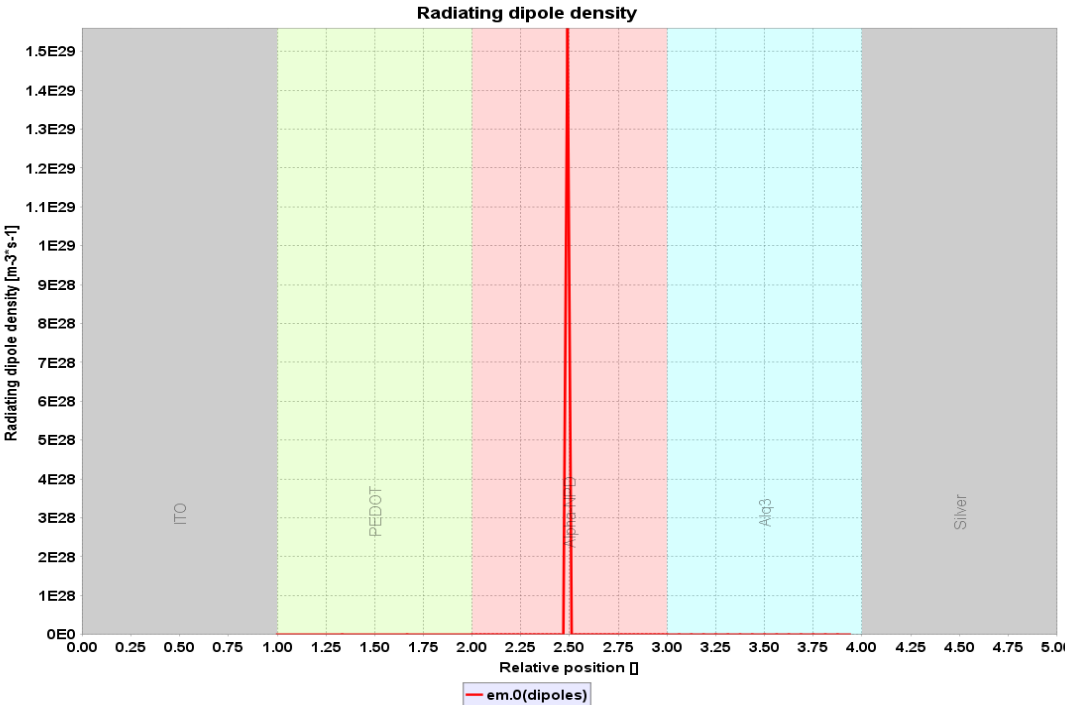

Figure G43. Emission spectrum of an optimized ITO/PEDOT/ALPHA-NPD/ALQ3/AL OLED.

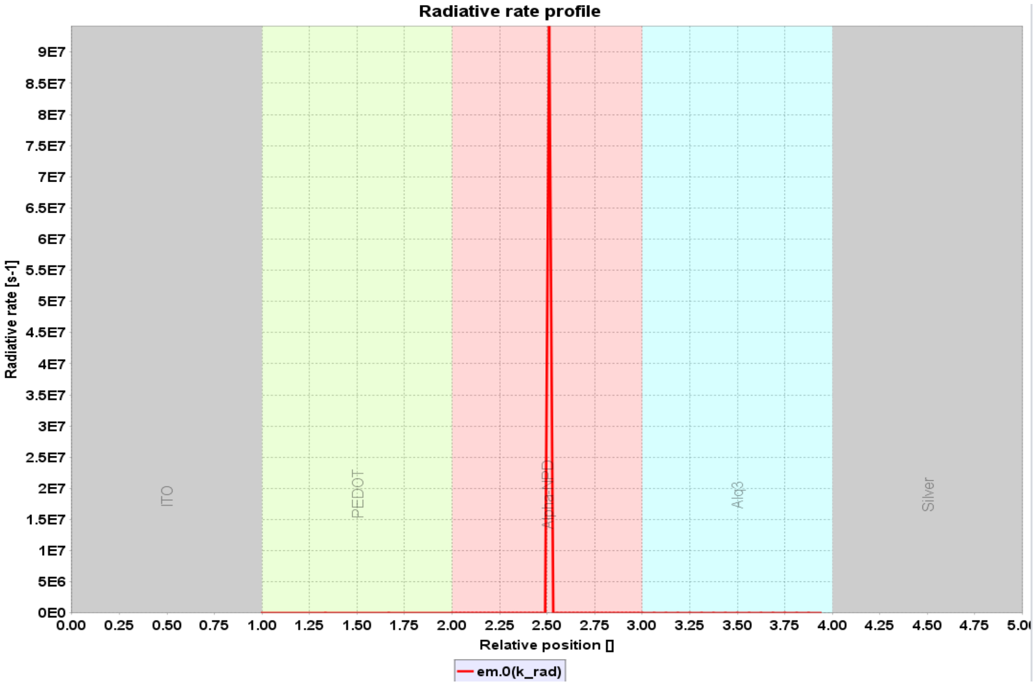

Figure G44. Radiative rate of an optimized ITO/PEDOT/ALPHA-NPD/ALQ3/AL OLED.

ADDENDUM H GPVDM SIMULATIONS

H.1 ITO/PEDOT/NPB/ALQ3/AL OLED

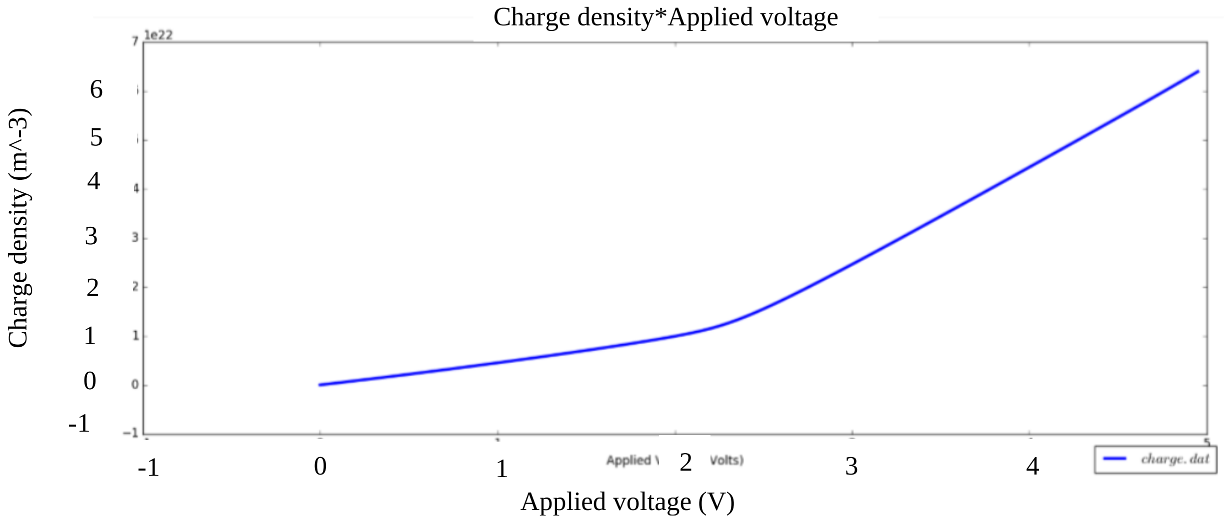

Figure H1. Charge density versus applied voltage of ITO/PEDOT/NPB/Alq3/Al.

Current*Applied voltage

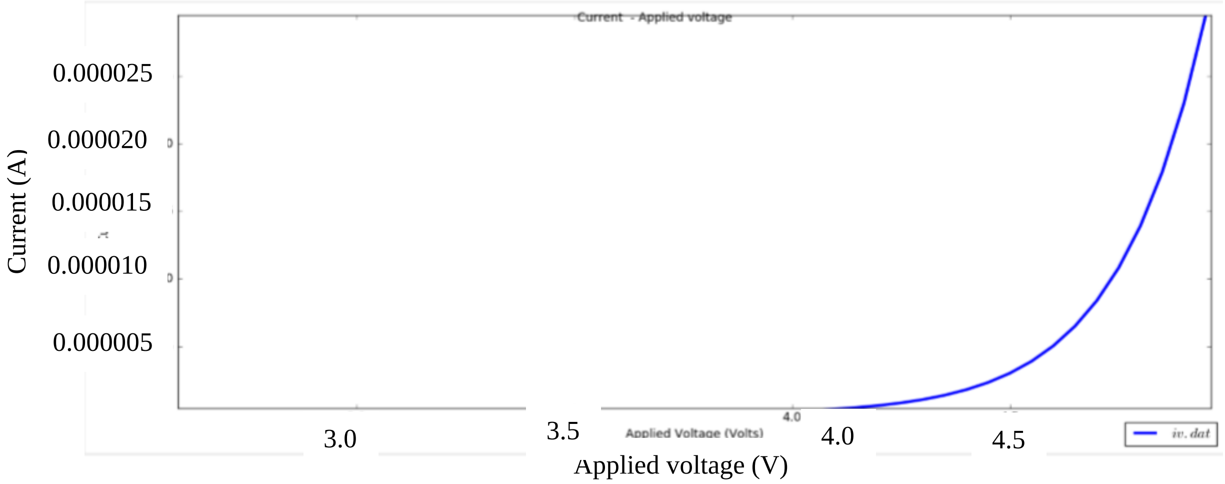

Figure H2. Current versus applied voltage of ITO/PEDOT/NPB/Alq3/Al.

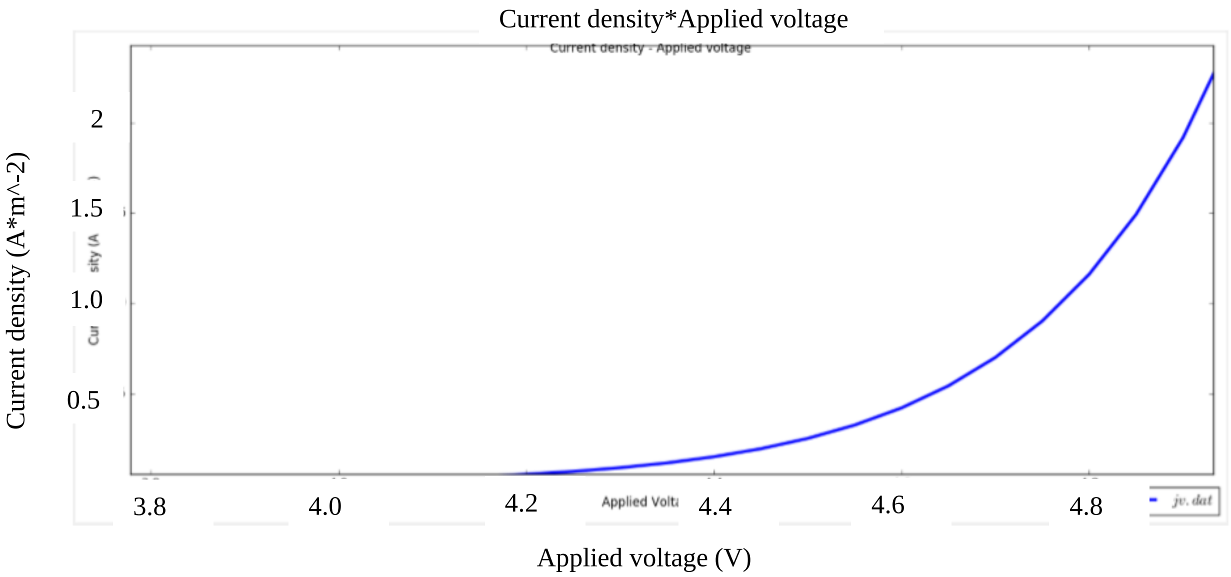

Figure H3. Current density versus applied voltage of ITO/PEDOT/NPB/Alq3/Al.

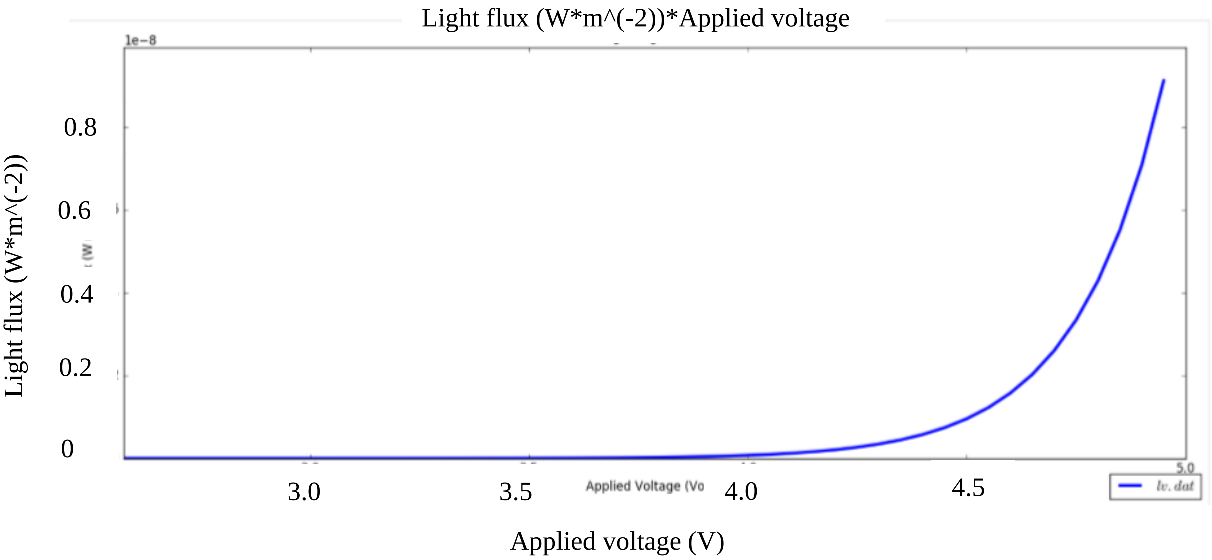

Figure H4. Light flux versus applied voltage of ITO/PEDOT/NPB/Alq3/Al.

H.2 ITO/PEDOT/NPB/ALQ3/AU OLED

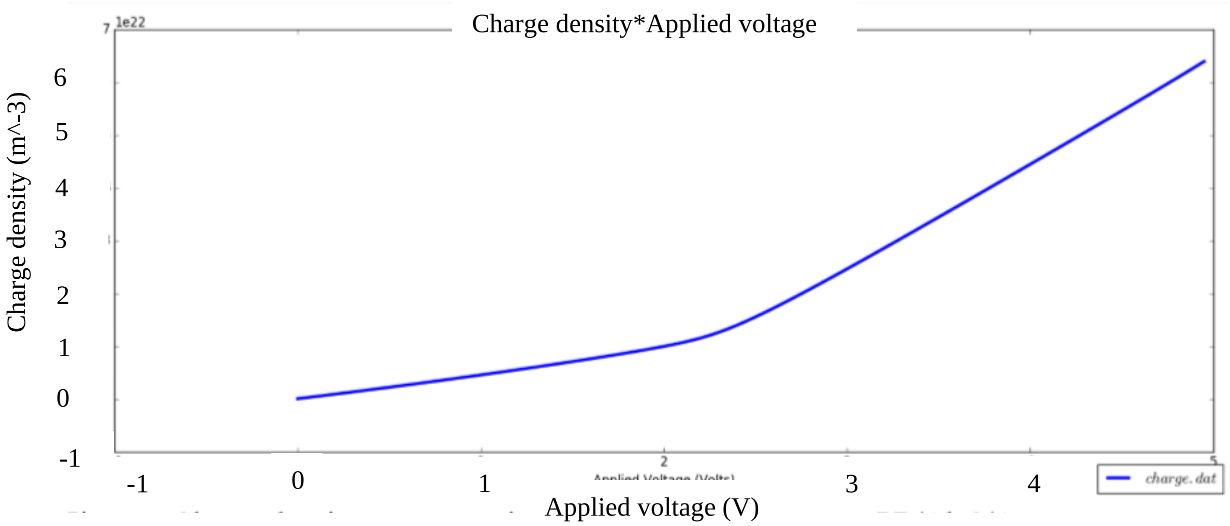

Figure H5. Charge density versus applied voltage of ITO/PEDOT/NPB/Alq3/Au.

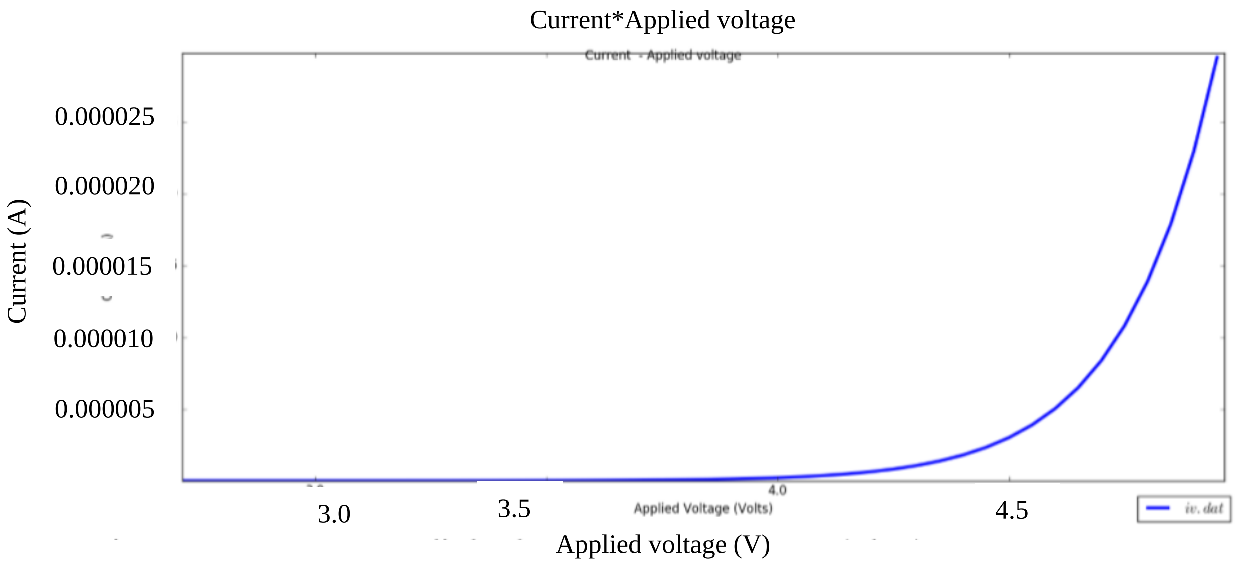

Figure H6. Current versus applied voltage of ITO/PEDOT/NPB/Alq3/Au.

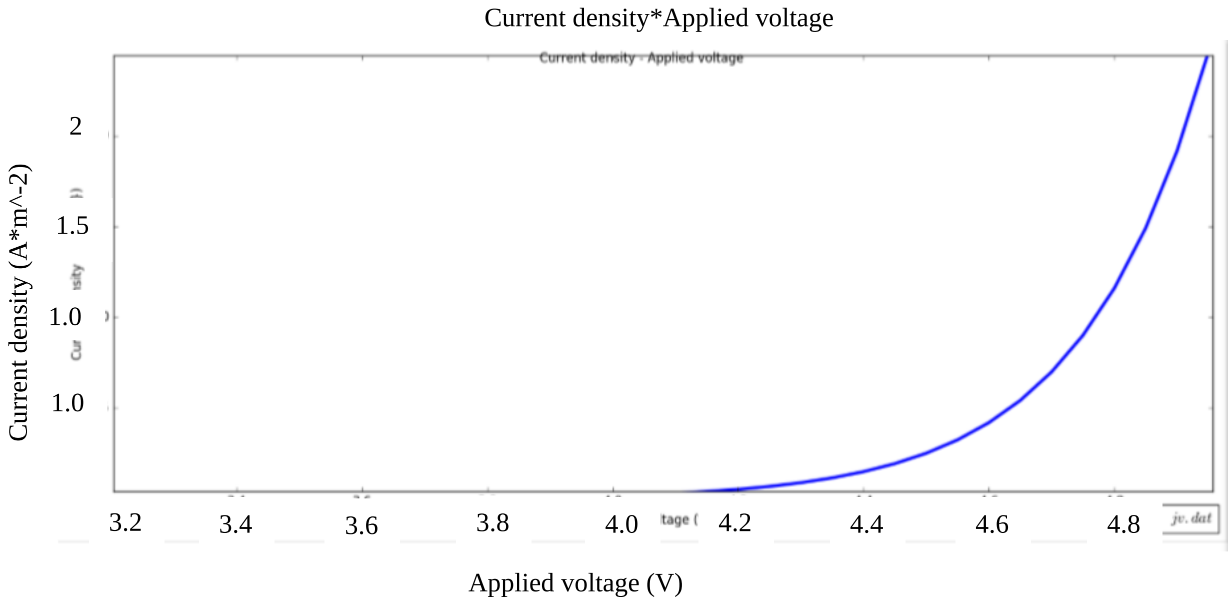

Figure H7. Current density versus applied voltage of ITO/PEDOT/NPB/Alq3/Au.

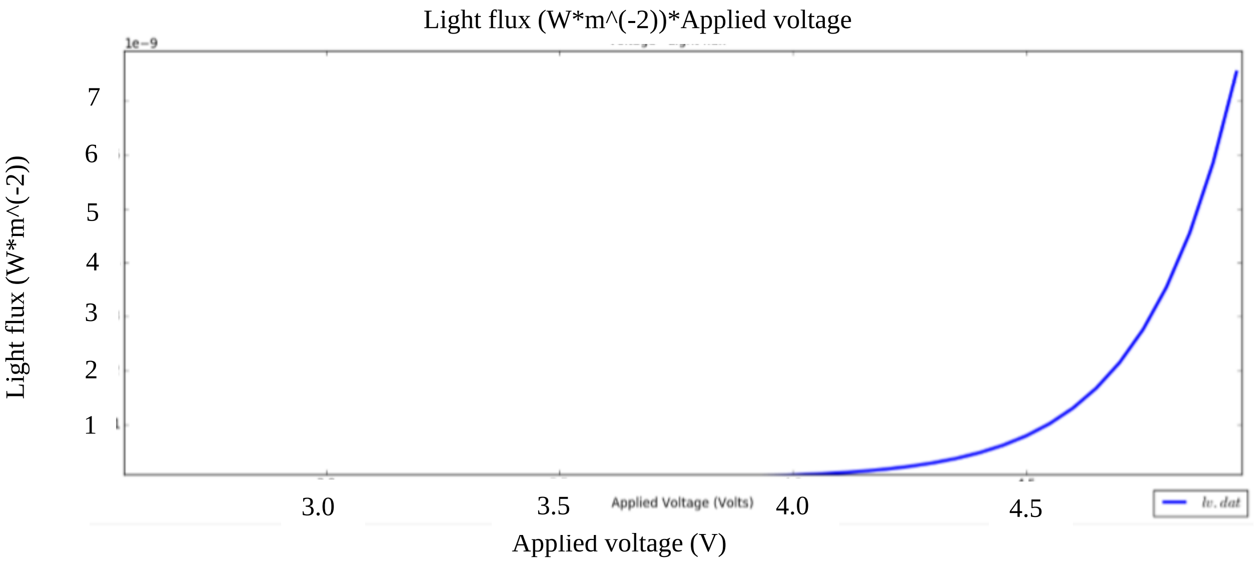

Figure H8. Light flux versus applied voltage of ITO/PEDOT/NPB/Alq3/Au.

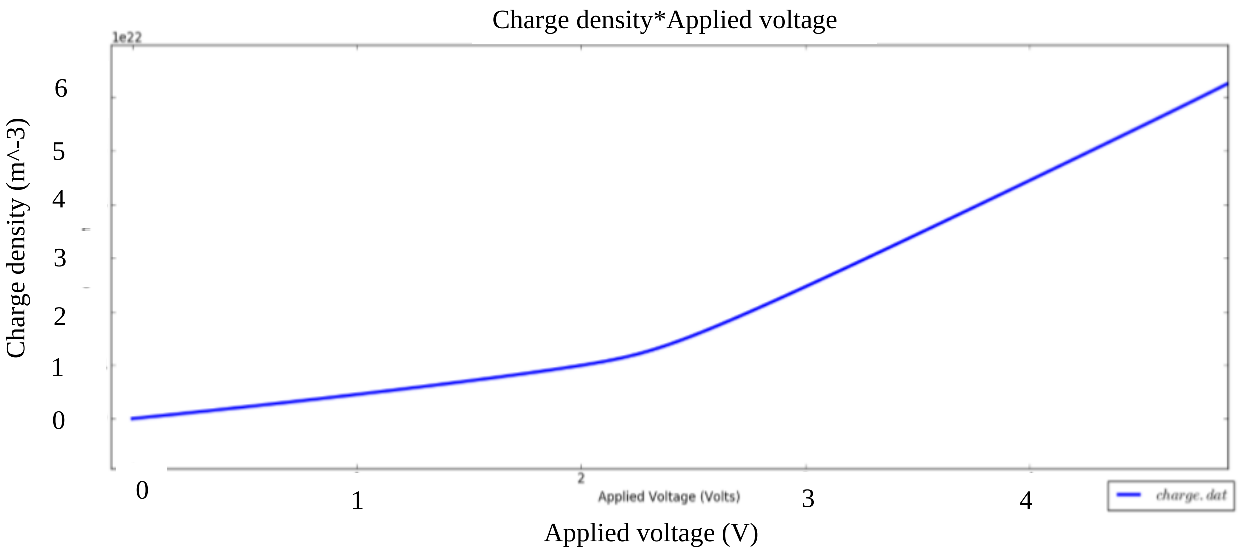

Figure H9. Charge density versus applied voltage of ITO/PEDOT/NPB/Alq3/Ag .

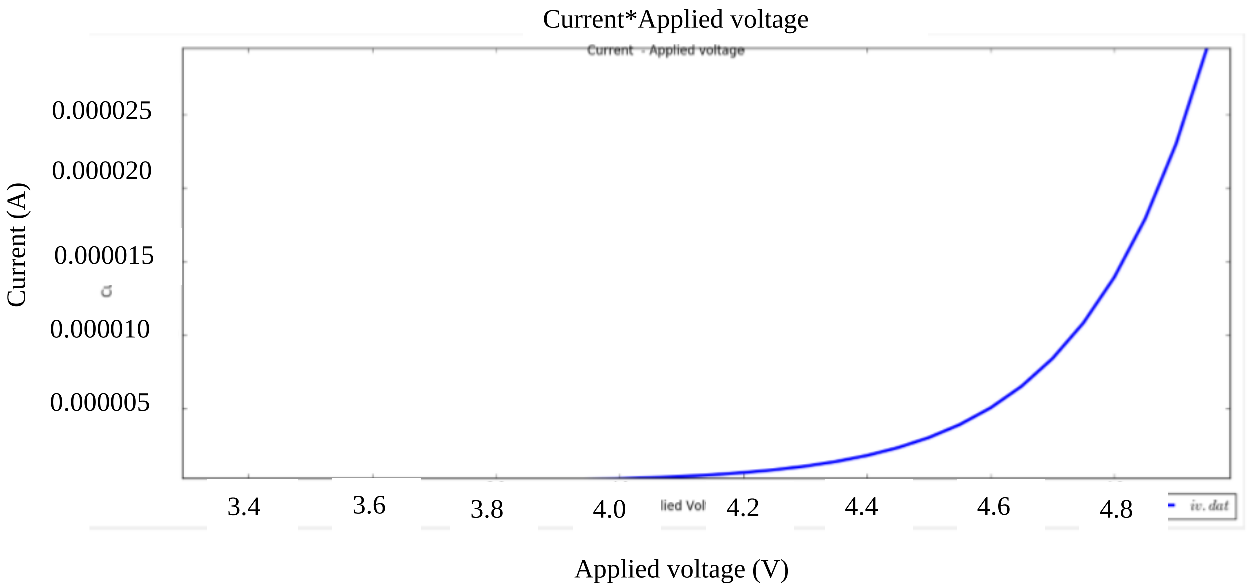

Figure H10. Current versus applied voltage of ITO/PEDOT/NPB/Alq3/Ag .

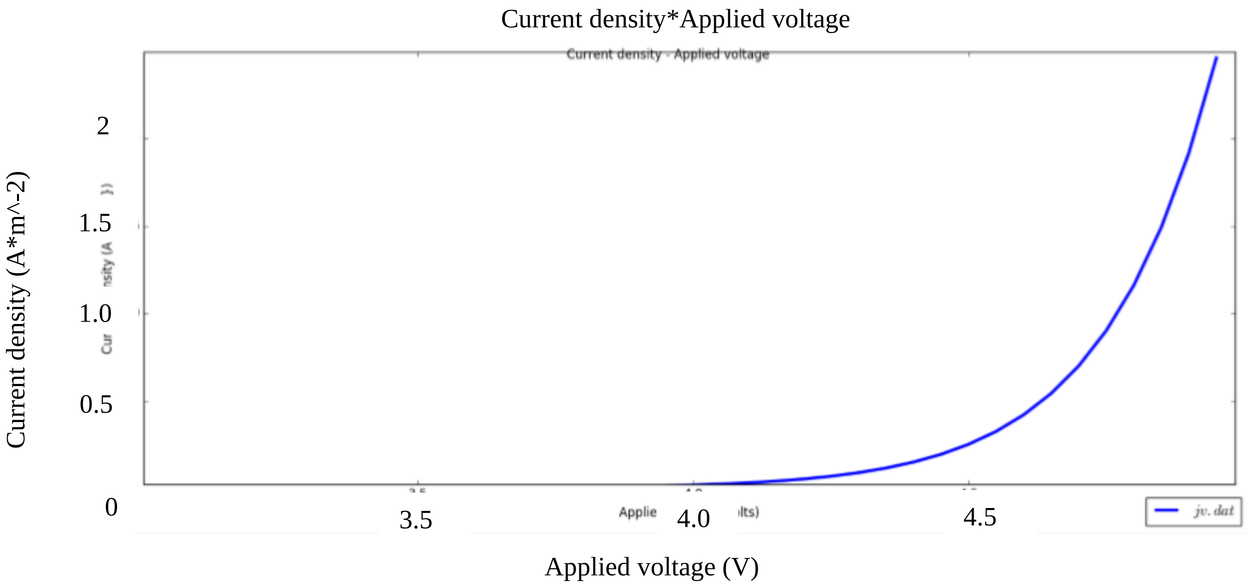

Figure H11. Current density versus applied voltage of ITO/PEDOT/NPB/Alq3/Ag .

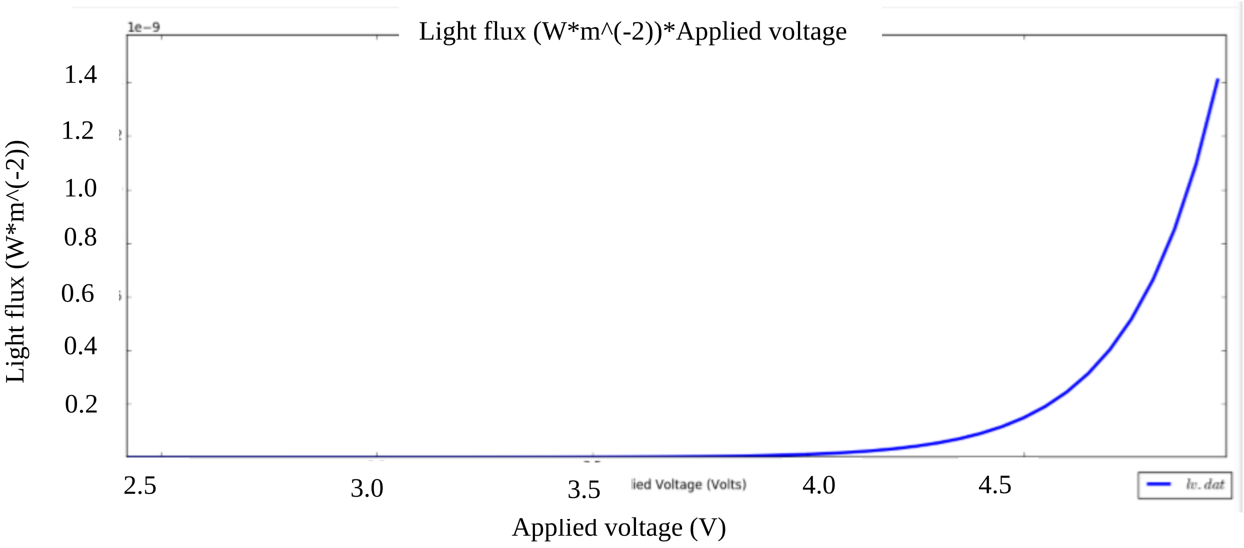

Figure H12. Light flux versus applied voltage of ITO/PEDOT/NPB/Alq3/Ag.

H3. Optimized layer thickness ITO/PEDOT/NPB/ALQ3/AG OLED

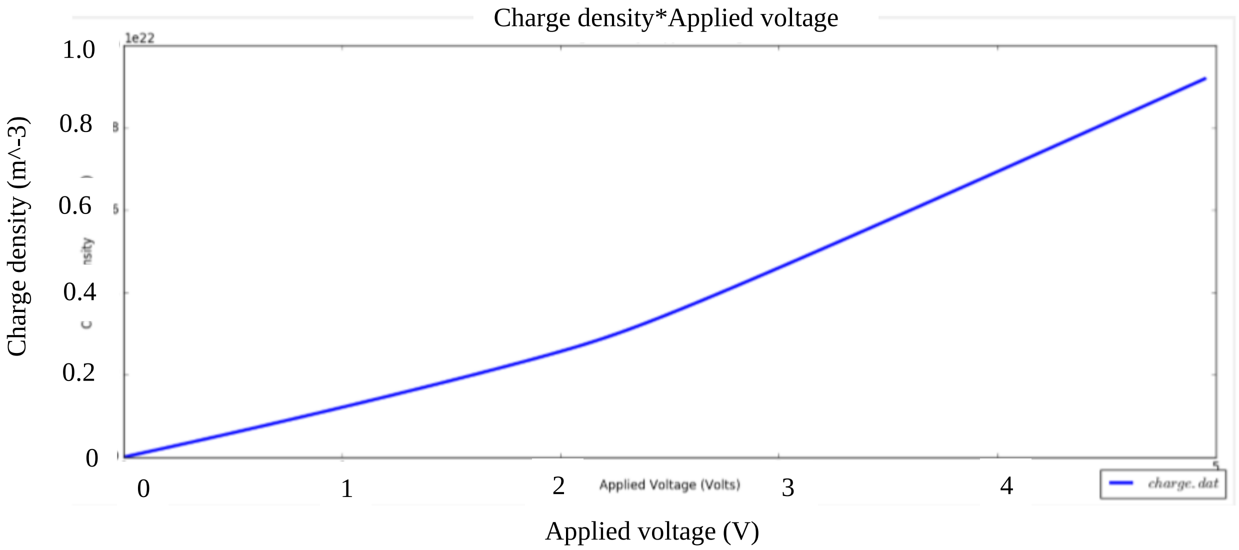

Figure H13. Charge density versus applied voltage of ITO/PEDOT/NPB/Alq3/Ag with optimal layer thicknesses.

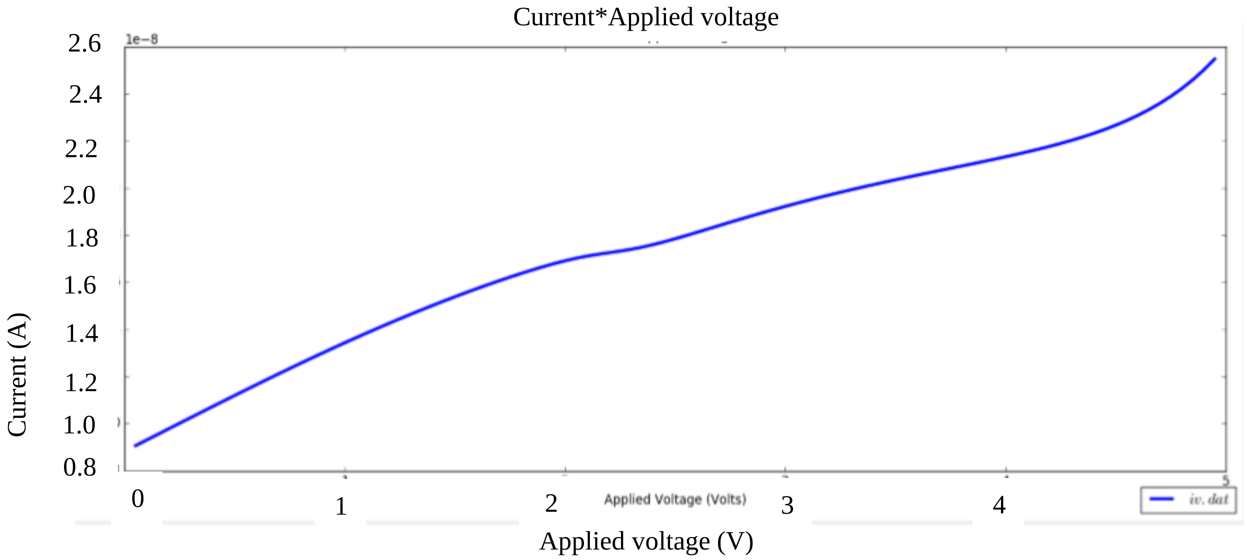

Figure H14. Current versus applied voltage of ITO/PEDOT/NPB/Alq3/Ag with optimal layer thicknesses.

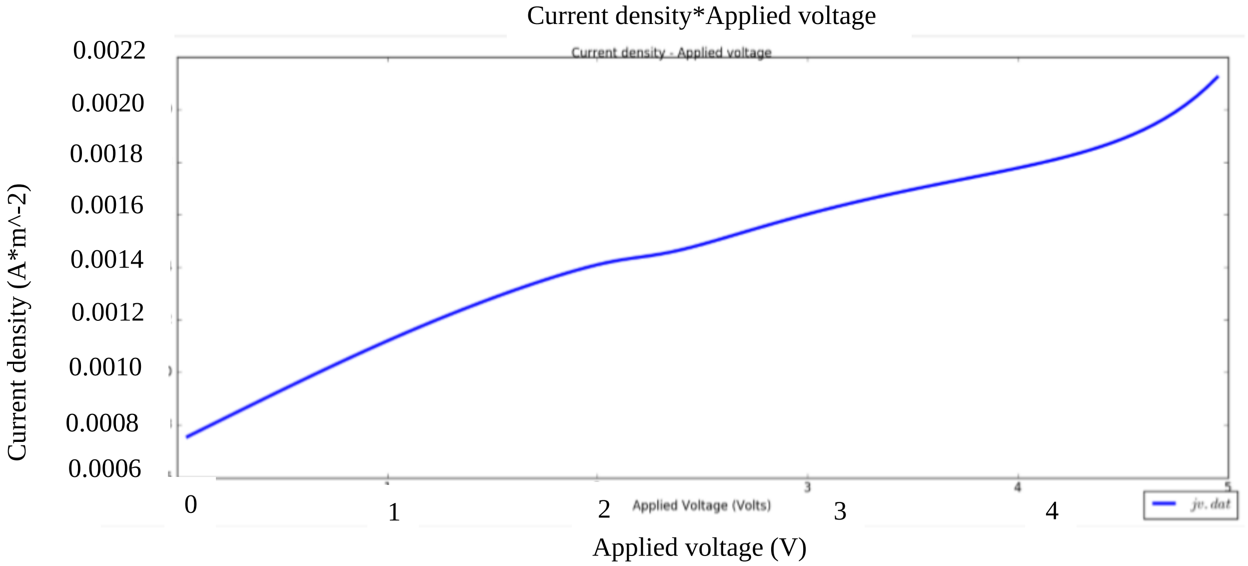

Figure H15. Current density versus applied voltage of ITO/PEDOT/NPB/Alq3/Ag with optimal layer thicknesses.

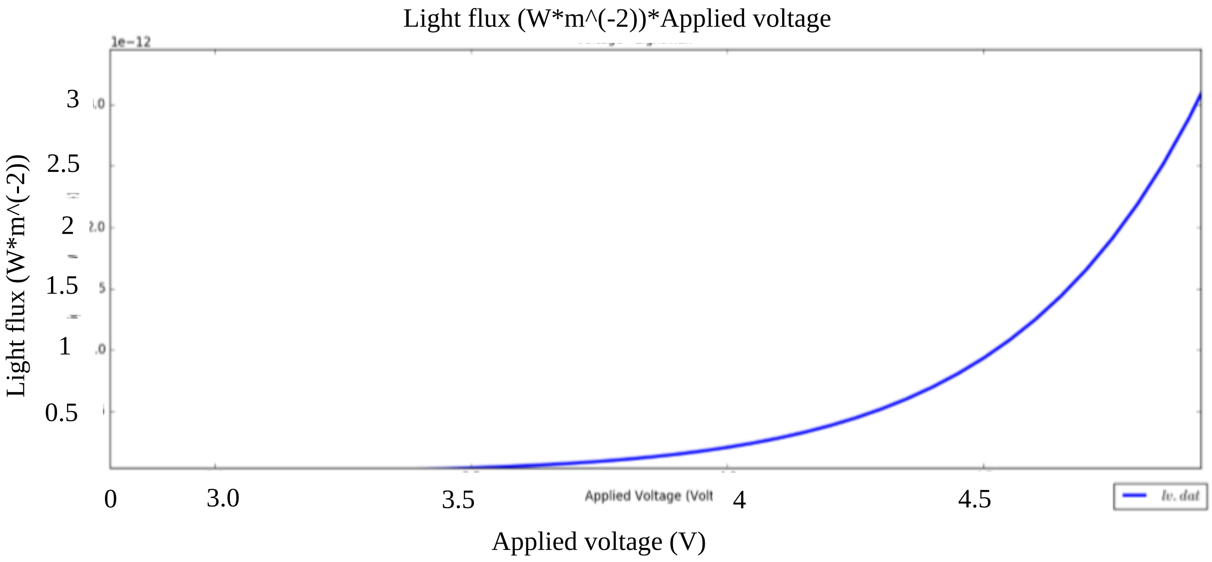

Figure H16. Light flux versus applied voltage of ITO/PEDOT/NPB/Alq3/Ag with optimal layer thicknesses.